THE UNIVERSITY OF
SYDNEY

Structural Studies of Lead-free Piezoelectrics with the Fresnoite Structure Type

A thesis submitted in fulfilment

of the requirements for the degree

of Doctor of Philosophy

Patryck K K Allen

School of Chemistry

The University of Sydney

2014

All the work presented in this thesis is my own unless otherwise stated.

Patryck Kevyn Kidd Allen

Acknowledgements

It is with great pleasure that I can take this opportunity to thank the following people and organisations for their support during what has been a challenging, yet motivating experience over the past four years:

First and foremost, I would like to send my deepest recognition and gratitude to my supervisor, Dr. Siegbert Schmid. Thank you for giving me the opportunity to work towards such an educational, challenging, and life changing experience. Thank you for your guidance, patience, and friendship throughout what has been a challenging project over the past four years. I'd also like to thank my associate supervisor, Professor Brendan Kennedy for his wise words and helpful guidance whenever I came knocking on his door.

My supervisor at The University of Cambridge, Professor Michael Carpenter for allowing me to come and work under his supervision for six weeks in The Department of Earth Sciences. You really made me feel welcome and I feel like I'm a better person because of my experiences accumulated during my time spent in Cambridge.

Beamline scientists Dr. Kia Wallwork, Dr. Qingfen Gu, Dr. Justin Kimpton for their assistance in data collection at the Australian Synchrotron, and Dr. Maxim Avdeev, Dr. James Hester and Dr. Andrew Studer for their assistance in data collection on the neutron powder diffraction beamlines at the Bragg Institute. Dr. Michael Cheah for his assistance at the ANBF during our X-ray absorption experiments.

Professor Ray Withers and Dr. Laure Bourgeois for their assistance in the collection of electron diffraction patterns and helpful discussions about modulated structures. Mr. Jason Schiemer for collecting physical property measurement data, and Dr. Hank De Bruyn for his assistance with collecting DSC data.

Associate Professor Chris Ling and the extended solid state group past and present for their ongoing guidance, support, ideas, and providing good company around the office, lab, and at Thai La Ong. A special thanks to Mr. William Brant for being a huge help with the proofreading of my work and always being willing to discuss interesting scientific and non-scientific ideas. I'm also very thankful for having Dr. Paul Saines help my feel at home in Cambridge, and Dr. Neeraj Sharma always being enthusiastic to help me out and offer new ideas and directions.

Mr Thomas Dicker for his assistance in the creation of attractive figures and animations. Your creativity and talent were a great help to me. Thank you to Mr. Doug Maiden, and Dr. Mark Butler for stimulating my interest in science as a teenager and always encouraging me to challenge myself my scientific thinking and studies.

Thank you to the University of Sydney, AINSE, AVCAT, AsCA, SCANZ, the Joan R Clark Scholarship, and the Davistown RSL club for their generous financial assistance over the years.

And of course a huge thank you to Mum, Dad, Warren, my beautiful girlfriend Wendy, and all my awesome friends for always being there to take my mind off chemistry when I needed it. Knowing that I always have your support has enabled me to maintain the confidence to continue tackling all these amazing adventures that I find myself getting involved in.

Abstract

The lead-free piezoelectric fresnoite $A_2M_3O_8$ (A = Ba, Sr, K, Cs; M = Ti, V, Si, Ge) modulated structure type has been investigated owing to its potential to exhibit excellent piezoelectric response coefficients. The $Ba_2TiSi_2O_8$, $Sr_2TiSi_2O_8$, and $Ba_2TiGe_2O_8$ end members in addition to members of the $Ba_{2x}Sr_{2-2x}TiSi_2O_8$, $Ba_{2x}Sr_{2-2x}TiGe_2O_8$, $Ba_2TiGe_{2y}Si_{2-2y}O_8$, and $BaSrTiGe_{2y}Si_{2-2y}O_8$ series were synthesised via conventional solid state synthetic methods and characterised using a combination of variable temperature electron diffraction, synchrotron X-ray powder diffraction, high resolution neutron powder diffraction and high intensity neutron powder diffraction.

The $Ba_2TiSi_2O_8$ and $Sr_2TiSi_2O_8$ modulated structures at ambient temperature were characterised using neutron powder diffraction for the first time. However, the absence or weakness of satellite reflections meant that only the average structures of many members of the $Ba_{2x}Sr_{2-2x}TiGe_{2y}Si_{2-2y}O_8$ system could be characterised. Variable temperature synchrotron X-ray diffraction data showed that the changes in the trends of the unit cell parameters a and c for $Ba_2TiSi_2O_8$ provide a new means of identifying the incommensurate to prototypic structural phase transition at 433 K even when no satellite reflections are observed. Resonant ultrasound spectroscopy has shown coupling between the elastic moduli and structural changes in fresnoite samples, demonstrating that this technique is useful for the identification and investigation of the very subtle structural changes involved in the incommensurate to prototypic phase transition in $Ba_2TiSi_2O_8$ and the 'lock-in' transition from the incommensurate to commensurate phases for $Ba_2TiGe_2O_8$.

Polycrystalline $Sr_2TiSi_2O_8$ samples were shown to undergo a first order phase transition from a two phase mixture of incommensurately modulated tetragonal and orthorhombic phases to a single incommensurately modulated orthorhombic phase that is complete by 567 K. The proportion of the orthorhombic phase in polycrystalline $Sr_2TiSi_2O_8$ samples was shown to slowly decrease (but was not completely removed) on cooling to 125 K. The $Sr_2TiSi_2O_8$ structure was

also shown to undergo an additional phase transition from the incommensurately modulated orthorhombic phase to a tetragonal phase at 1323 K for the first time.

The inclusion of barium or germanium into the $Sr_2TiSi_2O_8$ structure was shown to suppress the formation of the orthorhombic phase at ambient temperature and elevated temperatures. The maximum proportion of the orthorhombic phase formed on heating is reduced from almost 100 % in $Sr_2TiSi_2O_8$ to 30 % in $Ba_{0.2}Sr_{1.8}TiSi_2O_8$. The temperature at which the incommensurate phase transforms into the prototypic phase in the $Ba_{2x}Sr_{2-2x}TiSi_2O_8$ series linearly decreases from approximately 943 K for the $BaSrTiSi_2O_8$ member to 433 K for the $Ba_2TiSi_2O_8$ end member. Formation boundaries separating phases that do and do not form fresnoite structures occur between $0.9 \leq x \leq 1.0$ and $0.6 \leq y \leq 0.7$ for the $Ba_{2x}Sr_{2-2x}TiGe_2O_8$ and $BaSrTiGe_{2y}Si_{2-2y}O_8$ systems, respectively. New phase diagrams for the $Ba_{2x}Sr_{2-2x}TiSi_2O_8$ and $Sr_2TiGe_{2y}Si_{2-2y}O_8$ systems summarise the phase transitions investigated.

The intrinsic piezoelectric coefficients were calculated to be approximately 5 pm V^{-1} and 27 pm V^{-1} for polycrystalline samples of $Ba_2TiSi_2O_8$ and $Sr_2TiSi_2O_8$ respectively and compared to common piezoelectric materials. The absence of ferroelectricity in polycrystalline $Ba_2TiSi_2O_8$ and $Sr_2TiSi_2O_8$ samples synthesised in this project is discussed and explained in terms of the importance of the synthetic route.

Table of Contents

List of Figures

List of Tables

Glossary

ANBF	Australian National Beamline Facility
ANSTO	Australian Nuclear Science and Technology Organisation
ADP	Atomic displacement parameters that define a volume of displacement that an atom may occupy around its equilibrium position. Causes for these atomic displacements include but are not limited to atomic vibrational modes and thermal motion. ADPs in this thesis are expressed as U_{iso} for isotropic displacements and U_{11}, U_{22}, U_{33}, U_{13}, U_{12}, U_{23} for anisotropic displacements.
***Cmm*2**	Three-dimensional crystallographic space group number 35 in the international tables of crystallography. The *C* indicates *C*-centring of the Bravais lattice (with all $h + k = 2n$ reflections systematically extinct). "*X*" can be used to represent non-standard centring. The first and second "*m*" represent a mirror plane perpendicular to the [100]- and [010]-directions, respectively, and the "2" represents a two-fold rotation axis around the [001]-direction.
***Cmm*2(0, β, ½)*s*00**	Superspace setting of the *Cmm*2 space group where β represents the modulation wavevector along the **b***-direction, the "½" represents a doubling of the unit cell along *c*, and the *s* represents an hyper-glide plane.
DSC	Differential scanning calorimetry
EXAFS	Extended X-ray absorption fine structure
FWHM	Full width at half maximum height
Internal phase parameter, *t*	A parameter that defines all possible positions along the first modulation direction according to $t = \boldsymbol{q} \cdot \mathbf{T}$ (modulo an integer). "*u*" and "*v*" can be used to represent positions along the second and third modulation directions, respectively.
JCPDS	Joint Committee for Powder Diffraction Standards
Modulation	A periodic variation (*e.g.* in position, charge, spin) that propagates through a crystal.
Modulation wavevector, *q*	Additional basis vector that defines the periodicity and direction of a modulation in a crystal system.
Morphotropic Phase Boundary	An approximately temperature independent compositional boundary that separates two different ferroelectric phases.
NPD	Neutron Powder Diffraction

P*4*bm	Three-dimensional crystallographic space group number 100 in the international tables of crystallography. The *P* indicates a primitive Bravais lattice (with no systematically extinct reflections due to centring). "*X*" can be used to represent non-standard centring. The "4" represents a 4-fold rotation axis around the [001]-direction, the *b* represents a *b*-glide plane perpendicular to the [100]-direction, and the "*m*" represents a mirror plane perpendicular to the [110]-direction.
P*4*bm*(α, α, ½)0*gg	Superspace setting of the *P*4*bm* space group where α represents the modulation wavevector along the first and second modulation directions, and the "½" represents a doubling of the unit cell along *c*. The *g* represents a hyper-screw axis.
Phason	A special type of excitation corresponding to thermally excited fluctuations of the phase of the modulation function that can reduce the intensity of satellite reflections.
OPAL	Open pool Australian light-water reactor
PF	Photon Factory, a synchrotron facility in Tsukuba, Japan
Reflection	Spot of intensity produced by the constructive interference of X-rays or neutrons diffracted from a set of equivalent Bragg planes.
RUS	Resonant ultrasound spectroscopy
Satellite reflection	Reflection produced when X-rays, neutrons, or electrons are diffracted as a consequence of a frequency modulation in a structure.
Scattering factor/length	Function that describes the extent of scattering of X-rays or neutrons by an atom.
Superspace	Description of diffraction space that involves more than three basis vectors.
TEM	Transmission electron microscopy
X*4*bm	A non-standard centring condition of the *P*4*bm* space group.
***Xmm*2**	A non-standard centring condition of the *Cmm*2 space group.
XANES	X-ray absorption fine structure
XRD	X-ray diffraction

Chapter 1 Introduction

Research into new and interesting technologies has lead to the development of many devices that have seen rapid growth in a large number of different industries. The extensive use of mobile phones and laptop computers is a good example of how recent technological discoveries are being commercialised to improve convenience and productivity in the daily lives of most people in the developed world. The rapid development of such technologies would not be possible without a strong understanding of the structure and physical properties of the materials that are responsible for their functionality. Many of the materials utilised in modern technologies exhibit the unique ability to sense changes in their surrounding environment and respond with a useful action. Materials that exhibit one or more properties that can be changed in a controlled fashion by external stimuli can be defined under the term "smart materials".[1]

Smart materials are utilised in many of the technologies that are now part of the everyday lives of the majority of the developed world. They are widely applied across many industries for numerous important applications (*e.g.* piezoelectrics, pyroelectrics, electrorestrictive and magnetorestrictive materials, and shape memory alloys).[1] The concept of a smart material can be understood by considering the Toyota electronic modulated suspension shock absorber technology.[2] Road vibrations in motor vehicles are minimised by the use of a stack of piezoelectric ceramic materials that detect and respond to small vibrations in the road by producing an out of phase vibration that is amplified by a hydraulic system. The hydraulic response produces a force that suppresses the amplitude of the vibrations experienced by the vehicle and its passengers.

The market for smart materials in the electronics industry is currently dominated by compounds that have been shown to have negative effects on humans and the environment due to the presence of lead in their structure. Human exposure to lead has been shown to cause headaches,

nausea and stomach pains, in addition to more serious health problems including kidney, nerve, and brain damage after prolonged uncontrolled exposure.[3]

The large scale manufacture and irresponsible disposal of lead-based electronic components contributes to the release of large quantities of toxic lead oxide into the environment, leading to extensive pollution in many forms. The primary environmental risk is the leaching of lead into the soil where it can easily enter the waterways and affect humans and animals through processes of bioaccumulation. The Japanese government and the European Union have been the first bodies to adopt the recently updated Restriction on the use of Hazardous Substances (RoHS) regulations that control the production of electronic equipment that contains hazardous substances.[4,5] Adding to the push to minimise the use of lead in the electronics industry, China, the world's leading manufacturer of electronic components, has also recently adopted the new RoHS regulations. The RoHS regulations currently contain specific exemptions including lead in ceramic materials and solders for electronic infrastructure, however it is only a matter of time until these exemptions are removed. Currently, no viable alternatives to many of the smart materials in these categories have been developed.

The minimisation of the use of lead in electronic components has created a need to investigate possible lead-free alternatives to replace the lead-based materials that currently dominate the electronics market. However, no lead-free alternatives to many electronic materials have yet been discovered that exhibit comparable physical properties to the current lead-based materials. A comprehensive understanding of the underlying structural chemistry of electronic materials is crucial for the development of novel, environmentally friendly smart materials with comparable physical properties to the currently available lead-based compounds.

1.1 Smart Materials

The term smart materials can be used to classify a wide range of materials with different properties and applications, depending on their specific structure-property relationships. External stimuli that can be used to control the physical properties of smart materials include mechanical stress, temperature, electric and magnetic fields, moisture and pH.

Different physical properties of smart materials are defined by their unique relationship between different variables. Figure 1.1 illustrates the relationship between three common variables for smart materials, where the arrows define the physical properties between each set of two variables.

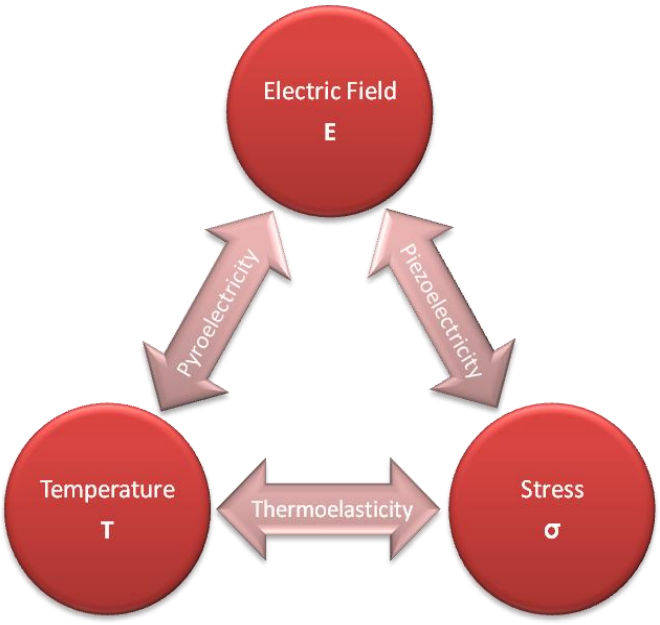

Figure 1.1: A representation of the physical properties that relate electrical, mechanical, and thermal changes to a system. Quantities at the vertices represent environmental variables, and the connecting arrows define the property related to each set of two variables.

1.2 The Structure of Smart Materials

Studies of the change in crystal structure versus composition, temperature, pressure, or electric field are extremely important for the understanding of the physical properties of materials. Atomic positions and electron density distribution determine the extent of the electrical polarisation that is directly responsible for many of the properties that smart materials are used for. Understanding the symmetry and how the polarisation changes as a function of different environmental variables is critical for the development of some of the most important types of smart materials to meet the needs for a growing number of important applications.[6]

1.2.1 Crystal Symmetry and Point Groups

There exists a strong relationship between physical properties and the crystal structure of a material; particularly the symmetry of the crystal structure.[7] A comprehensive understanding of the complex structure-property relationship is essential for the development of new materials with special properties for specific applications.

Piezoelectricity, for example, is only possible in structures that do not contain a centre of inversion in the symmetry of their unit cell (*i.e.* the unit cell must be noncentrosymmetric). The inversion centre means that any preferential direction of charge distribution within the unit cell (dipole moment) will be cancelled out by an equal and opposite distribution of charge elsewhere in the unit cell. Hence, only structural arrangements that do not contain an inversion centre (non-centrosymmetric structures) are capable of exhibiting a net dipole within their unit cell and hence exhibit the potential to display piezoelectricity.

Figure 1.2 illustrates the hierarchy of point group symmetries according to their potential to allow a material to display some common properties of smart materials. The symmetry about a

point in space can be completely described by 1 of 32 point groups, where each point group is defined by a set of "self consistent" symmetry elements. In this context, "self consistent" refers to the ability to return the starting point to its original position in a finite number of steps. Point groups are formed from either individually occurring or combinations of inversion centres (represented with an overbar), rotational axes (represented by a number that defines the symmetry of the rotation) and/or mirror planes (represented by *m*).[8]

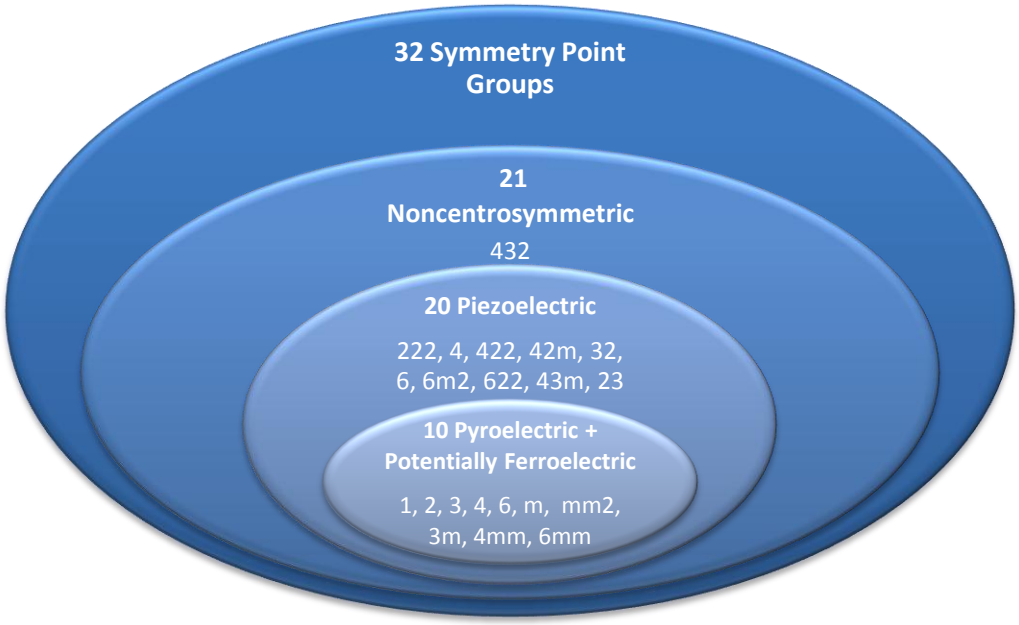

Figure 1.2: The hierarchy of the 32 point group symmetries according to their potential to display piezoelectricity, pyroelectricity, and ferroelectricity.

Only 21 of the 32 possible symmetry point groups are non-centrosymmetric. Of these 21 non-centrosymmetric point groups, 20 contain a combination of symmetry operators that permit an electric dipole to be induced by compressional and torsional stresses, leading to piezoelectricity. The one non-centrosymmetric point group that does not exhibit piezoelectricity is the 432 group, which contains a combination of rotational symmetry operators that cancel any dipole in the unit cell, despite the absence of an inversion centre.

10 of the 20 piezoelectrically active point groups are categorised as pyroelectric. Pyroelectric point groups allow an intrinsic macroscopic polarisation in a material due to a permanent electric dipole moment along a unique polar (symmetry) axis. This is only possible when every symmetry operation leaves more than one common point unmoved, creating a unique direction that is not repeated by other symmetry operations. Point groups cannot exhibit a unique direction if any combination of the symmetry elements defines a fixed origin within the unit cell. For example, the point of intersection of the three 2-fold axes in the 222 point group defines an origin, preventing the definition of a unique direction in the structure, hence preventing pyroelectricity.

All compounds with a unique polar axis (*i.e.* compounds with pyroelectric point groups) also have the ability to exhibit ferroelectricity. Ferroelectricity is defined as the phenomenon whereby the direction of the spontaneous electric dipole moment can be reversed by the application of an electric field. All ferroelectric materials exhibit pyroelectricity and piezoelectricity, but the converse is not necessarily true. The observation of ferroelectricity in pyroelectric materials is dependent on material- or sample-specific factors such as whether the field required to reverse the dipole (coercive field, $\pm E_c$) is greater than the electrical breakdown field (the field at which the resistivity suddenly decreases) and the degree of domain wall mobility.

The ability to reverse the spontaneous dipole moment within ferroelectric materials has led to their widespread application in the electronics industry. The typically high dielectric constants and electrical hysteresis have made ferroelectric materials extremely desirable for application in modern technologies owing to their potential to store large amounts of electrical energy and their unique polarisation properties which creates the ability to reverse their dipole into one of two possible polarisation states.[9-11] The different types of polarisation behaviour are discussed in the following section.

1.2.2 Polarisation of Materials

1.2.2.1 Dielectric materials

Materials with poor conductivity typically exhibit a linear relationship between an applied electric field and the induced polarisation. Materials such as diamond and water exhibit a linear dielectric relationship (Figure 1.3A). The linear relationship between an applied electric field and induced polarisation means that removal of the electric field will remove the polarisation from the material. Hence, dielectric materials display no memory of previously applied electric fields. Although dielectrics have been widely utilised in electronics (specifically as a means of increasing the amount of energy that can be stored in capacitors), most applications of dielectric materials involve a nonlinear relationship between the applied electric field and the induced polarisation.

1.2.2.2 Paraelectric materials

Paraelectric materials exhibit a nonlinear relationship between an applied electric field and polarisation with the condition that the polarisation can be returned to zero by switching off the applied field (Figure 1.3B). Examples of paraelectric materials include Al_2O_3 and TiO_2.[12] Neither dielectric nor paraelectric materials contain any remanent polarisation after the electric field has been switched off.

1.2.2.3 Hysteretic materials

Materials that exhibit a nonlinear relationship between induced polarisation and applied electric field, and display a remanent polarisation after the applied field has been switched off are said to display a special property called electrical hysteresis. Materials such as $BaTiO_3$ and $PbTiO_3$ are examples of hysteretic materials that have been used in a large range of lucrative applications in the electronics industry.[11,13]

The general term hysteresis describes a phenomenon that involves a remanent effect being present in a material after the original cause has been removed. Hysteresis is not only limited to an electrical context, but can be applied to other physical properties, including elasticity and magnetism. Figure 1.3C illustrates a typical hysteresis curve where an increase in applied electric field nonlinearly increases the induced polarisation through the reorientation of the polarisation vectors from random orientations into alignment at the saturation point.

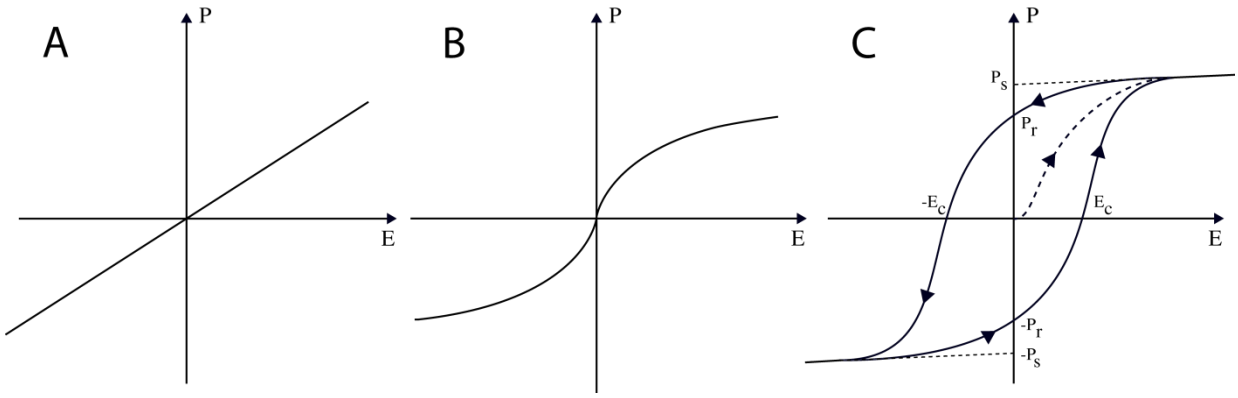

Figure 1.3: The linear dielectric (A), nonlinear paraelectric (B), and nonlinear ferroelectric (C) relationship between induced polarisation (denoted P) and applied electric field (denoted E). For the ferroelectric case, the polarisation is induced nonlinearly up to the saturation point when the electric field is applied. A remanent polarisation, P_r, remains when the applied electric field is removed. The polarisation can be returned to zero by applying a reversed electric field of magnitude $-E_c$.

Applying a stronger field beyond the saturation point will linearly increase the net polarisation by virtue of the intrinsic dielectric properties of the material. This increase in polarisation is achieved by increasing the magnitude of each individual polarisation vector until the electrical breakdown field is reached. Extrapolation of the linear dielectric component to zero field (Figure 1.3C) yields the magnitude of the spontaneous polarisation, $\mathbf{P_s}$, which represents the polarisation of the material with all of the spontaneous dipole moments aligned at zero applied field. A memory-effect is observed in materials that display electric hysteresis because a remanent polarisation, P_r, exists after the applied field has been switched off. A coercive electric field, $-E_c$, is required to return the net polarisation of the material back to zero. The induced polarisation can be cycled back and forth between positive and negative polarisation by changing the direction of

the applied electric field. This physical behaviour is caused by a reversal in the direction of the ionic displacements within the unit cell, which reverses the direction of the dipole along the unique polar axis, and hence changes the sign of the polarisation in the material.

The memory associated with the remanent polarisation has been shown to be an extremely useful property for the development of many new technologies, particularly in the development of new non-volatile memory devices for computational applications.[1,10,13,14]

1.2.3 Thermally-induced phase transitions

The relationship between structure and temperature is of high importance when considering the development and application of all materials. Changing the temperature of a material can induce significant structural changes and hence alter the physical properties of the material. Considerable research interest has been directed towards the investigation of changes in the crystal symmetry of materials across a wide range of possible operating temperatures.[9,10,15]

A thorough understanding of the changes that occur in a structure through a phase transition allows the identification and prediction of changes in physical properties for compounds of congruent or similar structure types. Hence, developing a comprehensive understanding of the structure and phase transitions of new and existing compounds is essential for the development of new materials with specifically designed structures that exhibit optimised physical properties.

At higher temperatures, compounds will typically exist in higher symmetry arrangements. For example, ferroelectric materials will only exhibit a spontaneous net polarisation below the Curie temperature, T_C, where a phase transition occurs from the low temperature ferroelectric phase into the high temperature paraelectric phase. Piezoelectric, pyroelectric, and ferroelectric materials must be operated at temperatures below T_C to ensure that the structure is in a

noncentrosymmetric arrangement, such that the desired physical properties can be observed. The T_C for a sample is highly dependent on its structure and composition, and must be carefully considered in the design of new materials.

1.3 Physical Properties of Common Smart Materials

There are many different ways that smart materials can respond to changes to their external environment. Piezoelectricity, pyroelectricity, ferroelectricity, and ferroelasticity are particularly interesting phenomena that are examples of properties that can define a material as a smart material. These properties are briefly discussed below.

1.3.1 Piezoelectricity

Piezoelectricity describes a unique relationship between electrical polarisation and mechanical stress in a crystalline material. The direct piezoelectric effect describes the phenomenon of the generation of an electric potential in response to an applied mechanical stress. The inverse piezoelectric effect describes the instance where the application of an electrical potential induces a mechanical strain into the material. Both effects are manifestations of the same fundamental relationship between internal electrical polarisation and mechanical stress.

There are two broad classes of piezoelectric materials. Non-ferroelectric piezoelectrics contain spontaneous dipoles that cannot be reoriented to align with each other on the application of an electric field. As a consequence of this, non-ferroelectric piezoelectrics (*e.g.* quartz or tourmaline) generally exhibit lower piezoelectric response coefficients than ferroelectric piezoelectrics (*e.g* $BaTiO_3$).[16,17] Ferroelectric piezoelectrics contain spontaneous dipoles that can be reoriented to align with each other in one of two or more possible directions. This can be achieved by the application of an electric field across the sample. The ability to reverse the direction of the dipoles

is the defining feature that makes a material ferroelectric. The presence of a remnant polarisation due to the aligned spontaneous dipoles remaining aligned after the applied electric field has been removed is the reason that ferroelectric piezoelectrics are capable of displaying electrical hysteresis. Ferroelectric piezoelectrics can occur in the form of single crystals or polycrystalline samples. Single crystal ferroelectrics usually contain a small number of ferroelectric domains which can be aligned by an electric field via a process called poling.[1,18,19] However, most ferroelectric piezoelectrics are polycrystalline materials that are comprised of many randomly oriented crystallites that contain randomly oriented domains (and hence, randomly oriented dipoles). Without external treatment, the random distribution of the dipoles produces a significantly lower piezoelectric response across the whole material than when the dipoles are all in alignment. Poling changes the material from containing an isotropic (or close to isotropic) distribution of dipoles to possessing a strong net dipole in a direction relative to the applied field. Poling cannot be performed on non-ferroelectric materials because they lack the ability to re-orient their dipoles.

The process of poling is illustrated in Figure 1.4A-B, where a net polarisation is induced in a material by the application of a strong electric field. Figures 1.4C-D represent generator actions, where a ceramic material converts the mechanical energy of compression or tension into electrical energy. Compression *along* the direction of the polarisation (or alternatively applying tension *perpendicular* to the direction of polarisation) generates a voltage of the *same polarity* as the poling voltage (Figure 1.4C). Alternatively, tension *along* the direction of polarization (or compression *perpendicular* to the direction of polarization) generates a voltage with *opposite* polarity to that of the poling voltage (Figure 1.4D). The relationship between the electrical potential produced and the applied mechanical stress is linear up to the materials specific stress limit. Poled piezoelectric ceramics such as $BaTiO_3$, $PbTiO_3$, or $PbZr_{0.48}Ti_{0.52}O_3$ are widely used in fuel-igniting devices, force-sensing devices, and many other applications.[20]

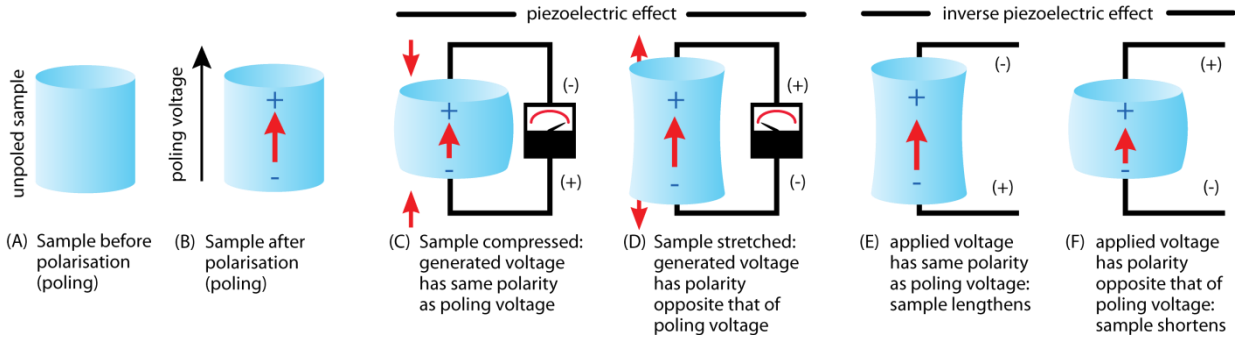

Figure 1.4: Generator and motor actions of a poled piezoelectric material. Adapted from "Piezoelectric ceramics: principles and applications".[20]

Figures 1.4E-F illustrate the motor action of the inverse piezoelectric effect. The application of a potential difference across the poled piezoelectric ceramic produces a mechanical distortion within the crystal structure. If a voltage of the same polarity as the poling voltage is applied to a ceramic material in the direction of the poling voltage, the element will lengthen and its diameter will become smaller (Figure 1.4E). If a voltage of polarity opposite to the poling voltage is applied, the material will become shorter and broader (Figure 1.4F). If an alternating voltage is applied, the element will lengthen and shorten cyclically (vibrate) at the frequency of the applied voltage. This principle is applied to piezoelectric motors, sound or ultrasound generating devices, inkjet printers, and many other products.[20] Equation 1.1 describes the linear relationship between the induced polarisation of a crystal, **P**, the piezoelectric coefficient d, and the mechanical stress σ experienced by the crystal.

$$\mathbf{P}_{ij} = d_{ij}\sigma_{\mathrm{ij}} \qquad \textbf{Equation 1.1}$$

The piezoelectric coefficient, d_{ij} (C N^{-1}), represents the relationship between the induced polarisation, $\mathbf{P}_{ij}$, and the mechanical stress (σ_{ij}) in the crystal structure. The anisotropic properties of ceramic samples means that the piezoelectric coefficient can be described in a variety of ways. Because the piezoelectric coefficient is dependent on the direction of the applied field and the piezoelectrically induced strain, two subscript numbers define these directions. The first number, i, defines the direction of the applied field relative to the polarisation. The second

number, *j*, defines the direction of the induced strain. The direction of positive polarisation is conventionally defined as the 3-axis, which coincides with the *z*-axes of an orthogonal *xyz* system. The directions of the 1- and 2-axes correspond to the *x*- and *y*-axes respectively, to form an orthogonal set of axes. The 4-, 5-, and 6-directions correspond to shear about the 1-, 2-, and 3-axes, respectively (Figure 1.5). d_{33} is the most commonly quoted piezoelectric coefficient, describing the response when the electrodes are oriented perpendicular to the 3-axis and the piezoelectrically induced strain is parallel to the 3-axis.

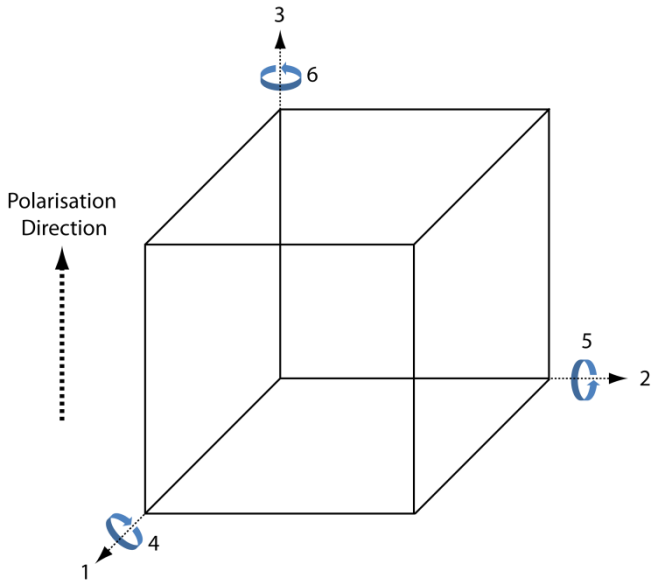

Figure 1.5: A representation of the different directions that can be quoted with the piezoelectric coefficient. The 3-axis is defined as the direction of positive polarisation. The 1- and 2-axes complete an orthogonal axis set relative to the 3-axis. The 4-, 5-, and 6-directions correspond to shear movements around the 1-, 2-, and 3-axes, respectively.

The magnitude of the induced voltage, movement, or force produced in a piezoelectric material is typically very small. A piezoelectric ceramic will usually only increase or decrease in thickness by a fraction of a millimetre when acted on by an applied voltage. A process of amplification is required to increase the piezoelectric response of a material by at least several orders of magnitude to produce a response that is sufficient for commercial applications.

1.3.2 Pyroelectricity

Although all pyroelectric materials exhibit piezoelectricity (*c.f.* section 1.2.1), they are unique because the magnitude of their spontaneous polarisation vector is temperature dependent. Changes in temperature change the magnitude of the polarisation in the material through induced structural distortions (*e.g.* changing the size of the unit cell relative to the polarisation vector).[21] This means that the magnitude of the electric potential across a pyroelectric material can be controlled through processes of heating or cooling (Figure 1.6).

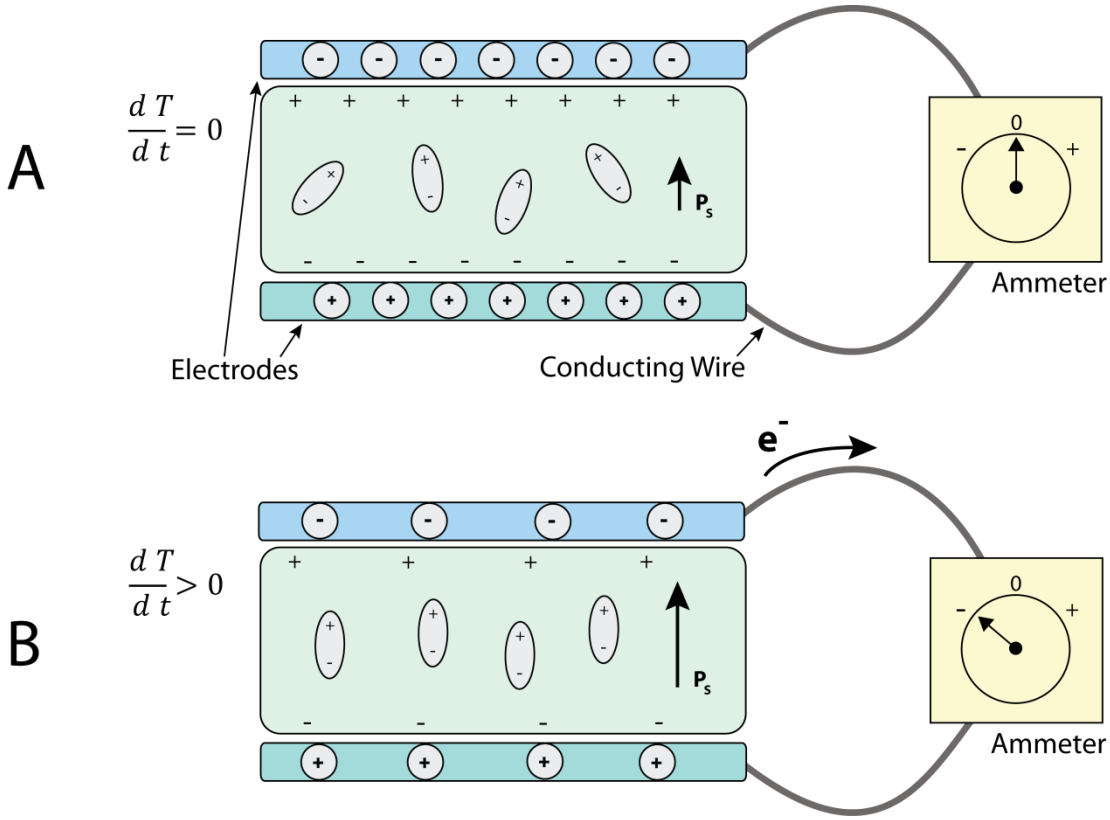

Figure 1.6: An example of a pyroelectric sample with a spontaneous polarisation at constant temperature with no current flow (A), and reduced polarisation due to current flow through an external circuit when the temperature is increased (B).

Pyroelectric materials exhibit a linear relationship between the change in polarisation $\Delta \mathbf{P}_{ij}$ and the change in temperature ΔT (Equation 1.2). The pyroelectric coefficient, p_i, describes the ratio of these quantities for a given material under constant stress and electric field (Equation 1.3). Pyroelectricity is utilised for many applications, including but not limited to intrusion alarms, thermal imaging, and geographical mapping.[22]

$$\Delta \mathbf{P}_{ij} = p_i \Delta T \qquad \textbf{Equation 1.2}$$

$$p_i = \left(\frac{\partial \boldsymbol{P_s}}{\partial T}\right)_{\boldsymbol{E},\boldsymbol{\sigma}} \qquad \textbf{Equation 1.3}$$

1.3.3 Ferroelectricity

The phenomenon of ferroelectricity was discussed in section 1.2.2.3. The applications of ferroelectric materials are widespread because of their ability to retain a remanent net polarisation after the application of an electric field. The ability to reverse the direction of the remanent polarisation vector is of crucial importance in technological applications because it allows one of two distinguishable states to be defined for digital data storage and non-volatile memory.[11]

1.3.4 Ferroelasticity

Ferroelasticity can be understood through direct analogy with ferroelectricity. While ferroelectricity describes the phenomenon involving the use an external electric field to align the spontaneous dipoles in a material, producing hysteresis, ferroelasticity describes a similar hysteretic relationship between applied stress and induced strain within the structure.

Ferroelasticity in a material is caused by stress-induced movement of domain boundaries which requires the crystal structure to distort to accommodate the induced stress. Specifically, a material is classified as ferroelastic if it can be transformed reversibly between two or more potential orientation states that differ in spontaneous strain. The transformation does not involve diffusion through the material or the breaking of any primary chemical bonds. Rather, the transformation involves small displacements of some atoms by less than ~0.1 Å that changes the symmetry or orientation of the crystal structure.[23]

1.4 Examples of Common Piezoelectric Materials

1.4.1 The Early Days

Rochelle salt, $KNaC_4H_4O_6 \cdot 4H_2O$, was one of the first materials that was shown to exhibit piezoelectricity.[13,14] Although single crystals of Rochelle salt can be easily grown, they are water soluble, and the piezoelectric response is very small relative to many other piezoelectric materials such as quartz.[24]

Quartz is a commonly used piezoelectric material that is a highly abundant and naturally occurring mineral with the composition SiO_2. Quartz was first commercialised in the form of a quartz oscillator in 1921, and has since been applied to a wide range of simple piezoelectric applications because of its ease of growth and extremely low cost relative to other piezoelectric materials such as $BaTiO_3$.[25]

Quartz is only useful for relatively simple piezoelectric applications because it is a non-ferroelectric material. This is significant because the range of potential applications of quartz is limited by its relatively small piezoelectric response that cannot be improved by poling. This important limitation has meant that ferroelectric piezoelectric materials have had to be developed to meet the needs of more complex technologically based applications.

1.4.2 Perovskite-type Compounds for Piezoelectric Applications

The perovskite structure of general formula ABX_3 can be described with a simple cubic unit cell consisting of a large cation (*A*) on the corners, a smaller cation (*B*) in the body centre, and oxygen or halide ions (*X*) in the centre of each unit cell face. The structure is a network of corner-linked oxygen or halide octahedra, with the smaller cation existing at the centre of the octahedra. The large cation is located in the dodecahedral positions at the corners of the unit cell (Figure 1.7).

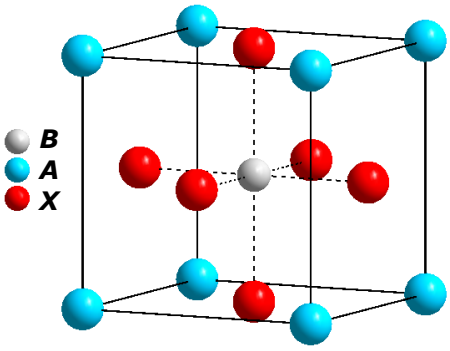

Figure 1.7: The general perovskite structure ABX_3, consisting of a large cation (*A*) on the corners, a smaller cation (*B*) on the body centre, and oxygen or halide ions (*X*) in the centre of each unit cell face.

The first perovskite observed to exhibit ferroelectricity was $BaTiO_3$, which contains a tetragonal distortion from the cubic perovskite structure at room temperature. The tetragonal distortion is responsible for the removal of the inversion centre and the origin of the ferroelectric properties. It was found that the physical properties of $BaTiO_3$ could be improved at room temperature by partially substituting some of the barium ions on the *A*-site with strontium ions.[26,27] In recent times, many members of mixed occupancy solid solutions have been investigated for their improved physical properties relative to their end members. The $PbZr_{1-x}Ti_xO_3$ ($0 \leq x \leq 1$) range of compositions has received a significant amount of research interest and includes the most successfully commercialised piezoelectric material to date.

1.4.2.1 The lead zirconate titanate system, $PbZr_{1-x}Ti_xO_3$ ($0 \leq x \leq 1$)

The $PbZr_{1-x}Ti_xO_3$ (PZT), ($0 \leq x \leq 1$) system contains multiple phases, depending on the relative amount of titanium and zirconium ions on the *B*-site of the perovskite structure (see Figure 1.8). The exact composition of $PbZr_{1-x}Ti_xO_3$ determines which space group symmetry will be adopted by the structure.[28] A morphotropic phase boundary is present in the PZT phase diagram at approximately $x = 0.52$. A morphotropic phase boundary is defined as a temperature independent compositional boundary that separates two different ferroelectric phases.[29] Until the year 2000, the morphotropic phase boundary in the PZT phase diagram was understood to divide a ferroelectric rhombohedral (*R*3*m*) phase from a ferroelectric tetragonal (*P*4*mm*) phase.[30] However, Singh *et al.*[31] established that the previously understood rhombohedral phase could be more correctly described using a pseudo-rhombohedral phase with monoclinic (*Cm*) symmetry. There is still considerable debate regarding the specific space group or groups present at compositions close to $x = 0.52$ below 200 K. The phase diagram for the $PbZr_{1-x}Ti_xO_3$ system showing the regions of the various monoclinic and rhombohedral phases is provided in Figure 1.8.[32]

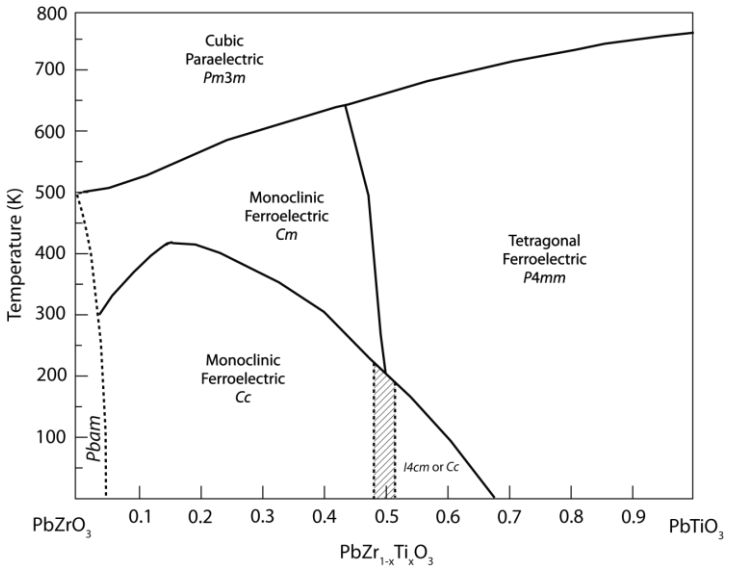

Figure 1.8: Phase diagram for the $PbZr_{1-x}Ti_xO_3$ ($0 \leq x \leq 1$) system including the morphotropic phase boundary between the ferroelectric monoclinic and ferroelectric tetragonal phases. Adapted from Welberry *et al.*[33] and Pandey *et al.*[32]

PZT is most commonly synthesised with the composition $PbZr_{0.48}Ti_{0.52}O_3$ such that the structure is poised near the morphotropic phase boundary between the monoclinic and tetragonal distortions of the perovskite structure above ~200 K.[32] Synthesising PZT with compositions close to the morphotropic phase boundary is desirable because of the increased dielectric and piezoelectric response coefficients observed.[1,24,29] The understanding of the reasoning behind the improved physical properties near the morphotropic boundary in PZT has significantly improved in recent years. When it was believed that a rhombohedral phase existed, the improved physical properties near the morphotropic phase boundary were attributed to the increase from either six or eight to a total of fourteen possible poling directions due to the coexistence of the tetragonal and rhombohedral phases at the morphotropic phase boundary (six [100] directions from the tetragonal phase and eight [111] directions from the rhombohedral phase) (see Figure 1.9A and B).[34,35] However, Pandey *et al*. recently reported that the previously believed rhombohedral region is actually a monoclinic *Cm* region.[32] The improved physical properties can be better explained with the presence of a monoclinic phase on one side of the morphotropic phase boundary because the number of possible poling directions is dramatically increased due to the polarisation vector in the monoclinic phase being free to orient in any direction in the (110)-plane (Figure 1.9C).[32] The polarisation vector can therefore easily align itself with the external electric field, improving the electromechanical response. This explanation has also been supported by first principles calculations on PZT which show that the freedom of the polarisation vector is responsible for the maximised ferroelectric response.[36,37] In addition, the distortion in the monoclinic phase is greater as the composition approaches the morphotropic phase boundary, hence increasing the magnitude of the polarisation vector and the electromechanical response relative to a less distorted monoclinic phase that has a composition further from the morphotropic phase boundary.[38]

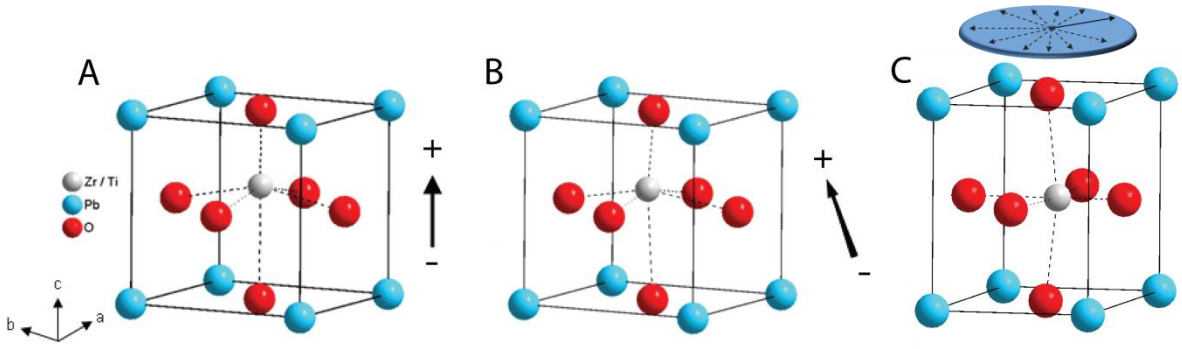

Figure 1.9: The tetragonally (A), rhombohedrally (B), and monoclinically (C) distorted perovskite structure of $PbZr_{1-x}Ti_xO_3$ below the ferroelectric to paraelectric transition temperature. The arrows indicate the direction of the net dipole along the [001]- (left), [111]- (middle) axes, and within the (110)-plane.

PZT is synthesised in polycrystalline form because it is impossible to reliably grow single crystals with compositions close to the morphotropic phase boundary. The polycrystalline nature of PZT samples means that the net piezoelectricity across a sample is not significant until the polarisation vectors are aligned by poling with a strong electric field as described in section 1.3.1.

Closer inspection of the $PbZr_{1-x}Ti_xO_3$ phase diagram shows that the Curie temperature ranges between approximately 500 - 750 K for ($0 \leq x \leq 1$). Piezoelectric materials must be operated at temperatures below their Curie temperature to maintain their noncentrosymmetry and hence maintain their physical properties. For this important reason, one must carefully consider the value of the Curie temperature for materials that will be used for high temperature applications. Through inspection of the d_{33} piezoelectric response coefficients of some well known piezoelectric materials and their maximum operating temperatures, it can be seen that materials capable of operating at higher temperatures produce smaller piezoelectric responses (Figure 1.10).[10] One of the reasons that PZT has proven to attract significant commercial interest over other materials such as $PbNb_2O_6$, $PbTiO_3$, or $GaPO_4$ is that it displays higher piezoelectric response coefficients while still capable of operation at moderate temperatures (up to approximately 650 K).[9,10]

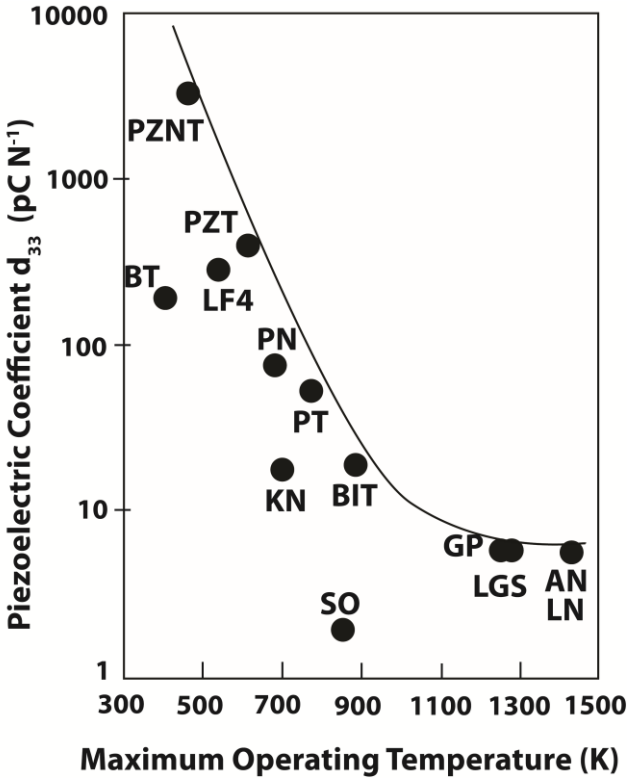

Figure 1.10: The relationship between piezoelectric response coefficient d_{33} and the maximum operation temperature for some piezoelectric ceramics. AN: AlN, BT: $BaTiO_3$, BIT: $Bi_4Ti_3O_{12}$, GP: $GaPO_4$, KN: $KNbO_3$, LF4: $K_{0.44}Na_{0.52}Li_{0.04})(Nb_{0.86}Ta_{0.10}Sb_{0.04})O_3$, LN: $LiNbO_3$, PN: $PbNb_2O_6$, PT: $PbTiO_3$, PZNT: $0.92Pb(Zn_{1/3}Nd_{1/3})O_3$-$0.08PbTiO_3$, PZT: $PbZr_{0.52}Ti_{0.48}O_3$, SO: SiO_2. Adapted from Zhang *et al.*[10]

Despite the numerous advantages of PZT, its chemical composition creates a crucial disadvantage in the context of long-term commercial mass application. PZT contains 60 wt. % lead which has been shown to have the potential to contribute to many serious health problems in humans and animals.[3] This primarily occurs through the wide scale pollution of our waterways due to the release of toxic lead oxide during the manufacturing process.[39,40] The recent changes regarding the use of lead in electronic materials have created significant research interest towards the development of lead-free alternatives to PZT and similar compounds. It is intended that newly developed, environmentally friendly materials will be used to phase out the wide scale manufacture and application of the lead-based electronic materials that currently dominate the electronics market.[4,5]

1.4.2.2 Lead-free perovskite-type piezoelectric materials

Several perovskite-type materials are currently under investigation for their potential application as lead-free ferroelectric materials. Materials such as $BaTiO_3$, $Bi_{0.5}Na_{0.5}TiO_3$ and $KNbO_3$ are known to exhibit larger piezoelectric response coefficients in comparison to other lead-free piezoelectrics (for example, $Bi_4Ti_3O_{12}$, $GaPO_4$, and $LiNbO_3$)[10], in addition to their suitability to high power applications such as ultrasonic motors or medical ultrasonic transducers. However, these perovskite-type materials exhibit lower piezoelectric responses than PZT, are difficult to pole, and exhibit low densities.[10]

$BaTiO_3$ is appropriate for application as a piezoelectric material in sonar devices because of its high electromechanical coupling factor relative to other lead free piezoelectrics. The relatively low temperature of the ferroelectric to paraelectric phase transition at 393 K has limited any potential commercial application of $BaTiO_3$ for high temperature applications.[10,41,42]

A similar perovskite, $Bi_{0.5}K_{0.5}TiO_3$ (BKT), has been shown to retain ferroelectricity up to ~650 K. Hiruma *et al.*[43], Takenaka *et al.*[44], and Sasaki *et al.*[45] investigated the physical properties of the $x(Bi_{0.5}Na_{0.5})TiO_3$-$y(Bi_{0.5}K_{0.5})TiO_3$-$zBaTiO_3$ ($x + y + z = 1$, $y : z = 2 : 1$) (BNBK) system, and reported that the Curie temperature and piezoelectric response coefficients can be tuned according to the chemical composition.

Since studies of PZT, BKT, and BNBK (and more) have established that small changes in composition can produce large changes in physical properties, many more systems based on the perovskite structure type have been studied to identify new compositions with improved physical response coefficients relative to their end members. Particular interest has been directed towards compounds with compositions poised on or near a morphotropic phase boundary.[46,47]

Other recent research efforts have extended beyond materials that exhibit perovskite-type structures. Recently, considerable interest has been directed towards the study of the structure and physical properties of a family of compounds that are based on the structure of fresnoite, a naturally occurring mineral of composition $Ba_2TiSi_2O_8$.[48-57] Fresnoite has been shown to be a ferroelectric material, exhibiting moderate dielectric, pyroelectric, and piezoelectric response coefficients.[51,56] These properties have led to significant research interest towards the fresnoite family of compounds owing to their potential suitability as environmentally friendly alternatives to some currently used lead-based electronic materials.[58-60]

1.5 An Introduction to the Fresnoite Family of Compounds

The fresnoite structure type is defined by the general formula $A_2M_3O_8$ (A = Ba, Sr, K, Cs; M = Ti, V, Si, Ge), and is based on the naturally occurring mineral, fresnoite, of composition $Ba_2TiSi_2O_8$. The mineral was first discovered in 1965 in sanbornite-bearing metamorphic rocks in the eastern Fresno county of California.[61] In 1967, Masse *et al.*[62] established that the $Ba_2TiSi_2O_8$ structure crystallises in either the *P*4*/mbm*, *P*4*bm*, or *P*4*b*2 space groups using two-dimensional Patterson and Fourier methods. Later in the same year, Moore and Louisnathan[63] used single crystal X-ray diffraction to establish the space group as *P*4*bm*, identifying similarities and differences to the structures of melilite, $(Ca,Na)_2(Mg,Al,Si)_3O_7$[64] and akermanite $Ca_2MgSi_2O_7$.[65]

The fresnoite structure is best described as an interlinked array of corner sharing TiO_5 square pyramids and SiO_4 tetrahedra that form heterocyclic five-membered rings. The bases of the interconnected polyhedra form flat sheets perpendicular to the [001]-direction (Figure 1.11A) and the ring-like structure forms channels along the [001]-direction which contain ten-fold co-ordinated barium ions (Figure 1.11B).

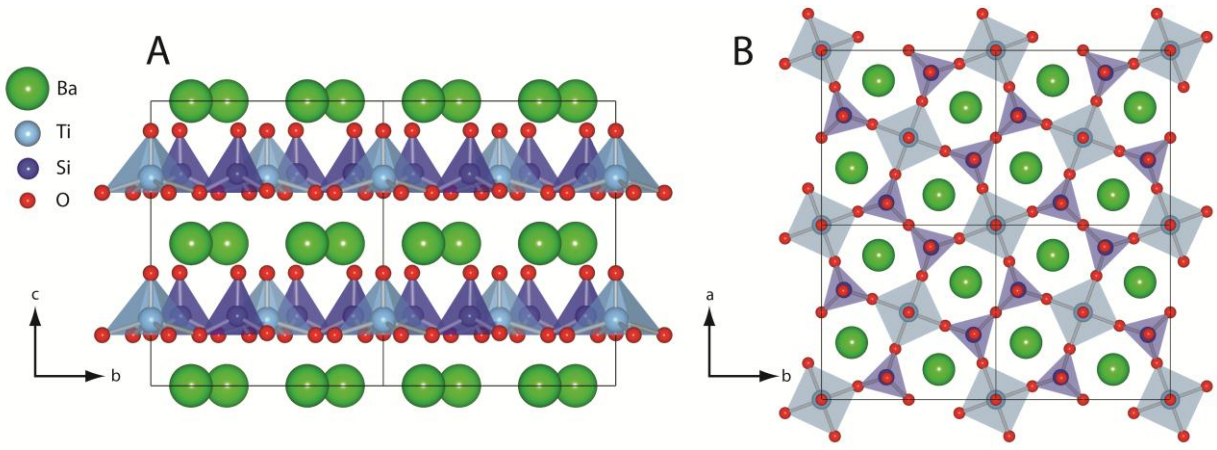

Figure 1.11: The crystal structure of fresnoite along the *a*-axis (A) and down the *c*-axis (B).

The titanium ion in fresnoite is located in a highly compressed TiO_5 square pyramid due to one short Ti-O bond (~1.7 Å). Although it is unusual for titanium to exist in a square pyramidal geometry, a small number of similar structures have been reported. Previous studies on the few compounds with titanium in a square pyramidal geometry have shown that the bonding environment of the titanium is rarely close to ideal (Table 1.1). This is determined using bond valence calculations whereby the bond valence sum (BVS) of an atom in a crystalline structure can be determined through the addition of the apparent valences (v_i) contributed from each bond (Equation 1.1 and Equation 1.2). The apparent valence contribution from each bond is calculated through the comparison of the actual bond distances (R_i) against atom-atom specific parameters (R_0 and b) that have been determined empirically from a large number of representative structures according to Equation 1.1.[66]

$$v_i = e^{\frac{R_0 - R_i}{b}} \qquad \textbf{Equation 1.1}$$

$$BVS = \sum v_i \qquad \textbf{Equation 1.2}$$

Table 1.1: Summary of the bond lengths and bond valence sums for various compounds containing compressed TiO_5 square pyramids.

Compound	Axial Ti-O bond length	Other Ti-O bond lengths	Ti Bond Valence Sum	Reference
In_2TiO_5	1.762(9)	2 x 1.833(9) 1 x 2.064(9) 1 x 2.009(9)	4.17	Gaewdang *et al.* [67]
Na_2TiSiO_5	1.695(5)	4 x 1.990(2)	3.87	Nyman *et al.* [68]
$(Ba,Sr,K)Na(Ti,Fe)\text{-}Ti[Si_2O_7](O,OH,F)_2$	1.69(1)	2 x 1.950(7) 2 x 1.957(7)	4.15	Woodrow *et al.*[69]
Na_2TiGeO_5	1.708(7)	4 x 1.993(2)	3.81	Yakubovich *et al.*[70]
$Ba_2TiGe_2O_8$	1.73(2)	1.88(1) 1.87(1) 1.90(2) 1.86(1)	4.14	Höche *et al.*[71]
$Sr_2TiSi_2O_8$	1.674(5)	4 x 1.9013(1)	4.30	Höche *et al.*[72]

Blasse[73] first reported that $Sr_2TiSi_2O_8$ and $Ba_2TiGe_2O_8$ are isomorphous with $Ba_2TiSi_2O_8$, both crystallising in the tetragonal *P*4*bm* space group. In the same publication, Blasse also commented on the synthesis of $Sr_2TiGe_2O_8$ and $Ca_2Ti\mathit{M}_2O_8$ (*M* = Si or Ge), reporting complicated X-ray diffraction patterns without further investigation for these compositions.

$Ba_2TiGe_2O_8$ was the first member of the fresnoite family to be investigated for its physical properties, including dielectric and piezoelectric constants, electromechanical coupling factor and the resonance frequency constant.[74] Through structural analogy with $Ba_2TiGe_2O_8$, $Ba_2TiSi_2O_8$ was predicted to also be a piezoelectric material having a coupling factor larger than quartz.[75] Measurement of the elastic, piezoelectric, and dielectric constants of $Ba_2TiSi_2O_8$ confirmed this hypothesis, creating interest in fresnoite for its large electromechanical coupling factor, small resonant frequency temperature coefficient, and small dielectric constant.[76] These physical properties, combined with the high mechanical stability established fresnoite as a potentially superior material for use in piezoelectric applications such as generators and sensors in the ultrasonic frequency ranges. The fresnoite Curie temperature is above its melting point at approximately 1450 K, making it a potentially appropriate compound for use in high temperature piezoelectric applications.

Ferroelastic behaviour in $Ba_2TiGe_2O_8$ was first reported by Kimura *et al*.[77] Optical, thermal, and elastic studies indicated that a phase transition occurs near 1083 K. The observation of a large resonance anomaly at 1083 K provided further evidence for a phase transition at this temperature. Halliyal *et al*.[58] published further details of the phase transitions observed in $Ba_2TiGe_2O_8$ single crystals with respect to dielectric and pyroelectric properties. Anomalies were found in the dielectric and frequency constants, as well as the pyroelectric and coupling coefficients at 223 K on cooling and 273 K on heating, suggesting hysteresis in a structural anomaly or phase transition. The possibility of a change in symmetry at this potential transition

was discussed, but no definitive argument could be presented with the data available at the time of the study. Further details of this transition are discussed further in section 1.7.

Anomalies were also observed in the pyroelectric coefficient for $Ba_2TiGe_2O_8$ near 408 K, however this has been explained in terms of the change in competition between the primary and secondary components of one of the terms that contributes to the pyroelectric response. Similar behaviour has been observed in $Li_2SO_4{\cdot}H_2O$ and $Ba(NO_2)_2{\cdot}H_2O$, among many other structures.[78,79]

Various studies have also been conducted on the synthesis, structure, and properties of other fresnoite family members with different substitutions and mixed occupancies ($Ba_2VSi_2O_8$ by Feltz *et al.*[80] and Höche *et al.*[81], $K_2V_3O_8$ by Galy *et al.*[82], $Rb_2V_3O_8$ by Withers *et al.*[83], $(NH_4)V_3O_8$ by Liu *et al.*[84], and $Cs_2V_3O_8$ by Andrukaitis *et al.*[85]). However, the potential toxicity of these compounds due to their vanadium content has led to considerably more research being performed on other compositions within the fresnoite $A_2M_3O_8$ system.

Barbar *et al.*[86] recently published evidence that the fresnoite structure is capable of incorporating up to 50 % calcium ions on the *A*-site. Although two additional reflections were found to correspond to SiO_2 and $BaTiO_3$, the main $Ca_{2x}Ba_{2-2x}TiSi_2O_8$ ($0 \leq x \leq 0.5$) phases were shown to form isostructurally with $Ba_2TiSi_2O_8$. However, the atomic positions and displacement parameters were not refined, and a modulated structure approach was not used because the quality of the data was not sufficient to do so.

Höche *et al*. postulated that the difference in ionic radii in the $A_2M_3O_8$ structure was an important factor for the formation of the fresnoite structure type.[50] It was proposed that the ratio of mean ionic radii of the ions on the *A*- and *M*-sites respectively should be greater than 3.35 for the structure to adopt the *P*4*bm* setting of the fresnoite structure type (Equation 1.3). It was also suggested that values between approximately 2.94 - 3.35 were too small to adopt the *P*4*bm* space

group, providing an explanation why $Ba_2TiGe_2O_8$ adopts the *Cmm*2 space group instead of *P4bm* (the *P*4*bm* and *Cmm*2 phases are structurally related by a doubling of the parent unit cell through a 45° rotation about the [001]-axis).[32] Similar reasoning was provided to justify why no stable phase was formed for $Sr_2TiGe_2O_8$, supporting the observations by Blasse *et al*. where single phase samples of $Sr_2TiGe_2O_8$ and $Ca_2TiM_2O_8$ (*M* = Si or Ge) could not be synthesised.[50,73]

$$\text{Ionic Radii Ratio} = \frac{\bar{r}_{Ba^{2+}/Sr^{2+}}}{\bar{r}_{Si^{4+}/Ge^{4+}}} \qquad \textbf{Equation 1.3}$$

The formation of different phases within the $Ba_{2x}Sr_{2-2x}TiGe_{2y}Si_{2-2y}O_8$ ($0 \le x \le 1$; $0 \le y \le 1$) system makes this family of compounds structurally interesting to investigate. Table 1.2 summarises which compositions within the $Ba_{2x}Sr_{2-2x}TiGe_{2y}Si_{2-2y}O_8$ system have been predicted to form phases with either *P*4*bm* (green) or *Cmm*2 (orange) symmetry, or not form fresnoite phases at all (red), using Equation 1.3 as postulated by Höche *et al*.[50]

Table 1.2: A summary of ratios of mean ionic radii for compositions in the $Ba_{2x}Sr_{2-2x}TiGe_{2y}Si_{2-2y}O_8$ ($0 \le x \le 1$; $0 \le y \le 1$) system calculated using Equation 1.3. These numbers are based on the predictions by Höche *et al.* for which space group will be adopted by each composition. Green and orange boxes indicate compositions that are predicted to form with the *P4bm*, *Cmm*2, space groups, respectively, while red boxes indicate phases that are predicted not to form fresnoite phases. The ionic radii used in the determination of these values were Ba = 156 pm; Sr = 140 pm; Si = 40 pm; Ge = 53 pm from Shannon.[87]

		x in $Ba_{2x}Sr_{2-2x}TiGe_{2y}Si_{2-2y}O_8$										
		0	0.1	0.2	0.3	0.4	0.5	0.6	0.7	0.8	0.9	1
y in $Ba_{2x}Sr_{2-2x}TiGe_{2y}Si_{2-2y}O_8$	0	3.50 (STS)	3.54	3.58	3.62	3.66	3.70	3.74	3.78	3.82	3.86	3.90 (BTS)
	0.1	3.39	3.43	3.47	3.51	3.54	3.58	3.62	3.66	3.70	3.74	3.78
	0.2	3.29	3.32	3.36	3.40	3.44	3.47	3.51	3.55	3.59	3.62	3.66
	0.3	3.19	3.23	3.26	3.30	3.33	3.37	3.41	3.44	3.48	3.52	3.55
	0.4	3.10	3.13	3.17	3.20	3.24	3.27	3.31	3.35	3.38	3.42	3.45
	0.5	3.01	3.05	3.08	3.11	3.15	3.18	3.22	3.25	3.29	3.32	3.35
	0.6	2.93	2.96	3.00	3.03	3.06	3.10	3.13	3.16	3.20	3.23	3.26
	0.7	2.85	2.88	2.92	2.95	2.98	3.01	3.05	3.08	3.11	3.14	3.18
	0.8	2.78	2.81	2.84	2.87	2.90	2.94	2.97	3.00	3.03	3.06	3.10
	0.9	2.71	2.74	2.77	2.80	2.83	2.86	2.89	2.92	2.96	2.99	3.02
	1	2.64 (STG)	2.67	2.70	2.73	2.76	2.79	2.82	2.85	2.88	2.91	2.94 (BTG)

Equation 1.3 was postulated as an empirical tool to justify the formation of different fresnoite phases (or non-fresnoite phases) for different compositions. However, no comprehensive experimental evidence has been produced that confirms or contradicts whether the ratio of ionic radii can be used to predict which space groups will be adopted by fresnoite phases for each composition in the $Ba_{2x}Sr_{2-2x}TiGe_{2y}Si_{2-2y}O_8$ system; particularly near the boundaries separating phases with different symmetry.

Schmid *et al.*[60] synthesised a series of compounds between the $Ba_2TiSi_2O_8$ and $Ba_2TiGe_2O_8$ end members, reporting the dielectric constants, optical birefringence, and pyroelectric coefficients across the entire series. The phase transition observed at 1103 K (1083 K for Kimura *et al.*[77]) for 0 % silicon content ($Ba_2TiGe_2O_8$) was found to reduce to 400 K at 40 % silicon substitution ($Ba_2TiGe_{1.2}Si_{0.8}O_8$). No transitions were observed in samples containing greater than 40 % silicon content, suggesting that a phase boundary exists at approximately $Ba_2TiGe_{1.2}Si_{0.8}O_8$ (y = 0.6) between the *Cmm*2 $Ba_2TiGe_2O_8$ and *P*4*bm* $Ba_2TiSi_2O_8$ end members.[60] This work was later supported by a structural study across the $Ba_2TiGe_{2y}Si_{2-2y}O_8$ ($0 \leq y \leq 1$) system by Iijima *et al.*[88] where it was confirmed that the incorporation of silicon into the $Ba_2TiGe_2O_8$ structure reduces the phase transition temperature from the orthorhombic to the tetragonal phase.

Detection of both AC and DC dielectric hysteresis[51] confirmed predictions based on atomic coordinates[89] that $Ba_2TiSi_2O_8$ is a ferroelectric piezoelectric material. A small calorimetric anomaly at 433 K was described as not being attributed to a structural phase transition because no atom position changes by more than 0.02 Å between 297 K and 573 K as initially reported by Markgraf *et al*. in 1985.[56] However, optical studies of $Ba_2TiSi_2O_8$ provided additional evidence of a phase transition at 433 K.[49]

The failure to account for the anomalies observed in $Ba_2TiSi_2O_8$ at 433 K and $Ba_2TiGe_2O_8$ at 223 K and 273 K (on cooling and heating, respectively) suggested that much of the behaviour of the

fresnoite structure is not well understood. In 1990, Markgraf *et al*.[53] observed additional reflections in transmission electron micrographs of $Ba_2TiSi_2O_8$ that did not correspond to the *P*4*bm* structure. Furthermore, these reflections were found to disappear at 433 K, establishing that the structural changes related to these additional reflections must be strongly correlated to the physical property anomalies at the same temperature.

The observation of additional reflections in diffraction patterns from pure phases can sometimes be attributed to the presence of a periodic distortion within the structure, called a modulation. Modulated structures have been characterised for a large number of different phases, including many naturally occurring minerals, such as melilite[90] and akermanite.[91] It is essential to understand the precise modulated structure of a phase to be able to completely and accurately account for its structural chemistry and physical properties. The following section provides an introduction to the crystallography of modulated phases such that a more comprehensive understanding of the modulated structures of fresnoite compounds can be established in section 1.7.

1.6 Crystallography of Modulated Phases

The unit cell of a crystalline structure is defined such that it contains the smallest volume with maximum symmetry. It is common practice to investigate crystal structures by analysing the position and intensity of diffracted X-rays, neutrons, or electrons to establish the periodicity and symmetry of the structure. Crystal structures with only conventional long range order produce diffraction patterns that contain Bragg reflections of position **G** that can be indexed using a linear combination of three basis vectors **a***, **b***, and **c*** and three indices *h*, *k*, and *l*, as shown in Equation 1.4.[92]

$$\mathbf{G} = h\mathbf{a}^* + k\mathbf{b}^* + l\mathbf{c}^* \qquad \textbf{Equation 1.4}$$

The crystal structure of conventional periodic crystals can be completely characterised by specifying the unit cell dimensions, symmetry, and positions of the atoms in the unit cell. The symmetry of periodic crystals is given by space groups that are based on combinations of different symmetry elements. A schematic of a hypothetical conventional periodic structure with one-dimensional translational symmetry is provided in Figure 1.12A. This example structure contains a unit cell consisting of only two atoms, repeated nine times in the *y*-direction. Figure 1.12B represents a hypothetical diffraction pattern from the above-mentioned structure that can be completely indexed by the three integer basis vectors described in Equation 1.4.

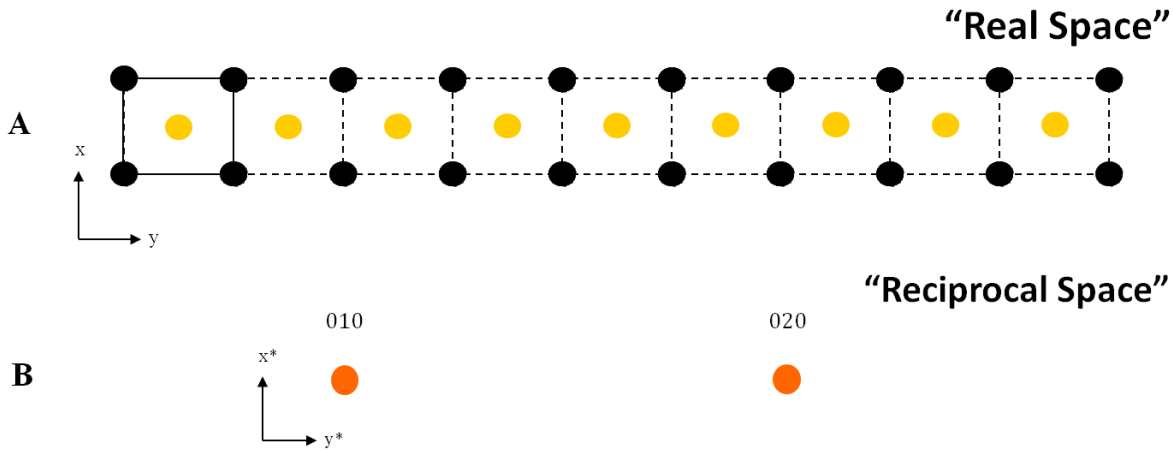

Figure 1.12: An illustration of a conventional crystal structure with a basic three-dimensional repeating unit cell (A) and a hypothetical diffraction pattern from the above structure that has been indexed with three indices (B).

It is convenient to extend the concept of indexing the diffraction pattern from a conventional crystal structure using Equation 1.4 to include structures that contain long range periodic distortions, called modulated structures. The long range periodic distortion removes three-dimensional translational symmetry from the basic crystal structure, which implies that the conventional approach is insufficient for modulated phases.[93] The formal theory of the symmetry of aperiodic crystals was introduced by Janner and Janssen.[94,95] Concurrently, De Wolff[96,97] proposed that periodicity can be maintained in aperiodic crystals by considering higher dimensional space. This was done by considering the Bragg reflections as projections of the nodes of a reciprocal lattice in (3+D)-dimensional space, otherwise called superspace, where the additional dimensions are related to internal degrees of freedom associated with the distortions relative to the basic crystal structure.[95]

Although aperiodic structures lack three-dimensional translational symmetry, the periodicity of the distortions from the basic structure can be described by atomic modulation functions. Through the use of modulation functions and superspace symmetry, the number of independent parameters can be reduced by reducing the number of independent variables.[98] The use of modulation functions allows the perfect long-range order of the phase to be described without

three-dimensional translational symmetry.[93] Modulation functions can be used to describe any refinable parameter, including variations in composition[99], spin[100], charge[101], and most commonly, atomic position (displacive modulations).[98,102-104]

The long range order of the periodic distortions produces additional sharp, Bragg (satellite) reflections that are regularly distributed around the reflections corresponding to the average structure (main reflections). Because the distortions from the basic structure do not necessarily need to be small, it is possible (but rare) for satellite reflections to occur with greater intensity than the main reflections. Hence, main reflections and satellites cannot be differentiated based solely on their intensity.

The reflections in a diffraction pattern from a modulated structure can be described by the vector **H** by using up to d additional integer indices (m_1, m_2, ..., m_d) in combination with up to d modulation vectors, or $\boldsymbol{q}$-vectors, $\boldsymbol{q_j}$ ($j = 1, 2, \dots, d$) according to Equation 1.5.[105,106] Reflections with $m = 0$ and $m \neq 0$ are reflections that correspond to the average structure and modulated structures, respectively. The intensity of satellite reflections vanishes rapidly for increasing values of m.[106]

$$\mathbf{H} = h\mathbf{a}^* + k\mathbf{b}^* + l\mathbf{c}^* + m_1\boldsymbol{q_1} + m_2\boldsymbol{q_2} + \cdots + m_d\boldsymbol{q_d} \qquad \textbf{Equation 1.5}$$

The magnitude of the $\boldsymbol{q}$-vector(s) represents the ratio between the periodicity of the conventional basic structure and the distorted structure in reciprocal space (Equation 1.6). The direction of the $\boldsymbol{q}$-vector(s) propagates in the same direction as the modulation function(s) in real space.

$$\boldsymbol{q} = \frac{period\ of\ long\ range\ distortion}{period\ of\ basic\ structure} \qquad \textbf{Equation 1.6}$$

Figure 1.13A illustrates an example of a displacively modulated structure where the yellow atom is periodically displaced from the centre of the unit cell of the basic structure from Figure 1.12A. A hypothetical diffraction pattern for the structure in Figure 1.13A is illustrated in Figure 1.13B. The modulation vector for this hypothetical example using Equation 1.6 would be $\mathbf{q} \sim 0.219\mathbf{b}^*$. The black line represents the atomic modulation function that describes the periodic atomic displacements along the direction of the modulation. Although the atomic displacements in this example are in the $\pm x$ direction, the $\boldsymbol{q}$-vector propagates in the y-direction (the $\mathbf{b}^*$ direction in reciprocal space), demonstrating that the $\boldsymbol{q}$-vector is not necessarily constrained to propagate in the same direction as the displacement.

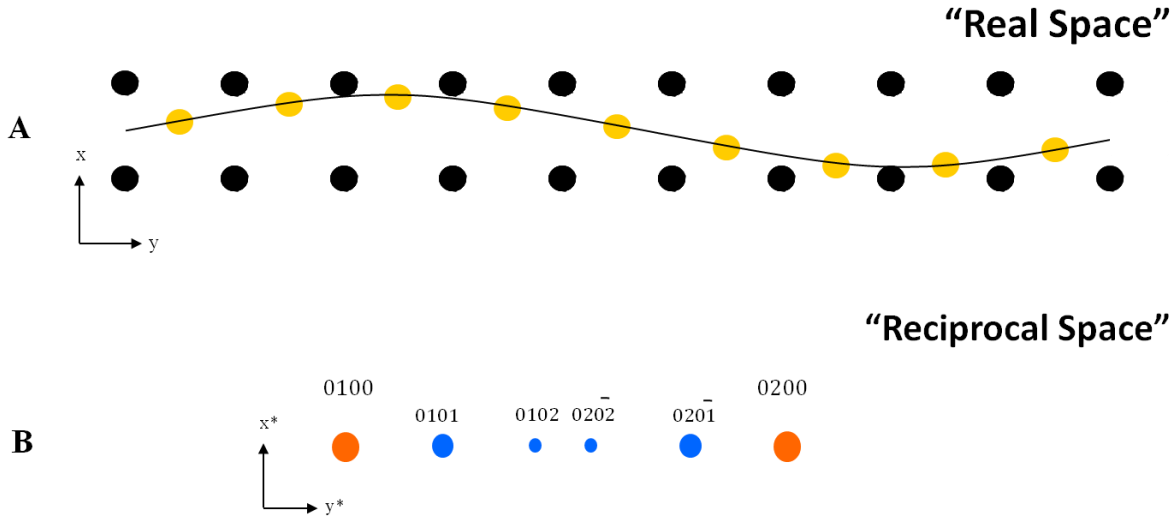

Figure 1.13: An illustration of a crystal system that contains a long range periodic distortion in the *y*-direction (A). A hypothetical diffraction pattern from the above structure containing main reflections (orange) and satellite reflection (blue) that have been indexed using four indices (B).

Because it can be a challenging exercise to model a modulated structure in the first instance, it is a common approach to start the modelling process by ignoring the modulation. It is possible to model only the average structure because once the satellite reflections are omitted, the structure obtained is based on the average distortion of the modulation. Hence, modulated structures are typically first modelled using an "average" structure which describes the structure containing the average distortion from the basic unit cell. The modulated structure can then be determined as a result of structural refinement with respect to the average structure.[95,98]

In special cases where the periodicity of the distortions of the modulated structure is commensurate with the periodicity of the basic structure, a three-dimensional space group can be used to describe the whole modulated structure. For these special cases, the structure is said to form a superstructure of the basic structure. Such structures can be defined by using a larger super-cell, whose length is defined by the number of basic unit cells that are required for the modulation function to complete one period. However, the use of a modulation function to describe the periodicity of the distortions from the basic structure instead of defining every characteristic of every atom in a large superstructure is more desirable because of the significantly reduced number of refinable parameters.

In many cases, including the example provided in Figure 1.13, the period of the modulation wave does not exactly correlate to an integer multiple of the period of the basic structure. The incommensurate relationship between the basic structure and the modulation wave means that ***q***-vector will often contain at least one irrational component (Equation 1.6). However, the equivalent satellite reflections from corresponding main reflections must also overlap and be correlated with each other for the structure to be correctly classified as incommensurately modulated. This second condition must be met because some structures will contain ***q***-vectors that are dependent on other variables such as composition or temperature, which means that the ***q***-vector can be arbitrarily close to rational values, or pass through rational and irrational values, while still exhibiting incommensurate behaviour.

The symmetry group of incommensurately modulated structures cannot be three-dimensional because the unit cell has an infinite volume. The (3+D)-dimensional space group can be determined once the (3+D)-dimensional Bravais lattice has been established.[8] Just as is the case for conventional three-dimensional structures, superspace centring also gives rise to centring conditions which must be considered. Once **a***, **b***, and **c*** have been established, the ***q***-vector can

be defined according to Equation 1.7 where the components α, β, and ϒ are given with respect to the three basis vectors α = $\boldsymbol{q}$. **a**, β = $\boldsymbol{q}$. **b**, and ϒ = $\boldsymbol{q}$. **c** respectively.

$$\boldsymbol{q} = \alpha\mathbf{a}^* + \beta\mathbf{b}^* + \Upsilon\mathbf{c}^* \qquad \textbf{Equation 1.7}$$

The definition of α, β, and ϒ allow the direction of the modulation to be specified in the (3+D)-dimensional space group. The special extinction conditions pertaining to non-primitive translations in superspace are denoted by additional letters after the directions of the $\boldsymbol{q}$-vector in the three-dimensional Bravais lattice have been defined. '*s*' and '*g*' represent additional extinction conditions arising from glide planes and screw axes in superspace, respectively.

A complete (3+D)-dimensional space group representation consists of three sections. The first section represents the Bravais lattice of the basic structure where standard three-dimensional extinction conditions apply. The second section represents the direction(s) in which the modulation occurs relative to the basic Bravais lattice defined in the first section. Finally, the last section uses letters such as '*s*' and '*g*' to define any extinction conditions that may occur due to additional superspace symmetry elements. These letters indicate the type and direction of the superspace symmetry elements and corresponding extinctions that will be observed. For example, the space group *P*4*bm*(α, α, ½)(-α, α, ½)0*gg* describes a primitive three-dimensional space group (within the 4*mm* point group) which contains equal $\boldsymbol{q}$-vectors $\boldsymbol{q}_1$ = (**a*** + **b***) +0.5**c*** and $\boldsymbol{q}_2$ = (**-a*** + **b***) + 0.5**c***. This space group can be condensed to *P*4*bm*(α, α, ½)0*gg* seeing as the first and second $\boldsymbol{q}$-vectors are both related through the tetragonal symmetry. In some cases, non-standard superspace centring is necessary to correctly describe the space group. For example, for many compounds in this thesis, the *X*4*bm*(α, α, 0)*0gg* space group is used where *X* denotes the superspace centring {0,0,½,½,½} with $\boldsymbol{q}_1$ = (**a*** + **b***) and $\boldsymbol{q}_2$ = (-**a*** + **b***).

Although the Fresnoite structure type described above contains two symmetry related modulation vectors, structures with one or two independent modulation wave vectors are common (four-, and five-dimensional structures, respectively), however, modulated structures that contain three independent modulation wave vectors are also possible (six-dimensional structures).[107-111]

The long range perturbation in modulated structures means that the magnitude of the displacement from the basic structure varies according to the position along the period of the modulation wave. Hence, many of the structural parameters such as atomic position and bond valence sum vary along the modulation direction. The continual change in these parameters is efficiently summarised through the use of atomic modulation functions (AMF's) where the parameter of interest is plotted against an internal phase parameter, *t*.[97] The internal phase parameter defines all possible positions along the modulation wave according to Equation 1.8 where the internal phase parameter *t* is equal to the dot product of the modulation vector (***q***) and the translational vector specifying the position relative to the basic structure (***T***).[112] The internal phase parameter is calculated modulo an integer such that it always takes values between 0 and 1, removing repetition due to the inherent periodicity. The letters *u* and *v* are also used in an analogous way to *t* to describe positions along additional modulation directions in five- and six-dimensional structures.

$$t = \boldsymbol{q} \,.\, \boldsymbol{T} \quad \text{(modulo an integer)} \qquad \textbf{Equation 1.8}$$

For the special case of commensurately modulated structures, the atomic modulation function is only sampled at a finite number of values due to the repeatability of the modulation with respect to the basic unit cell.[113] However, for the more general case of incommensurately modulated structures, the atomic modulation function adopts the form of a continuous line of an infinite number of values between 0 and 1. The concept of the internal phase parameter can be

understood by considering the eleven basic unit cells of a hypothetical incommensurately modulated crystal structure in Figure 1.14 where the displacement of the yellow atom varies incommensurately with the basic structure. The displacement at each position is represented in a hypothetical atomic modulation function where red lines originate from atoms corresponding to the first period of the modulation, and green lines originate from the first two atoms that have been drawn from the second period of the modulation. It can be seen that the points corresponding to the second period of the modulation lie in between the points corresponding to the first period of the modulation. As the modulation repeats itself over and over again, an infinite number of points are added in the spaces between the points of the atomic modulation function from the previous period(s) of the modulation to create a continuous line, indicative of the infinite number of values adopted by incommensurate structures.

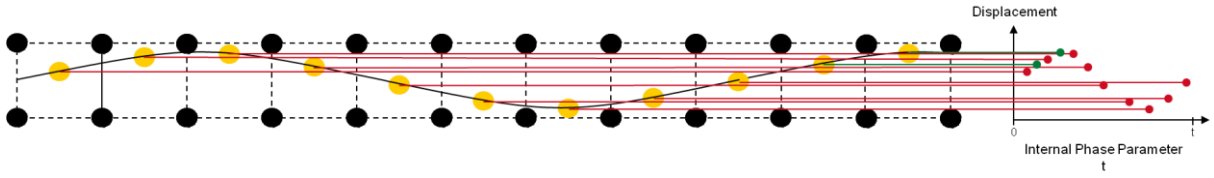

Figure 1.14: Eleven basic unit cells of a hypothetical incommensurately modulated crystal structure. Lines drawn from the atoms corresponding to the first period of the modulation (red) and the first two atoms of the second period of modulation (green) show that the line will become continuous as the modulation repeats infinitely; also demonstrating that adjacent (infinitely small) points on the atomic modulation function do not correspond to adjacent basic unit cells.

The fresnoite structure type is one of many structure types that can be described using a modulated structure approach. The presence and behaviour of displacive modulations in the fresnoite structure have created significant research interest owing to evidence that a strong relationship exists between thermally-induced changes in the modulation and improved physical properties.

1.7 Applying a Modulated Structure Approach to the Fresnoite Family of Compounds

$Ba_2TiGe_2O_8$ was the first member of the fresnoite family of compounds shown to exhibit a modulated structure. Although Iijima *et al.*[57] were the first to suggest that long period ordering occurred in the $Ba_2TiGe_2O_8$ structure, Markgraf *et al.*[55] published evidence of the modulated structure in 1989, reporting that X-ray precession photographs of $Ba_2TiGe_2O_8$ single crystals showed an incommensurate modulation along the **a*** and **b*** directions. In agreement with IIijima *et al.*, it was reported that strain-induced positional disorder of the pyrogermanate groups is responsible for the ferroelastic properties and also accounts for the existence of a modulated structure.[55,57] The previously reported $Ba_2TiGe_2O_8$ phase transitions at 223 K on cooling and 273 K on heating were confirmed to coincide with the modulation 'locking in' at a value of $\boldsymbol{q} = 1/3\mathbf{a^*}$, while the modulation along **b*** remains incommensurate.[55]

Markgraf *et al.*[53] also published the first evidence of a modulated structure for $Ba_2TiSi_2O_8$. It was reported that the satellite reflections could be indexed with $\boldsymbol{q} = 0.4\mathbf{a^*} + 0.5\mathbf{c^*}$ (although the accuracy of these measurements was noted as not being high). The satellite reflections were found to disappear at 433 K, establishing that the property anomalies reported by Chang *et al.*[114] and Markgraf *et al.*[56] on heating $Ba_2TiSi_2O_8$ above 433 K are due to the removal of the incommensurate modulation.

Structural modulations have been shown to occur along the [100]- and [010]-directions in $Ba_2TiSi_2O_8$, and the [110]-direction for $Ba_2TiGe_2O_8$. The $Ba_2TiSi_2O_8$ modulation is attributed to the presence of the large barium ions causing distortions in the basal Si_2O_7 and TiO_5 linkages. Unlike $Ba_2TiGe_2O_8$, the strain in $Ba_2TiSi_2O_8$ is insufficient to induce ferroelastic behaviour, but significant enough to introduce the need for a structural modulation.[53]

Assuming that the induced strain does not displace the centre of mass of any polyhedra, Höche *et al*.[50] proposed that the cause of the modulation is a force that shifts the bridging oxygen ion between the two adjacent SiO_4 tetrahedra along the [001]-direction (as observed in $Ba_2TiGe_2O_8$ by Iijima *et al*.[57]). The upwards shift of the bridging oxygen ion introduces a frustration within the structure because the remaining oxygen on the (110)-plane of the SiO_4 tetrahedra must sometimes rotate upwards, and sometimes rotate downwards to prevent the centre of mass of the tetrahedra moving. The variation in the direction and magnitude of the movement of the oxygen ions forming the SiO_4 tetrahedra has hence been proposed as the driving force for the incommensurate modulation.

Markgraf *et al*.[54] also reported the synthesis of polycrystalline samples in the $Ba_2TiGe_{2y}Si_{2-2y}O_8$ ($0 \leq y \leq 1$) system. Transmission electron microscopy revealed that even compositions within the orthorhombic phase (up to approximately $Ba_2TiGe_{0.9}Si_{1.1}O_8$) still exhibited satellite reflections along the [100]- and [010]-directions, indicating that some of the structure was adopting the $Ba_2TiSi_2O_8$ tetragonal structure type. It was established that the evolution of $Ba_2TiSi_2O_8$ satellite reflections against the $Ba_2TiGe_2O_8$ satellite reflections is not as clearly defined as suggested in the proposed phase diagram by Schmid *et al*.[60]

In recent times, the difficulties associated with synthesising homogeneous single crystals of sufficient size for X-ray or neutron diffraction have made it desirable to utilise complementary techniques to further investigate the incommensurate modulations in complex structures. In particular, research interest has been directed towards the use of experimental techniques that are capable of detecting the atomic displacements that cause incommensurate modulations to provide useful information that is necessary to understand the cause and effect of displacive modulations.

The interconnectivity of the polyhedra in the fresnoite structure and their role in forming displacive modulations has meant that rigid unit modes have been a useful tool in advancing our understanding of the origin of the modulations in members of the fresnoite family of compounds. The concept of rigid-unit modes (RUM's) was developed by Dove *et al*. to address the general problem of describing the complete set of all possible distortions of any crystal structure that contains linked polyhedra. In particular, the rigid structural units that are linked together to form these silicate frameworks have made the rigid unit mode approach extremely useful in the investigation of framework silicates.[115,116] The rigid unit mode approach only considers the relative orientation of the corner-linked polyhedra, and has been used to investigate the soft vibrational modes involved in displacive phase transitions. The concept of rigid unit modes has been successfully applied to a series of incommensurately modulated structures, including tridymite[117], quartz[116], cristobalite[118], and leucite.[119]

A rigid unit mode analysis of the inherent structural flexibility of the ideal fresnoite structure conducted by Withers *et al*.[120] established the significance of the modulation wave vectors in $Ba_2TiSi_2O_8$ and $Ba_2TiGe_2O_8$. The energies associated with the deformation of the constituent tetrahedra and square pyramids are typically much larger than the energies associated with the rotation of neighbouring polyhedral units about a common vertex atom[121], or the energies associated with the bonding interactions between the oxygen ions in the SiO_4 tetrahedra and the barium ions. Hence, polyhedral rotations are far more likely to be responsible for the various phase transitions in fresnoites rather than polyhedral deformation.[120]

Six zero frequency and two close to zero frequency quasi-RUM modes were found to exist for any modulation wave vector in these structures. It was identified that these RUM modes are all primarily associated with rotations of the constituent SiO_4 or GeO_4 tetrahedra and TiO_5 square pyramids about the *c*-axis. A seventh RUM involving the rotation of the constituent rigid polyhedra around *c* combined with shifts in the basal plane was found, but only at very specific

modulation wave vector $\boldsymbol{q} = 0.30[110]^*_p$, in close agreement with the RUM found in the electron diffraction study by Withers *et al.*[120] It is proposed that the condensation of this RUM plays a major role in the various incommensurately modulated structures observed in $Ba_2TiSi_2O_8$, $Ba_2TiGe_2O_8$, and $Sr_2TiSi_2O_8$.[120]

Electron diffraction images proved that the orthorhombic *Cmm*2 $Ba_2TiGe_2O_8$ structure is modulated along one of the two initially symmetry equivalent $[110]^*_p$ directions. The $Ba_2TiGe_2O_8$ structure was refined against neutron powder diffraction data by Höche *et al*. using a (3+1)-dimensional superspace approach.[71] The structure was reported to adopt the *Cmm*2(0, β, ½)*s*00 pace group with $\beta \sim 0.635$ (*i.e.* $\boldsymbol{q} = 0.635\mathbf{b^*}$) at ambient temperature. The modulation parameters supported the idea of frozen-in rigid unit modes being responsible for the structural modulation. The introduction of a displacive modulation significantly improved the bond valence sum for both barium positions, suggesting that bonding requirements of the underbonded barium positions are a driving force for the incommensurate modulation in $Ba_2TiGe_2O_8$.[120]

The incommensurately modulated structure of a $Sr_2TiSi_2O_8$ single crystal was also determined by Höche *et al.*[72] X-ray diffraction provided evidence that the $Sr_2TiSi_2O_8$ structure belongs to the five-dimensional superspace group *P*4*bm*(α, α, ½)0*gg* with modulation vectors $\boldsymbol{q_1} = 0.3(\mathbf{a^*} + \mathbf{b^*}) + 0.5\mathbf{c^*}$ and $\boldsymbol{q_2} = 0.3(-\mathbf{a^*} + \mathbf{b^*}) + 0.5\mathbf{c^*}$ at ambient temperature. Electron diffraction patterns revealed that the two-dimensional modulation appears to be superimposed by some one-dimensional modulation waves, suggesting that two different phases are coexisting in the one crystal.

Recent work on $Ba_2TiSi_2O_8$ and other members of the fresnoite family of compounds has discovered a new, low temperature route of synthesis.[122] The hydrothermal reaction of fresnoite precursors in sealed autoclaves at 500 °C for three days produced single crystals suitable for X-ray

diffraction. $Ba_2TiGe_2O_8$ crystals grown via the hydrothermal synthesis method were found to display the same incommensurate modulation as those prepared from the conventional high temperature melt, thus suggesting that the differing modulation characteristics of $Ba_2TiGe_2O_8$ are truly inherent to the structure rather than being a consequence of the high temperature environment during synthesis.[123] Only three-dimensional models were developed to describe the hydrothermally synthesised samples, despite several references to other work that used a modulated structure approach.

Electron diffraction patterns from a natural single crystal of $Ba_2TiSi_2O_8$ have proved the presence of a five-dimensional incommensurately modulated structure similar to $Sr_2TiSi_2O_8$.[124] The superspace symmetry of $Ba_2TiSi_2O_8$ was reported as $P4bm(\alpha, \alpha, ½)0gg$, with modulation vectors $\boldsymbol{q_1} = 0.302(\mathbf{a^*} + \mathbf{b^*}) + 0.5\mathbf{c^*}$ and $\boldsymbol{q_2} = 0.302(\mathbf{-a^*} + \mathbf{b^*}) + 0.5\mathbf{c^*}$.

The most recent work on the fresnoite family of compounds has provided more insight into the formation and coexistence of commensurately and incommensurately modulated structures in the $Ba_{2x}Sr_{2-2x}TiSi_2O_8$ ($0 \leq x \leq 1$) system.[124] A combination of electron diffraction and energy-dispersive spectroscopy have been used to show that regions that deviate from the ideal fresnoite stoichiometry are characteristic of incommensurately modulated structures. Conversely, regions with a stoichiometry closer to the $A_2M_3O_8$ composition were shown to display commensurately modulated structures. The significance of this work is high because it implies that polycrystalline samples are not necessarily completely homogenous, and that this is responsible for potential changes in the modulation characteristics of different samples.

The work summarised in the previous sections has vastly improved the understanding of the fresnoite structure type. In particular, the identification of different types of modulated phases in the fresnoite structure type has increased interest in these compounds. Most of the research into compounds with the fresnoite structure type has been primarily based on the use of single crystal

diffraction techniques, and has provided important information about the structural modulations present.[50,72,125] However, investigations into the structure and phase transitions of the end members and members across the $Ba_{2x}Sr_{2-2x}TiGe_{2y}Si_{2-2y}O_8$ ($0 \leq x \leq 1$; $0 \leq y \leq 1$) system in polycrystalline form have been limited. Understanding the structural behaviour of these compounds could lead to the discovery of new compositions or compounds that display vastly improved physical properties. Hence it is timely to conduct a comprehensive study on the structure and phase transitions of the $Ba_{2x}Sr_{2-2x}TiGe_{2y}Si_{2-2y}O_8$ ($0 \leq x \leq 1$; $0 \leq y \leq 1$) system.

1.8 Aims

This project aims to investigate the structure and phase transitions of the end members and members of mixed compositions in the fresnoite $Ba_{2x}Sr_{2-2x}TiGe_{2y}Si_{2-2y}O_8$ ($0 \leq x \leq 1$; $0 \leq y \leq 1$) system. Given the importance of the polycrystalline forms for potential applications of these materials, emphasis will be placed on the synthesis of pure polycrystalline samples and their characterisation using powder diffraction methods. The structure of the end members will be fully characterised as a benchmark for the members of mixed compositions. An improved understanding of the structures and phase transitions in the $Ba_{2x}Sr_{2-2x}TiGe_{2y}Si_{2-2y}O_8$ ($0 \leq x \leq 1$; $0 \leq y \leq 1$) system will be beneficial for the targeted development of new smart materials with improved physical properties for the benefit of the electronics industry and the wider global community.

The specific aims of the research presented in this thesis are to:

- Characterise the average and modulated structures (where possible) for the end members of the $Ba_{2x}Sr_{2-2x}TiGe_{2y}Si_{2-2y}O_8$ ($0 \leq x \leq 1$; $0 \leq y \leq 1$) system at ambient temperature using a powder diffraction approach.
- Identify any new phase boundaries separating compositions of different symmetry in the $Ba_{2x}Sr_{2-2x}TiGe_{2y}Si_{2-2y}O_8$ ($0 \leq x \leq 1$; $0 \leq y \leq 1$) system.
- Improve the understanding of the position of any phase boundaries separating fresnoite type compounds and other structure types in the $Ba_{2x}Sr_{2-2x}TiGe_{2y}Si_{2-2y}O_8$ ($0 \leq x \leq 1$; $0 \leq y \leq 1$) system.
- Investigate the temperature dependent phase transitions of the end members in the $Ba_{2x}Sr_{2-2x}TiGe_{2y}Si_{2-2y}O_8$ ($0 \leq x \leq 1$; $0 \leq y \leq 1$) system using a powder diffraction approach and investigate how changes in composition influence the properties of these phase transitions.

- Investigate the elastic properties of selected members of the $Ba_{2x}Sr_{2-2x}TiGe_{2y}Si_{2-2y}O_8$ ($0 \leq x \leq 1$; $0 \leq y \leq 1$) system and use these properties to complement the structural information gained about their phase transitions.
- Investigate the physical properties such as the dielectric, piezoelectric, and ferroelectric responses of selected end members in polycrystalline form within the $Ba_{2x}Sr_{2-2x}TiGe_{2y}Si_{2-2y}O_8$ ($0 \leq x \leq 1$; $0 \leq y \leq 1$) system.

Chapter 2 Experimental Techniques

A variety of complementary experimental techniques have been utilised to characterise the samples investigated in this thesis. These techniques include synchrotron X-ray and neutron powder diffraction, electron diffraction, differential scanning calorimetry, X-ray absorption spectroscopy, resonant ultrasound spectroscopy, and physical property studies. The investigation of physical properties included measurement of dielectric, piezoelectric, and ferroelectric responses using an electrical properties measurement system and piezoforce microscopy. This chapter describes the various techniques used throughout this thesis with an emphasis on powder diffraction techniques and the Rietveld refinement method due to the importance of the characterisation of polycrystalline samples to this project.

2.1 Powder Diffraction

Powder diffraction patterns are produced by passing an incident beam of X-rays or neutrons through a sample where the wavelength is similar to the interplanar spacing of the samples' crystal structure. The incident beam is scattered off successive crystallographic planes of atoms in the compound. The intensity of the scattered beam is dependent on whether constructive or destructive interference occurs. Bragg's law (Equation 2.1) defines the conditions for constructive interference of the *n*th order reflection, according to the wavelength of incident radiation (λ), the incident angle (θ), and the distance between successive planes of atoms (d):

$$n\lambda = 2d\sin\theta \text{ (where } n \text{ is an integer)} \qquad \textbf{Equation 2.1}$$

The intensity of the scattered beam as a function of Bragg angle 2θ can be used to identify which phase(s) are present in a sample, track the progress of a reaction (*e.g.* identify whether or not

particular reaction conditions are improving the purity of the sample), characterise crystal structures, and/or identify/investigate phase transitions.

The information in powder diffraction patterns is far lower than in complete data sets from single crystal diffraction patterns collected up to the same maximum diffraction angle. However, powder diffraction can be a useful technique for phases that cannot be investigated using single crystal diffraction techniques. For example, powder diffraction is appropriate for the characterisation of phases that do not form sufficient single crystals for single crystal diffraction methods, for samples of specific mixed compositions, or when information about the bulk sample is important. Powder diffraction was the primary analytical tool used for structural characterisation in this thesis because of the interest in specific compositions of mixed stoichiometry within the $Ba_{2x}Sr_{2-2x}TiGe_{2y}Si_{2-2y}O_8$ ($0 \leq x \leq 1$; $0 \leq y \leq 1$) system and the importance of understanding the structure of bulk polycrystalline samples.

The diffraction profiles collected from aperiodic crystalline materials are typically more complicated than those obtained from periodic structures because they include contributions from main and satellite reflections. In the case of a 1-dimensional modulation, the positions of the main reflections are determined by the reflection indices (*hkl0*) and the lattice parameters of the unit cell of the basic structure. Positions of the satellite reflections (*hklm*) with $m \neq 0$ depend on the order of the indices, the lattice parameters, and the modulation wave vector as discussed in Chapter 1.

A potentially complicating factor is that the dense distribution of all the possible satellite reflections along the two theta axis can lead to significant reflection overlap. However, the observation of sharp, resolved diffraction maxima rather than a continuum of intensity corresponding to all of the potential reflections means that only a fraction of the satellite reflections are observed. This implies that reflection intensities fall to zero for satellite reflections

beyond some order m. Patterns with up to m^{th} order satellites contain up to $(2m+1)$ as many reflections as a pattern produced from only the basic structure.

Powder diffraction experiments in this thesis were performed using an incident beam from sealed tube X-ray sources, synchrotron sources, and neutron sources. The different advantages of these sources were useful in obtaining different information about the fresnoite structure type. Each of these sources will now be discussed in further detail, followed by a discussion of the importance of the complementarity of X-ray and neutron powder diffraction techniques.

2.1.1 X-ray Powder Diffraction from Sealed Tube X-ray Sources

X-ray diffraction from sealed tube X-ray sources (often called laboratory X-ray diffraction, or conventional X-ray diffraction) is typically performed using a tube containing a copper target which produces an incident beam consisting of the $K_{\alpha 1}$ and $K_{\alpha 2}$ copper emission wavelengths ($\lambda_{\alpha 1}$ = 1.5406 Å and $\lambda_{\alpha 2}$ = 1.5444 Å). However, other targets such as molybdenum are also common. X-ray diffraction patterns from a sealed tube X-ray source in this project were collected using a PANalytical X'Pert PRO MPD X-ray diffractometer (45kV, 40mA, divergence slit 0.25° and anti scatter slits 0.5°) configured in Bragg PDS mode, using a PIXcel detector in scanning mode (active length 3.347°) with Cu K_{α} radiation. Data were typically collected in the range $10° \leq 2\theta \leq 70°$ with a step size of 0.0394°, for 63.75 seconds per step for ambient and non-ambient temperature experiments on this instrument. Finely ground samples were placed in instrument specific holders and smoothed with a glass microscope slide to achieve a flat surface. The samples were rotated at approximately 0.5 revolutions per second during data collection to minimise the effects of preferred orientation. Data were collected between 350 K - 1050 K using the XRK-900 furnace attachment under vacuum in the same experimental configuration as described above.

2.1.2 Synchrotron X-ray powder diffraction

The use of X-rays generated at a synchrotron source has numerous advantages over X-rays generated from sealed tube sources. Synchrotron sources produce intense Bremsstrahlung (braking radiation) by injecting charged particles (electrons) from a linear accelerator (typically) into a circular or almost circular ring. Inside the ring, variable electric and magnetic fields are used to accelerate the charged particles up to relativistic speeds. Electromagnetic forces are created between strong 'bending' magnets and the charged particles such that their direction constantly changes, producing high energy electromagnetic radiation. This radiation contains a wide range of energies, from which X-rays of a desired energy can be selected using a monochromator. The highly monochromatic and collimated beam produces diffraction peaks that are orders of magnitude more intense and have a much higher angular resolution than those produced using sealed tube X-ray sources.

Well-resolved reflections with a high signal to noise ratio are especially important in the study of modulated phases because of the importance of identifying the position and intensity of the satellite reflections. Synchrotron X-ray powder diffraction can therefore allow for the more precise determination of structural characteristics such as atomic positions and the amplitude of structural modulations than diffraction from sealed tube X-ray sources.

2.1.2.1 Beamline 10-BM at the Australian Synchrotron

Synchrotron X-ray powder diffraction patterns were collected on beamline 10-BM at the Australian Synchrotron.[126] Beamline 10-BM is located on a bending magnet source and is capable of operating between 6 keV - 30 keV. The incoming beam is conditioned using vertically and horizontally collimating mirrors and the wavelength is selected using a flat Si(111) double crystal monochromator.

Low temperature *in situ* experiments were performed using an Oxford cryostream liquid nitrogen attachment, which is capable of maintaining temperatures between approximately 100 K - 500 K. High temperature *in situ* experiments were performed using a Cyberstar Eurotherm hot air blower, which is capable of maintaining temperatures between 300 K - 1273 K. The temperatures measured for the hot air blower experiments in this project have been calibrated against a curve supplied by the facility that was produced from the analysis of well known phase transition temperatures from selected compounds. The facility reports the error in the temperatures measured from the low and high temperature attachments to be ± 1 K.

Samples were typically packed into 0.3 mm glass or quartz capillaries for data collections between 125 K - 450 K, and 450 K - 1273 K, respectively. Capillaries were aligned concentric to the rotation of the axis of the three-circle diffractometer and rotated during data collection to minimise the observation of preferred orientation of the crystallites in the diffraction patterns. The X-ray absorption from the sample in the beam was included by using the linear X-ray absorption cross section calculated for each composition. This was calculated by multiplying the X-ray absorption coefficient for each composition by the radius of the capillary that the X-rays passed through. Based on the difficulty of pressing dense pellets of these samples, a low packing density in polycrystalline from of 30 % was assumed when calculating the absorption correction for each sample.

Data were collected above 1273 K using an Anton Paar HTK 2000 furnace. Samples were homogenously spread across a small region of a Pt-strip using an ethanol slurry. The facility estimates the error in the measured temperature for this instrument to be ± 1 K. The Pt-strip attachment was mounted at a 7° omega angle and rocked backward and forward between 7 - 8.5° to the horizontal during data collection to minimise the effects of preferred orientation in the samples.

Synchrotron X-ray powder diffraction data were collected using a Mythen strip detector.[127] The principle advantages of the Mythen microstrip detector are the parallel detection of X-rays at the detector and the fast readout time of 250 ms, dramatically reducing the time required to record a full diffraction pattern. The Mythen detector consists of 16 modules allowing 80° of data to be simultaneously acquired. There are small gaps between each module (0.2°), resulting in data missing at regular intervals along the histogram (5°). Data were collected across two individual frames with a small angular difference (0.5°) to ensure that data were collected for the entire angular range $1.0° \leq 2\theta \leq 81.5°$.

Data from the two frames collected from each sample were spliced together using the software package *DataPro*. *DataPro* was written using Interactive Data Language (IDL) routines to process data collected using the Mythen detector at beamline 10-BM at The Australian Synchrotron. The program provides a convenient means of normalising and combining powder diffraction data in preparation for analysis using structural refinement software.

Most data were collected at ~15.0 keV (~0.827 Å) to optimise the resolution of the collected pattern and minimise the X-ray absorption of atoms within the sample. However, data collected using the Pt-strip furnace attachment were collected at 10.7 keV (1.15864(1) Å) such that the reflections corresponding to the Pt-strip would not appear in the diffraction patterns. For ~15.0 keV experiments, the wavelength was determined using the NIST standard reference material 660a (SRM 660a), LaB_6. The specific wavelengths determined for each experiment at ~15.0 keV are quoted in the relevant sections. For experiments at 10.7 keV, the wavelength was determined using a standard containing a mixture of both SRM 660a and Diamond. This standard was necessary to minimise the high X-ray absorption from the lanthanum in pure SRM 660a at 10.7 keV.

2.1.3 Neutron Powder Diffraction

The use of neutrons for diffraction experiments is extremely useful for the characterisation of crystalline materials. Neutrons can be produced for diffraction experiments using two different methods. The first of these methods uses neutrons produced from the fission of a heavy nucleus (typically ^{235}U) in a nuclear research reactor. The other method involves generating neutrons using a spallation source where a heavy metal target is bombarded with high energy protons that are generated from a particle accelerator. Upon collision, enough energy is transferred into the target to produce spallation neutrons. Both of these methods produce neutrons that are too high in energy for immediate use in diffraction experiments. Hence, the neutrons are passed through a moderator such as heavy water, to reduce their energy such that their wavelength is of the order of 1-2 Å.

The experiments contained in this thesis were conducted on two different instruments that receive neutrons from the Open Pool Australian Lightwater (OPAL) reactor at the Australian Nuclear Science and Technology Organisation (ANSTO) Bragg Institute. The OPAL reactor operates at up to 20 MW using low enriched uranium fuel rods and is cooled by light water. The two instruments used will now be discussed.

2.1.3.1 Echidna – The High Resolution Powder Diffractometer at OPAL

Echidna is the High Resolution Neutron Powder Diffractometer that receives neutrons from the OPAL reactor located at the Bragg Institute at ANSTO. A wide range of wavelengths are possible for constant wavelength experiments through the use of a variable germanium (115) monochromator that can be used to select take off angles between 90° and 140°. The scattered radiation from the sample is collected by a set of 128 detector units that each contain a 5° collimator in front of a vertically oriented linear position sensitive ^{3}He detector of 25 mm diameter and 300 mm height. The detector design is very similar to, and shares many common

characteristics with the detector on the refurbished D2B powder diffraction beamline at the Institute Laue Langevin (ILL).[128]

Variable temperature *in situ* experiments were performed using a top loading cryofurnace attached to a LakeShore temperature control unit. The top loading cryofurnace is capable of maintaining temperatures from 4 K - 700 K.

A wavelength of ~2.25 Å was chosen to provide sufficient intensity to the sample for the experiment and enough resolution to resolve adjacent Bragg reflections. The precise wavelength was determined by using an Al_2O_3 NIST 676a standard.

2.1.3.2 Wombat – The High Intensity Powder Diffractometer at OPAL

Wombat is the High Intensity Neutron Powder Diffractometer that receives a high flux of neutrons from the OPAL reactor.[129] Wombat utilises a 120° position sensitive detector that is nearly identical to that used at the protein crystallography instrument at the Los Alamos Neutron Science Centre (LANSCE).[130] The position sensitive detector consists of eight 15° curved panels with a radius of curvature of 700 mm and a height of 200 mm. The panels are perfectly adjacent to each other so that 120° continuous coverage is possible. The panels are two-dimensional position sensitive detectors along the curved and vertical directions with a full width at half maximum height (FWHM) resolution of about 1.5 mm.[131] The detector is filled with 7 atm of ^{3}He and 2.5 atm of propane. *In situ* variable temperature experiments were performed using the top loading cryofurnace described in section 2.1.3.1.

2.1.3.3 The Complementarity of X-ray and Neutron Diffraction Techniques

X-ray and neutron powder diffraction are complementary crystallographic techniques because they can provide very different information about identical structures. Access to synchrotron and neutron facilities is typically very expensive and highly competitive. Hence, it is essential to fully understand the strengths and weaknesses of both techniques in order to understand how, when, and why each should be utilised for a particular problem.

Firstly, the difference in the resolution of the patterns collected using synchrotron X-ray powder and neutron powder diffraction techniques can vary considerably. This is shown in Figure 2.1 where a much higher resolution is observed in synchrotron X-ray powder diffraction patterns than in patterns collected using sealed tube X-ray sources or a neutron source. The different levels of resolution arise from the different properties of the incident beam and the different geometries of the diffractometers that are used.

The highly monochromatic nature of the X-ray beam and the lower divergence of the incident radiation are responsible for the superior resolution observed in synchrotron X-ray powder diffraction patterns.[132] The higher intensity of X-rays available from synchrotron sources is also important because it allows the X-ray beam to be highly focused and monochromated while still maintaining sufficient flux on the sample to allow for rapid data collection. The higher resolution achieved in synchrotron X-ray powder diffraction experiments means that sharper reflections are observed in the diffraction pattern, making it possible to resolve very small distortions that could not be otherwise observed in experiments using a sealed tube X-ray source, or a neutron source.

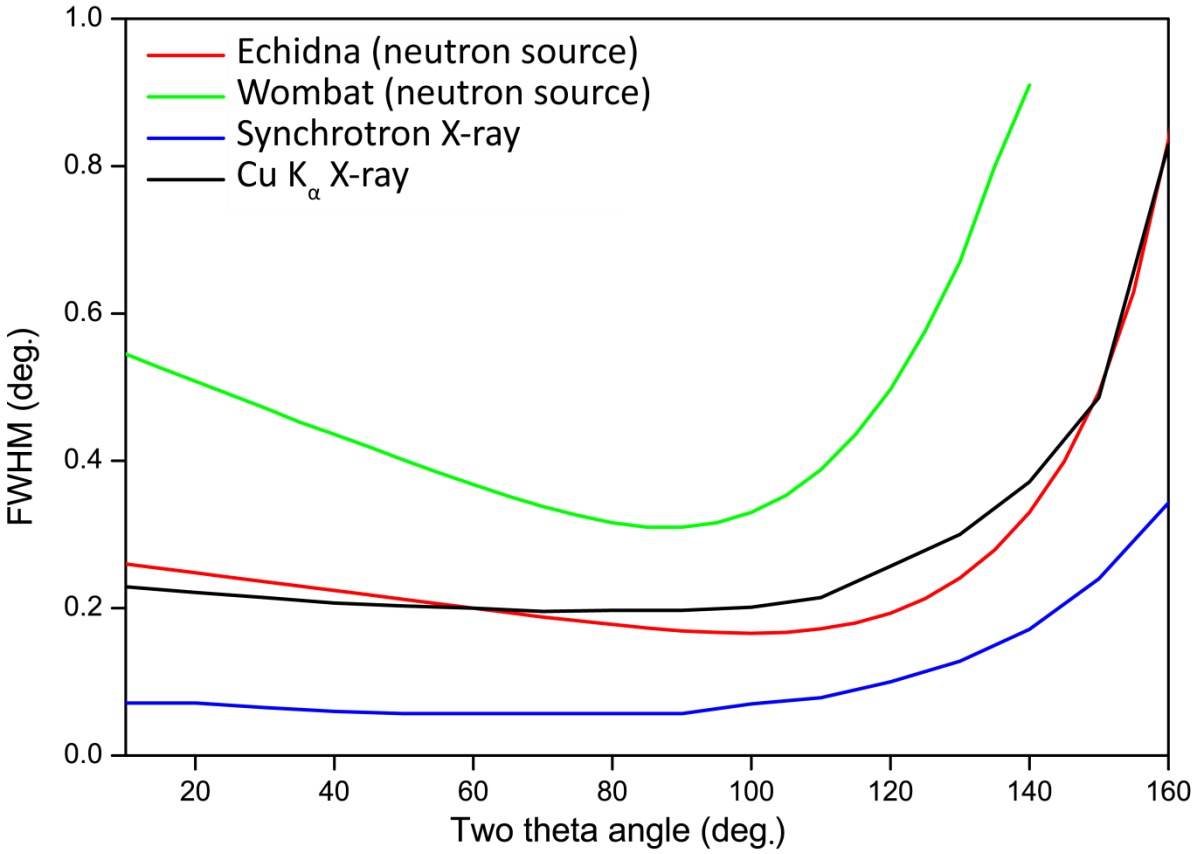

Figure 2.1: Comparison of the resolution available from different diffraction experiments (measured as the full-width of reflections at half maximum height). This figure has been reconstructed from data in Howard & Kennedy[133] and the online specification pages for Echidna and Wombat using parameters that are relevant to the studies conducted in this project.[134,135]

There is a rapid reduction in the X-ray scattering power of atoms at high diffraction angles because the scattering of the X-rays off the large electron cloud means that more of the scattered beam destructively interferes with itself at higher diffraction angles. It is desirable to maximise the quality of the data collected by achieving the highest resolution at the lowest angles, where scattering is the strongest. It is important, however, to still have as high resolution as possible at higher angles because this enables the more precise determination of structural parameters. With synchrotron X-ray powder diffraction this can, in part, be achieved by selecting a shorter wavelength and therefore obtaining lower d-values at the same two theta angles compared to those obtainable at a longer wavelengths using X-rays from a sealed tube. Using a shorter wavelength to collect a synchrotron X-ray powder diffraction pattern, however, also leads to less

angular separation between reflections in the pattern, so care must be taken to ensure that any splitting of reflections, particularly at lower angles can still be observed.

However, in neutron diffraction, the neutrons diffract off the nucleus instead of the electron cloud. The smaller volume that the neutrons scatter from (a nucleus, as opposed to the electron cloud) means that there is a smaller path difference for neutrons diffracting at higher angles, producing less destructive interference. This means that the neutron scattering efficiency remains essentially unchanged up to high two theta angles.[136] In order to maximise the quality of the data obtained at higher two theta values, a diffractometer geometry with a high monochromator "take off" angle is typically chosen. The "take off" angle is the angle at which the neutrons leave the monochromator. The data for the neutron sources in Figure 2.1 have been calculated for experimental setups using a take off angle of ~114°, representing the conditions used in the neutron diffraction experiments in this project.

It should be noted that the preceding discussion has focussed on the continuous wave diffraction methods used in this project rather than time-of-flight neutron diffraction. In general, the errors in the time of flight of the neutrons produces poorer resolution than what can be achieved using synchrotron X-ray powder diffraction. The only exception to this generalisation is the High Resolution Powder Diffractometer at ISIS, which has comparable resolution to synchrotron diffractometers due to its significantly longer flight path (~ 100 m).[137]

The second major advantage of synchrotron X-ray powder diffraction compared to diffraction using sealed tube X-ray sources and neutrons is the much higher flux available to investigate the sample. The higher flux combines with the higher resolution to focus the total intensity of each reflection into a narrower angular range, which increases the height of each reflection and hence leads to a higher signal to noise ratio. Diffraction patterns with higher signal to noise ratios are more likely to show weak features such as superlattice or satellite reflections that may otherwise

be unobserved due to their small intensity relative to the background. The combination of the improved signal to noise ratio with the higher resolution and the ability to tune the incident radiation to different wavelengths as required makes synchrotron X-ray powder diffraction a superior technique for determining the structures of materials compared to diffraction from sealed tube X-ray sources.

The interaction of X-rays with matter is also much stronger than that of neutrons, improving the intensity of the diffracted beam in synchrotron X-ray powder diffraction compared to neutron diffraction.[136] This means that X-ray diffraction can be performed using both a smaller sample size (typically 50 - 100 mg compared to 1 g - 15 g for neutron diffraction), and shorter collection times (~10 - 20 minutes per pattern for a synchrotron X-ray powder diffractometer compared to 1 - 8 hours for a neutron diffractometer).

The shorter collection time and smaller sample size makes synchrotron X-ray powder diffraction the ideal technique for structurally characterising a large number of samples or conducting variable temperature measurements. This is the underlying reason why synchrotron X-ray powder diffraction was primarily used to characterise all samples before further studies were performed using other methods. Additionally, the reduced collection times for synchrotron X-ray powder diffraction allow finer temperature intervals to be selected during variable temperature studies relative to neutron studies; particularly for cases where the main objective was to obtain precise lattice parameters of the unit cell of the structure under investigation.

Synchrotron X-ray powder diffraction may appear to be a far better tool than neutron diffraction for the characterisation of samples due to the higher resolution, improved signal to noise ratio and shorter collection times available. However, the way that X-rays interact with matter is fundamentally different to neutrons and this gives rise to different trends in the sensitivity of the two techniques to different elements.

Since the X-ray scattering factor of an atom is proportional to the number of electrons, heavier atoms scatter X-rays far more strongly than lighter atoms (see Figure 2.2, green). Conversely, there is no clear relationship between the interaction of neutrons and the atomic nuclei in the sample since it depends on the short range nuclear forces and resonance scattering (see Figure 2.2, blue). This means that nuclear scattering power of elements next to each other in the periodic table or even isotopes of the same element can be very different. Hence, in many cases, neutron diffraction can be an extremely useful technique for examining structures that contain two or more elements with similar atomic numbers.

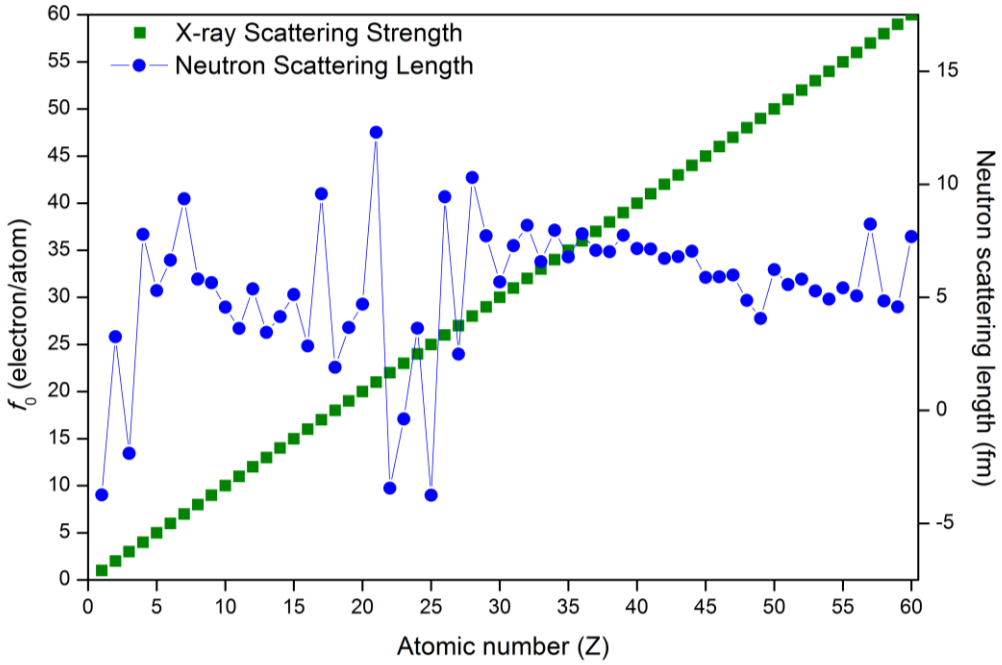

Figure 2.2: Comparison between the scattering strengths of X-rays (green squares) and neutrons (blue circles) for the first 60 elements of the periodic table, as indicated by the X-ray form factor (f_0) and neutron scattering length, respectively.[138]

Since the neutron scattering length of an element does not necessarily increase with increasing atomic number, neutron diffraction is relatively more sensitive to lighter elements in the presence of heavier elements than X-ray diffraction. This property of neutron diffraction was particularly useful in this study where the structures of metal oxides were examined. The relatively high X-ray scattering power of cations such as barium and strontium relative to oxygen anions can reduce

the relative contribution to the diffraction pattern from oxygen anions in X-ray diffraction experiments. Neutron diffraction was an important technique for the investigation of the fresnoite structures in this thesis because the diffraction patterns from these structurally modulated samples contain inherently weak satellite reflections that correspond primarily to the displacements of the oxygen ions in the structure. The use of neutron diffraction in combination with X-ray diffraction is an extremely useful strategy to create a comprehensive understanding of the precise lattice parameters, atomic positions, and anisotropic displacement parameters of all atoms in the structure.

2.2 Structure Solution

Solving the crystal structure of a completely unknown compound typically requires either single crystal X-ray and/or neutron diffraction. In cases where only a polycrystalline sample of the material is available, some structures can be solved using very high quality synchrotron and/or neutron diffraction patterns in combination with computational *ab initio* simulation/solution methods. However, these methods are typically time consuming and extremely difficult to apply to incommensurately modulated structures correctly.

Solving a crystal structure from its diffraction pattern involves three main stages. Firstly, the unit cell, Bravais lattice, and space group of the average structure must be determined. This is achieved through analysis of the position of the main reflections and identifying systematically extinct reflections. To extend the symmetry to describe a modulated structure, it is necessary to consider all superspace groups compatible with the Laue symmetry in addition to the relevant additional superspace extinction conditions.[94,106,139]

Once the space group of the unknown phase has been established, it is necessary to determine the approximate positions for the atoms in the structure and place them into a starting model. The

positions can be determined through direct methods which analyse the Fourier intensity in the diffraction pattern, however, this approach is typically more suited towards structure solution from single crystal diffraction data. In many cases, characterisation from powder diffraction data commences by entering the parameters from a model of a well known reference compound that is ideally very similar to the phase under investigation. Visual inspection to check that the differences between the experimental pattern and the pattern from the reference compound are minimal ensures that a plausible starting model has been chosen. If the difference between the parameters (such as the atomic positions) in the starting model and the unknown phase are small enough, these starting values may be a sufficient starting point for the characterisation of the unknown phase.

The next step involves the refinement of the atomic positions and other parameters to produce a model with parameters that are a correct and plausible representation of the unknown phase. Confirmation that the correct indexing and space group assignment have occurred can only occur through the successful refinement of the structure. This is most commonly achieved through the Rietveld refinement method,[140] which will now be discussed in further detail.

2.2.1 Rietveld Method

The Rietveld refinement[140] method involves the application of a least squares optimisation process to systematically refine one or more parameters at a time until stable (and plausible) parameters that agree with the experimental profile are reached.[132] A reasonable starting model of the unknown structure is always required when using the Rietveld method to characterise structures using X-ray and/or neutron diffraction data. The refinement procedure usually starts by refining a small number of parameters in the starting model, and releasing more parameters as the model approaches a better description of reality.

Parameters that are likely to produce the largest changes in the model are typically refined at an earlier stage of the process than parameters that may produce smaller changes. Refinements are repeated until all parameters remain stable when refined simultaneously to produce a plausible model whose calculated pattern agrees with the experimental profile.

The calculation of reflection intensities in powder diffraction patterns can be complicated by the extent of overlapping independent reflections in one-dimensional space that are typically resolved in three-dimensional space in single crystal diffraction patterns. Rietveld refinement overcomes this complication by using every data point in the powder diffraction pattern instead of only peak intensities that are extracted from the experimental pattern. This allows the position and intensity of reflections to be calculated individually instead of integrating the grouped intensity of overlapping reflections.[140]

The Rietveld method calculates the intensity at any point y_{ic} according to Equation 2.2. The variables are defined as follows: y_{ic} is the net intensity at point i, y_{ib} is the background intensity, G_{ik} is the normalised peak profile function, i_k is the intensity of the k_{th} Bragg reflection contributing intensity at point i, and p is the number of phases present.

$$y_{ic} = y_{ib} + \sum_{p} \sum_{k=k_1^p}^{k_2^p} G_{ik}^p I_k \qquad \textbf{Equation 2.2}$$

The Rietveld method uses two different categories of parameters to model diffraction data. These are global parameters that are determined by the experimental apparatus used, and the structural parameters, which depend on the structure of the compound. Global parameters include but are not limited to variables such as the zero-offset correction, background parameters, peak shape parameters, and where necessary, absorption and preferred orientation coefficients.[132] Structural parameters are used to fit the integrated intensities of the model to the experimental profile, and

include but are not limited to cell parameters, phase scale(s), atomic positions, occupancies, and atomic displacement parameters (ADPs). Some refinable parameters are exclusively sample-dependent (*e.g.* atomic positions), while some are instrument-dependent (*e.g.* zero-offset correction), and some are affected by both (*e.g.* some peak shape parameters).

The background parameters are one of the first sets of parameters to be fitted. The backgrounds in this project were fitted using up to 15th order Legendre polynomial functions (Equation 2.3) where B_m is one of 15 refinable functions.

$$y_{ib} = \sum_{m=-1}^{n} B_m \, (2\theta)^m \qquad \textbf{Equation 2.3}$$

Other critically important instrumental parameters are the peak shape parameters. Pseudo-Voigt functions were used to fit the peak shapes in all diffraction patterns in this project because of the superior fit obtained in modelling both X-ray and neutron diffraction patterns owing to their sensitivity to both Lorentzian and Gaussian components of the peak shape.[141] The pseudo-Voigt function (G_{ik}) is defined in Equation 2.4 where $C_0 = 4$, $C_1 = 4ln2$, H_k is the FWHM of the k^{th} Bragg reflection, $X_{jk} = \frac{(2\theta_i - 2\theta_k)}{H_k}$ and γ is a refinable "mixing" parameter with $\gamma = 0$ and 1 being the Gaussian and Lorentzian limiting cases respectively.[142] Where necessary, an asymmetry correction can be applied using either the Simpson asymmetry function or asymmetry by divergence, depending on the geometry of the diffractometer used.[143] In this project, diffraction patterns containing significant asymmetry collected from the Australian synchrotron powder diffraction beamline and Echidna were modelled using the Simpson asymmetry function and asymmetry by divergence, respectively.

$$G_{ik} = \gamma \frac{C_0^{1/2}}{H_k \pi} \left[1 + C_0 X_{ik}^2\right]^{-1} + (1 + \gamma) \frac{C_1^{1/2}}{H_k \pi^{1/2}} exp\left[-C_1 X_{jk}^2\right] \qquad \textbf{Equation 2.4}$$

The Rietveld refinement of models that incorporate modulated structures requires additional input data compared to conventional three-dimensional models. Models of modulated structures require the correct superspace group, the number of dimensions that the modulation occurs in, and the maximum order of satellite reflections to be included in the calculation. This information is not refinable. The modulation is most commonly parameterised through the use of a truncated Fourier series that represents the amplitudes of the functions describing the modulations from the basic structure.[93] Each harmonic involves up to six parameters for each atom in the unit cell of the basic structure. In this project, the initial refinements were restricted to one or a few atoms to improve the probability of arriving at the correct structure. Likewise, the refinement of modulated structures was performed starting with a single harmonic for up to first-order satellite reflections to increase the probability of arriving at the appropriate minimum. If observed, higher harmonics corresponding to higher reflection orders can generally be introduced to improve the fit of the modulation parameters and correctly account for the satellite reflections in the experimental pattern.[92]

The quality of a model is quantified after each cycle of calculation through the profile factor R_p, the weighted profile factor R_{wp}, expected profile factor R_{exp}, the Bragg profile factor, R_B, the weighted Bragg factor R_{wB}, and the goodness of fit term, χ^2 (Equations 2.5 to 2.9).[144,145] These values are used to determine the agreement between the calculated structural model and the observed pattern. In a reasonable model, these values should converge to a minimum after each successful set of refinement cycles. Different *R*-factors represent different ways of quantifying the fit between the calculated model and the observed data. For example, the weighted profile *R*-factor, R_{wp} depends on the fit of the model at each point in the profile, while the Bragg factor, R_B, depends on the fit of the set of integrated reflection intensities. While it is ideal to obtain the lowest possible values for these figures, the addition of more parameters to the refinement such as additional background parameters to obtain a minor improvement in the fit should be avoided to prevent over-parameterisation.[132]

The profile factor $R_p = \frac{\sum|y_{i\,(obs)} - y_{i\,(calc)}|}{\sum y_{i\,(\mathrm{obs})}}$ x 100 **Equation 2.5**

The weighted profile factor $R_{wp} = \frac{\left[\sum w_i (y_{i\,(obs)} - y_{i\,(calc)})^2\right]^{1/2}}{\left[\sum w_i\, y_{i\,(obs)}{}^2\right]^{1/2}}$ x 100 **Equation 2.6**

The expected profile factor $R_{exp} = \left[\frac{N-P+C}{\sum w_i y_{i\,(obs)}^2}\right]^{1/2}$ x 100 **Equation 2.7**

The Bragg profile factor $R_B = \frac{\sum|I_{k\,(obs)} - I_{k\,(calc)}|}{\sum I_{k\,(obs)}}$ x 100 **Equation 2.8**

The weighted Bragg profile factor $R_{wB} = \frac{\left[\sum w_i (I_{k\,(obs)} - I_{k\,(calc)})^2\right]^{1/2}}{\left[\sum w_i\, I_{k\,(obs)}{}^2\right]^{1/2}}$ x 100 **Equation 2.9**

The goodness of fit term $\chi^2 = \frac{\sum \mathrm{w_i}(\mathrm{y_{i\,(obs)}} - \mathrm{y_{i\,(calc)}})^2}{\mathrm{N-P+C}} = \left[\frac{\mathrm{R_{wp}}}{\mathrm{R_{exp}}}\right]^2$ **Equation 2.10**

Where:

$y_{i(obs)}$ is the set of observed diffraction intensities collected at each step across the pattern

$y_{i(calc)}$ is the set of corresponding calculated values

w_i is the weight assigned to the individual step intensity given by:

$$w_i = \frac{1}{\sigma_i^2} = \frac{n}{y_{i(calc)}} \qquad \textbf{Equation 2.11}$$

n is the number of detectors contributing to the step intensity average and σ_i^2 is the variance at the i^{th} step.

N is the total number of observations, *i.e.* the total number of y_{obs} values when the background is refined.

P is the number of refined parameters

C is the number of constraints

$I_k\ (obs)$ is the observed intensity assigned to the K^{th} Bragg reflection at the end of the refinement cycles.

$I_k\ (calc)$ is the calculated intensity assigned to the K^{th} Bragg reflection at the end of the refinement cycles.

Very few refinement programs can handle the extra information required to model a modulated structure. Jana2006 is one of the most commonly used programs for the refinement of modulated structures because of its unique capability of calculating commensurate and incommensurate structures for both single crystal and powder data, multiphase models, magnetic structures, and conventional three-dimensional structures. Jana2006 also contains powerful constraints and rigid unit restrictions which were used in this project.[146]

2.3 Electron Diffraction and Imaging

Electron diffraction and imaging can be an extremely useful tool for the investigation of symmetry and ordering of crystal structures. The electron-electron interaction used in electron diffraction techniques is significantly stronger that the X-ray-electron and neutron-nucleus interactions used in X-ray and neutron diffraction, respectively.

Electron diffraction uses a high voltage to produce an extremely small electron beam that can be focused by a series of lenses before passing through the sample. The wavelength of the electrons accelerated in electron diffraction is much smaller than the wavelengths used in other types of diffraction. This fundamental difference means that the region in reciprocal space where the diffraction conditions can be satisfied (the Ewald sphere, of radius $r = 2\pi/\lambda$) is much larger in electron diffraction experiments than for X-ray or neutron diffraction experiments. Hence, more information about the two-dimensional distribution of reciprocal lattice points can be determined from electron diffraction over X-ray or neutron diffraction.

The extremely strong interactions utilised in electron diffraction produce diffraction patterns with intense Bragg reflections which may not be observed using other diffraction techniques. Modulated structures are particularly good candidates to be investigated using electron

diffraction because of the importance of identifying the positions of the relatively weaker satellite reflections that appear between the strong main Bragg reflections.

The extremely small size of the beam allows only very small spatial regions of a crystallite to be studied at any one time. The collection of high quality electron diffraction patterns is also complicated by the need to find crystals of the appropriate quality, size, thickness, and the correct orientation. Investigating a crystal without all of these requirements will produce either diffraction patterns of poor intensity, containing additional erroneous spots, or potentially irrelevant information due to looking along the wrong direction of the crystal. Because the electron beam must pass through the sample, only crystals with thicknesses less than approximately 100 nm can be typically investigated to ensure that reasonable intensity of the diffracted beam is detected and that to prevent the observation of multiple scattering events as the electrons pass through the sample.

Electron diffraction patterns are typically collected along a zone axis of the crystal to ensure that the pattern contains information that can be interpreted appropriately to deduce structural information from the sample. It is often necessary to tilt the orientation of the sample with respect to the incident beam to ensure that the incident electron beam is travelling exactly along a zone axis of the crystal.

The use of a very short wavelength of the electrons accelerated towards the sample allows very high resolution images of the crystallite structure and morphologies to be obtained. Under these conditions, images of sufficient resolution can be obtained to identify boundaries between individual domains and, in some cases, even individual atoms within the crystallite.

High resolution images and electron diffraction patterns were collected from finely ground polycrystalline samples that were suspended in an ethanol solution which was evaporated after

placement onto a holey carbon surface. Electron diffraction experiments in this project were collected from three different instruments. These instruments are the Philips EM 430 transmission electron microscope (TEM) in the Research School of Chemistry at the Australian National University, and the JEOL JEM-2011 and -100F TEMs in the Monash Centre for Electron Microscopy at Monash University. Electron diffraction patterns were recorded using both a charge-coupled device (CCD) camera and photographic film. All instruments were operated under vacuum at 200 kV. *In situ* variable temperature experiments were performed between 300 K - 543 K using a Gatan double-tilt furnace sample stage.

2.4 X-ray Absorption Spectroscopy

X-ray absorption spectroscopy (XAS) includes both extended X-ray absorption fine structure spectroscopy (EXAFS) and X-ray absorption near edge structure spectroscopy (XANES). These techniques measure the X-ray absorption coefficient, μ, of a sample as a function of energy by measuring the intensities of an incident beam relative to a transmitted or reflected beam after interaction with the sample. The incident and transmitted (or reflected) intensity of highly collimated X-rays are measured using ion counters located before and after the sample as the energy is scanned across an energy region of interest. The intensity of the transmitted beam (I_t) is equal to the intensity of the incident beam (I_0) multiplied by a decreasing exponential that is determined by the atoms in the sample, the absorption coefficient μ, and the thickness of the sample x (Equation 2.12).

$$I_t = I_0 e^{-\mu x} \qquad \textbf{Equation 2.12}$$

When the energy of the incident X-ray beam matches the binding energy of an electron of a specific atom in the sample, the X-ray absorption increases dramatically, producing an absorption edge in the X-ray absorption spectrum. The position and features of absorption edges can provide information about the oxidation state and coordination environment of specific atoms in the

sample when compared against standard X-ray absorption spectra collected from well known compounds with a similar composition to the sample of interest.

The X-ray absorption spectrum of a sample can be divided into 3 different regions which are defined relative to the absorption edge of interest. The pre-edge region typically includes the range of energies from approximately 200 eV - 10 eV before the absorption edge, providing information about the coordination environment of the atom under investigation. The edge region typically includes the range of energies approximately 10 eV before and 60 eV after the absorption edge, providing information about the oxidation state and coordination environment of the atom of interest. Finally, the post-edge region typically includes the range of energies beyond approximately 60 eV after the absorption edge, typically providing information about nearest neighbour and second nearest neighbour interactions for the target element. The difference between EXAFS and XANES is simply the size of the post-edge region investigated beyond the edge. In this thesis, the post-edge region in XANES experiments was defined from approximately 60 eV - 200 eV beyond the edge. For EXAFS experiments, the post-edge region was defined as being from 60 eV - 600 eV beyond the edge.

The EXAFS and XANES spectroscopic measurements in this project were conducted at beamline 20B at the Australian National Beamline Facility (ANBF), located at the High Energy Accelerator Research Organisation, Tsukuba, Japan. The apparatus was set up in transmission geometry for all experiments in this project. Samples were diluted homogeneously in a boron nitride matrix to ensure that the intensity of the transmitted X-ray beam was within the necessary range to be detected by the ion counter. The diluted samples were held between two pieces of kapton tape in 1 mm thick sample holders that could hold up to 4 samples.

The coordination environment of the titanium atom in the fresnoite structure type was investigated by collecting EXAFS and XANES spectra across the titanium edge at 4966 eV. The

investigation of any samples and standards containing barium was conducted across the titanium K-edge between 4755 eV - 5200 eV (XANES) in order to avoid collecting spectra across the barium L_3-edge at 5247 eV. Data were collected across the titanium K-edge between 4755 eV - 5600 eV (EXAFS) for samples and standards that did not contain barium.

EXAFS spectra were collected with a count time of 3 seconds per step, however the step size was varied according to the distance from the edge. Spectra in the pre-edge region (4755 eV - 4955 eV) were collected in 20 eV energy steps. Spectra in the edge region (4955 eV - 5025 eV) were collected in 0.00025 eV steps. Spectra in the post-edge region (5025 eV - 5600 eV) were collected in 0.05 eV steps. All XANES spectra were collected using identical collection times and step sizes as described for EXAFS experiments, with the exception that the step size used in the post-edge region was 0.25 eV.

Data were averaged, analysed, and plotted using software packages Average 2.0, Athena, and Microcal Origin, respectively. Plotting spectra from different samples and standards on the same graphs allowed for the direct comparison of the position and features of the absorption edges such that any changes in coordination environment between different samples could be identified.

2.5 Resonant Ultrasound Spectroscopy

Resonant ultrasound spectroscopy (RUS) is a technique used to measure the normal frequencies of vibration of an object to deduce information about its elastic constants and mechanical dissipation. The frequencies and dissipation of the vibrations of an object depends on its physical symmetry (*i.e.* its shape), crystal symmetry, density, and its dimensions. Because the frequencies of the resonances from a sample are dependent on the crystal symmetry, RUS can be a useful technique for the investigation of changes in crystal structure that occur across structural phase transitions.

The bulk and shear moduli (K and G, respectively) can be determined from the position of each resonance for high quality polycrystalline samples. The bulk modulus describes the uniform deformation experienced by an object under the force of a uniform load, and the shear modulus describes the sheared deformation of an object when it is under the force of two or more opposing loads. In principle, all independent elastic constants can be measured from single crystal samples, while only K and G can be determined for polycrystalline samples. The square of the resonance frequency of any peak in a RUS spectrum scales linearly with the square of the effective elastic modulus (or combination of moduli) associated with that vibrational mode.[147] Therefore, it is possible to observe the variation of elastic constants directly from the variation of the resonance peaks measured as a function of temperature in a RUS experiment. The quality factor, Q, which is a measure of anelastic dissipation (defined as dissipation showing no obvious relationship between stress and strain), can also be obtained from the full width at half maximum height of each resonance in the spectra. The elastic constants and quality factor of a compound are both very susceptible to structural changes, making RUS a useful tool for the investigation of phase transitions.

The first step in determining the elastic constants of a sample with known dimensions (shape, size and density) using RUS involves experimentally measuring its natural resonance frequencies. In principle, any shape of sample can be used, however, rectangular parallelepipeds with significantly different edge lengths (*e.g.* > 0.5 mm difference) are the ideal geometry. This geometry is preferred because the orthogonal faces make the calculation of elastic constants significantly more achievable. Rectangular parallelepipeds are preferred over cubes because none of the resonances will be degenerate and all modes can be observed individually. Samples of significantly different edge lengths produce spectra where the resonance peaks are more widely distributed and hence easier to measure than for almost cubic samples. Optimal dimensions of each edge of the parallelepipeds used in this project are of the order of a few mm. The dimensions of each sample investigated are provided in the relevant experimental method sections of each chapter.

A general RUS setup consists of the parallelepiped sample being held lightly, without bonding agents, across diametrically opposite corners between two piezoelectric transducers. The corner-mount geometry is chosen for two reasons. Firstly, this geometry greatly reduces loading on the sample during the experiment. Secondly, the corners of the sample are never nodes of the vibration, which means that they couple to all normal modes and hence no resonances will be missed during measurements.[148]

The resonance frequencies of a sample are measured by using a frequency synthesizer to drive a vibrating transducer at constant amplitude across a range of ultrasonic frequencies that are dependent on the sample experimental setup. The vibrations cause the sample to resonate at particular sample-dependent frequencies. The second transducer detects and records the signal from the sample in terms of its displacement across the frequency range. The vibrations are recorded as a series of peaks which occur at the frequencies of the natural mechanical resonances of the sample. The signal sent from the computer to the synthesiser is independent of the

incoming signal that has been sent from the amplifier through the phase sensitive detector to the computer. A schematic diagram of this setup is provided in Figure 2.3.

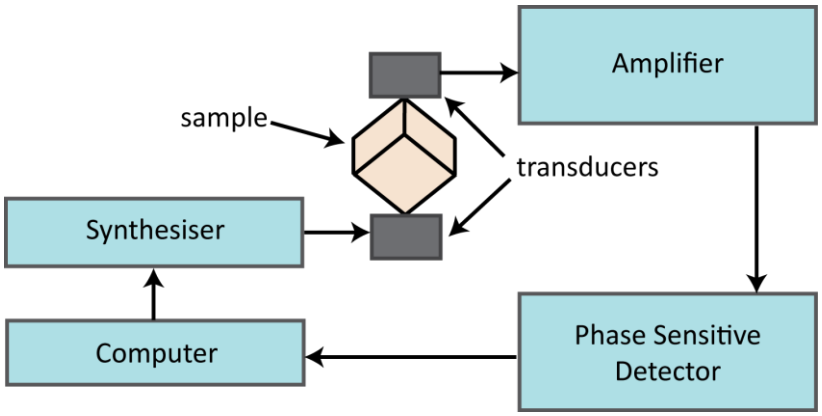

Figure 2.3: Schematic diagram of the RUS system. Adapted from Migliori and Maynard (2005).[149]

The general RUS setup can be adapted to examine samples in high and low temperature environments, such that the variations of elastic behaviour with temperature may be measured. Resonance frequencies typically show an overall gradual decrease with increasing temperature, associated with normal thermal elastic softening. However, in analogy to monitoring the cell parameters using diffraction techniques, more interesting changes can be observed when a sample undergoes a phase transition or any other structural change that affects its elastic behaviour. These changes commonly result in the rapid softening or stiffening of the elastic constants which can be seen in the change in frequency of resonances in the spectrum. It is desirable to collect resonance spectra in small temperature intervals (~3 K) near a suspected phase transition temperature to ensure that the changes can be easily and accurately identified.

2.5.1 Sample Preparation

Careful preparation of the sample is critically important before starting an RUS experiment. Samples must be cut into rectangular parallelepipeds with orthogonal faces using a high precision annular diamond saw in combination with paraffin lubricant. Meaningful results can only be

obtained from densely packed parallelepipeds (> ~90 % of the theoretical density) that do not contain cracks or flaws of any kind. In this project, polycrystalline samples were cut into parallelepipeds with edge lengths ~1-3 mm from homogeneous cylindrical pellets (13 mm diameter, ~8 mm thick), avoiding any visible cracking. During the cutting process, samples were adhered to glass blocks using Crystalbond™ adhesive with a softening temperature of 120 °C - 130 °C. Two parallel cuts were made into the original sample to make a slice. This slice was then removed from the glass block and re-glued such that one of the cut surfaces sat exactly flat on the glass block. Several parallel cuts were made perpendicular to the flat surface. The glass block (including the attached sample) was then rotated by 90° such that several more parallel cuts could be made to complete the parallelepipeds. Each cut was calculated and positioned to ensure that none of the dimensions of the parallelepipeds were equal. This method allowed up to six rectangular parallelepipeds to be cut from any one pellet. The adhesive was removed from the samples using acetone. The density of each parallelepiped was determined from the dimensions and mass which were measured using a standard digital micrometer and an electronic balance, respectively.

2.5.2 RUS Experiments at Ambient Temperature

The elastic properties of all parallelepipeds were measured at room temperature before high and low temperature experiments were conducted. The RUS stage for frequency measurements at ambient temperature is pictured in Figure 2.4. The transducers are coated in gold to reduce radio interference in the output signal, and are directly connected to the signal generator and detector electronics which are in turn connected to a computer for recording of the signal.

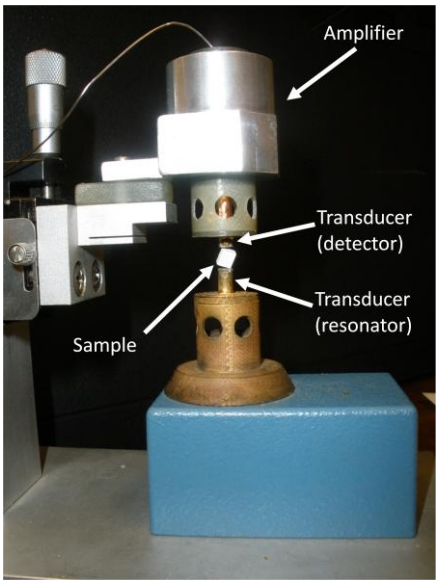

Figure 2.4: RUS apparatus for data collection at ambient temperature.

All resonances of the sample should be measured at ambient temperature to ensure that a complete analysis can be conducted. Hence, spectra are collected from each parallelepiped in at least four different orientations (*e.g.* different corner-, edge-, and face-mounted geometries) to ensure that as many resonances are identified as possible so they can be considered in the analysis of the results. -

Spectra were typically collected across the frequency range 200 kHz - 1200 kHz. The exact frequency range measured for each parallelepiped was dependent on the sample size because larger samples give resonances at lower frequencies. Frequency ranges were chosen based on preliminary checks that identified the position of the resonance peaks for each sample.

2.5.3 Low temperature RUS experiments

Samples that had the potential to show interesting behaviour below ambient temperature were studied using a specially adapted low temperature RUS apparatus fitted to the end of a stick that is inserted vertically into a standard AS Scientific Products Ltd. orange 50 mm helium cryostat

that is capable of maintaining temperatures as low as 5 K, using liquid helium and/or liquid nitrogen as the cryogens depending on the temperatures required (Figure 2.5). Temperature regulation and measurement are achieved using a silicon diode attached to a LakeShore controller with an accuracy of ± 1 K.[150] Samples were positioned between the two transducers with no bonding agents or adhesives required to fix them in place.

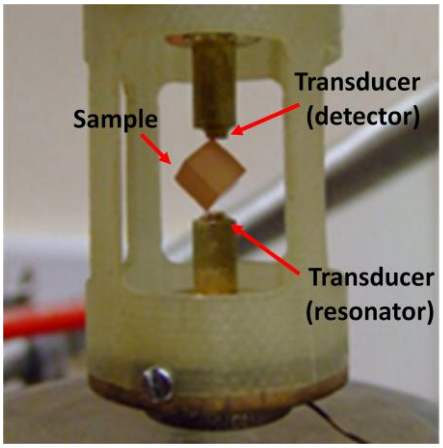

Figure 2.5: Low temperature RUS apparatus Image adapted from McKnight (2009).[150]

Spectra were collected at large temperature intervals (20 K - 40 K) during cooling from ambient temperature, and then in smaller steps (1 K - 10 K) on heating back to ambient temperature. This strategy ensures that the changes in resonance frequencies can be monitored on cooling for samples with relatively unknown behaviour so that specific temperature regions of interest can be targeted in detail during heating. This cooling regime also reduces the amount of cryogen gas consumed during the experiment by reaching the lowest temperature quickly, followed by slow heating. Spectra were typically collected between 200 kHz - 1200 kHz for low temperature experiments.

2.5.4 High temperature RUS experiments

The high temperature RUS apparatus (Figure 2.6) is ideal for the investigation of samples that have the potential to show interesting behaviour above ambient temperature. The sample is

lightly held without bonding agents between the ends of two horizontal long, thin, alumina buffer rods (0.3 m each). The two transducers are located at the other ends of the rods such that the input and output signals are communicated between the sample and transducers through the rods. The sample is heated inside a commercial Netzsch 1600 °C resistance furnace which operates in air. The furnace is slid over the rods such that the sample is heated while the ends connected to the transducers stay outside the furnace tube. One important disadvantage of this arrangement is that the signal becomes noisy due to unavoidable resonances in the rods.

The temperature of the furnace is set and monitored using a Eurotherm controller in combination with a thermocouple held a few millimeters away from the sample. This apparatus has been shown to be accurate and stable to ± 0.1 K for temperatures below 1268 K and approximately ± 1 K for temperatures above 1268 K.[150] The temperature scales for each data set were calibrated with respect to data obtained from the well known $\alpha \leftrightarrow \beta$ transition in quartz as described by McKnight.[150]

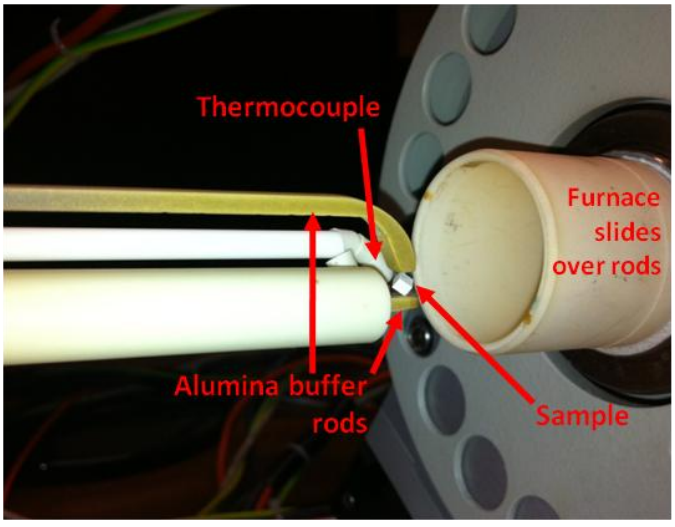

Figure 2.6: High temperature RUS apparatus.

Spectra were collected at large temperature intervals (20 K - 40 K) as the samples were heated from room temperature. Detailed measurements were carried out in smaller temperature

intervals (1 K - 10 K) during cooling rather than heating because the coupling between the sample surface and the rods improves once high temperatures have been reached. The improved coupling improves the signal to noise ratio, and hence improves the quality of the spectra collected after the highest temperature has been reached. Additionally, the large temperature collection intervals on heating can provide information on which temperature intervals to target with smaller cooling increments for relatively unknown samples. Spectra were typically collected in the frequency range 200 kHz - 1200 kHz using the high temperature RUS apparatus. In high temperature experiments, additional peaks are often present at regular frequency intervals due to vibrational resonances of the alumina rods. These additional peaks can be easily identified because their elastic properties are relatively constant across the temperature range of the instrument, and hence their position is independent of temperature. The presence of these additional peaks can complicate the analysis of the spectra when they overlap with the peaks from the sample.

2.5.5 Data Analysis

A RUS spectrum collected from a typical parallelepiped using the ambient temperature apparatus is pictured in Figure 2.7. Peaks in the spectrum occur at the resonant frequencies of each of the normal modes of the sample. Absolute values of the amplitudes are highly variable because they are very dependent on the mechanical coupling of the parallelepiped with the transducers, and hence its orientation between them. The peak frequencies and their widths however, are characteristic of any sample, and if measurable, provide information about the elastic behaviour. A set of resonance frequency values measured from a single RUS spectrum can be used to determine the elastic moduli of the sample using the fitting procedure described in section 2.8.2 of McKnight.[150]

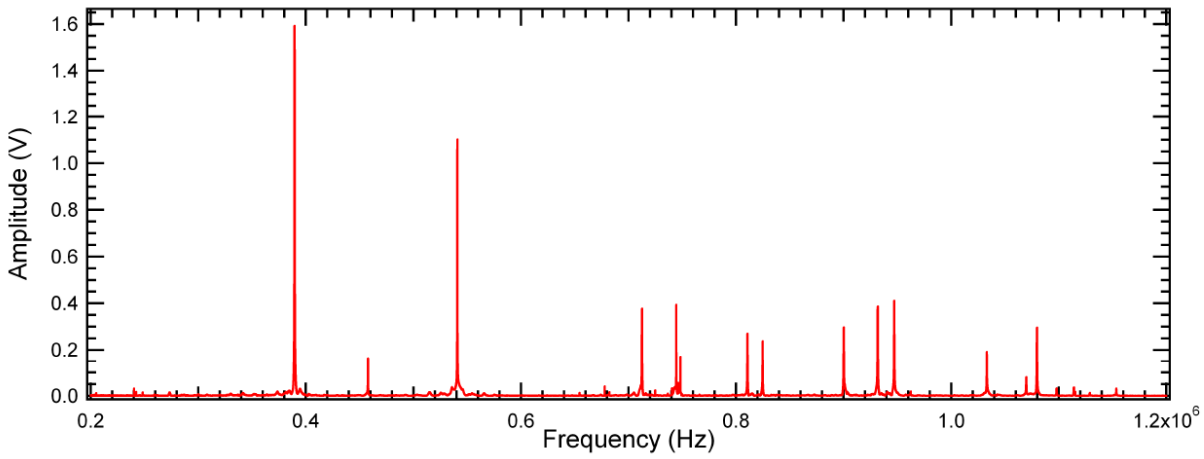

Figure 2.7: A typical RUS spectrum collected between 200 kHz - 1200 kHz at ambient temperature. Peaks represent resonances of each of the vibrational modes of the sample. Sourced from McKnight.[150]

The position and FWHM of all measured peaks are determined by transferring the data into the software package Igor Pro (Wavemetrics). The peaks are modelled using an asymmetric Lorentzian function (Equation 2.13) where a(f) is the amplitude, which is a function of frequency f, a_0 is the baseline, f_0 is the frequency at the peak maximum, and A and B are constants that describe the extent of asymmetry of the peak with the ratio A/B equal to the height of the peak above the baseline at $f = f_0$. Different Lorentzian profiles were fitted for the lower ($f < f_0$) and higher frequency ($f > f_0$) parts of each resonance, but the baseline, the value of f_0, and the ratio A/B were kept the same for both fits to maintain an asymmetric Lorentzian peak profile. Peak fitting was carried out using the curve fitting feature of Igor Pro by inserting the text shown in Appendix A into the Procedure Window of Igor Pro.

$$a(f) = a_0 + \frac{A}{(f - f_0)^2 + B} \qquad \textbf{Equation 2.13}$$

The 'lorentz2' function defined in Appendix A requires a number of input parameters that will be refined to fit the position and shape of the resonance being modelled. The boundaries of the peak to be fitted were defined manually. Starting values for the coefficients in the `lorentz2' function are typically of the order of $w_0 = w_5 = 0$ (these two coefficients describe the baseline),

w_1 = estimated frequency of the peak maximum (in Hz), w_2, w_3, w_4 describe the peak shape. w_2 and w_3 describe the Lorentzian fit (shape and height) for the low frequency ($f < f_0$) side of the peak, and w_4 is the only variable for the high frequency ($f > f_0$) side, so that the peak height (A/B in Equation 2.13) is the same for both fits. The output coefficient w_1 provides an exact value for the peak position and therefore the resonance frequency of that vibrational mode. A plot of the square of the frequency for a single resonance peak as a function of temperature provides a detailed view of how the elastic moduli associated with that mode behaves as a function of temperature. This simple comparison is possible because of the directly proportional relationship between the elastic moduli and the frequency squared, f_0^2 for any mode.[147]

An example of the analysis of a single resonance peak using the procedure described here is provided in Figure 2.8 where the raw RUS data are plotted as a full red line, the `lorentz2' curve fit using an asymmetric Lorentzian function is shown as a dashed blue line, and Δf is the full peak width at half maximum height (FWHM).

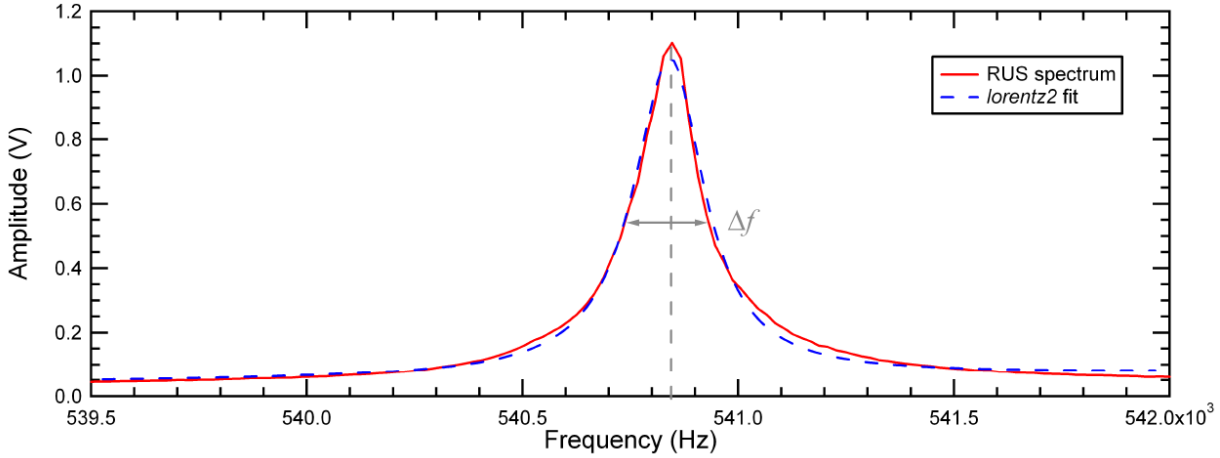

Figure 2.8: A typical resonance peak from a RUS spectrum. The raw RUS data are plotted as a red full line, the 'lorentz2' curve fit using an asymmetric Lorentzian function is shown as a dashed blue line, and Δf is the full peak width at half maximum height. Sourced from McKnight (2009).[150]

Measurements of the FWHM may be used to determine the quality factor, Q, according to Equation 2.14 where f_0 is the peak frequency and Δf is the FWHM obtained from the peak fitting process.

The inverse quality factor, Q^{-1}, is a direct measure of the acoustic dissipation (internal friction or loss) for each resonance. A plot of Q^{-1} as a function of temperature can therefore provide information about any relaxation mechanisms that may operate in the material. Peaks are often seen in Q^{-1} at phase transition temperatures due to the changes in dissipation when structural changes occur.

$$Q = \frac{f_0}{\Delta f} \qquad \textbf{Equation 2.14}$$

The advantages of the direct relationship between elastic moduli and the square of the resonance frequency, and the mechanical dissipation and FWHM should not be underestimated. The true resonance frequency and FWHM values can be difficult to define due to potential difficulties in distinguishing them from background noise, or because of complication due to their convolution with other overlapping resonance peaks. In these cases, even if a peak fit is not possible, the general form of the variation of peak frequencies can be easily seen in a stacked plot of resonance spectra as a function of temperature. Such plots will be used in this thesis to follow the trends of resonant frequencies, and therefore elastic moduli, as they evolve with temperature.

2.6 Differential Scanning Calorimetry

Differential scanning calorimetry (DSC) is a technique that measures the amount of heat required to increase the temperature of a sample relative to a reference material of well known heat capacity. DSC is useful for the investigation of phase transitions because it measures the amount of heat passing through a sample as energy is absorbed or released when a phase change occurs. The location and size of any anomalies in a heat flow versus temperature DSC curve can provide information about the precise temperature and the order of the transition. Therefore, in the context of metal oxide chemistry, DSC is a useful tool that can provide valuable information on structural phase transitions.

DSC experiments in this project were conducted on a TA Instruments 2920 Differential Scanning Calorimeter using a N_2 purge rate of 60 ml min^{-1}. Approximately 15 mg - 30 mg samples were weighed into 40 μL aluminium pans. Data were typically collected during both heating and cooling cycles for each sample between approximately 325 K - 780 K. The cooling rate was maintained using the TA Instruments Liquid Nitrogen Cooling Accessory. Heating and cooling were typically conducted at 20 K min^{-1} and 2 K min^{-1} respectively. The baseline for this instrument was collected from an empty sample pan. A reproducible feature was observed in the baseline of the instrument at 723 K (Figure 2.9) which has been neglected in the analysis of DSC curves in this project.

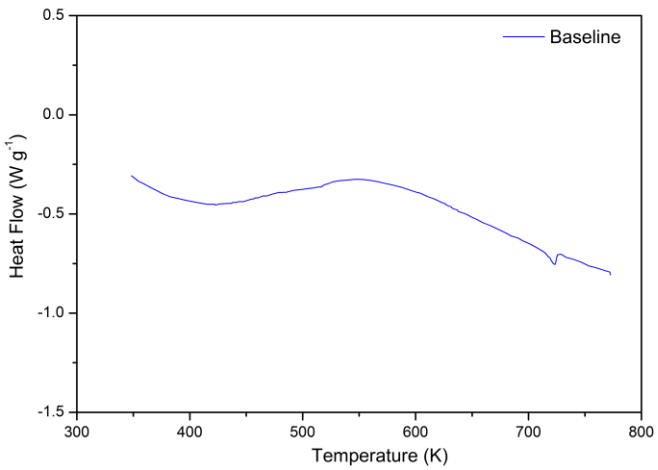

Figure 2.9: Differential scanning calorimetry baseline between 325 - 780 K.

2.7 Physical Property Measurements

Investigations into the physical properties of samples can provide important information about the physical response a sample may produce to external stimuli. The data obtained from these measurements can also complement the findings of structural investigations.

Dielectric properties in this project were investigated using a precise Agilent 4284A LCR meter. Piezoresponse force microscopy (PFM) was performed on selected samples to check their piezoelectric response and search for evidence of ferroelectricity. Measurements were performed on a Cypher SPM from Asylum Research using an internal 15x high voltage amplifier and Olympus AC240TM electrilevers with a spring constant $k \sim 2$ N m^{-1} and a tip radius of $\sim$ 25 nm. Single frequency measurements were performed at 10 kHz applied frequency, $\sim$ 1 V applied voltage and a contact force of about $\sim$ 100 nN. A dual frequency resonance enhanced approach was also used, with a contact force of $\sim$ 100 nN and an applied voltage of about 45 mV. Piezoresponse curves were measured using an AC signal ($f \sim$ 10 kHz, $V_{AC} = \sim$ 0.75 V, phase offset = 180°) superimposed on a 0.2 Hz triangular square-stepping wave with bias up to ± 60 V and a reading and writing time of 25ms.

Chapter 3 Structural Investigation of $Ba_2TiSi_2O_8$

3.1 Introduction

It is important to comprehensively understand the structure and properties of the $Ba_2TiSi_2O_8$ parent compound of the fresnoite structure type before investigating other, more complex compositions within the $Ba_{2x}Sr_{2-2x}TiGe_{2y}Si_{2-2y}O_8$ ($0 \leq x, y \leq 1$) system. Previously published work on $Ba_2TiSi_2O_8$ from electron diffraction patterns and X-ray precession photographs has established that the crystal structure adopts the *P4bm*(α, α, ½)0*gg* space group.[53] This was determined from satellite reflections at $\frac{(1+\delta)a^*}{3}$ ($\delta \sim 0.2$) in diffraction patterns collected down the [001]-axis and the *hk½* level when tilting the sample off the [001]-axis. The presence of *hk½* reflections effectively doubles the *c* unit cell parameter.

Markgraf *et al*.[59] reported that the dielectric constant, planar coupling coefficient, frequency constant, and pyroelectric coefficient reach a maximum value at 433 K. Chang *et al*.[114] established that anomalies also occur in the elastic properties at 433 K. Single crystal X-ray diffraction studies on $Ba_2TiSi_2O_8$ at ambient temperature and 573 K established that the structure undergoes a phase transition from an incommensurate phase to the prototypic phase on heating, and that the presence of the modulation is likely to be associated with the large barium ion inducing distortions into the Si_2O_7-TiO_5 linkage in the *a*-*b* plane.[53]

Polycrystalline and single crystal samples of $Ba_2TiSi_2O_8$ were predicted and then shown to exhibit ferroelectricity by Foster *et al*.[51] through the detection of both AC and DC dielectric hysteresis. It was also established that the transition at 433 K does not coincide with the removal of ferroelectricity and that the atomic displacements required for the transition to the paraelectric phase do not occur below the melting point. Other ferroelectrics with a Curie temperature above their melting point include $LiH_3(SeO_3)_2$,[151] and $BaMgF_4$.[152]

The investigation of a naturally occurring single crystal of fresnoite provided a large amount of new information about this structure. The structure was refined using a five-dimensional superspace approach with the space group $P4bm(\alpha, \alpha, ½)0gg$ with $\boldsymbol{q_1} = 0.302(\mathbf{a^*} + \mathbf{b^*}) + 0.5\mathbf{c^*}$ and $\boldsymbol{q_2} = 0.302(-\mathbf{a^*} + \mathbf{b^*}) + 0.5\mathbf{c^*}$.[125] The composition was determined to be $(Ba_{1.962}Ca_{0.038})Ti_{1.000}Si_{2.000}O_{8.000}$ from wavelength dispersive analysis against baryte (Ba), rutile (Ti) and diopside (Ca, Si) standards. The stoichiometry was found to be consistent throughout the crystal within experimental error.

In 2010, work by Wong *et al*. established that the local composition of polycrystalline $Ba_2TiSi_2O_8$ varies across different regions of each crystallite. Regions of chemical inhomogeneity were shown to be characteristic of incommensurate structural modulations, while regions close to the nominal $Ba_2TiSi_2O_8$ stoichiometry display commensurate modulations or no modulations at all.[124]

This chapter will present the synthesis and precise structural determination of synthetic polycrystalline samples of $Ba_2TiSi_2O_8$ over a wide range of temperatures using X-ray and neutron powder diffraction methods. The $Ba_2TiSi_2O_8$ modulated structure as determined using a neutron powder diffraction approach will be discussed for the first time. The behaviour of the elastic moduli will also be discussed in the context of the known phase transition from the incommensurate to prototypic structure at 433 K.

3.2 Synthesis

The reagents used for synthesis were obtained from Sigma-Aldrich Pty. Ltd and Aithaca Chemical Corporation and were 99.5 % or higher purity. Prior to use, barium carbonate, strontium carbonate, silicon dioxide, and germanium dioxide were dried overnight at 500 °C to remove any water or other unwanted components. Compounds were prepared via conventional solid state synthetic techniques that involved thoroughly grinding an appropriate stoichiometric mixture of oxides and carbonates under acetone using an agate mortar and pestle. Where not otherwise stated, approximately 2 g samples were made. Larger sample sizes (5 g) were prepared for neutron diffraction experiments. In later heating stages, samples were pressed into pellets or rods using a mass of approximately 10 tons on a 13 mm dye for small samples, or approximately 13 tons on a 20 mm dye for medium sized samples, or approximately 50 MPa in a hydrostatic press for larger samples.

Samples of $Ba_2TiSi_2O_8$ were synthesised from a stoichiometric mixture of $BaCO_3$, TiO_2, and SiO_2. These precursors were initially heated at 1000 °C for 20 hours, followed by subsequent heating steps at 1100 °C and 1200 °C, for 20 hours with a regrinding step after each heating cycle to improve sample homogeneity and reduce the particle size to increase the rate of the reaction. After the first 1200 °C heating step, samples were pressed into pellets and heated at 1200 °C, and 1250 °C for 20 hours between 4 to 6 times with a regrinding step after each heating cycle. A very small proportion (< 2 %) of Ba_2SiO_4 could not be removed from the sample despite repeated heating steps for longer periods of time. Samples synthesised using only 3 x 12 hour heating steps at 1200 °C as used by Wong *et al.*[124] contained larger proportions of the additional phase than the samples that had been heated for additional heating steps. It was found that a minimum of 4 x 20 hour heating steps at 1250 °C with regrinding between each step is necessary to synthesise polycrystalline $Ba_2TiSi_2O_8$ samples of the highest purity,

3.3 Results and Discussion

The following discussion of the $Ba_2TiSi_2O_8$ structure will be divided into three sections. The first section will discuss the determination of the $Ba_2TiSi_2O_8$ structure at ambient temperature as determined using synchrotron X-ray powder diffraction and high resolution neutron powder diffraction. The second section will discuss the variable temperature behaviour of the structure and the elastic moduli; particularly across the phase transition at 433 K which is known to remove the structural modulation. Lastly, a discussion of the physical property measurements of $Ba_2TiSi_2O_8$ will be provided.

3.3.1 $Ba_2TiSi_2O_8$ structure at ambient temperature

The structure of $Ba_2TiSi_2O_8$ at ambient temperature has been characterised using synchrotron X-ray powder diffraction using the experimental setup described in section 2.1.2.1 at a wavelength of $\lambda = 0.826108(1)$ Å. The *X*4*bm* space group with {0, 0, ½} centring was used instead of the primitive *P*4*bm* space group for the refinement of this structure to double the *c* parameter to remain consistent with (and allow for direct comparison against) previously reported models for $Ba_2TiSi_2O_8$ (for example, Markgraf *et al.*[53]). Figure 3.1 illustrates the fit of the calculated pattern (red line) against synchrotron X-ray powder diffraction data (black crosses) collected at ambient temperature. Reflections corresponding to the very small proportion of Ba_2SiO_4 that could not be removed during synthesis are marked by asterisks. No satellite reflections were found in the diffraction patterns despite the excellent signal to noise ratio of the data collected. The absence of any observable satellite reflections made the modelling of these data using a modulated structure approach significantly more difficult.

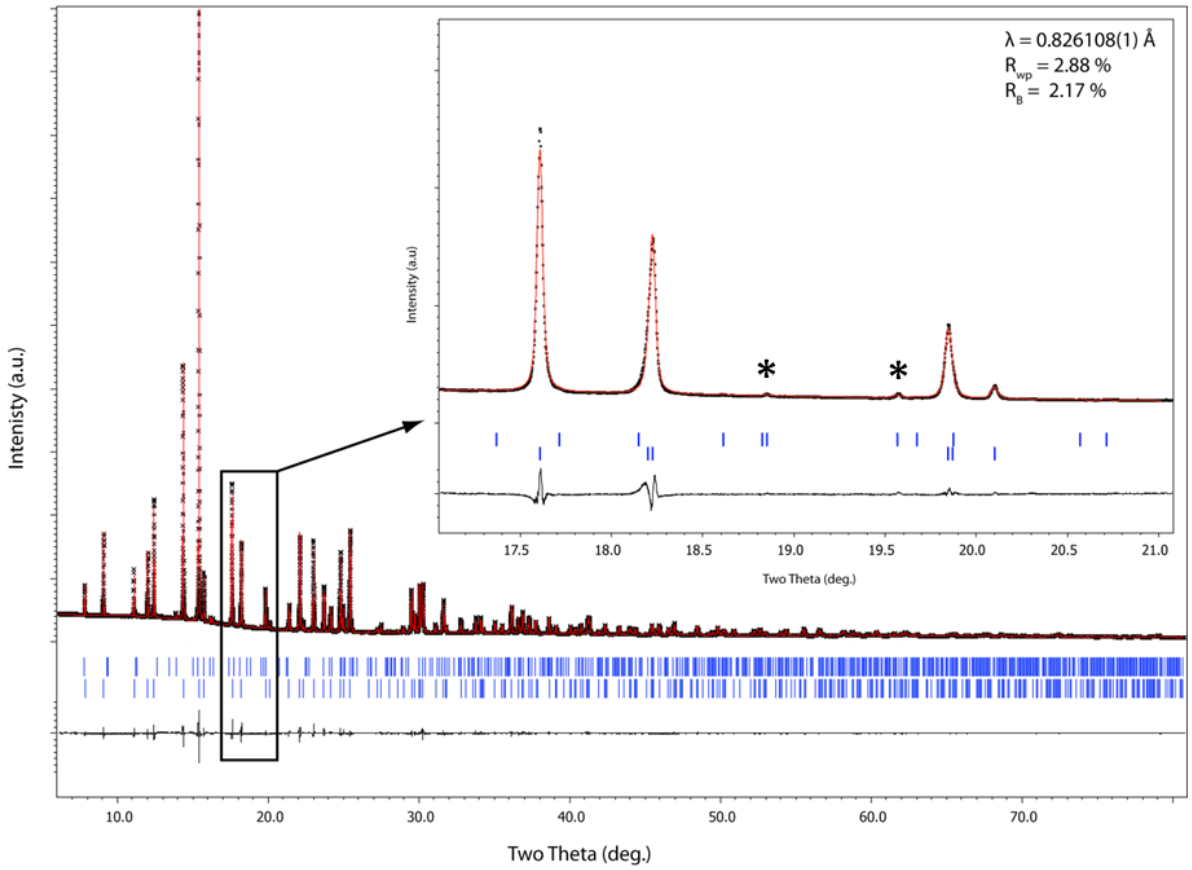

Figure 3.1: Observed, calculated, and difference plots for the refinement of the $Ba_2TiSi_2O_8$ average structure at ambient temperature against synchrotron X-ray powder diffraction data. The black crosses, and the red and black continuous lines represent the observed and calculated intensities and the difference between these respectively. The top and bottom rows of blue markers represent the positions of the Bragg reflections of the Ba_2SiO_4 and $Ba_2TiSi_2O_8$ phases, respectively. Asterisks in the insert indicate the strongest two reflections corresponding to the Ba_2SiO_4 impurity phase at 18.9° and 19.6° two theta.

The structural model developed from the Rietveld refinement against synchrotron X-ray powder diffraction data converged to R_B = 2.17 and R_{wp} = 2.88. The experimental data and important parameters from the determination of the $Ba_2TiSi_2O_8$ average structure at ambient temperature are provided in Table 3.1. The *a* and *c* unit cell parameters were refined to values within approximately 0.5 % of those published by Markgraf *et al.*[56] Small variations in the dimensions of fresnoite unit cell parameters of this magnitude from different samples have been previously reported for polycrystalline samples that have been synthesised using different heating temperatures and heating times.[153]

Table 3.1: Experimental data and important parameters for $Ba_2TiSi_2O_8$ at ambient temperature from (a) Synchrotron X-ray powder diffraction, (b) Single crystal X-ray diffraction from Bindi *et al.*[125]

	[a]Current Study	[b]Bindi *et al.*
Wavelength (Å)	λ = 0.826108(1)	λ = 0.70932
Molar mass (g mol^{-1})	506.72	506.72
Unit Cell	Tetragonal	Tetragonal
a (Å)	8.533582(8)	8.5353(6)
c (Å)	10.43160(2)	10.4128(7)
V (Å^3)	759.650(1)	758.59(9)
Space group	*X4bm*	*P4bm*(α, α, ½)0*gg*
Z	4	4
Linear abs. coeff. (mm^{-1})	17.43	11.67

The refinement of anisotropic atomic displacement parameters (ADPs) produced non-positive definite values. In an attempt to correct this, various estimates of the X-ray absorption from the sample were entered into the model by estimating different packing densities ranging between 30 % - 60 % based on the knowledge that the density of polycrystalline samples is typically low. However, the variation of the estimated X-ray absorption of the sample did not improve the refined ADPs. The background calculated from Legendre polynomials was also replaced with a manually fitted background in case any difficulty associated with the modelling of the background may have been contributing to the refinement of non-positive definite ADPS, however, the reasonableness of the model was still not improved. It is proposed that either the presence of a second phase in the sample could be introducing a level of convolution that inhibits the calculation of reliable anisotropic ADPs, or simply that the powder diffraction pattern collected from this sample may not contain sufficient detail to extract this information. For this reason, only isotropic ADP parameters were refined in the final model of the $Ba_2TiSi_2O_8$ structure. The $Ba_2TiSi_2O_8$ structure determined from Rietveld refinement against synchrotron X-ray powder diffraction data at ambient temperature is illustrated in Figure 3.2.

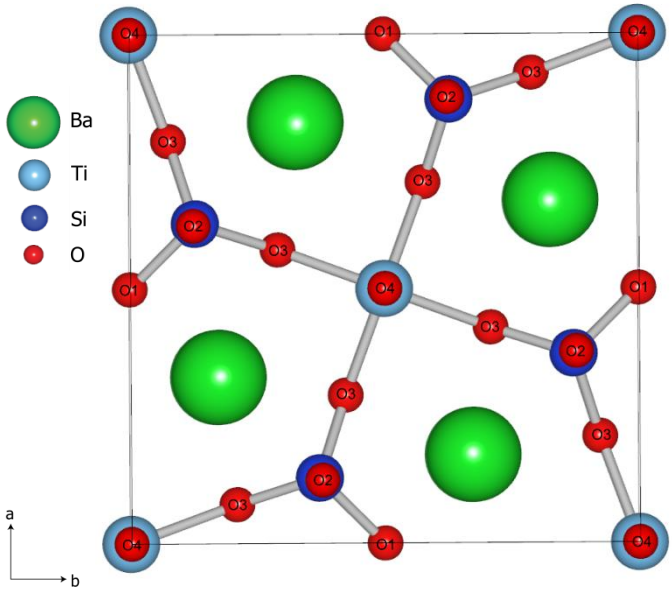

Figure 3.2: $Ba_2TiSi_2O_8$ average structure at ambient temperature refined against synchrotron X-ray powder diffraction data using isotropic atomic displacement parameters. Oxygen ions are labelled for later reference.

Once a reasonable and stable model of the $Ba_2TiSi_2O_8$ average structure had been constructed, structural modulations were added to establish whether any information about the modulation could be extracted from the diffraction pattern despite the absence of satellite reflections. Modulation wave vectors of $\boldsymbol{q_1} = 0.302(\mathbf{a^*} + \mathbf{b^*})$ and $\boldsymbol{q_2} = 0.302(\mathbf{-a^*} + \mathbf{b^*})$ and modulation amplitudes obtained from the single crystal study of natural fresnoite by Bindi *et al.*[125] were entered into the model. The calculated pattern based on these parameters contained a very small amount of intensity corresponding to satellite reflections in some regions of the pattern as shown in Figure 3.3. However, these calculated satellite reflections do not correspond to any reflections in the observed pattern, including the reflections corresponding to the small proportion of the second phase, Ba_2SiO_4. Once it was established that the Bindi model couldn't describe the experimental data, the modulation parameters were systematically refined to determine whether the fit could be improved. However, chemically implausible results were produced and this line of action was abandoned.

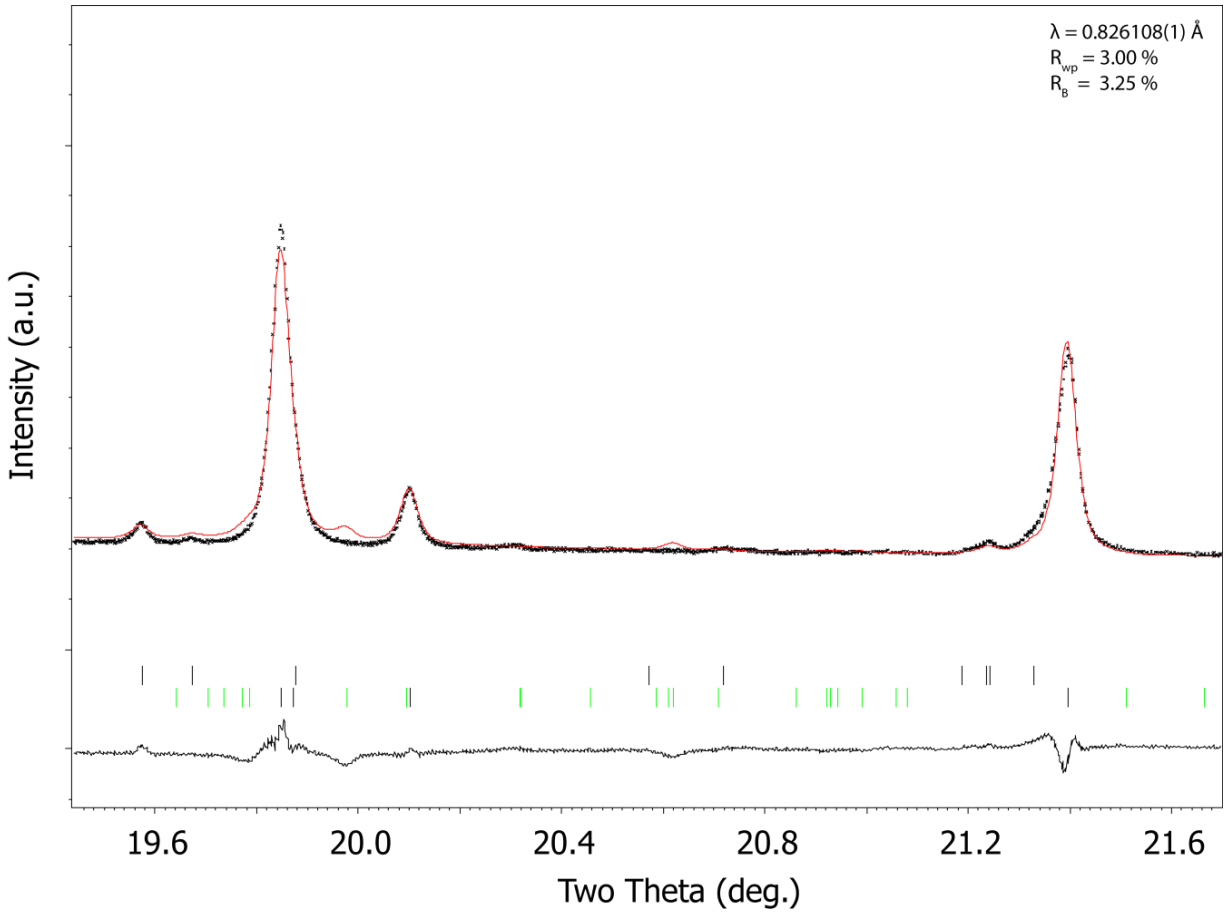

Figure 3.3: Observed, calculated, and difference plots for the refinement of the $Ba_2TiSi_2O_8$ modulated structure against synchrotron X-ray powder diffraction data. The top and bottom rows of reflection markers represent the positions of the Bragg reflections of the Ba_2SiO_4 and $Ba_2TiSi_2O_8$ phases, respectively. The weak satellite intensities calculated for the $Ba_2TiSi_2O_8$ phase (indexed by the green peak markers) defined using the modulation parameters obtained from Bindi *et al.*[7] do not correspond to any observed intensity in the pattern.

Modulation amplitudes were also systematically refined from arbitrarily small values (*c.f.* 0.001) in case the Bindi *et al.* model was an inappropriate starting point to describe the $Ba_2TiSi_2O_8$ sample in the current project. However, the models refined using this approach did not show any signs of convergence, nor produce chemically reasonable results. It was therefore concluded that the lack of satellite reflections in the synchrotron X-ray powder diffraction pattern would not allow for the determination of the modulated $Ba_2TiSi_2O_8$ structure.

The atomic positions and isotropic atomic displacement parameters for the $Ba_2TiSi_2O_8$ average structure determined from refinement against synchrotron X-ray powder diffraction data are provided in Table 3.2 where values quoted without errors are constrained by symmetry.

Table 3.2: Atomic positions and atomic displacement parameters for the $Ba_2TiSi_2O_8$ average structure at ambient temperature.

Atom	Ba	Ti	Si	O1	O2	O3	O4
x	0.32699(2)	0	0.12848(7)	0	0.1240(2)	0.2909(2)	0
y	0.82699	0	0.62848	0.5	0.6240	0.5767(2)	0
z	0	-0.2682(2)	-0.2551(3)	-0.3152(3)	-0.1031(2)	-0.3219(1)	-0.1046(4)
U_{iso} ($Å^2$)	0.01431(4)	0.0119(3)	0.0127(3)	0.013(1)	0.0115(7)	0.0105(5)	0.022(1)

Given that satellite reflections have been reported in electron and single crystal X-ray diffraction patterns collected from $Ba_2TiSi_2O_8$ numerous times in the literature[50,53,56], one must explain why these satellite reflections are not observed in the synchrotron X-ray powder diffraction patterns. Three arguments that might explain the absence of satellite reflections will be discussed below.

The first argument explaining the absence of satellite reflections in the synchrotron X-ray powder diffraction pattern considers a combination of the relatively weak X-ray scattering power of the oxygen ions in the presence of barium ions and the smaller domain sizes in polycrystalline samples relative to single crystals. It has been well established that the oxygen ions in the $Ba_2TiSi_2O_8$ structure experience the greatest displacements from their average positions due to the modulation.[57,120] Hence, the relatively weak X-ray scattering power of the oxygen ions relative to the barium ions in $Ba_2TiSi_2O_8$ means that any satellite reflections in an X-ray diffraction pattern will be very weak (as discussed in section 2.1.3.3). This is demonstrated by the tiny intensities calculated by the Bindi *et al*. single crystal model for the synchrotron powder diffraction profile in Figure 3.3. Sizes of individual domains constituting each crystallite in polycrystalline samples are considerably smaller than those constituting single crystals, and any lattice imperfection will cause the broadening of reflections in diffraction experiments.[154] The broadening of any reflection will increase its FWHM in the diffraction profile and hence reduce its maximum

height.[155,156] Although the effects of slightly smaller domains are typically negligible, their effect on very weak reflections can be so significant that they cannot be observed above the background anymore. Hence, it is possible that the presence of smaller domains in polycrystalline samples may explain why the satellite reflections that were observed in the single crystal X-ray diffraction experiment by Bindi *et al*. were not observed in the synchrotron X-ray powder diffraction patterns in the current study.

The second argument considers the potential for phason excitations to occur in $Ba_2TiSi_2O_8$ samples. A phason describes a special type of excitation that corresponds to thermally excited fluctuations of the phase of the modulation function(s) that describe the modulation of the average structure.[157] The effect of phase fluctuations in a modulated structure has been shown to reduce the intensity of satellite reflections in an analogous way to how the Debye-Waller factor accounts for the reduction of scattered intensity due to the thermal motion of atoms about their equilibrium positions.[158] The reduction of the diffracted intensity is only observed in the satellite reflections because the phase fluctuations do not induce changes into the average structure. The relationship between satellite intensity and phase fluctuations has been justified mathematically using two different methods by Overhauser *et al*.[158] and Axe.[159]

Evidence of phasons has been inferred from anomalies in low-temperature specific heat data of some metals and alloys[160,161] and point-contact spectroscopy experiments.[162] The existence of phasons has also been shown experimentally by inelastic neutron scattering[163] and elastic X-ray scattering[164] in $ThBr_4$ and $TaSe_2$ respectively. These studies have shown that phasons give rise to a temperature factor that is independent of the main Bragg reflections. For compounds containing phasons, the decrease in satellite reflection intensity has been shown to be different from the intensity decrease of the main Bragg reflections, and most importantly, independent of the index and the relative intensity of the reflection.

The absence of satellite reflections in the X-ray powder diffraction patterns collected from $Ba_2TiSi_2O_8$ samples in this study suggests that phase fluctuations may be present. This theory does not contradict previous work on $Ba_2TiSi_2O_8$ because it is plausible that phason excitations may be more prevalent in polycrystalline samples than in single crystal samples that exhibit higher crystal quality, reducing the likelihood of any boundaries or defects in the sample, including phase fluctuations.

The third argument is presented after consideration of the most recently published work on $Ba_2TiSi_2O_8$ by Wong *et al*.[124] which suggests that different regions of polycrystalline samples contain different modulation characteristics. High resolution electron microscopy and electron diffraction of polycrystalline samples, in combination with energy dispersive spectroscopy, were used to establish that each crystallite contains nanodomains which have compositional inhomogeneity. The presence of satellite reflections in these polycrystalline samples suggests that phasons may not be present, or only present in sufficient proportions to be observed on the larger sample volumes investigated using X-ray powder diffraction rather than the tiny samples volumes investigated in electron diffraction.

Because the $Ba_2TiSi_2O_8$ samples in this study were synthesised using a method similar to the solid state synthetic methods used by Wong *et al*.[124] (albeit, with additional heating steps), it is plausible to suggest that the samples synthesised and characterised in the current study may display similar behaviour to the samples studied previously. The potential for chemical inhomogeneity in these samples means that each crystallite could contain many small modulated nanodomains of slightly different local composition and hence exhibit slightly different modulation characteristics. Under these conditions, it would be plausible that no one region containing a common type of structural modulation would be present in the necessary proportions to produce sufficiently intense satellite reflections to be observed above the background. Instead, the intensity corresponding to each different structural modulation in

different regions of each crystallite may be distributed over slightly different regions of reciprocal space, hence reducing the intensity of the satellite reflections such that they cannot be observed above the background.

It is difficult to conclude which of the three arguments are the most appropriate to justify why satellite reflections are not observed in the synchrotron X-ray powder diffraction patterns collected from $Ba_2TiSi_2O_8$ samples in this study. However, based on the limited evidence of the occurrence of phasons and the uncertainty surrounding their identification in complex systems, it is proposed that the phason argument may not be the most appropriate explanation. The argument based on the presence of different modulated nanodomains due to chemical inhomogeneity also has merit. However, of the three arguments discussed, the relatively weak scattering power of oxygen combined with the reduced domain size in polycrystalline samples relative to single crystal samples is the most plausible. The true reason for the absence of satellite reflections may not be as simple as only one of these explanations, but could be a result of one or more contributing to the final result.

Once it was established that synchrotron X-ray powder diffraction did not provide the necessary information to characterise the modulated structure of polycrystalline $Ba_2TiSi_2O_8$, neutron powder diffraction data were collected to determine whether further structural information could be obtained. The relatively increased scattering factor of the oxygen ions in the presence of barium ions in neutron diffraction compared to X-ray diffraction is a particularly advantageous property to utilise in the current study because the satellite reflections produced by the large displacive modulations of the oxygen ions from neutron diffraction are likely to be of greater intensity than those produced from X-ray diffraction.

Neutron powder diffraction data were collected using Echidna - the high resolution neutron powder diffractometer using the setup described in section 2.1.3.1 at a wavelength of

λ = 1.885(1) Å. The sample investigated was a physically different sample of the same composition to the sample studied using X-ray diffraction. Both samples were synthesised under identical conditions. No evidence of a second phase was identified in the neutron diffraction pattern collected from this sample, however it is anticipated that a very small proportion of Ba_2SiO_4 is present (< ~2 % from XRD), but not observed due to the poorer signal to noise ratio typically expected from neutron diffraction experiments. Two reflections were identified that could be indexed as satellite reflections. Based on this observation, a modulated structure approach was applied to attempt to refine a stable and reasonable $Ba_2TiSi_2O_8$ model against the neutron powder diffraction data.

The structural parameters determined from the X-ray powder diffraction study were used in the starting model to be refined against the neutron diffraction data. However, in a similar fashion to the behaviour of the models refined against the X-ray diffraction data, the systematic introduction of small amplitude modulation functions to the model resulted in large fluctuations in the modulation amplitude parameters without accounting for any intensity that corresponded to satellite reflections. Hence, modulation amplitudes published by Bindi *et al*.[125] were again inserted and systematically refined for each atom.

The refinement of anisotropic ADPs returned non-positive definite values which rendered the model unreasonable. A manual background was trialled instead of the use of Legendre polynomials to determine whether this approach could resolve the non-positive definite ADPs, however this failed to improve the sensibility of the model. Hence only isotropic ADPs are reported for the $Ba_2TiSi_2O_8$ structure refined against high resolution neutron diffraction data.

The refined model of the modulated structure contains small amounts of intensity that correspond to the satellite reflections in the neutron diffraction pattern (marked by asterisks in Figure 3.4). The $\boldsymbol{q}$-vector was refined to $\boldsymbol{q_1}$ = 0.2977(**a*** + **b***) and $\boldsymbol{q_2}$ = 0.2977(-**a*** + **b***) in the

*X*4*bm*(α, α, 0)*0gg* space group (*c.f.* $\boldsymbol{q_1}$ = 0.302(**a*** + **b***) + ½**c*** and $\boldsymbol{q_2}$ = 0.302(-**a*** + **b***) + ½**c*** from Bindi *et al.*[125] using the *P*4*bm*(α, α, ½)0*gg* space group). Note that the *X* denotes the non-standard centring condition {0, 0, ½, ½, ½}. The small discrepancy in the magnitude of the ***q***-vector between this study and the previously published modulated structure for $Ba_2TiSi_2O_8$ can be explained by the dependency of the specific properties of the modulated structure on the local composition and the conditions of synthesis as discussed by Höche *et al.*[72] and Wong *et al.*[153]

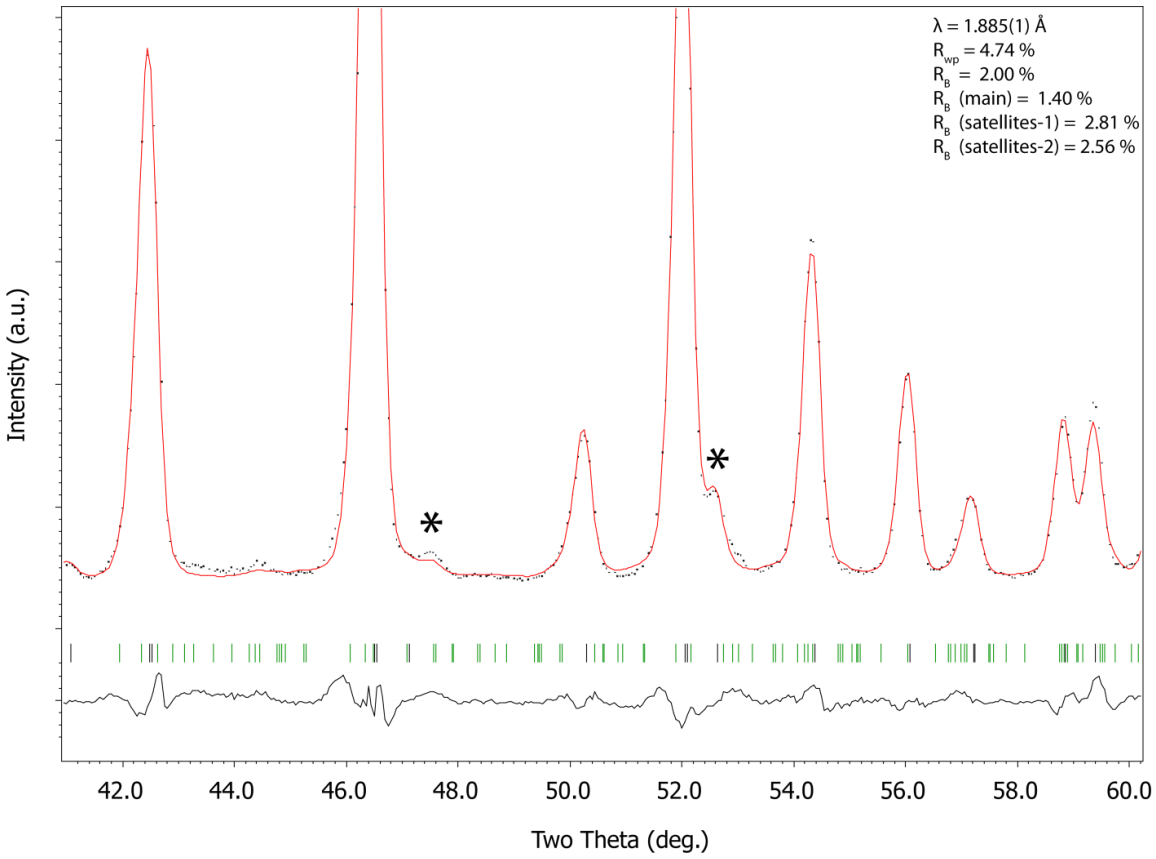

Figure 3.4: Observed, calculated, and difference plots for the refinement of the $Ba_2TiSi_2O_8$ modulated structure at ambient temperature against high resolution neutron powder diffraction data. Asterisks mark satellite reflections with calculated intensity from the model. Black and green reflection markers indentify main and satellite reflections, respectively.

The experimental data and important parameters for the model refined against neutron powder diffraction data are provided in Table 3.3. The unit cell parameters obtained from this model are comparable to those determined from synchrotron X-ray powder diffraction (Table 3.1) or from single crystal X-ray diffraction.[125] Note that (satellites-1) and (satellites-2) represent parameters

corresponding to the satellite reflections associated with the first ($\mathbf{q_1}$, $\mathbf{q_2}$) and second ($\mathbf{q_1} + \mathbf{q_2}$, $\mathbf{q_1} - \mathbf{q_2}$) order satellites, respectively.

Table 3.3: Experimental data and important parameters for $Ba_2TiSi_2O_8$ at ambient temperature from (a) high resolution neutron powder diffraction (Echidna), and (b) single crystal X ray diffraction from Bindi *et al.*[125]

Parameter	[a]Current Study: Echidna	[b]Bindi et al.[125]
Wavelength (Å)	λ = 1.885(1)	λ = 0.70932
Molar mass (g mol^{-1})	506.72	
Unit Cell	Tetragonal	Tetragonal
a (Å)	8.52083(11)	8.5353(6)
c (Å)	10.4323(20)	10.4128(7)
V (Å^3)	758.90(2)	758.59(9)
Space group	*X*4*bm*(α, α, 0)*0gg*	*P*4*bm*(α, α, ½)0*gg*
Z	4	
Linear abs. coeff. (mm^{-1})	0.0047	11.67
R_B (%)	2.00	1.2
R_B (main) (%)	1.40	1.0
R_B (satellites-1) (%)	2.81	1.4
R_B (satellites-2) (%)	2.56	3.4
R_{wp}	4.74	-

The refined atomic positions, atomic displacement parameters, and modulation amplitudes for $Ba_2TiSi_2O_8$ structure are provided in Table 3.4 where values without errors are constrained by symmetry. The calculation and analysis of the atomic modulation functions pertaining to the modulated structure provides further insight into the specific behaviour of the structure along each point of the modulation wave. For example, the largest modulation amplitudes correspond to the O1 and O3 oxygen ions which form the bases of the SiO_4 and TiO_5 polyhedra in the *a*-*b* plane respectively. The O2 and O4 oxygen ions corresponding to the axial positions of the SiO_4 and TiO_5 polyhedra respectively are smaller, confirming that the modulation is primarily associated with the rotation of the polyhedra about the *c*-axis.

Table 3.4: Atomic positions, atomic displacement parameters (ADPs), and modulation amplitudes for the $Ba_2TiSi_2O_8$ structure at ambient temperature as refined against neutron powder diffraction data. The suffix numbers (1's and 2's) for each modulation amplitude represent directions along the first (a* + b*) and second (-a* + b*) modulation directions, respectively.

	Ba	Ti	Si	O1	O2	O3	O4
x	0.3276(3)	0	0.1280(3)	0	0.1250(2)	0.2927(2)	0
y	0.8276	0	0.6280	0.5	0.6250	0.5756(2)	0
z	0	-0.2676(6)	-0.2557(4)	-0.3139(5)	-0.1040(3)	-0.3213(3)	-0.1064(4)
U_{iso} (Å^2)	0.0051(8)	0.002(2)	0.0015(8)	0.008(1)	0.0017(8)	0.0086(5)	0.0053(18)
***x* sin 1**	0.004(1)	-0.008(2)	-0.003(1)	0.003(1)	-0.005(9)	0.0048(8)	0.011(1)
***y* sin 1**	0.004	0.003(2)	-0.003	0.003	-0.005	0.0014(8)	-0.011
***z* sin 1**	0.002(1)	0	0.002(1)	0	-0.002(1)	-0.0028(9)	0
***x* cos 1**	0.0049(8)	0	-0.004(1)	0	0.0067(8)	-0.0069(7)	0
***y* cos 1**	0.0049	0	-0.004	0	0.0067	-0.0188(7)	0
***z* cos 1**	-0.007(1)	-0.004(2)	0.002	0.01(2)	0.0037(1)	-0.0033(7)	0.000(1)
***x* sin 2**	0.002(9)	0.003(2)	-0.002	0.0188(8)	-0.0076(8)	-0.0025(9)	-0.011(1)
***y* sin 2**	0.002	0.008	0.002	-0.0188	0.0076	-0.0047(9)	-0.011
***z* sin 2**	0	0	0	0	0	-0.0014(8)	0
***x* cos 2**	-0.0004(1)	0	0.007(1)	0	-0.0020(8)	0.0003(8)	0
***y* cos 2**	-0.0004	0	0.007	0	-0.0020	-0.004(1)	0
***z* cos 2**	0.008(1)	0.004	0.006(1)	0.007(2)	0.011(1)	0.0072(8)	-0.000(1)

Inspection of the atomic modulation functions representing the displacements of each ion as a function of the internal phase parameters *t* and *u* (defined in section 1.6) confirms that the largest deviations from the average structure are experienced by the oxygen ions. This is shown in Figure 3.5 where the displacements of the barium (A), titanium (B), oxygen-1 (C) and oxygen-3 (D) ions are provided for $0 \leq t \leq 1$ and $u = 0$ where *t* and u represent the positions along the first (**a*** + **b***) and second (**-a*** + **b***) modulation directions, respectively. The $u = 0$ case has been chosen as a representative cross section of the entire $0 \leq u \leq 1$ range.

The oxygen ions display the largest deviations on average, while the displacements of the titanium and barium (to a lesser extent) ions are more subtle. There are significant contributions to the oxygen ion displacements in the oxygen-1 and -3 ions in the *x* and *y* directions, providing evidence of polyhedral rotation about the *c*-axis. However, the contribution in the *z*-direction cannot be ignored. The *z*-contribution is indicative that although rotation about *c* is occurring, a slight buckling of the polyhedra also occurs, such that the base of each polyhedron is no longer parallel with the *a*-*b* plane.

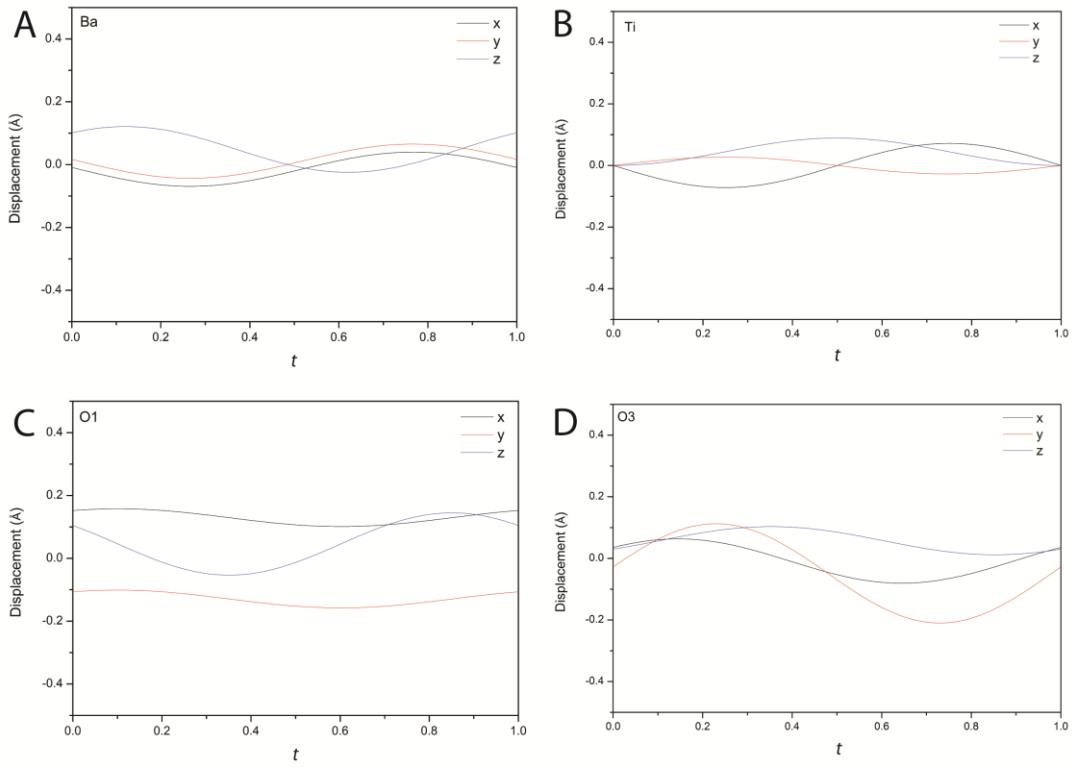

Figure 3.5: Atomic modulation functions showing the variation in the atomic displacements in $Ba_2TiSi_2O_8$ for barium (A), titanium (B), oxygen-1 (C), and oxygen-3 (D) ions for $u = 0$ and $0 \leq t \leq 1$, where t and u represent positions along the (a* + b*) + ½c* and (-a* + b*) + ½c* modulation directions, respectively. The $u = 0$ case has been chosen as a representative cross section of the entire $0 \leq u \leq 1$ range.

Bindi *et al.*[125] first discussed the extent of the modulations in the fresnoite structure by considering the variation in the bond angles between adjacent polyhedra. The atomic modulation function showing the variation in the Ti-O3-Si bond angle (and hence a parameter describing the extent of the relative buckling of adjacent polyhedra) for $0 \leq t \leq 1$ and $u = 0$ is provided in Figure 3.6, demonstrating that the bond angle varies by approximately ± 2.5 degrees. This shows that $Ba_2TiSi_2O_8$ exhibits similar behaviour to the behaviour reported for $Ba_2TiGe_2O_8$ by Iijima *et al.*[57] who claimed that the long period modulation occurs in the non-isomorphic (but structurally similar) $Ba_2TiGe_2O_8$ in the form of the buckling of adjacent polyhedra relative to each other.

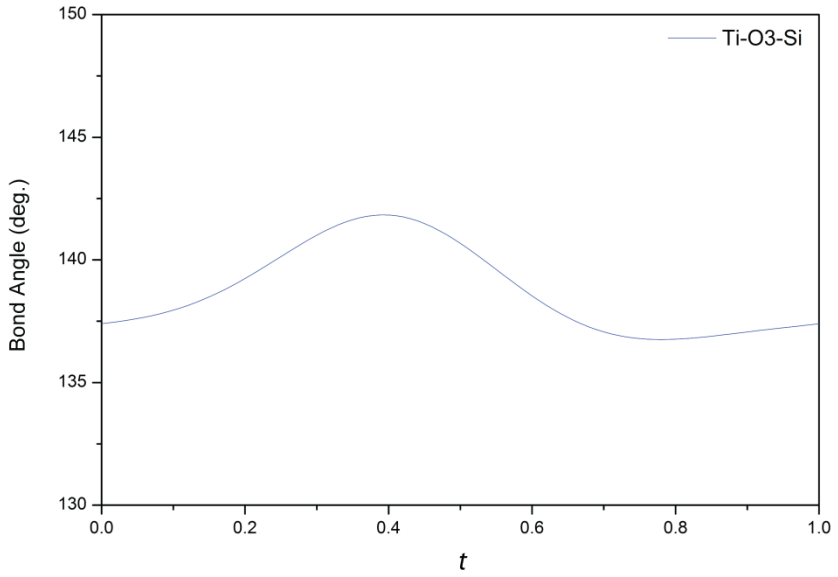

Figure 3.6: Atomic modulation function showing the variation of approximately ± 2.5 degrees in the Ti-O3-Si bond angle for $u = 0$ and $0 \leq t \leq 1$, where t and u represent positions along the (a* + b*) + ½c* and (-a* + b*) + ½c* modulation directions, respectively. The $u = 0$ case has been chosen as a representative cross section of the entire $0 \leq u \leq 1$ range.

The atomic modulation functions representing the calculated bond valence sums for all atoms in the $Ba_2TiSi_2O_8$ structure are provided in Figure 3.7 where the dotted lines represent the hypothetical bond valence sum of the atom in the average structure, and solid lines represent the bond valence sum for $0 \leq t \leq 1$ and $u = 0$. Large variations can be seen in the bond valence sum of the barium ion in Figure 3.7A, demonstrating the susceptibility of the position of the barium ion to the introduction of the structural modulation.

The introduction of the modulation improves the average bond valence sums of the oxygen-1 and oxygen-4 ions, while the silicon, titanium, oxygen-2, and oxygen-3 ions experience bond valence sums further from their ideal values relative to their calculated bond valence sums in the average structure (Figures 1.7B-C). However, the net changes in the bond valence sums in the $Ba_2TiSi_2O_8$ structure are advantageous due to the large improvements for the barium, oxygen-1 and oxygen-4 ions outweighing the small deviations from more ideal bond valence sums of the remaining ions in the average structure.

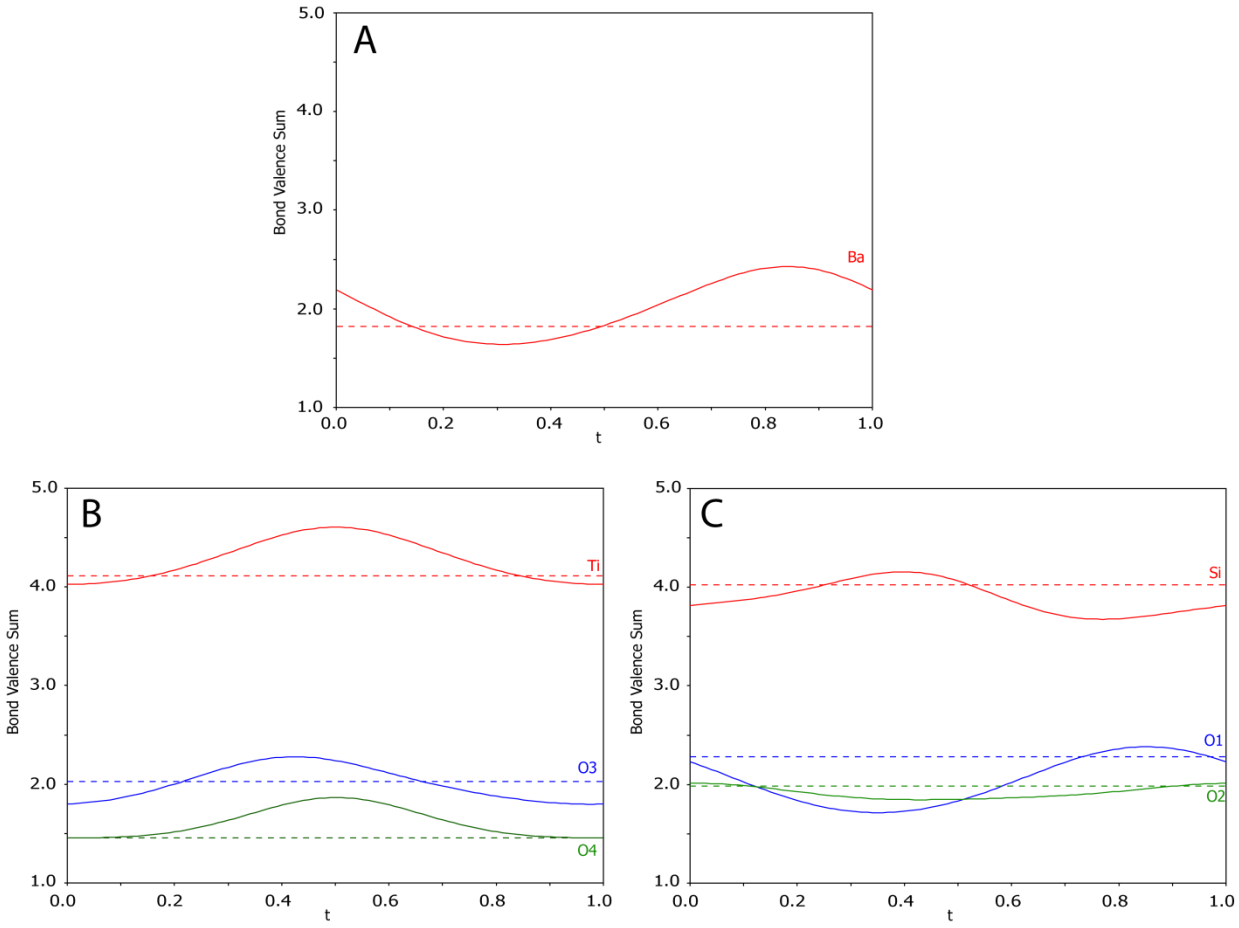

Figure 3.7: Atomic modulation function showing the variation of the bond valence sum for all atoms in $Ba_2TiSi_2O_8$ for $u = 0$ and $0 \leq t \leq 1$ along the (a* + b*) + ½c* and (-a* + b*) + ½c* modulation directions, respectively. The $u = 0$ case has been chosen as a representative cross section of the entire $0 \leq u \leq 1$ range. The solid and dashed lines represent the bond valence sum for the modulated and average structures, respectively.

The $Ba_2TiSi_2O_8$ modulated structure determined in the current study is the first to be determined from neutron diffraction data. A 3x3 approximation of this structure is illustrated in Figure 3.8 where it can be seen that the smallest deviations from the average structure occur for the barium, titanium and silicon atoms, while the largest deviations are seen for the oxygen ions in the *x*- and *y*-directions. The large displacements of these oxygen ions are consistent with those previously published from single crystal X-ray diffraction analysis and correspond to the almost-rigid-body rotations of the TiO_5 and SiO_4 polyhedra around the *c*-axis. Small displacements supporting the slight tilting of the polyhedra can also be seen in the basal polyhedral plane perpendicular to the [001]-direction in Figure 3.8 (bottom).

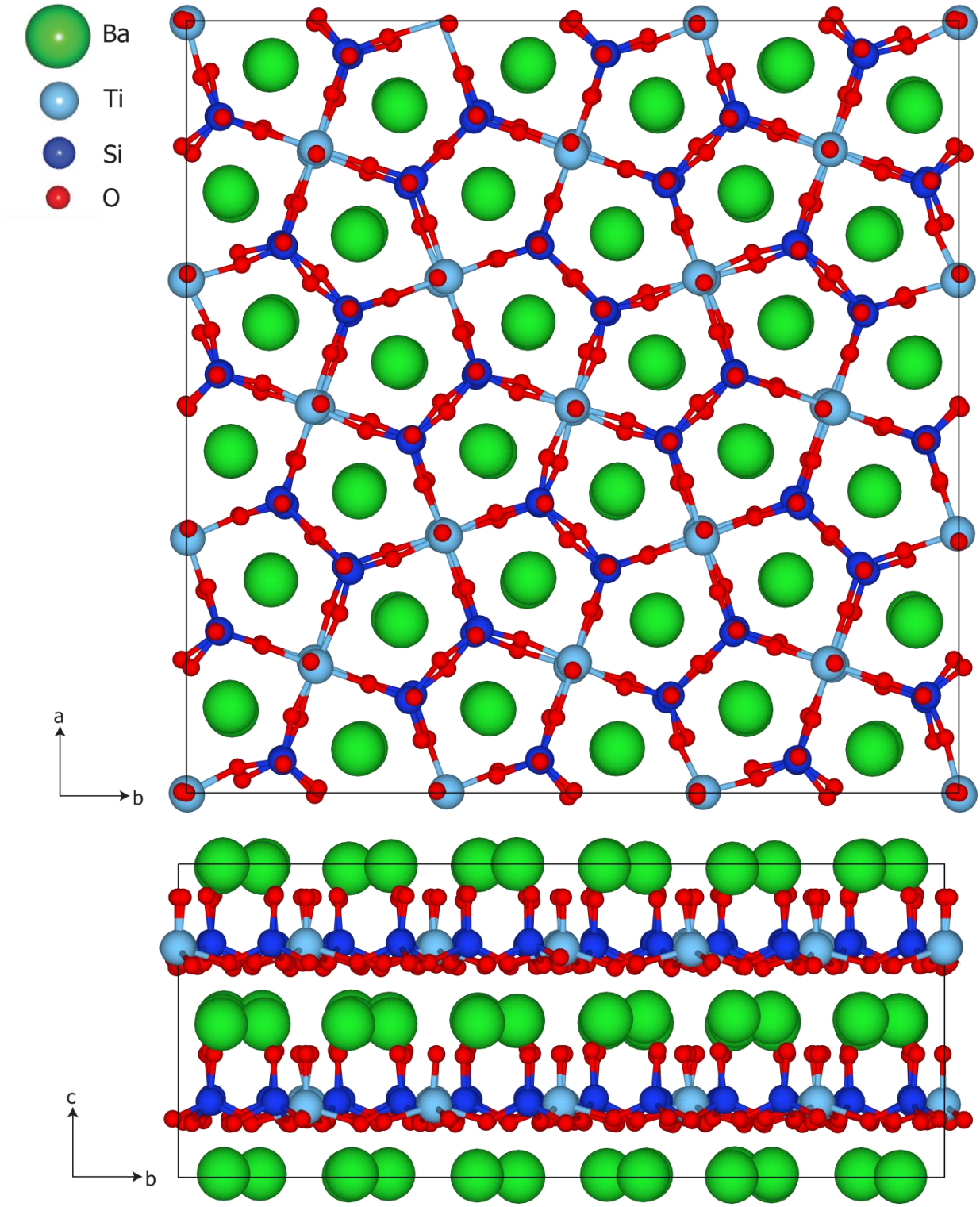

Figure 3.8: 3x3x1 approximation of the $Ba_2TiSi_2O_8$ modulated structure from refinement against high resolution neutron powder diffraction data projected along the [001]- (top) and [100]-direction (bottom).

3.3.2 $Ba_2TiSi_2O_8$ structure at non-ambient temperatures

Variable temperature synchrotron X-ray powder diffraction data were collected from a $Ba_2TiSi_2O_8$ sample to investigate the structure across a wide range of temperatures, including the transition at 433 K. Data were collected between 125 K - 475 K and 298 K - 1196 K using a cryostream liquid nitrogen attachment and Eurotherm hot air blower, respectively. This is the first investigation of the $Ba_2TiSi_2O_8$ structure to be conducted at temperatures higher than 573 K.

The high resolution of the diffraction patterns ensured that the unit cell parameters of the sample could be determined with high precision. The *a* and *c* unit cell parameters calculated from Rietveld refinement against synchrotron X-ray diffraction data collected between 125 K - 1196 K are provided in Figure 3.9 where there is a distinct change in the gradient close to 433 K, coinciding with the known transition from the modulated to the parent phase as reported by Markgraf *et al*.[53] It should be noted that the different scales of the left and right axes have been chosen to show the changes in gradient of the cell parameters concisely. This behaviour is similar to (but more pronounced than) the behaviour shown for the unit cell parameters of the structurally similar melilite compounds across the incommensurate to prototypic phase transitions.[165] The constant volume expansion and second order nature of this transition are also consistent with the theoretical and experimental investigations on incommensurate to prototypic phase transitions reported by Aizu[166] and Ishibashi.[167] The intersection of the lines of best fit of the *a* and *c* unit cell parameters for the high and low temperature phases were used to determine that the changes occur at 466 K and 447 K, respectively.

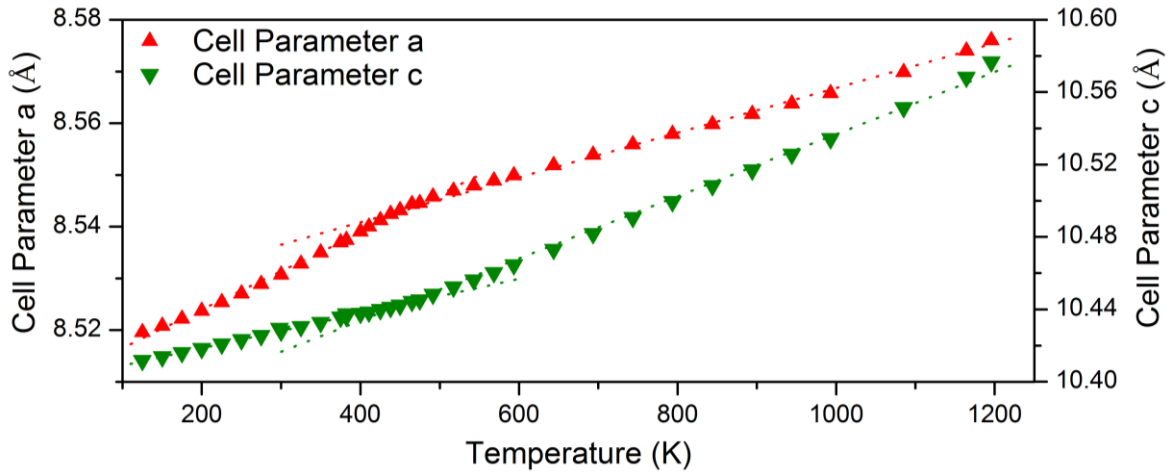

Figure 3.9: Unit cell parameters *a* (left), and *c* (right) for $Ba_2TiSi_2O_8$ between 125 K - 1196 K as calculated from Rietveld refinement against synchrotron X-ray diffraction data.

The change in the gradients of the *a* and *c* cell parameters across the 433 K transition are such that that the change in the trend of *a* cancels out the change in trend of *c*. This produces constant unit cell volume expansion across the transition (Figure 3.10) as required for second order phase transitions.[168]

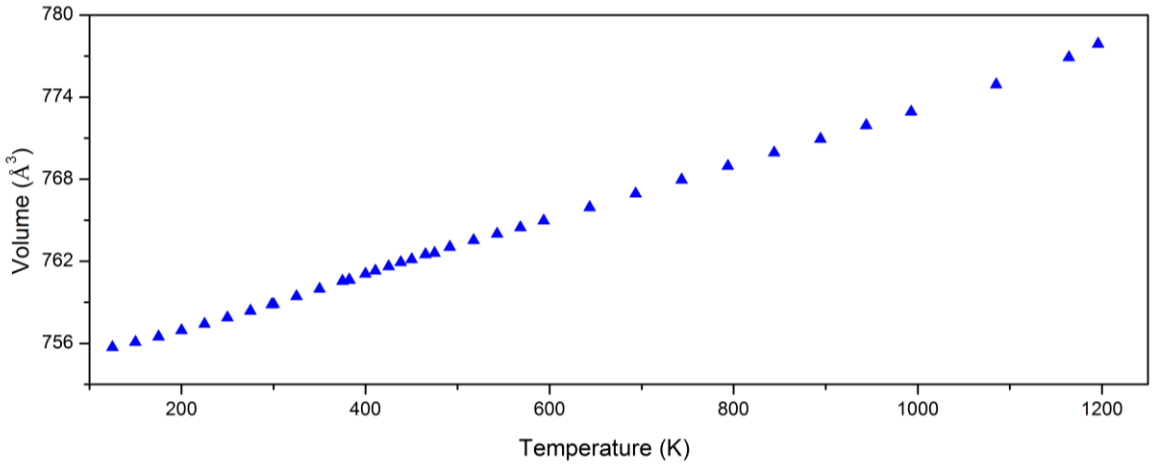

Figure 3.10: Unit cell volume for $Ba_2TiSi_2O_8$ between 125 K - 1196 K as calculated from Rietveld refinement against synchrotron X-ray diffraction data.

The temperature of the transition can also be identified through the consideration of the *a*/*c* ratio of the tetragonal structure as shown in Figure 3.11. The maximum value of the *a*/*c* ratio occurs at 442 K, in close agreement with the published value of 433 K.[53] Hence, it has been shown that the

change in the trend of the unit cell parameters provides a reliable method to identify the subtle phase transition from the modulated to the prototypic phase despite the absence of satellite reflections in the powder diffraction pattern. Analysis of the trends of the unit cell parameters will be used to identify the presence of this transition for other $Ba_2TiSi_2O_8$ samples in the following section. The structural parameters for all models refined for $Ba_2TiSi_2O_8$ between 125 K - 1373 K are provided in Appendix B of the attached Appendix DVD.

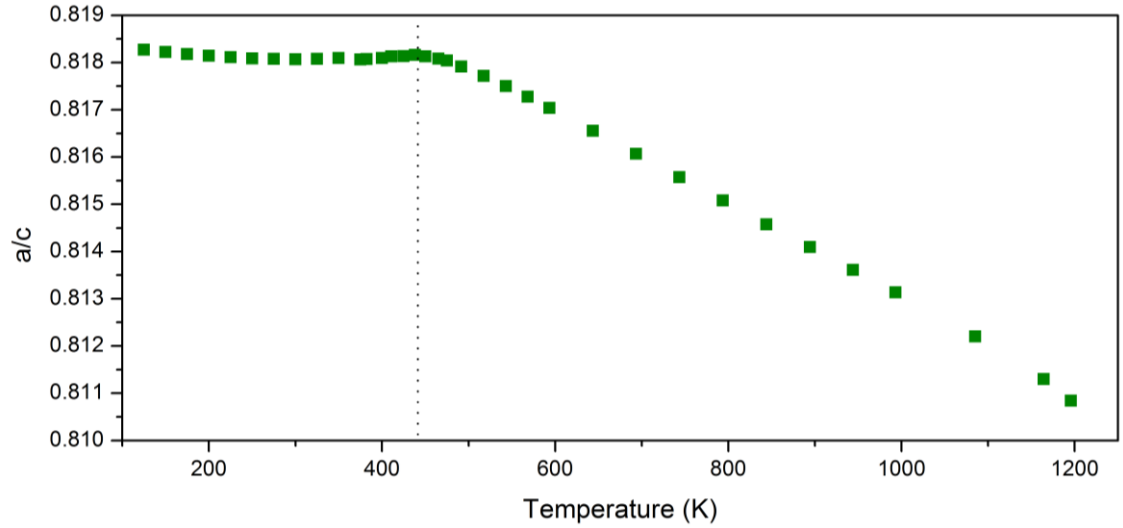

Figure 3.11: $Ba_2TiSi_2O_8$ cell parameter *a/c* ratio, indicating a change at approximately 440 K as determined from the intersection of the lines of best fit determined for each section of the plot.

Variable temperature high intensity neutron powder diffraction data were collected using Wombat with the experimental setup described in section 2.1.3.2 at a wavelength of $\lambda = 2.8638(2)$ Å. The very high flux obtained from this instrument significantly reduces the collection time required to obtain patterns with reasonable signal to noise ratio. The ability to collect patterns quickly makes this technique appropriate for the collection of variable temperature diffraction patterns in very small increments to track any changes in the structure that may be observed in the diffraction pattern. Neutron diffraction patterns were collected from a $Ba_2TiSi_2O_8$ sample between 275 K - 600 K on heating, and 600 K - 300 K on cooling with a collection time of 1 minute per pattern. The patterns collected on heating and cooling are collated

in Figure 3.12 where the black box indicates the region corresponding to temperatures above the 433 K transition. Conventional thermal expansion and contraction on heating and cooling respectively can be identified in the shift of all reflections, however a closer inspection reveals very subtle differences in the diffraction patterns above 433 K.

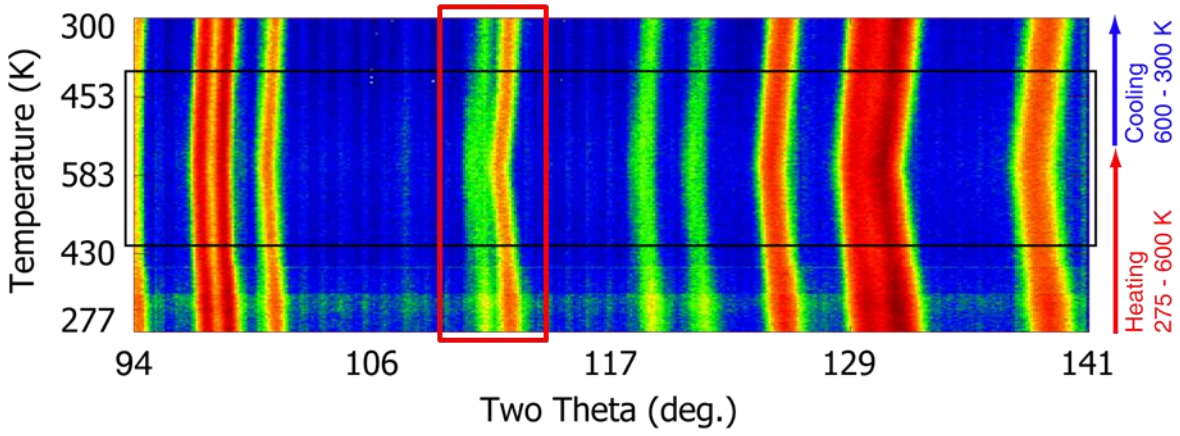

Figure 3.12: High intensity neutron powder diffraction ramping plot. Patterns were collected in 2.5 K intervals as the $Ba_2TiSi_2O_8$ sample was heated from 275 K - 600 K, then cooled from 600 K - 300 K. The black box indicates the temperatures in the figure above the transition, and the red box indicates the two theta region of the two reflections of interest.

The most prominent change in the diffraction patterns above 433 K can be seen in the spacing between the 322 and 003 reflections at approximately 111° and 112° two theta, respectively (inside the red box in Figure 3.12). As the sample is heated above 433 K, the FWHM of the 322 reflection is increased, suggesting that there may be a small degree of disorder in the high temperature prototypic structure. Similar behaviour can be observed to a lesser extent in other high angle reflections, for example, the 113 and 510 reflections at 119° and 120° two theta, respectively. The observed changes do not coincide with the positions of expected satellite reflections, however, the reduction of the FWHM on cooling indicates that the behaviour is reversible without hysteresis. The presence of this broadening may be indicative of disorder across the sample in the planes associated with the 322 and 003 reflections. Further work would need to be conducted to investigate this possibility properly.

3.3.2.1 Quenching polycrystalline $Ba_2TiSi_2O_8$

$Ba_2TiSi_2O_8$ was cooled rapidly from above 433 K to investigate whether the high temperature prototypic structure could be quenched and observed at ambient temperature. Polycrystalline $Ba_2TiSi_2O_8$ was pressed into two pellets and heated to 773 K (340 K above the 433 K transition temperature) for 2 hours. The "quenched" pellet was cooled rapidly by transfer from the furnace into a dish of liquid nitrogen, and the other "standard" pellet was allowed to cool to ambient temperature slowly by switching off the furnace. X-ray diffraction patterns were collected between 298 K - 773 K using Cu K_α radiation to determine whether a phase transition could be identified from inspection of the unit cell parameters as described in section 3.3.2.

Because the instrument used for this particular experiment produces diffraction patterns that contain lower resolution than would be obtained from a synchrotron source, much larger errors are associated with the values obtained. However, conducting the experiment on the standard in addition to the quenched sample introduces internal consistency into the experiment, allowing conclusions to be drawn from the presence or lack of differences between the quenched sample and the standard.

The cell parameters *a* and *c* (left) and the *a/c* ratio (right) that were calculated from Rietveld refinement against X-ray diffraction data between 298 K - 773 K are provided in Figure 3.13 for both the quenched (bottom) and standard (top) $Ba_2TiSi_2O_8$ samples. The behaviour of the standard and the quenched sample is identical to the behaviour observed for the sample in section 3.3.2, confirming that the *X4bm*(α, α, 0)*0gg* structure is still present at ambient temperature after rapid cooling from 773 K.

The fact that the prototypic *X4bm* structure returns to the incommensurately modulated *X4bm*(α, α, 0)*0gg* structure upon rapid cooling suggests that the phase transformation from the

modulated to the prototypic structure involves the transfer of only a very small amount of energy. This observation is supported by the computational studies of the very small energy differences in some incommensurate crystals by Pokrovsky and Talapov.[169]

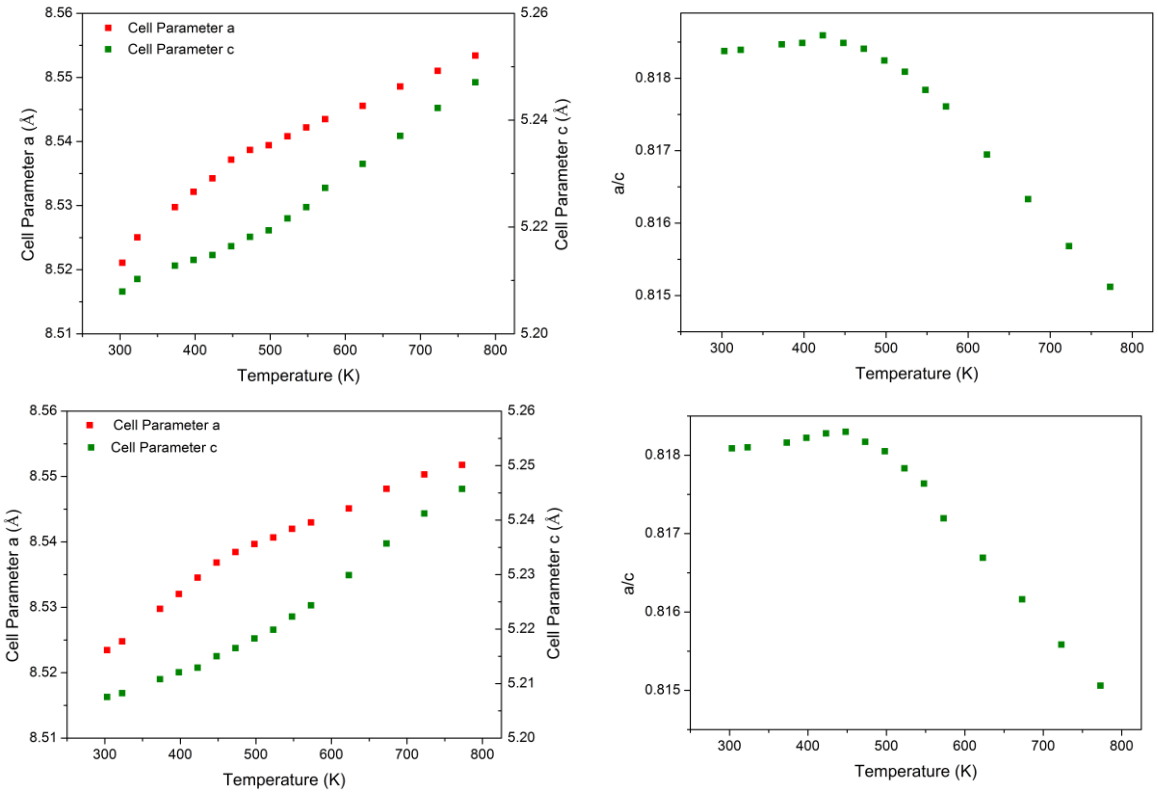

Figure 3.13: Unit cell parameters *a* and *c* (left) and the *a*/*c* ratio (right) for $Ba_2TiSi_2O_8$ in quenched (top) and standard (bottom) samples between 298 K - 773 K.

It was shown in the previous section that the change in the unit cell parameters as determined from diffraction using a synchrotron source provides a useful crystallographic method to identify the subtle *X4bm*(α, α, 0)*0gg* to *X4bm* phase transition in $Ba_2TiSi_2O_8$. This quenching experiment in the current section has shown that diffraction using Cu K_α radiation is sufficient for the identification of this transition. This method will be used to investigate this transition in barium rich members of the $Ba_{2x}Sr_{2-2x}TiSi_2O_8$ system in Chapter 6.

3.3.2.2 $Ba_2TiSi_2O_8$ heat flow across the 433 K transition

Differential scanning calorimetry was performed on a 26.5 mg polycrystalline $Ba_2TiSi_2O_8$ sample on cooling between 723 K - 323 K using a cooling rate of 2 K min^{-1} on a TA Instruments 2920 Differential Scanning Calorimeter as described in section 2.6. The measurement of heat flow through the sample was used to investigate whether any thermal anomalies associated with the phase transition could be identified (Figure 3.14).

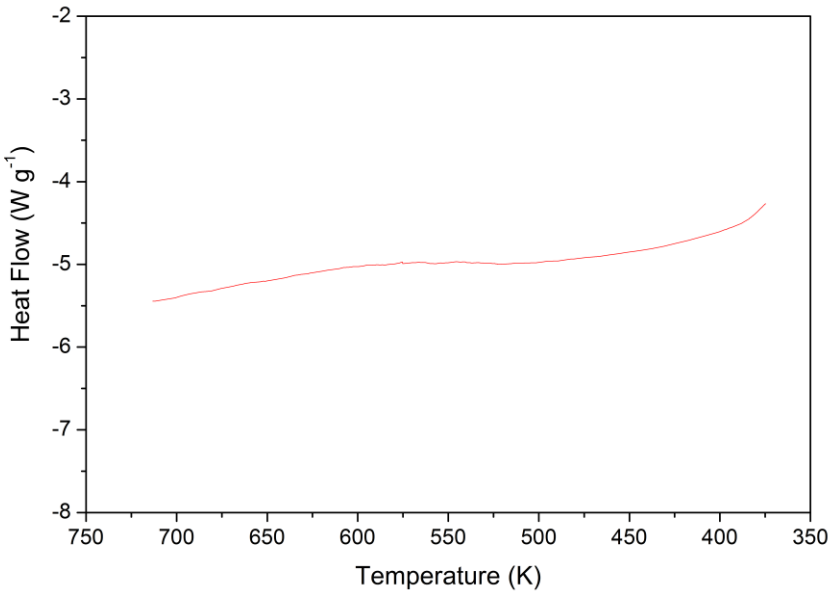

Figure 3.14: Heat flow for $Ba_2TiSi_2O_8$ on cooling between 723 K - 323 K using a cooling rate of 2 K min^{-1}.

The absence of any thermal anomalies in the heat flow curve for $Ba_2TiSi_2O_8$ confirms that the difference between the prototypic and incommensurately modulated $Ba_2TiSi_2O_8$ energy states must be extremely small, as shown for the incommensurate to prototypic transition for Cs_2ZnI_4 by Melero *et al.*[170] The minimal energy difference between the incommensurate and prototypic phases also supports the conclusion from the quenching experiment that the prototypic structure cannot be preserved by rapid cooling from above the phase transition temperature.

3.3.2.3 Elastic properties of $Ba_2TiSi_2O_8$ across the 433 K transition

The elastic properties of $Ba_2TiSi_2O_8$ were investigated between 298 K - 620 K using resonant ultrasound spectroscopy as described in section 2.5.4. Resonant ultrasound spectroscopy data were collected from a single crystal sample of dimensions 4.170 x 3.390 x 4.827 mm^3 and mass = 0.2837 g (supplied by Prof. T. Höche, Leibniz-Institut für Oberflächenmodifizierung e.V., Leipzig, Germany). The sample shape formed an approximate parallelepiped, however, the faces of the sample were visibly inclined to adjoining faces at angles ≠ 90°.

Spectra were collected from the single crystal $Ba_2TiSi_2O_8$ sample across the frequency range 50 kHz - 1200 kHz at a resolution of 50 000 data points at ambient temperature as shown in Figure 3.15. The observed peaks were well defined and exhibited low dissipation (Q^{-1}), however, attempts to model the elastic constants using the standard rectangular parallelepiped resonance method were not successful, because the fit to all the recorded resonances did not converge to a satisfactory level. The most likely explanation for the difficulty in determining the elastic constants of this sample is the imperfect shape of the crystal. Generally, the deviation from the ideal parallelepiped shape should be approximately < 1 % from 90° angles to achieve good convergence in the fitting process. However, this deviation in the samples was estimated to be significantly larger than the recommended orthogonality, explaining the difficulty experienced in the fitting process.

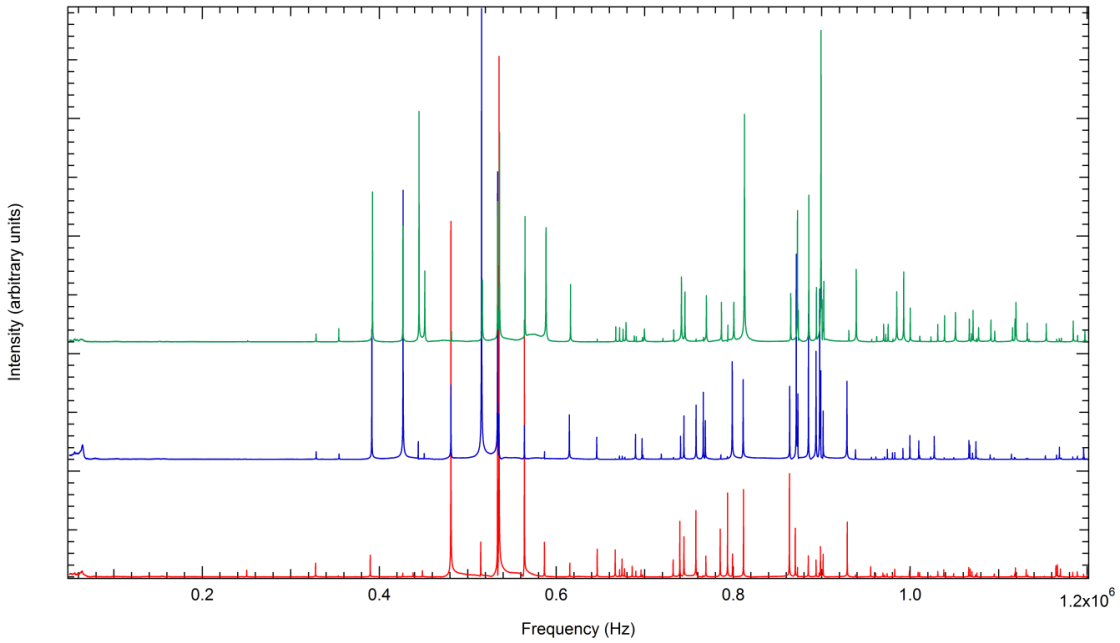

Figure 3.15: Resonant ultrasound spectroscopy spectra collected from a $Ba_2TiSi_2O_8$ single crystal at ambient temperature in three different orientations. The red and blue lines represent spectra collected with the sample oriented in the [100]- and [010]- directions, respectively, and the green line represents the spectra collected from the sample mounted across diametrically opposite corners ([111]-direction).

Spectra were also collected at ambient temperature from a polycrystalline $Ba_2TiSi_2O_8$ sample of dimensions 3.779 x 3.226 x 1.825 mm^3 and mass = 75.5 mg that was cut from a densely pressed pellet with high precision in the 90° angles between adjoining faces (Figure 3.16). The fitting process for the elastic constant was conducted using the fitting procedure described in section 2.8.2 of McKnight (2009)[150], however a satisfactory fit could not be achieved. The difficulty associated with calculating the elastic constants from the polycrystalline sample of $Ba_2TiSi_2O_8$ are likely to be attributed to the tendency for the crystallites to adopt highly anisotropic forms due to the layering of the polyhedra that form planes perpendicular to the [001]-direction.

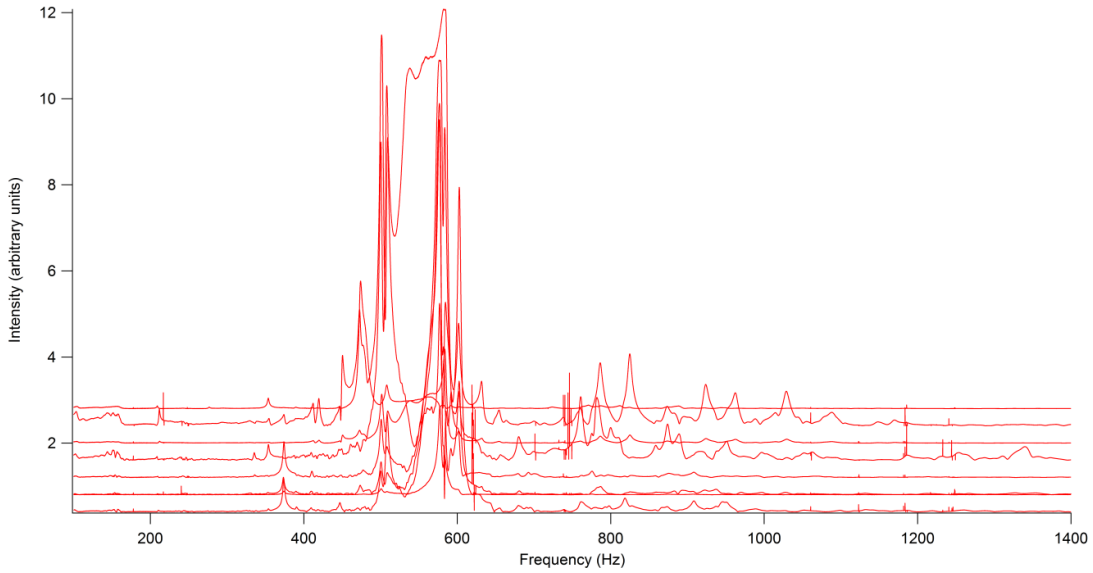

Figure 3.16: Resonant ultrasound spectroscopy spectra collected from a $Ba_2TiSi_2O_8$ polycrystalline sample at ambient temperature in a combination of seven different orientations including a combination of corner-mounted, edge-mounted, and face-mounted orientations.

Spectra were collected on cooling between 621 K - 298 K, at 10 K intervals between 621 K - 485 K, 5 K intervals between 485 K - 362 K, and 10 K intervals between 361 K - 298 K. Smaller intervals were used in the region of temperatures near the phase transition to collect more data points around the region of interest. The close-up of the 850 kHz - 1000 kHz region of the spectrum in Figure 3.17 clearly shows a strong relationship between the position of the resonant frequencies in the spectrum and temperature. The blue lines overlayed onto the peak at approximately 860 kHz represent the fit of the asymmetric Lorentzian function to the target peak at each temperature. The process of modelling the peak position and shape allowed the determination of the precise temperature at which the minima in the elastic moduli occurs.

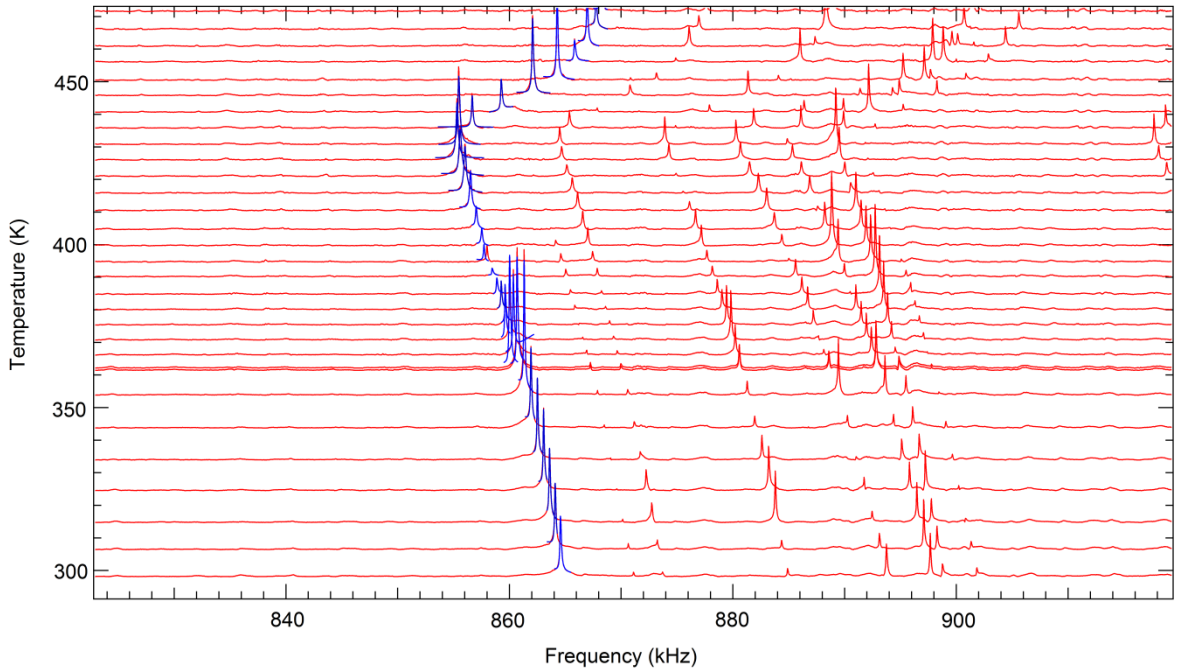

Figure 3.17: Resonant ultrasound spectra collected from a $Ba_2TiSi_2O_8$ single crystal on cooling between 471 K - 298 K (red lines). Blue lines indicate the Lorentzian curve calculated to fit a representative peak at each temperature.

The square of the resonant frequency (proportional to the elastic moduli, as discussed in section 2.5) of the peak near ~860 kHz is plotted as a function of temperature in Figure 3.18. Softening of the elastic constants occurs on heating up to 431 K, followed by a sharp increase once the transition has occurred. The error quoted for this value is based on the error of the thermocouple and furnace used in the experiment.

The elastic softening as the sample approaches the transition is common and is most likely due to fluctuations in the sample that can be attributed to dynamic short range order as has been discussed for the perovskite structure by Carpenter *et al.*[171]. The specific behaviour observed for the $Ba_2TiSi_2O_8$ structure is identical to the behaviour observed across the incommensurate to prototypic phase transition in $NaNO_2$.[172] The changes that have been observed in the elastic moduli are typical of structural phase transitions in metal oxide materials[173,174], providing additional evidence of the incommensurate to prototypic transition and emphasising that

although the structural changes across the transition are subtle, significant changes in the elastic properties occur.

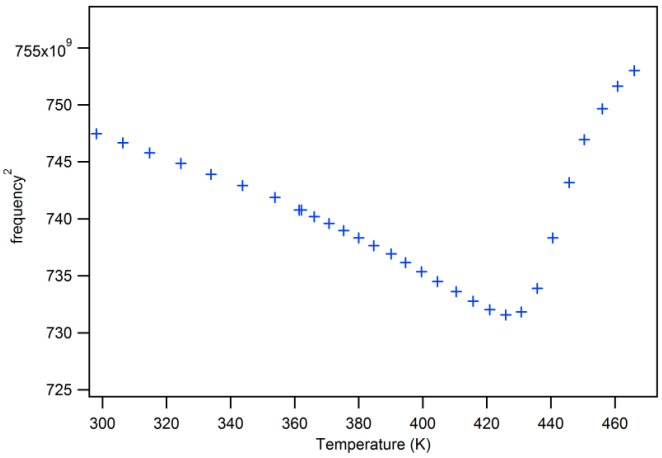

Figure 3.18: Variation in the square of the resonant frequency of the ~860 kHz peak from $Ba_2TiSi_2O_8$ between 298 K - 471 K. A softening of the elastic constants occurs on heating up to the transition at 431 K.

As introduced in Section 2.5.5, the inverse mechanical quality factor (Q^{-1}) can provide information about relaxation mechanisms that may operate in the material. These values were plotted for $Ba_2TiSi_2O_8$ between 300 K - 980 K (Figure 3.19), however no meaningful correlations were identified due to the high uncertainty for the FWHM that can be attributed to the convolution of the resonances of the sample and the rods holding the sample in the instrument.

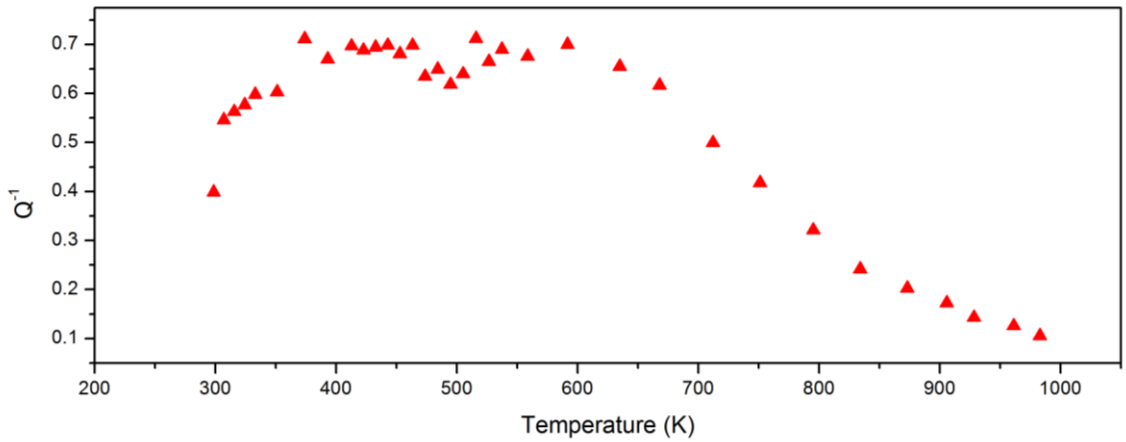

Figure 3.19: Inverse mechanical quality factor for the 818 kHz resonance as a function of temperature from resonant ultrasound spectroscopy of a polycrystalline $Ba_2TiSi_2O_8$ sample between 300 K - 980 K.

3.3.3 Physical property measurements from $Ba_2TiSi_2O_8$

Physical property measurements were conducted on polycrystalline $Ba_2TiSi_2O_8$ to build a basic understanding of the physical behaviour and electric responses of the samples synthesised in the current project.

The dielectric properties were measured using an Agilent 4284A LCR metre from a pellet of 13 mm diameter and 2 mm thickness pressed from polycrystalline $Ba_2TiSi_2O_8$. Silver paste was painted on the flat surfaces of the disc to measure the capacitance across the pellet. The capacitance (measure of ability to store charge) and loss tangent (measure of inherent dissipation of energy) was measured between 10 Hz - 1 MHz to determine the change in properties over a wide range of frequencies (Figure 3.20). The capacitance was not converted into a dielectric constant for the material because the surface area of the sample was not deemed sufficiently greater than the distance between the electrodes to ensure that a constant electric field was applied across the sample. However, the measured capacitance of the material provides a good guide of the trend of the dielectric properties of the sample.

The capacitance of the sample is moderate at low frequency, and reduces to significantly smaller values at high frequency as is observed in most dielectric materials.[175] The dielectric loss measured from the sample is relatively high in comparison to typical dielectrics on the market.[175,176] The high loss tangent measured from this sample may be attributed to the sample not being packed as densely as can be achieved for commercial samples.

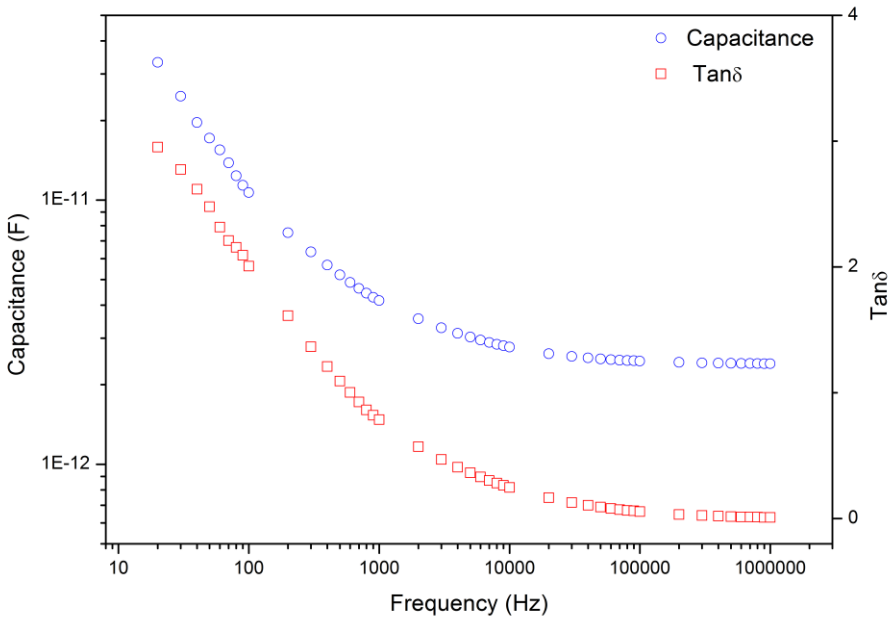

Figure 3.20: Capacitance (blue) and loss tangent (red) measured from a $Ba_2TiSi_2O_8$ pellet from 10 Hz - 1 MHz.

Piezoforce microscopy and ferroelectric measurements were performed on a Cypher scanning probe microscope from Asylum Research using an internal 15x high voltage amplifier and Olympus AC240TM electrilevers, spring constant k ~ 2 N/m, and tip radius ~25 nm. Single frequency measurements were performed at 10 kHz applied frequency, ~1 V applied and a contact force of approximately 100 nN. The dual frequency resonance-enhanced approach (DART, Asylum Research) was also used, with a contact force of approximately 100 nN and an applied voltage of about 45 mV. Piezoresponse curves were collected from ceramic samples using an AC signal (f ~ 10 kHz, V_{AC} ~ 0.75 V, phase offset = 180°) superimposed on a 0.2 Hz triangular square-stepping wave with bias up to ±60 V and a read/write time of 25 ms.

The $Ba_2TiSi_2O_8$ sample was shown to be piezoelectric through the measurement of the induced mechanical response from piezoresponse force microscopy. Figure 3.21A shows the out of plane mechanical deviation and phase of the piezoresponse from switching spectroscopy. The linear relationship between the induced mechanical deviation and the applied voltage is indicative of a

good piezoelectric material. The switch in phase at approximately 4 V indicates the surface potential of the sample. Figure 3.21B illustrates the results of the identical experiment with the switching field turned off. The lack of any mechanical deviation or change in phase as the voltage is varied indicates that no poling has occurred and hence no evidence of ferroelectricity, contradicting the work of Foster *et al*.[51] where dielectric hysteresis loops were collected from a polycrystalline sample.

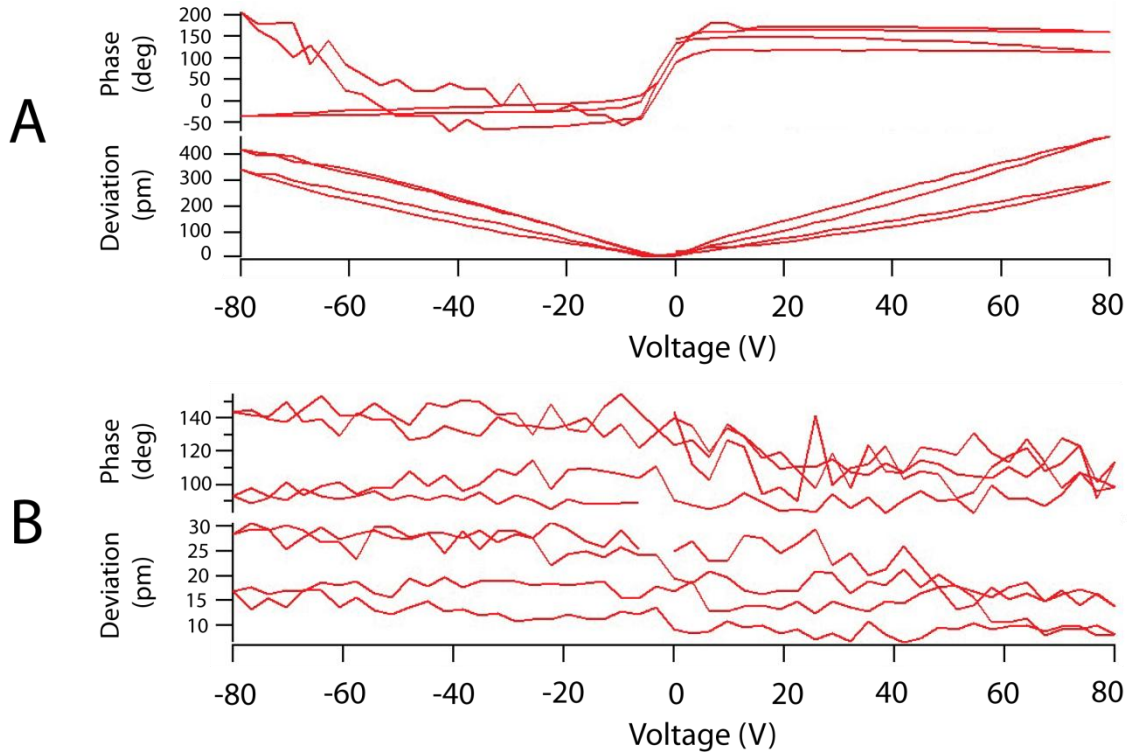

Figure 3.21: Out of plane mechanical deviation and phase recorded from switching spectroscopy conducted on $Ba_2TiSi_2O_8$ with applied field on (A) and off (B).

The confirmation of piezoelectricity in this bulk sample is a result in itself, however, an attempt was made to quantify the piezoelectric response recorded such that a comparison to common materials could be made. The quantification of the piezoelectric response coefficient from bulk materials using piezoresponse force microscopy is a difficult exercise, however the effective piezoelectric coefficient, d_{33}^* can be estimated for bulk samples under a uniform electric field

using Equation 3.1 where u_3 represents the mechanical out of plane deviation and V_0 represents the applied voltage.[177]

$$d_{33}^{*} = \frac{u_3}{V_0} \qquad \textbf{Equation 3.1}$$

The effective piezoelectric response calculated using the out of plane mechanical deviation recorded from the PFM experiment and Equation 3.1 was approximately 5 pm V^{-1}. Because the relationship between the effective piezoelectric coefficient (d_{33}^{*}) and the intrinsic piezoelectric coefficient (d_{33}) is sensitive to a variety of factors that are intrinsic to the probed material, it is challenging to convert from one term to another with high precision. However, Pan *et al.* have shown that the correlation factor between d_{33}^{*} and d_{33} can vary between positive and negative values, but is typically close to one for common piezoelectric materials such as $BaTiO_3$, $PbTiO_3$, and $PbZr_{0.48}Ti_{0.52}O_3$.[177] Using this assumption, it is concluded that for the purposes of a simple comparison to other common piezoelectric materials the intrinsic piezoelectric coefficient determined for $Ba_2TiSi_2O_8$ in the current study is approximately 5 pm V^{-1}. The intrinsic piezoelectric response coefficients for $Ba_2TiSi_2O_8$, $BaTiO_3$, $PbTiO_3$, and $PbZr_{0.48}Ti_{0.52}O_3$ have been provided in Table 3.5 where it is shown that the intrinsic piezoelectric coefficient determined for $Ba_2TiSi_2O_8$ is of the same order of magnitude of quartz, but significantly lower than the published values for the piezoelectrics that are currently popular for commercial applications.

Table 3.5: Comparison of the intrinsic piezoelectric coefficient for $Ba_2TiSi_2O_8$ and well-known piezoelectric materials.

Material	d_{33} (pm V^{-1})	Reference
$Ba_2TiSi_2O_8$	5	Current study
Quartz	2.3	Smith[178]
$BaTiO_3$	190	Jaffe *et al.*[179]
$PbTiO_3$	50	Ueda *et al.*[180]
$PbZr_{0.48}Ti_{0.52}O_3$	110	Berlincourt *et al.*[181]

The phase of the induced polarisation was also mapped using piezoresponse force microscopy from a small region of a representative crystallite. The different colours in Figure 3.22 represent the in plane and out of plane components of the polarisation vector in the sample. The 180° difference in the phase of these components in different domains is typical of piezoelectric materials and succinctly illustrates the piezoelectricity of the sample. No evidence of switching the direction of the polarisation vectors was observed in the piezoforce microscopy experiments conducted on this sample.

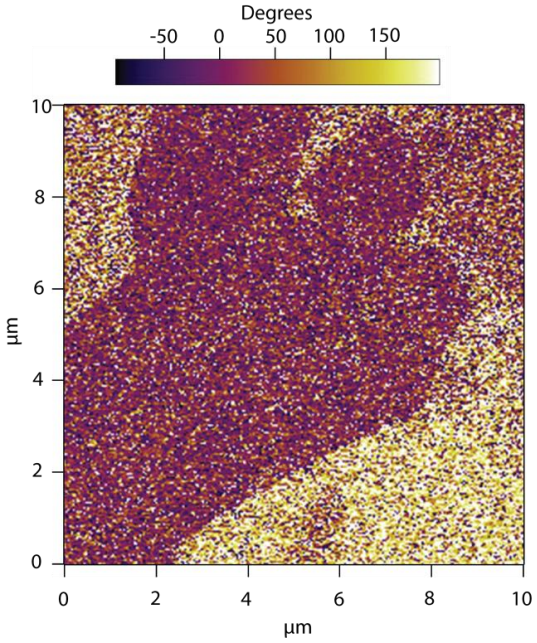

Figure 3.22: Image of the phase of the signals detected using piezoresponse force microscopy from polycrystalline $Ba_2TiSi_2O_8$.

A polarisation versus applied electric field loop was recorded using a ferroelectric analyser to establish whether any evidence of ferroelectricity could be found in the sample (Figure 3.23). Although the loop obtained resembles a hysteresis loop, it was established that no ferroelectric behaviour was observed from the sample despite increasing the applied field to approximately 35 kV cm^{-1} (well above the applied field of 12 kV cm^{-1} by Foster *et al.*[51]). This conclusion was reached based on two observations from the polarisation versus applied field graph. Firstly, the shape of the loop does not indicate that a saturation in polarisation is occurring at high fields, supported by the lack of change in concavity in the loop. Secondly, the supposedly induced

"polarisation" recorded is in the order of pico-Coulombs, significantly lower than the expected induced polarisation. This small signal suggests that the minimal polarisation observed is simply a very small charge or leakage current which would normally be overshadowed by the true polarisation from a ferroelectric material.[182]

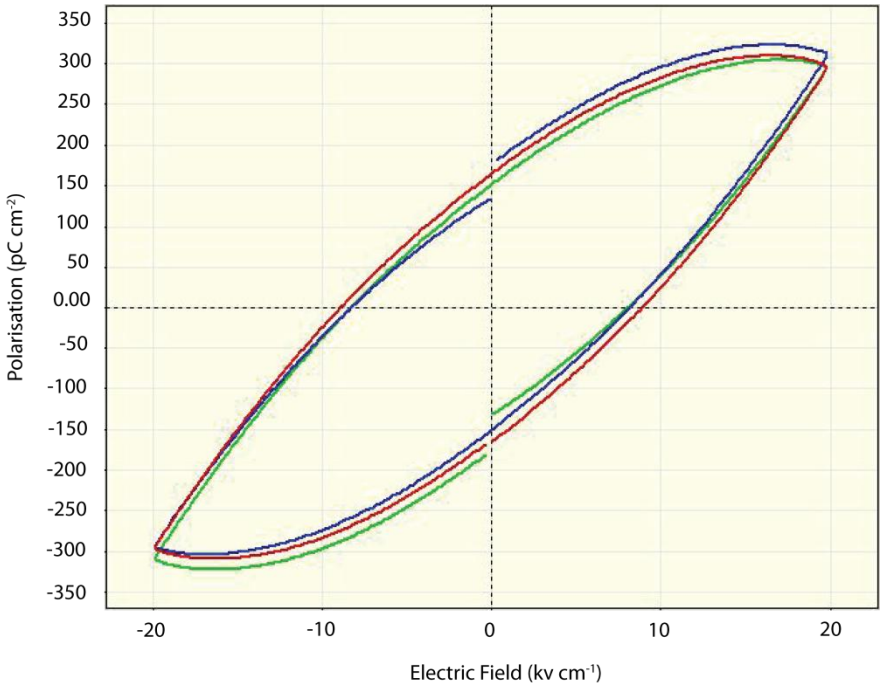

Figure 3.23: Polarisation versus electric field curve collected from polycrystalline $Ba_2TiSi_2O_8$. The lack of saturation at high field and the small induced polarisation indicate that no ferroelectric properties are present.

The results from Figure 3.23 are further supported by the current/voltage versus time plot in Figure 3.24 where the smooth change in current without any sudden peaks or drops is typical of a non-ferroelectric material. Combining the results from the ferroelectric analysis and the piezoresponse force microscopy, it can be concluded that the polycrystalline samples investigated in this project are piezoelectric, but not ferroelectric. Although this result is inconsistent with the predictions and results published by Foster *et al.*[51], the variations in the local composition and structure that are known to occur when the sample is in polycrystalline form means that it is not implausible that some samples show ferroelectricity while other samples do not.

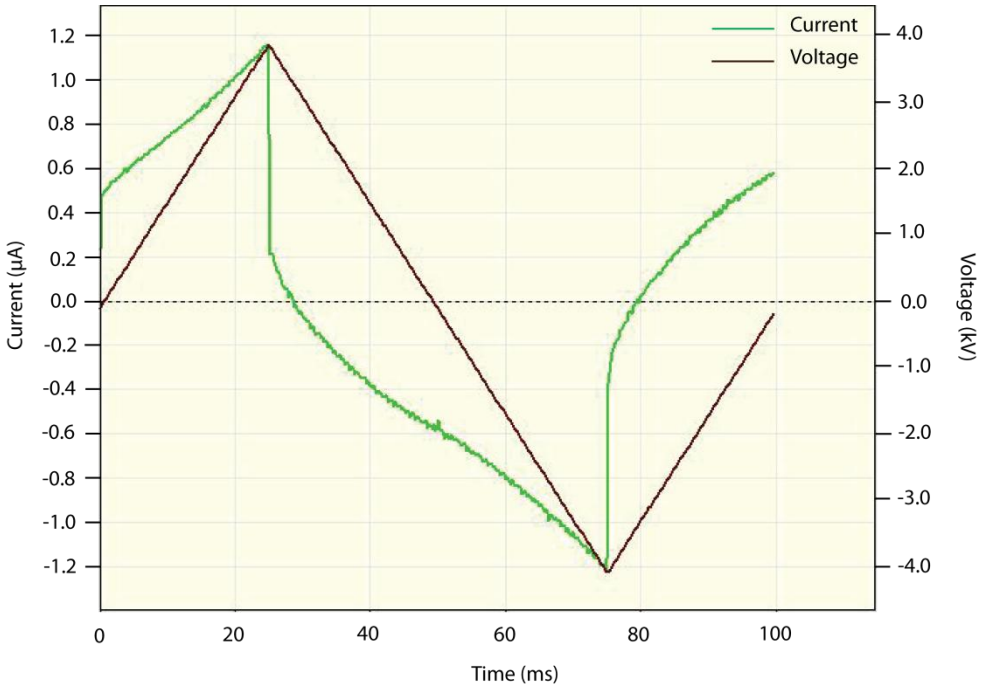

Figure 3.24: Current (left axis) and voltage (right axis) versus time curve collected from polycrystalline $Ba_2TiSi_2O_8$. The smooth change in current as the voltage is varied provides additional evidence that the sample does not exhibit ferroelectricity.

The difference in the synthetic methods for the sample investigated by Foster *et al.*[51] and the sample in the current study is the heating regime and cooling methods. The polycrystalline $Ba_2TiSi_2O_8$ sample in the literature that was shown to exhibit ferroelectricity was synthesised at 900 °C for 12 hours, 1100 °C for 36 hours, and 1410 °C for 24 hours. The final heating step was followed by cooling at 1 °C min^{-1} to 1380 °C, 5 °C min^{-1} to 1300 °C, 20 °C min^{-1} to 900 °C, and finally 100 °C min^{-1} to ambient temperature. These samples were hence synthesised using a significantly higher maximum synthesis temperature and shorter heating periods than the samples in the current study. According to the experimental synthesis conducted in the current study, a maximum heating temperature of 1410 °C produces an unidentified second phase (*c.f.* Section 3.2) which may have been contributing to the ferroelectricity observed by Foster *et al.* However, the bulk sample investigated by Foster *et al*. was ferroelectric, while the samples synthesised via conventional solid state synthesis methods in the current project are not.

3.4 Summary

The $Ba_2TiSi_2O_8$ structure has been characterised at ambient temperature using synchrotron X-ray powder diffraction, high resolution neutron powder diffraction, and high intensity neutron powder diffraction. The average $Ba_2TiSi_2O_8$ structure was determined from the synchrotron X-ray powder diffraction study. Three arguments were presented to explain the absence of satellite reflections in synchrotron X-ray powder diffraction patterns when they have been previously observed in single crystal X-ray diffraction patterns. The most likely explanation considered the possibility that the smaller domain sizes in polycrystalline samples may contribute to the broadening of the already weak satellite reflections such that they cannot be observed above the background anymore.

Only weak intensity corresponding to a small number of satellite reflections was observed in the high intensity neutron powder diffraction patterns. However, the $Ba_2TiSi_2O_8$ modulated structure was refined using the $X4bm(\alpha, \alpha, 0)0gg$ space group. The bond valence sums calculated for each atom in the structure indicate that the introduction of the modulation significantly improves the bond valence sum of the barium and oxygen-1, -2, and -4 ions on average. The successful refinement of the $Ba_2TiSi_2O_8$ modulated structure at ambient temperature has shown for the first time that although difficult, neutron powder diffraction can be a useful technique for the investigation of the modulated structure of $Ba_2TiSi_2O_8$.

The $Ba_2TiSi_2O_8$ structure was also investigated between 125 K - 1273 K using synchrotron X-ray powder diffraction, and 275 K - 600 K using high intensity neutron powder diffraction. The unit cell parameters were determined with high precision from the X-ray diffraction study, providing new evidence of the structural phase transition from the incommensurate to the prototypic phase at approximately 433 K. The nonlinear change in the unit cell parameters had never been reported before and may be used to identify this incommensurate to prototypic phase transition

despite the absence of any satellite reflections in the powder diffraction patterns. The determination of the significant drop in the *a/c* cell parameter ratio also provided a new way to identify this phase transition. It was also established that quenching $Ba_2TiSi_2O_8$ from above the 433 K transition temperature does not preserve the high temperature structure at ambient temperature, which was justified by the extremely small difference in energy states between the phases above and below the transition temperature as confirmed by the absence of any thermal anomaly between 373 K - 723 K from differential scanning calorimetry.

The variations in the elastic moduli as determined from resonant ultrasound spectroscopy were reported across the 433 K transition, indicating softening up to the phase transition temperature. These elastic constants were shown to be an excellent parameter to track the second order *X*4*bm*(α, α, 0)*0gg* to *X*4*bm* phase transition despite the subtlety of the structural changes that can be difficult to identify using other techniques. This also demonstrated that changes in the sample properties (such as the elastic moduli) as the structure passes through the phase transition are significant despite the small structural changes that occur.

An investigation into some of the physical properties of $Ba_2TiSi_2O_8$ found moderate capacitance at low frequency with a relatively high dielectric loss. Piezoresponse force microscopy was used to confirm that the compound investigated was piezoelectric, and the intrinsic piezoelectric coefficient was calculated to be approximately 5 pm V^{-1}, significantly lower than the commonly used commercial piezoelectrics. The $Ba_2TiSi_2O_8$ samples investigated did not show any evidence of ferroelectricity from the PFM experiments in the form of poling or domain switching when the strong electric field was reversed. The absence of ferroelectricity in polycrystalline $Ba_2TiSi_2O_8$ samples does not agree with the work of Foster *et al.*,[51] where dielectric hysteresis loops were recorded from a ceramic $Ba_2TiSi_2O_8$ sample synthesised via a melt/slow cool method. It can be concluded that the samples synthesised in the current study using conventional synthetic methods involving heating below the melting point are non-ferroelectric. This result is highly

significant in the context of the possible application of $Ba_2TiSi_2O_8$ as a ferroelectric material because the specific synthetic method chosen could play a critical role in the extent of ferroelectric properties that may be observed for different samples. An investigation into the extent of ferroelectricity in samples that have been synthesised via different methods would be an interesting direction to continue this work and build on the recently published study on fresnoite synthesis by Wong *et al*.[153]

Chapter 4 Structural Investigation of $Sr_2TiSi_2O_8$

4.1 Introduction

The first published $Sr_2TiSi_2O_8$ structure was determined by Höche *et al*.[1] using single crystal X-ray diffraction, whereby single crystals grown via Czochralski pulling, flux-growth, and electrochemically induced nucleation were found to exhibit subtle differences in their structural modulations. In all cases, it was reported that $Sr_2TiSi_2O_8$ crystallises isostructurally to $Ba_2TiSi_2O_8$ in the tetragonal $P4bm(\alpha, \alpha, ½)0gg$ ($\alpha \sim 0.3$) space group. A combination of single-crystal X-ray diffraction and electron microscopy was used to construct a full (3+2)-dimensional structural model of $Sr_2TiSi_2O_8$, incorporating the modulation along the (**a*** + **b***) + ½**c*** and (**-a*** + **b***) + ½**c*** directions.

Electron diffraction patterns collected from $Sr_2TiSi_2O_8$ provided evidence of the superposition of the two-dimensional modulation along the [100]- and [010]-directions, and an additional one-dimensional modulation along the [110]-direction. It was claimed that the growth rate, stoichiometry of the melt, and crystallite size all have a significant influence on the formation of the modulated structure. The position and relative intensity of the reflections observed in the [110]-direction were comparable to those observed for $Ba_2TiGe_2O_8$, leading to the conclusion that the crystal contained two coexisting modulated phases with satellites observed along one- or two-dimensions. Other examples of mixed-dimensional modulations have been reported by van Heurck *et al.*[2] for the $Ca_2ZnGe_2O_7$ structure type, which exhibits layers of corner-sharing tetrahedra that produce an irregular pentagonal arrangement surrounding a large highly-coordinated group 2 ion, in a similar way to the fresnoite structure.

This chapter extends on the work of Höche *et al*.[1,3], investigating the specific phase behaviour and formation of the modulated phases of $Sr_2TiSi_2O_8$ between 125 K - 1373 K. A combination of

synchrotron X-ray powder diffraction, electron diffraction, and neutron powder diffraction data are presented to construct a more complete understanding of the various phases of $Sr_2TiSi_2O_8$ and the associated phase transitions. Resonant ultrasound spectroscopy and differential scanning calorimetry experiments will also be presented to support the conclusions drawn from the diffraction experiments. This chapter has been divided into four sections. Firstly, a discussion of the synthesis of $Sr_2TiSi_2O_8$ will be provided. Secondly, the characterisation of the $Sr_2TiSi_2O_8$ modulated structure at ambient temperature will be discussed. This will be followed by a discussion of the first ever reported thermally-induced phase transformations of the $Sr_2TiSi_2O_8$ structure. Finally, a brief investigation into the physical properties of $Sr_2TiSi_2O_8$ will be presented and briefly discussed.

4.2 Synthesis

The determination of a method to synthesise pure polycrystalline samples of $Sr_2TiSi_2O_8$ was non-trivial. Various attempts to synthesise $Sr_2TiSi_2O_8$ using procedures outlined in the literature[3,4] produced samples that contained significant proportions of $SrTiO_3$ as a second phase. This section discusses the synthesis and formation of $Sr_2TiSi_2O_8$, including the tendency of the mixture to form $SrTiO_3$ and what is likely to be a combination of silicates between 1250 °C - 1275 °C.

The synthesis of $Sr_2TiSi_2O_8$ at temperatures between 1200 °C - 1350 °C as reported by Coats *et al.*[4] did not produce single phase $Sr_2TiSi_2O_8$. X-ray diffraction using synchrotron and Cu K_α radiation revealed small proportions of $SrTiO_3$ in all $Sr_2TiSi_2O_8$ samples synthesised via this method.

It is possible that the formation of $SrTiO_3$ in $Sr_2TiSi_2O_8$ samples may be attributed to a shortage of available SiO_2 due to the loss of silicon to the surrounding environment or the crucible at high temperatures, forcing the formation of the $SrTiO_3$ in addition to other silicates with the remaining

reagents. To test this hypothesis, samples of $Sr_2TiSi_2O_8$ were synthesised with 0 %, 2.5 %, 5 % and 10 % proportions of excess SiO_2 to test whether the presence of additional silicon in the reaction mixture could prevent or reduce the formation of the $SrTiO_3$ phase. The diffraction patterns collected from each of these samples are provided in Figure 4.1 where the asterisks identify reflections at 32.5°, 40° and 46.5° two theta that cannot be indexed by the $Sr_2TiSi_2O_8$ unit cell. The intensity of these reflections was significantly reduced when the reaction was performed using 2.5 % excess silicon. The patterns collected from the samples synthesised using 5 % and 10 % excess SiO_2 contain increased intensity of the reflections corresponding to the impurity phase(s), suggesting that at least one additional phase is formed due to the presence of too much SiO_2. It is unclear why the additional reflections are similar in the 0 %, 5 %, and 10 % samples, however the strongest reflections at 22.5°, 32.5°, 40° and 46.6° two theta can be indexed by $SrTiO_3$. None of the powder diffraction patterns in the International Centre for Diffraction Data (ICDD) database could correctly index the extraneous reflections, suggesting that they may correspond to at least two or more additional impurity phases. However, repeating the experiment found that the use of a 2.5 % excess of SiO_2 via conventional solid state synthetic methods produces $Sr_2TiSi_2O_8$ samples with smaller proportions of $SrTiO_3$ and other impurity phases relative to no excess or the other excesses investigated. Further attempts to synthesise pure $Sr_2TiSi_2O_8$ samples were based on these findings.

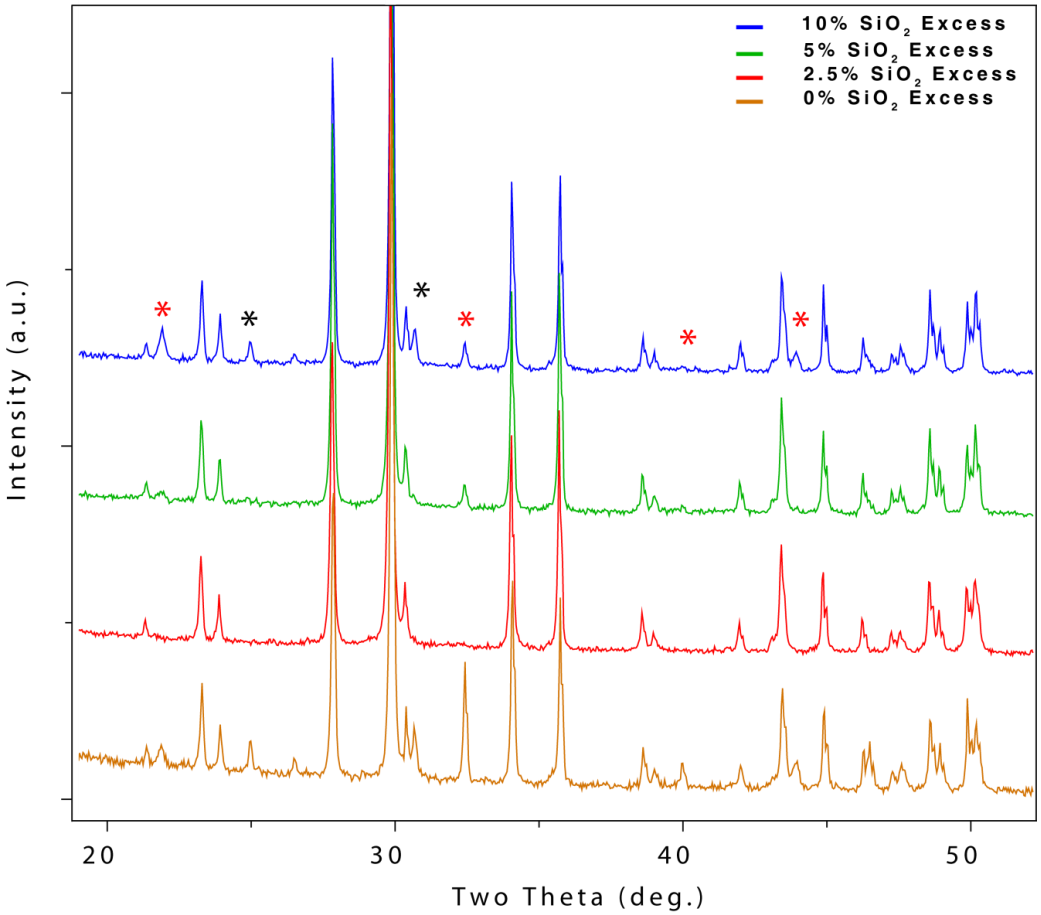

Figure 4.1: X-ray diffraction patterns (Cu K_α radiation) collected from $Sr_2TiSi_2O_8$ synthesised with 0% (orange), 2.5% (red), 5% (green), and 10% (blue) excess SiO_2. Red and black asterisks indentify reflections corresponding to the $SrTiO_3$ impurity phase and unidentified impurity phases, respectively.

Figure 4.2A shows that heating $Sr_2TiSi_2O_8$ at 1275 °C for 1 week transforms the sample into $SrTiO_3$. This is compared with a $Sr_2TiSi_2O_8$ sample heated at 1250 °C for 1 week in Figure 4.2B where the fresnoite structure has been retained after heating. The conversion of $Sr_2TiSi_2O_8$ to $SrTiO_3$ raises the question of where the silicon has gone in the sample. Energy dispersive X-ray (EDX) analysis was performed on the sample from Figure 4.2A to determine whether any evidence of SiO_2 or other silicates could be found in case they were present as amorphous phases that would not be visible in diffraction patterns. However, this was not possible because the coincidental overlap of the silicon K_α (1.7 keV) and strontium L_α (1.8 keV) characteristic X-ray energies made it extremely difficult to differentiate between these two elements using this technique.

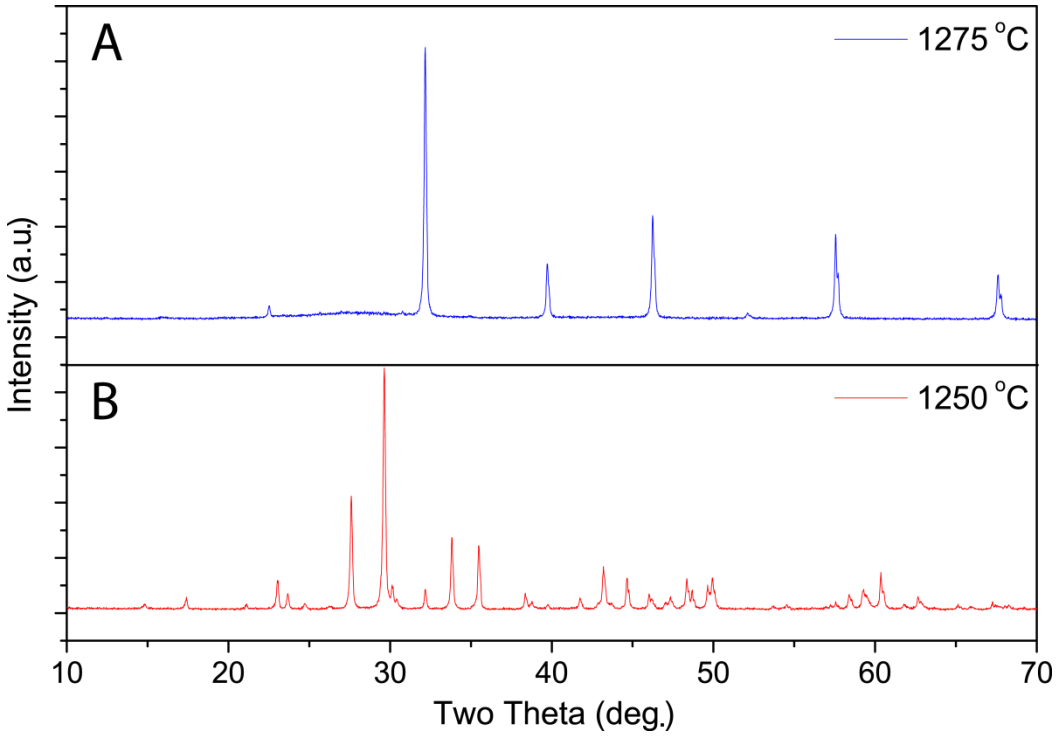

Figure 4.2: X-ray diffraction patterns (Cu K_α radiation) collected from $Sr_2TiSi_2O_8$ samples after heating for one week at 1275 °C (A) and 1250 °C (B) and.

The conversion of $Sr_2TiSi_2O_8$ to $SrTiO_3$ at 1275 °C can potentially be explained by the preferred octahedral coordination environment of the Ti^{4+} ion. During the conventional solid state synthesis of $Sr_2TiSi_2O_8$, the coordination environment of Ti^{4+} must change from sixfold coordinate in the TiO_2 rutile phase precursor to fivefold coordinate in the $Sr_2TiSi_2O_8$ phase. It has also been shown that Ti(IV) can exhibit sixfold coordination in glassy $Sr_2TiSi_2O_8$ samples which are synthesised above the melting point (~1300 °C)[5], suggesting that a six-fold coordination might be a stable environment for Ti^{4+} at these high temperatures. It is plausible that continued heating at high temperatures could favour the formation of $SrTiO_3$ because the Ti^{4+} will adopt the favourable sixfold coordination in the *B*-site of the $SrTiO_3$ perovskite structure instead of the less favourable five-fold coordination required in the square pyramidal polyhedra in the $Sr_2TiSi_2O_8$ structure.

The conversion from $Sr_2TiSi_2O_8$ to $SrTiO_3$ at 1275 °C also means that higher reaction temperatures cannot be used to increase the purity of the sample. Using this knowledge, repeated heating at 1250 °C was conducted to investigate whether the purity of the sample could be improved by

heating for longer periods of time in pellet form with frequent homogenisation. X-ray diffraction data were collected after each heating stage of 20 - 48 hours at 1250 °C to monitor the progress of the reaction after each homogenisation step. The X-ray diffraction patterns in Figure 4.3 show that the intensity of the reflections corresponding to the impurity phases (marked by asterisks) were gradually removed with continued heating and homogenisation.

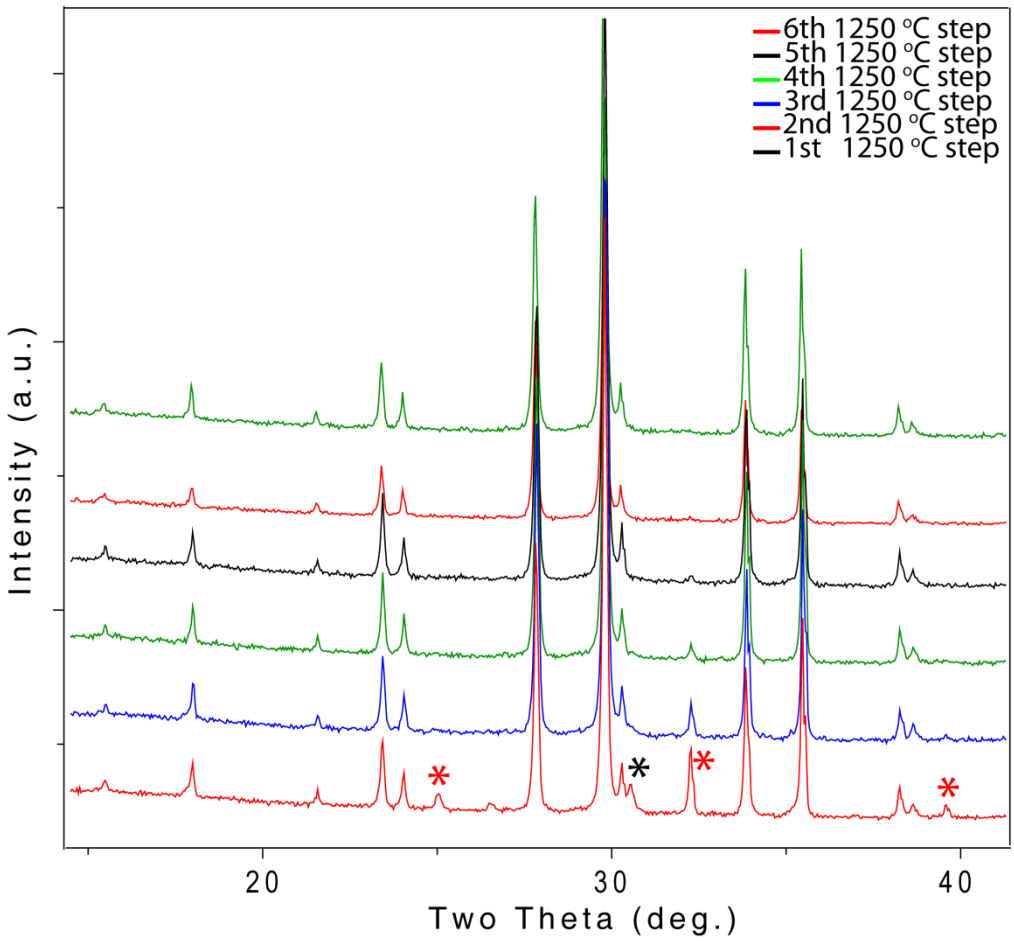

Figure 4.3: Comparison of X-ray diffraction patterns (Cu K_α radiation) collected from $Sr_2TiSi_2O_8$ after each successive heating step at 1250 °C. Red and black asterisks identify reflections corresponding to the $SrTiO_3$ and unidentified phases, respectively.

From the evidence collected in this study, it is proposed that the thermodynamically stable phase changes from $Sr_2TiSi_2O_8$ to $SrTiO_3$ + silicates between 1250 °C and 1275 °C. The combination of the use of 2.5 % excess SiO_2 and six heating stages in pellet form between 20 - 48 hours at 1250 °C with homogenisation after each step was established as the optimum method to synthesise pure polycrystalline $Sr_2TiSi_2O_8$ samples. No other methods of synthesis were investigated for

$Sr_2TiSi_2O_8$ because of the anticipated difficulties associated with the formation of glassy fresnoite and the evidence that the samples made via the methods outlined in this section were single phase according to refinements against synchrotron X-ray diffraction data.

4.3 Results and Discussion

4.3.1 $Sr_2TiSi_2O_8$ structure at ambient temperature

Electron diffraction patterns were collected from tiny crystallites of $Sr_2TiSi_2O_8$ at ambient temperature to understand the structural modulations in the samples synthesised in this project. Electron diffraction was performed at 200 kV using a JEOL JEM-2011 transmission electron microscope (TEM) and JEOL JEM-2100F TEM at the Australian National University Research School of Chemistry and Monash Centre for Electron Microscopy. A typical $Sr_2TiSi_2O_8$ crystal that was investigated during these studies is pictured in Figure 4.4.

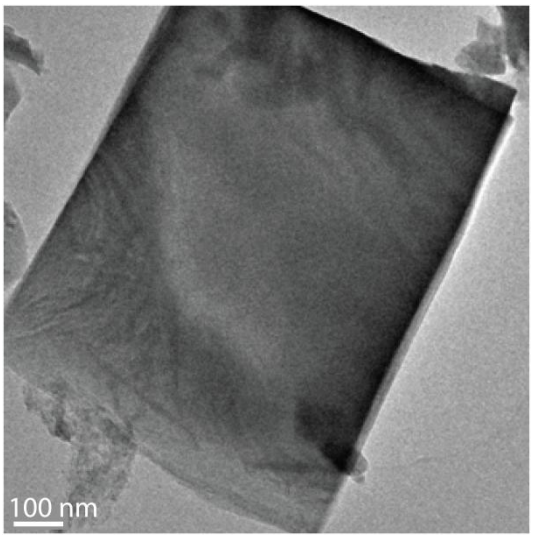

Figure 4.4: Transmission electron microscope image of a typical $Sr_2TiSi_2O_8$ crystal.

The presence of satellite reflections corresponding to two different fresnoite-type phases reproduced the work of Höche *et al.*[1] Two electron diffraction patterns collected at ambient

temperature from adjacent regions of the same crystallite are provided in Figure 4.5, where the main Bragg reflections in both electron patterns can be indexed using a tetragonal *P*4*bm* parent setting. The position of the satellite reflections along the $[110]_p$ direction (Figure 4.5A) and the $[100]_p$ and $[010]_p$ directions (Figure 4.5B) indicate that the symmetry of the two different structures is not identical.

The *Xmm*2(0, β, ½)*s*00 space group that was reported by Höche *et al.*[6] for $Ba_2TiGe_2O_8$ could not successfully index the diffraction pattern collected from the orthorhombic phase of $Sr_2TiSi_2O_8$. This was seen through the violation of the F(hklm) = 0 unless $l + m = 2n$ extinction condition. Hence, the *Cmm*2(0, β, 0)*s*00 was used to correctly index the diffraction pattern given that F(*hklm*) = 0 unless $h + k = 2n$. Figure 4.5A was indexed with respect to **M*** = {**a*** = ½$[1\bar{1}0]_p$*, **b*** = $[110]_p$*, **c*** = $[001]_p$* using the ***q***-vector:

$$\boldsymbol{q} = 0.29[110]_p^* \qquad \textbf{Equation 4.1}$$

Figure 4.5B was indexed with respect to **M*** = {**a*** = $[100]_p$*, **b*** = $[010]_p$*, **c*** = ½$[001]_p$*, using the previously reported[1] *X*4*bm*(α, α, 0)0*gg* space group where *X* represents the {0,0,½,½,½) superspace centring such that *hklmn*: $l + m + n = 2n$. The satellite reflections along the [100]- and [010]-directions in Figure 4.5B were indexed with respect to using the two modulation vectors:

$$\boldsymbol{q_1} = 0.30[110]_p^* \qquad \textbf{Equation 4.2}$$

$$\boldsymbol{q_2} = 0.30[\bar{1}10]_p^* \qquad \textbf{Equation 4.3}$$

The diffraction pattern in Figure 4.5B also contains a small contribution from the orthorhombic phase shown in Figure 4.5A. This occurs when the electron beam passes through a small proportion of the second phase in addition to the targeted phase. This could either be spatially adjacent to, or above/below the intended phase, depending on the intergrowth of the two phases.

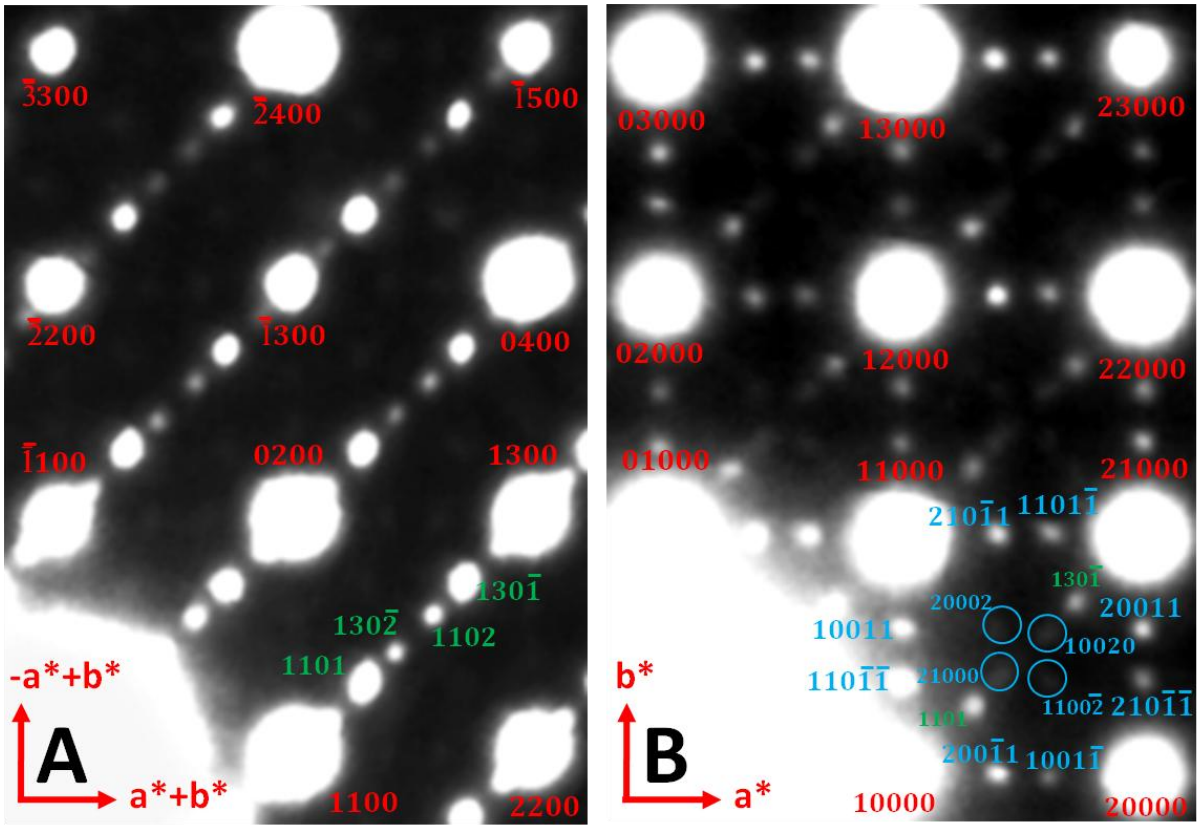

Figure 4.5: Electron diffraction patterns collected from polycrystalline $Sr_2TiSi_2O_8$ along the [001]-direction, providing evidence of two coexisting modulated phases in adjacent regions of the same crystallite at ambient temperature. Bragg reflections corresponding to the average structure have been indexed in red. The satellites have been indexed using an orthorhombic unit cell (A, green) and a tetragonal unit cell (B, circled in blue). B also contains a small contribution from the orthorhombic unit cell (indexed in green).

The overlapping of the main Bragg reflections from both phases means that the second phase has a unit cell with very similar dimensions to the tetragonal phase at ambient temperature. The coexistence of two extremely similar incommensurately modulated phases complicates the structural investigation of $Sr_2TiSi_2O_8$ because of the difficulty of extracting information from each individual phase when there is little evidence to differentiate them. It is impossible to estimate the relative proportions of each phase present in the bulk sample using electron diffraction because only very tiny proportions of sample are investigated at any one time. Similar behaviour has been observed in electron diffraction patterns collected from $Ba_2NaNb_5O_{15}$ whereby satellite reflections corresponding to tetragonal and orthorhombic incommensurate phases have been observed at approximately 573 K.[7-9]

Synchrotron X-ray powder diffraction patterns were collected at the powder diffraction beamline of the Australian synchrotron using the experimental setup described in section 2.1.2.1 at a wavelength of λ = 1.158706(1) Å. The refinement of structural models against all X-ray powder diffraction data collected from $Sr_2TiSi_2O_8$ in this project was a challenging process. The first problem involved the under calculation of many of the main reflections, particularly the 310 and 004 reflections at 25.4° and 26.7° two theta, respectively. No structurally significant changes could be introduced to the model to correctly describe these reflections. However, the inclusion of correction for anisotropic strain broadening significantly improved the fit of the calculated intensities for these reflections as shown in the minimised difference in the black difference curve in Figure 4.6. Additionally, inclusion of preferred orientation in the 202 direction drastically improved the quality of the fit. The 202 direction was chosen because the h0k family of reflections was identified as the group of reflections that could not be fitted satisfactorily.

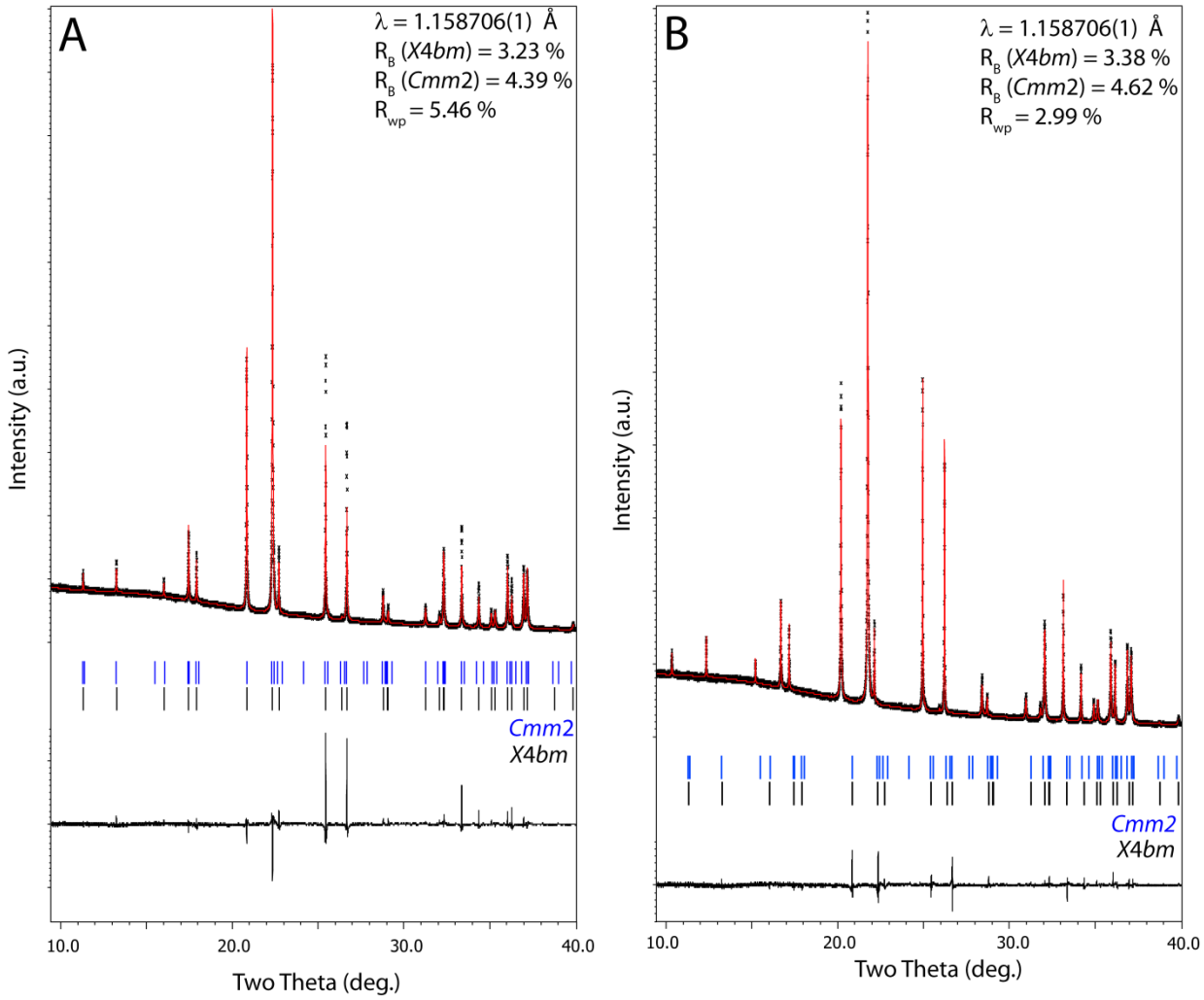

Figure 4.6: Observed, calculated, and difference plots for the refinement of the $Sr_2TiSi_2O_8$ average structure against synchrotron X-ray powder diffraction data before (A) and after (B) anisotropic strain broadening correction. The blue and black reflection markers identify reflections corresponding to the *Cmm*2 and *X*4*bm* phases, respectively. The improvement in the fit of many reflections is evident in the difference plot (black) below the rows of reflection markers.

Using the corrections for anisotropic strain broadening and preferred orientation, a two phase model of the $Sr_2TiSi_2O_8$ average structures (consisting of *X*4*bm* and *Cmm*2 space groups) at ambient temperature was refined against the synchrotron X-ray powder diffraction pattern to produce an excellent fit to the data as shown in Figure 4.7. The X's denote the non-standard centring {0, 0, ½, ½. ½,} where applicable to remain consistent and comparable to other refinements throughout the thesis. The asterisks in Figure 4.7 identify the extremely weak 400 and 420 reflections at 22.9° and 25.5° two theta, respectively, which correspond to the orthorhombic phase that was identified in the electron diffraction patterns.

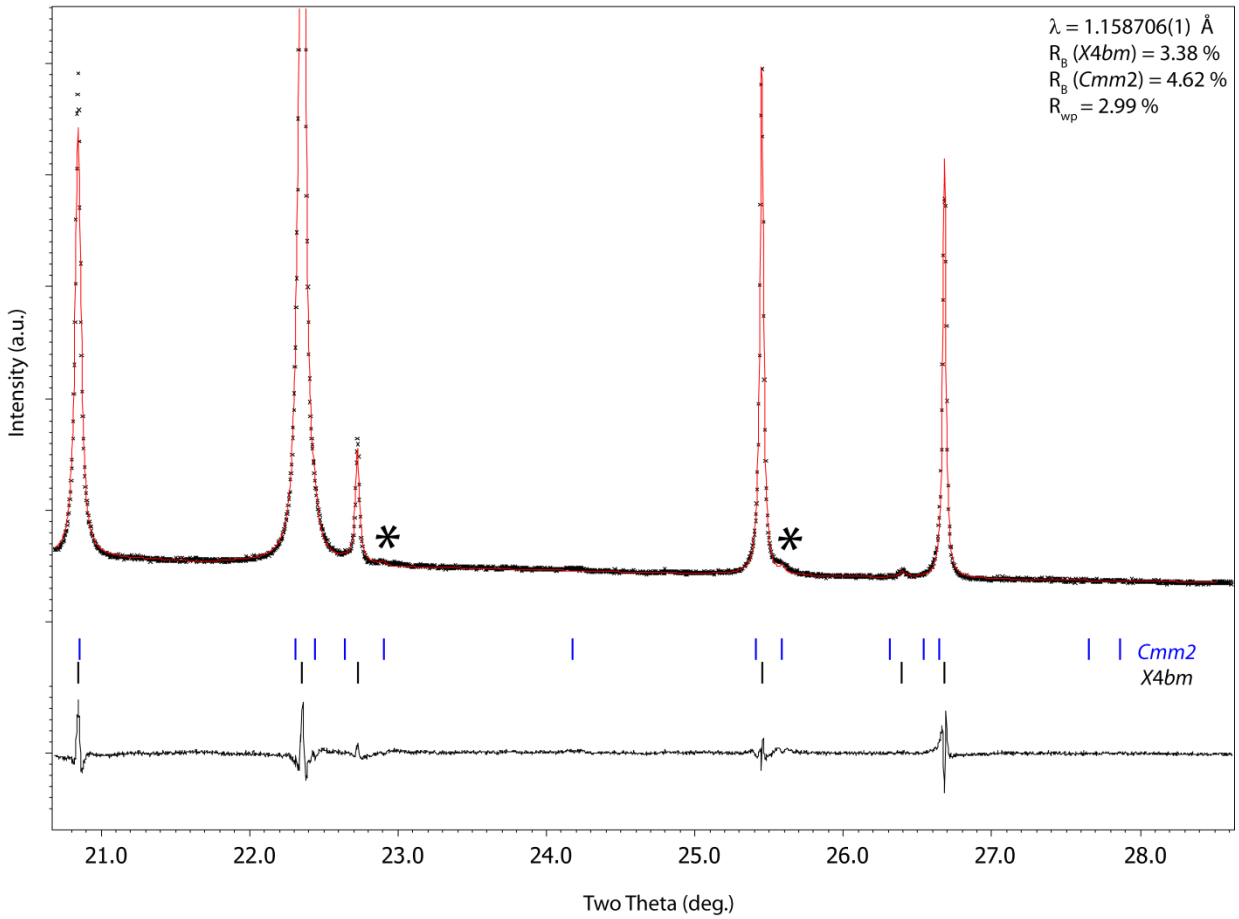

Figure 4.7: Observed, calculated, and difference plots for the refinement of the two $Sr_2TiSi_2O_8$ phases at ambient temperature against synchrotron X-ray powder diffraction data collected at λ = 1.158706(1). Asterisks mark the positions of the very weak reflections corresponding to the *Cmm*2 phase.

No satellite reflections were observed in the synchrotron diffraction patterns despite the excellent signal-to-noise ratio. Satellite reflections have been reported from single crystal X-ray diffraction by Höche *et al.*[1] and electron diffraction by Withers *et al.*[10] and Höche *et al.*[3], however, the reasoning presented for the absence of satellite reflections in synchrotron X-ray powder diffraction patterns collected from $Ba_2TiSi_2O_8$ in Chapter 3 also applies to $Sr_2TiSi_2O_8$. Although the strontium in $Sr_2TiSi_2O_8$ would not dominate the contribution to the X-ray diffraction patterns as much as barium in $Ba_2TiSi_2O_8$, the scattering power of the strontium ions relative to the oxygen ions is still substantial and this is likely to contribute to the lack of intensity corresponding to the satellite reflections. Once a reasonable average structure had been refined against the synchrotron data, modulation terms from the Höche *et al.*[1] model determined from single crystal

X-ray diffraction were used as a starting model to be refined against the data collected in the current project. The observed, calculated, and difference plots obtained when the Höche *et al*. modulation parameters were entered are presented in Figure 4.8, where no intensity corresponding to calculated satellite reflections is observed.

Despite the absence of evidence for any satellite reflections in the experimental pattern, or calculated satellite reflections from the Höche *et al*. model, the modulation amplitudes were systematically refined to check whether a stable, reasonable model could be obtained. However, as one might expect, this was not possible. Modulation amplitudes were also refined from arbitrarily small values (*c.f.* 0.001) without any success.

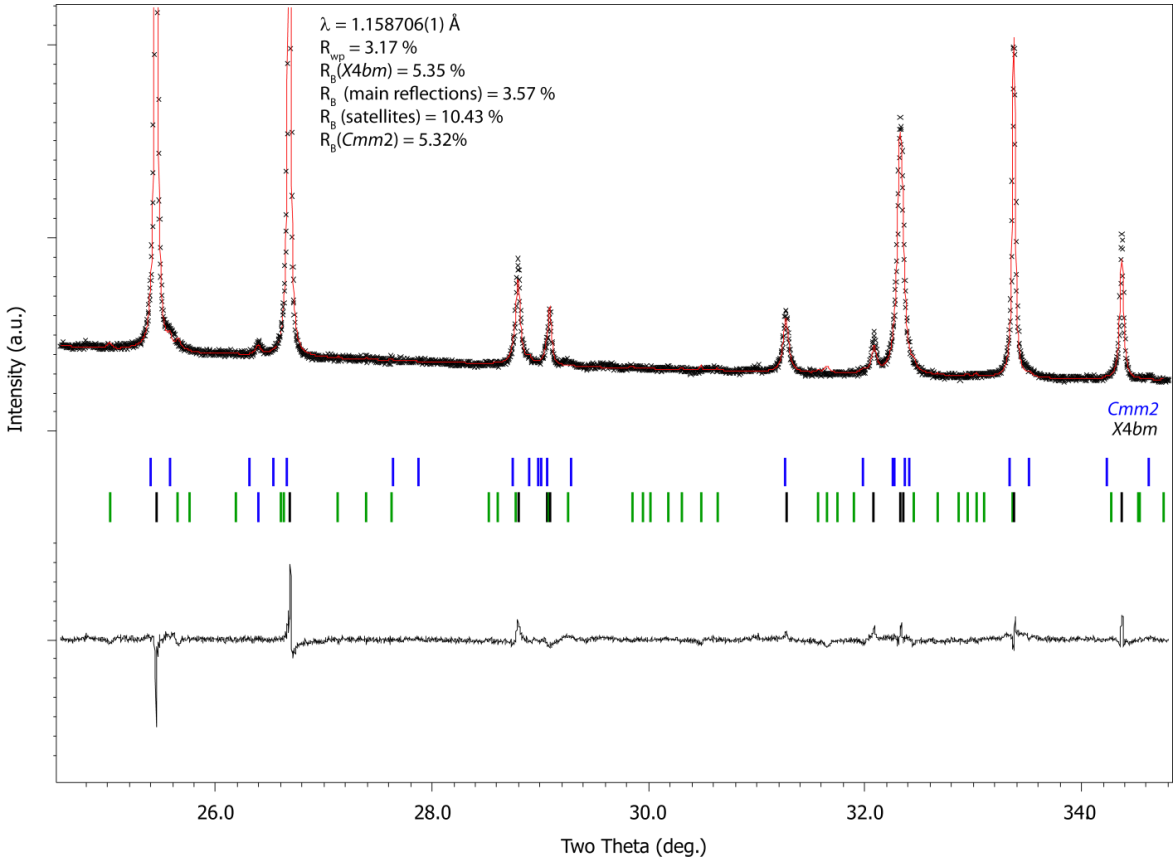

Figure 4.8: Observed, calculated, and difference plots for the refinement of the $Sr_2TiSi_2O_8$ structure at ambient temperature against synchrotron X-ray powder diffraction data using modulation amplitudes from Höche *et al*. Blue and black peak markers identify reflections corresponding to the C*mm*2 and *X*4*bm* average structures, respectively. Green markers identify satellite reflections corresponding to the *X*4*bm* modulated structure.

The average $Sr_2TiSi_2O_8$ structures of both phases were included in a model refined against synchrotron X-ray powder diffraction data. The experimental data and important parameters for this refinement are provided in Table 4.1. The atomic positions and atomic displacement parameters were not refined for the orthorhombic phase because of the tiny proportion of the phase present and the presence of only one independent reflection in the observed diffraction pattern.

Table 4.1: Experimental data and important parameters for both $Sr_2TiSi_2O_8$ phases at ambient temperature.

Parameter	*X*4*bm* Phase	*Cmm*2 Phase
Wavelength (Å)	λ = 1.158706(1)	
Molar mass (g mol^{-1})	407.28	
Z	4	
a (Å)	8.321814(9)	11.8137(7)
b (Å)	8.321814(9)	11.6846(6)
c (Å)	10.04866(1)	5.0297(3)
V (Å^3)	695.895(2)	694.285(3)
Phase Fraction	99.53(1) %	0.47(1) %
D_{calc} (g cm^{-3})	3.88620(1)	3.8952(7)
Linear abs. coeff. (mm^{-1})	15.0	
R_B (%)	3.38	4.62
R_{wp} (%)	2.99	

The atomic positions and anisotropic atomic displacement parameters for the dominant tetragonal phase at ambient temperature are provided in Table 4.2 and illustrated in Figure 4.9. The (unrefined) structural parameters that were used in the model for the orthorhombic phase are available in Appendix B on the attached Appendix DVD.

The U_{12} atomic displacement parameter for the strontium and oxygen-2 ions refined to negative values, however the overall anisotropic atomic displacement parameters remained positive definite for all atoms as required. The atomic displacement parameters are considerably larger for the oxygen-1 and oxygen-3 ions than the other ions in the structure, however the shape they

produce in Figure 4.9 confirms that these are caused by the rotation of the TiO_5 and SiO_4 polyhedra due to the modulation.

Table 4.2: Atomic positions and atomic displacement parameters (ADP's) for the (main) *X*4*bm* phase, determined from refinement against synchrotron X-ray powder diffraction data collected from $Sr_2TiSi_2O_8$ at ambient temperature.

	Sr	Ti	Si	O1	O2	O3	O4
x	0.32825(4)	0	0.1293(1)	0	0.1271(3)	0.2928(3)	0
y	0.82825	0	0.62931	0.5	0.6271	0.5805(4)	0
z	0.00044(5)	-0.265(2)	-0.2600(3)	-0.3083(5)	-0.0918(3)	-0.3185(2)	-0.0970(5)
U_{11}	0.0330(2)	0.0301(5)	0.0312(6)	0.107(4)	0.025(2)	0.056(3)	0.050(3)
U_{22}	0.0330	0.0301	0.0312	0.107	0.025	0.179(4)	0.050
U_{33}	0.0188(2)	0.017(1)	0.0150(1)	0.010(4)	0.023(2)	0.029(2)	0.009(4)
U_{12}	-0.0140(3)	0	0.0083(7)	0.080(6)	-0.012(2)	0.057(2)	0
U_{13}	0.0006(6)	0	-0.004(1)	0	-0.002(1)	0.013(1)	0
U_{23}	0.0006	0	-0.004	0	-0.002	0.014(2)	0

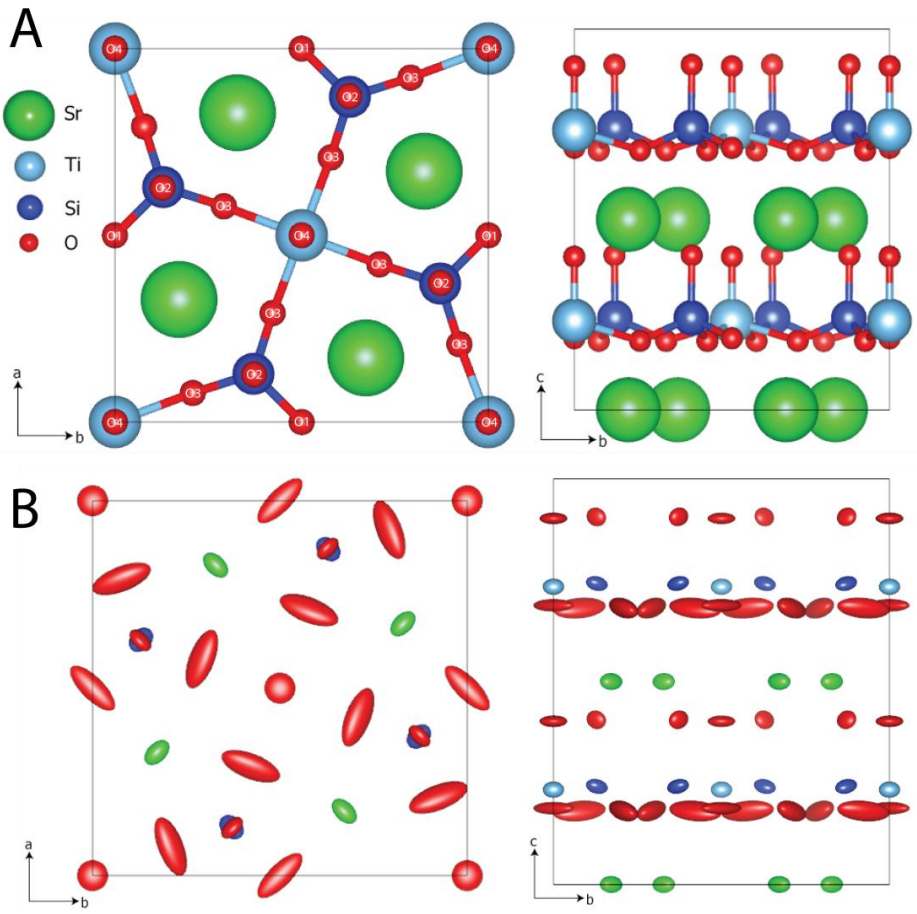

Figure 4.9: $Sr_2TiSi_2O_8$ structure (A) and anisotropic displacement parameters (based on 50 % probability) (B) of the *X*4*bm* phase at ambient temperature as refined against synchrotron X-ray powder diffraction data.

Because a stable model of the $Sr_2TiSi_2O_8$ modulated structure could not be refined against the synchrotron X-ray powder diffraction data, high intensity neutron powder diffraction data were collected using the setup described in section 2.1.3.2 at a wavelength of λ = 2.8639(2) Å.

A single phase *X*4*bm*(α, α, ½)0*gg* model was refined against the high intensity neutron diffraction pattern because no evidence of the orthorhombic phase was present. The refinement of atomic positions and modulation amplitudes for each ion frequently led to the divergence of the model, or chemically implausible results. The inclusion of rigid unit restrictions through the use of "keep geometry-rigid" command in Jana2006 did not sufficiently improve the quality of the fit nor preserve the chemical reasonableness of the model to justify their inclusion. Hence, this approach was abandoned. The modulation amplitudes published by Höche *et al*.[1] were sufficient starting parameters to provide a model that could be successfully refined against the high intensity neutron diffraction data as shown in Figure 4.10. The insert in Figure 4.10 provides an enlarged view of the region of the pattern containing satellite reflections and demonstrates how the intensity corresponding to these reflections has been calculated correctly. The experimental data and important parameters for this refinement are provided in Table 4.3. Note that (satellites-1) and (satellites-2) represent parameters associated with the first ($\mathbf{q_1}$, $\mathbf{q_2}$), and second ($\mathbf{q_1} + \mathbf{q_2}$, $\mathbf{q_1} - \mathbf{q_2}$) order satellites, respectively.

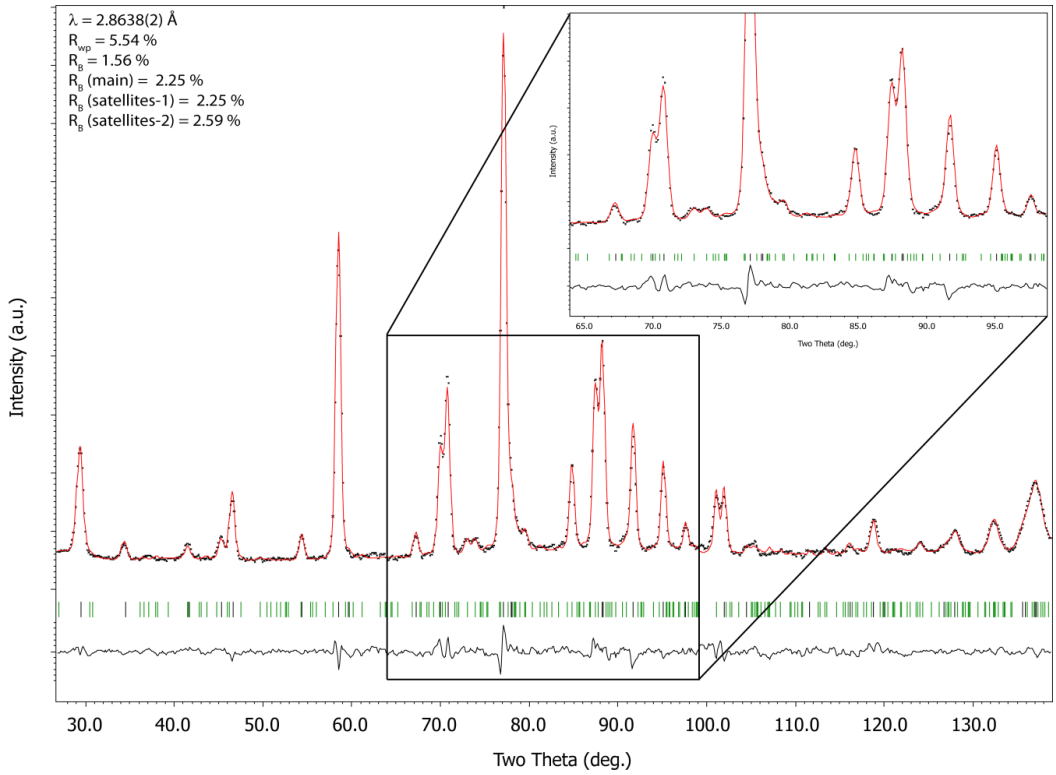

Figure 4.10: Observed, calculated, and difference plots for the refinement of the $Sr_2TiSi_2O_8$ modulated structure at ambient temperature against high intensity neutron powder diffraction data.

Table 4.3: Experimental data and important parameters for $Sr_2TiSi_2O_8$ at ambient temperature as determined by refinement against high intensity neutron powder diffraction data.

Parameter	$Sr_2TiSi_2O_8$
Wavelength (Å)	λ = 2.8638(2)
Molar mass (g mol^{-1})	407.28
Crystal system	Tetragonal
Space group	$X4bm(\alpha, \alpha, 0)0gg$
Z	4
a (Å)	8.3239(2)
c (Å)	10.0529(6)
V (Å^3)	696.54(4)
q_1	0.2617(6)**a*** + 0.2617(6)**b***
q_2	-0.2617(6)**a*** + 0.2617(6)**b***
D_{calc} (g cm^{-3})	3.88254(2)
Linear abs. coeff. (mm^{-1})	0.008226
R_B (%)	1.56
R_B(main) (%)	1.01
R_B(satellites-1 (%))	2.25
R_B(satellites-2) (%)	2.59
R_{wp} (%)	5.54

The atomic positions, displacement parameters, and modulation amplitudes refined for each atom are provided in Table 4.4. The simultaneous refinement of some parameters with the rest of the stable parameters caused divergence and produced implausible results. These parameters are the atomic displacement parameters for the titanium and silicon ions, and the modulation amplitudes for the silicon and oxygen-4 ions. The problematic modulation amplitudes were refined independently, and have been listed in bold in Table 4.4 to reflect that they were not refined in the final model. Isotropic values for the problematic atomic displacement parameters were sourced from the refined values obtained from the refinement against synchrotron X-ray powder diffraction data as listed in Table 4.2. These concessions are unfortunately unavoidable and have been attributed to a limit in the amount of information that can be determined from this neutron powder diffraction experiment.

Table 4.4: Atomic positions, atomic displacement parameters (U_{iso}), and modulation amplitudes determined from refinement against high intensity neutron powder diffraction data collected from $Sr_2TiSi_2O_8$ at ambient temperature. Values in bold were not refined due to their instability during the refinement.

	Sr	Ti	Si	O1	O2	O3	O4
x	0.3294(6)	0	0.134(1)	0	0.125(7)	0.2931(7)	0
y	0.8294	0	0.634	0.5	0.625	0.5793(8)	0
z	0.0041(9)	-0.248(3)	-0.251(1)	-0.303(2)	-0.0858(1)	-0.321(1)	-0.087(2)
U_{iso}(Å²)	0.004(3)	**0.03**	**0.03**	0.083(7)	0.014(1)	0.0318(4)	0.017(5)
x sin 1	0.013(2)	0.008(6)	**-0.00839**	-0.006(4)	-0.002(2)	-0.010(2)	**0.020**
y sin 1	-0.013	-0.007(6)	**0.00839**	0.006	0.002	-0.033(2)	**0.002**
z sin 1	0	0	**0**	0	0	0.002(3)	**0**
x cos 1	-0.007(2)	0	**-0.0066**	0	0.011(2)	0.008(2)	**0**
y cos 1	0.007	0	**0.0066**	0	-0.012(2)	0.018(3)	**0**
z cos 1	0	-0.008	**0**	0	0	0.005(3)	**-0.009**
x sin 2	-0.004(2)	0.007	**-0.02629**	-0.010(4)	0.007(2)	0.009(2)	**-0.002**
y sin 2	-0.004	0.008	**-0.02629**	-0.010	0.007	-0.020(2)	**0.020**
z sin 2	-0.004	0	**-0.003066**	0	0.019(3)	-0.012(2)	**0**
x cos 2	0.005(2)	0	**0.001035**	0	-0.005(2)	0.009(2)	**0**
y cos 2	-0.005	0	**-0.001035**	0	0.005	0.0305(2)	**0**
z cos 2	0	-0.008	**0**	0	0	0.011(3)	**-0.009**

The largest amplitudes of modulation in Table 4.4 occur for the oxygen-3 ions in a similar fashion to the oxygen-3 ions in $Ba_2TiSi_2O_8$. This supports the hypothesis that the bridging oxygen ions experience the greatest deviations as a result of the modulation in the structure. The atomic modulation functions in Figure 4.11 graphically show the large displacements that occur for the oxygen ions due to the modulation. Similarly to the method used in for $Ba_2TiSi_2O_8$ in Chapter 3, these data are plotted for $0 \leq t \leq 1$ and $u = 0$ where t and u represent the atomic displacements along the modulation in the first (**a*** + **b***) and second (-**a*** + **b***) modulation directions, respectively. The $u = 0$ case has been chosen as a representative cross section of the entire $0 \leq u \leq 1$ range.

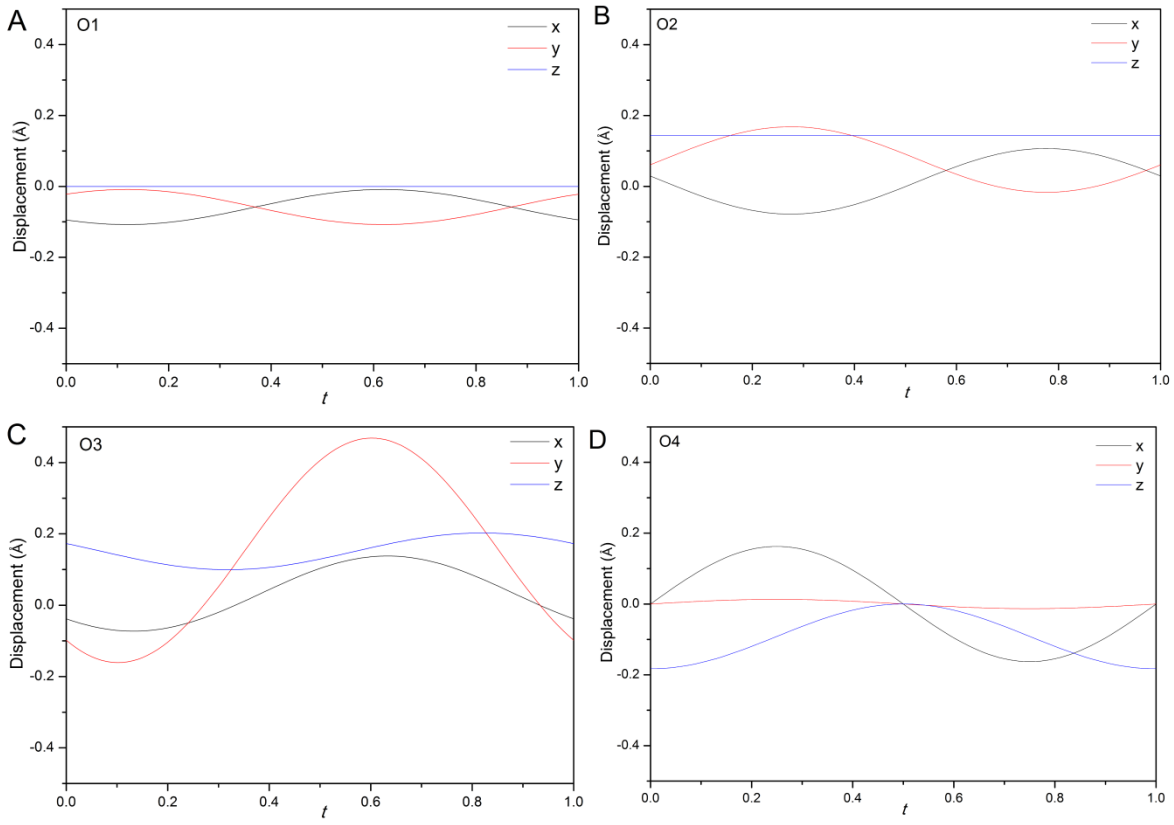

Figure 4.11: Atomic modulation functions showing the displacements of the oxygen-1 (A), -2 (B), -3 (C), and -4 (D) ions respectively for $u = 0$ and $0 \leq t \leq 1$ along the (a* + b*) and (-a* + b*) modulation directions, respectively. The $u = 0$ case has been chosen as a representative cross section of the entire $0 \leq u \leq 1$ range.

The atomic modulation functions showing the variation in the bond valence sum of each ion in the $Sr_2TiSi_2O_8$ structure are provided in Figure 4.12. On average, the introduction of the modulation improves the bonding environment of the strontium, titanium, silicon, and oxygen-4 ions, while the bond valence sum for the oxygen-1, oxygen-2, and oxygen-3 ions are displaced slightly further from their ideal values relative to the average structure. It can also be seen that the largest variations in the bond valence sum are experienced by the oxygen-3 ion, as would be expected after considering the displacement of each ion in Figure 4.11. The modulation amplitudes for the silicon ion could not be refined simultaneously with the other parameters in the model. Hence, it is difficult to determine whether the large variation in the bond valence sum for the silicon is a real feature of the $Sr_2TiSi_2O_8$ modulated structure, or an artefact produced by the limitations of the model.

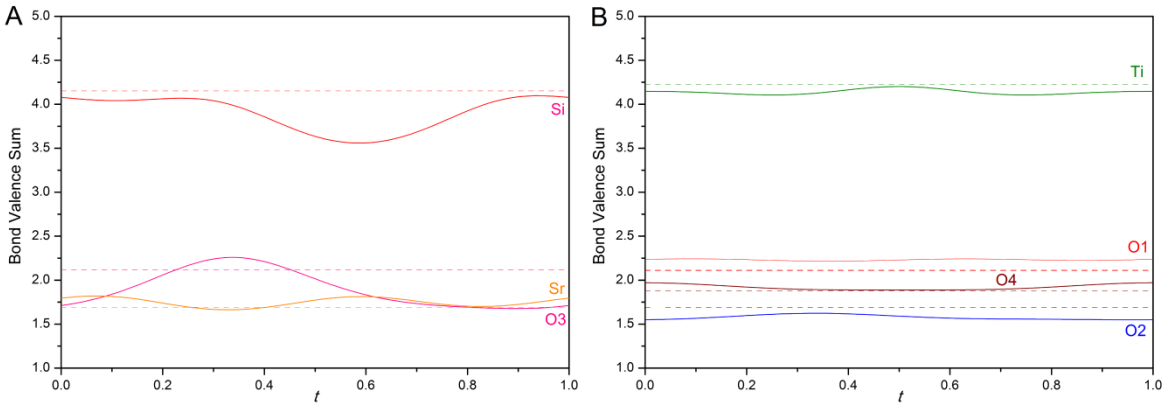

Figure 4.12: Atomic modulation functions showing the variation of the bond valence sum for strontium, silicon, and oxygen-3 (A), and titanium, oxygen-1, oxygen-2, oxygen-4 (B) for $u = 0$ and $0 \leq t \leq 1$ along the (a* + b*) and (-a* + b*) modulation directions, respectively. The $u = 0$ case has been chosen as a representative cross section of the entire $0 \leq u \leq 1$ range.

A 3x3 approximation of the $Sr_2TiSi_2O_8$ modulated structure projected down the *c*-axis is illustrated in Figure 4.13 where the atomic displacements of the oxygen ions suggests that the modulation does not occur in the form of rigid-unit rotations of the TiO_5 and SiO_4 polyhedra about the *c*-axis. This is inconsistent with the proposed theories presented in the literature based on single crystal X-ray diffraction and rigid unit mode calculations.[3,10] This result is a sign that the

level of detail that can be gathered from the powder diffraction data collected in this study is insufficient to retain the rigid unit nature of the structure during refinement.

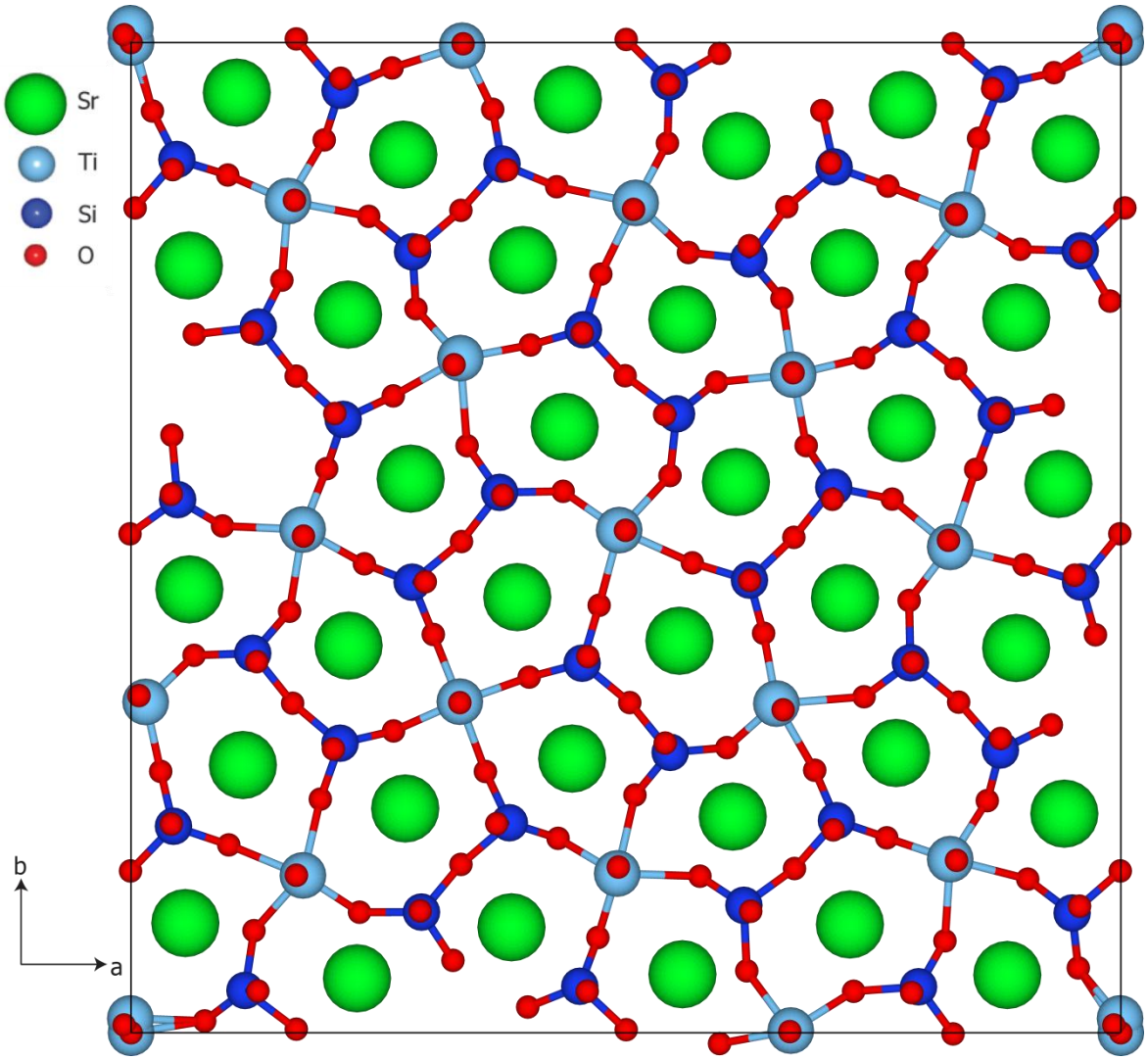

Figure 4.13: A 3x3 projection along the *c*-axis of the refined (3+2)-dimensional modulated structure showing large distortions of the TiO_5 and SiO_4 polyhedra.

4.3.2 High Resolution Imaging and Fast Fourier Transform Calculations

Several high resolution images were collected from $Sr_2TiSi_2O_8$ crystals to further investigate the two phases that are known to be present. Two representative images are provided in Figure 4.14. The resolution achieved in these images is sufficient such that evidence of the ring-like structure formed by the corner sharing TiO_5 and SiO_4 polyhedra can be clearly identified as dark spots

(labelled with red circles) (Figure 4.14A). Figure 4.14B is an image collected down the [100]-direction such that the stacking of layers in the [001]-direction can be easily recognised at an approximately 45 degree angle to the horizontal.

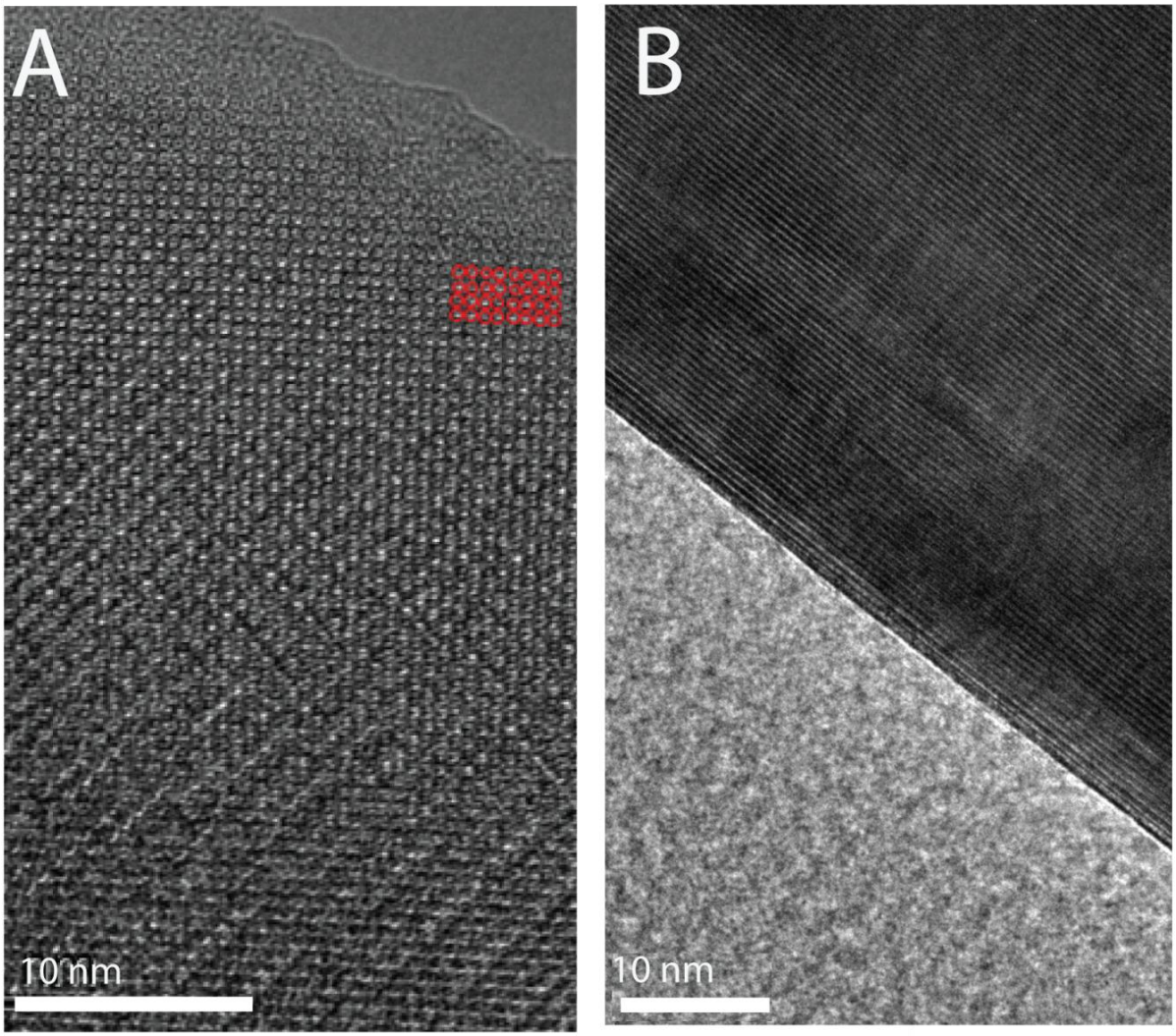

Figure 4.14: High resolution images of $Sr_2TiSi_2O_8$ along the [001]- (A) and [100]- (B) directions at ambient temperature. The red circles in A indicate the evidence of the ring-like structure from the interconnected TiO_5 and SiO_4 polyhedra. The layering of rows of ions in the [001]-direction can be identified at an approximately 45 degree angle to the horizontal in B.

The high resolution images in Figure 4.15 demonstrate that the appearance of $Sr_2TiSi_2O_8$ crystals can vary greatly over small spatial regions. Distinct modulation domain boundaries (as first discussed for $Sr_2TiSi_2O_8$ by Höche *et al.*[1]) can be identified in both images in Figure 4.15, demonstrating how abruptly the structure can change from one phase to another.

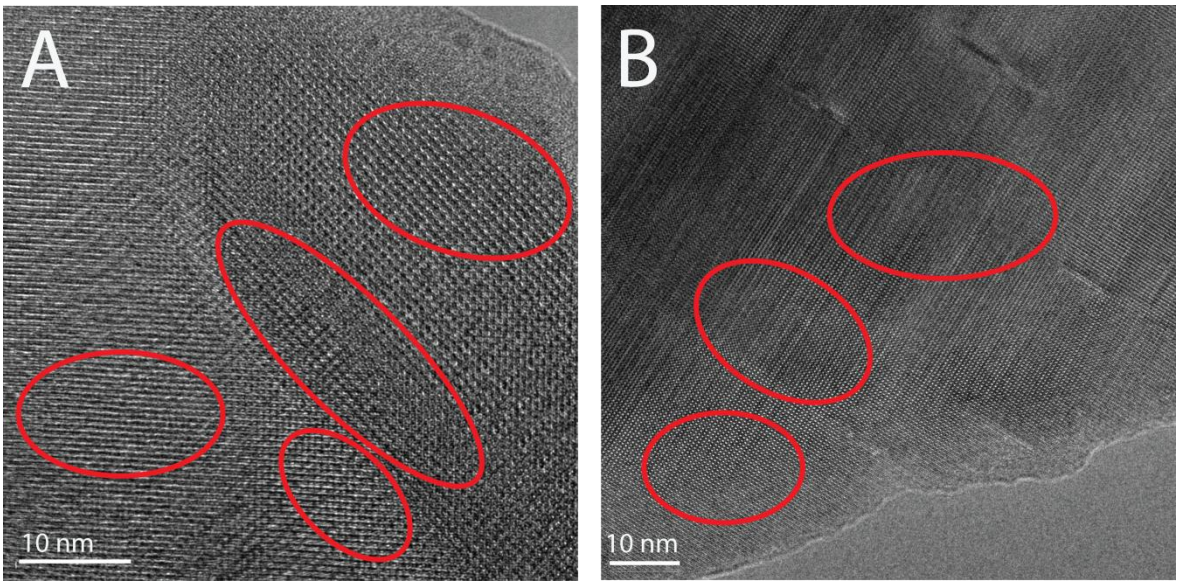

Figure 4.15: High resolution images collected from $Sr_2TiSi_2O_8$ at ambient temperature, where red ellipses identify regions of the crystal that are visually different to each other.

The Fast Fourier Transform (FFT) method was applied to a representative high resolution image collected from a $Sr_2TiSi_2O_8$ crystal (Figure 4.16). The FFT of region (i) produced a pattern that contained satellite reflections in the [100]-, [010]-, and [110]-directions, providing strong evidence that both the tetragonal and orthorhombic modulated phases can be identified from the high resolution images in this region. The FFT calculation of region (ii) produced a pattern that contained satellite reflections in only the [110]-direction, corresponding to only the orthorhombic modulated phase. This neatly demonstrates that information about the different modulated structures is contained in the high resolution images, despite the structural differences between the two phases being extremely small.

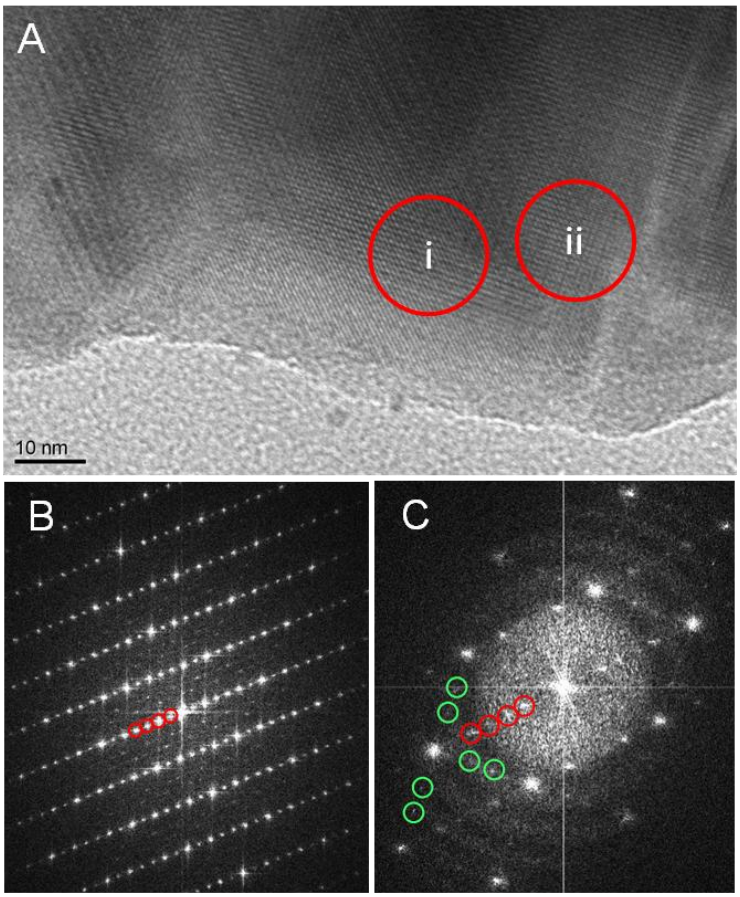

Figure 4.16A) High resolution transmission electron microscopy image collected from $Sr_2TiSi_2O_8$ at ambient temperature. B) Fast Fourier Transform calculations of region (i) and C) (ii), with satellite reflections corresponding to the tetragonal and orthorhombic phases circled in green and red, respectively.

The diffraction pattern (not FFT calculation) collected from a "pure" tetragonal region of the crystal changes after the collection of a high resolution image. This is shown in Figure 4.17 where A and B are patterns collected from the same region of a crystal before and after the collection of a high resolution image, respectively. Before the collection of the high resolution image (A), satellites were initially observed only in the [100]- and [010]-directions. However, after the collection of the high resolution image, satellite reflections are also observed in the [110]-direction, suggesting that part of the sample has transformed from the tetragonal to the orthorhombic phase. Hence, the appearance of the new satellite reflections occurs as direct consequence of exposure to increased intensity required for the collected of high resolution images. This can be attributed to beam damage or the additional heat directed towards the sample under these conditions.

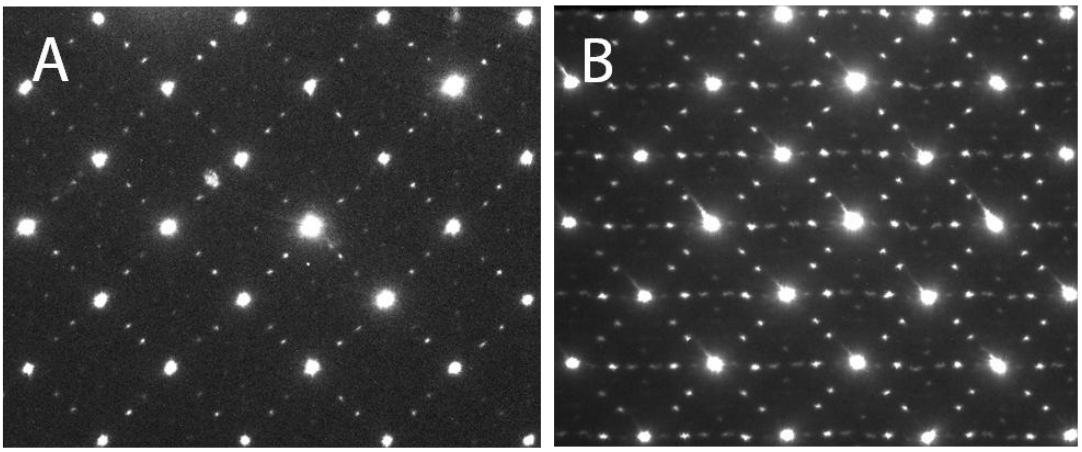

Figure 4.17: Electron diffraction patterns collected from an identical region of the $Sr_2TiSi_2O_8$ crystal A) before, and B) after the collection of a high resolution image.

An additional electron diffraction pattern was also collected on a nearby region which had been previously shown to exhibit the tetragonal phase (Figure 4.18). The presence of satellite reflections in only the [100]- and [010]-directions confirmed that this region had not undergone a phase transition and the change in structure is localised to only the region of the crystal that was exposed to the additional energy from the beam used for the collection of the high resolution image.

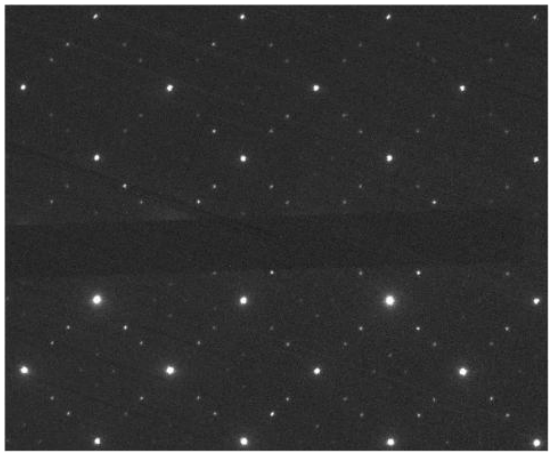

Figure 4.18: Electron diffraction pattern collected from a region of the $Sr_2TiSi_2O_8$ crystal that has not been exposed to the increased beam intensity associated with the collection of a high resolution image.

The ability to induce a structural phase transition through the collection of a high resolution image suggests that the energy of the beam is sufficient to convert at least part of the tetragonal phase region into the orthorhombic phase. The ease with which the transition between these two phases can be driven suggests that a temperature-dependent study of the $Sr_2TiSi_2O_8$ structure may provide more information about the nature of the two incommensurately modulated phases and their thermal behaviour. The following section uses a variety of techniques to investigate this behaviour at non-ambient temperatures for the first time.

4.3.3 $Sr_2TiSi_2O_8$ structure at non-ambient temperatures

4.3.3.1 Transmission electron microscopy

In situ electron diffraction patterns were collected between ambient temperature and 543 K on the crystallite in Figure 4.4 to monitor the position of the satellite reflections on heating, and determine whether any further information could be gathered about the behaviour of the two known phases. The *in situ* sample heating attachment was a Gatan double-tilt furnace holder for the JEOL JEM-2011 TEM. Electron diffraction patterns were collected on a region of the crystallite that exhibited strong satellite reflections in the [100]- and [010]-directions (corresponding to the tetragonal phase) and very weak satellite reflections in the [110]-direction (corresponding to the orthorhombic phase) at 323 K, 473 K, 498 K, 543 K, and at 296 K after cooling (Figure 4.19).

No significant change was observed in the relative intensity of the satellite reflections in either crystallographic direction between 323 K - 473 K. However, the appearance of satellite reflections in the [110]-direction in the electron diffraction pattern collected at 498 K provided evidence that at least part of the region under investigation had undergone a phase transition between 473 K - 498 K. The decrease in the intensity of the satellite reflections in the [100]- and [010]-directions and the increase in intensity in the [110]-direction at 543 K suggests that the

phase transition is almost complete. No diffraction patterns were collected at higher temperatures because the heating stage was incapable of safely and accurately maintaining temperatures higher than ~543 K. Hence, variable temperature electron diffraction was useful for confirming that a structural phase transition exists above ambient temperature, but could not be used to determine whether the tetragonal phase could be completely be removed at higher temperatures.

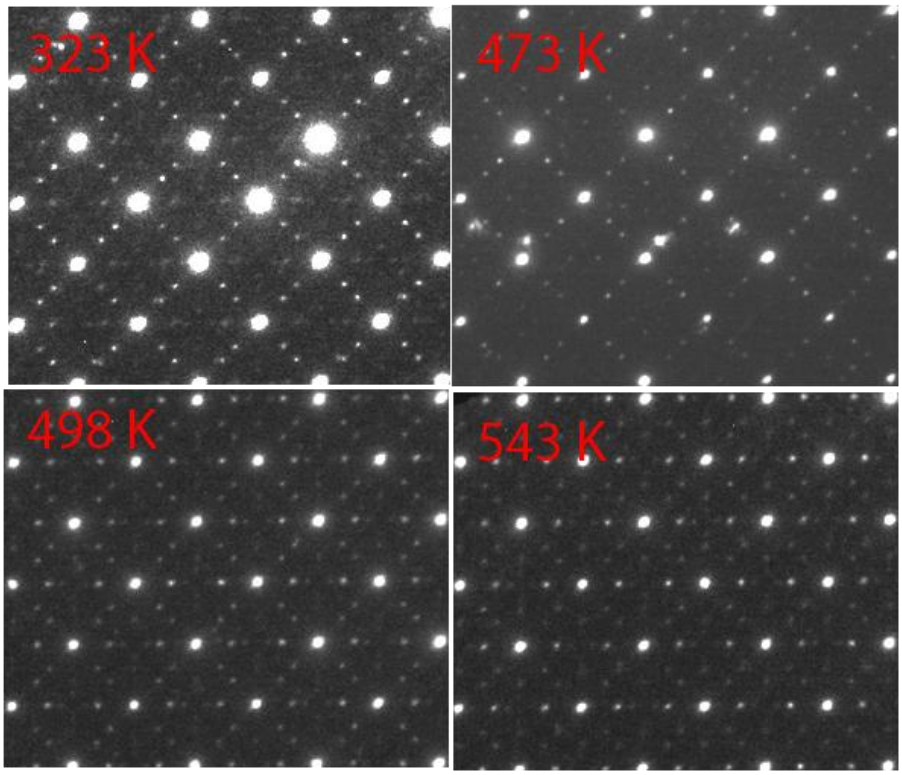

Figure 4.19: Electron diffraction patterns collected from $Sr_2TiSi_2O_8$ at 323 K, 473 K, 498 K, and 543 K where the intensity of the satellite reflections corresponding to the tetragonal and orthorhombic phases decreases and increases on heating, respectively.

Figure 4.20 shows an additional electron diffraction pattern that was collected from the same region of the crystallite from Figure 4.19 at ambient temperature after natural cooling from 543 K over approximately 45 minutes. The re-appearance of satellite reflections in the [100]- and [010]-directions suggests that the $Sr_2TiSi_2O_8$ structure has returned to a state that exhibits both of the tetragonal and orthorhombic phases after cooling. The position of the weak satellite reflections corresponding to the orthorhombic phase have also changed their direction from the

[110]-direction in the previous low temperature phase to the $\bar{1}10$ direction in the newly formed low temperature phase, demonstrating that the direction of the modulation can randomly adopt one of the two possible perpendicular orthorhombic directions in the *a*-*b* plane.

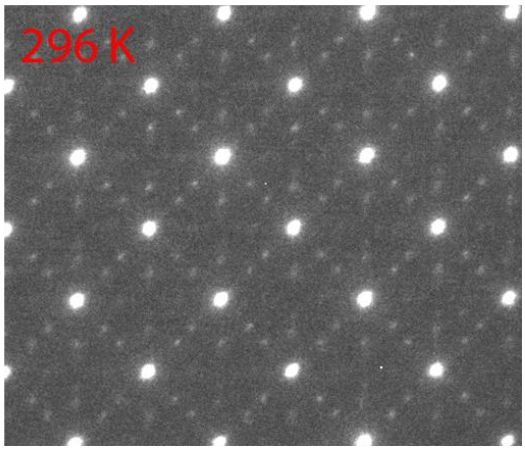

Figure 4.20: Electron diffraction pattern collected from $Sr_2TiSi_2O_8$ at 296 K after heating to 548 K where satellite reflections corresponding to both phases are present.

The confirmation of a thermally-induced structural phase transition using variable temperature electron diffraction was a good starting point in the investigation of the $Sr_2TiSi_2O_8$ phase behaviour. However, in order to perform a more comprehensive study of the transition from the tetragonal to the orthorhombic phase, further diffraction studies on bulk $Sr_2TiSi_2O_8$ samples were required.

4.3.3.2 Synchrotron X-ray diffraction

Variable temperature synchrotron X-ray powder diffraction patterns were collected from $Sr_2TiSi_2O_8$ between 125 K - 1373 K to build an understanding of the changes that may occur in the $Sr_2TiSi_2O_8$ structure over this temperature range. As shown for the sample investigated using synchrotron X-ray diffraction at ambient temperature, the lack of intensity corresponding to satellite reflections meant that only the average structure could be determined. Data were collected using the cryostream attachment, hot air blower attachment, and Pt-strip furnace

attachments using the experimental setups described in section 2.1.2.1 to ensure that a large range of temperatures could be investigated. The range of set point temperatures, step sizes, and wavelengths used for this experiment are summarised in Table 4.5.

Table 4.5: Summary of set point temperature ranges, steps sizes, and wavelengths used for the collection of variable temperature synchrotron X-ray diffraction data.

Set-point Temperature Range	Step Size	Attachment	Wavelength
125 K - 450 K	25 K	Cryostream	λ = 0.8261(1) Å
300 K - 567 K	25 K	Hot air blower	λ = 1.1587(1) Å
567 K - 1480 K	50 K	Hot air blower	λ = 1.1587(1) Å
1148 K - 1250 K	25 K	Hot air blower	λ = 1.1587(1) Å
1223 K - 1373 K	50 K	Pt-strip furnace	λ = 1.1587(1) Å

The diffraction patterns from this experiment are shown in Figure 4.21, demonstrating that significant structural changes occur between 125 K - 1373 K. Data collected at λ = 0.82703(1) Å have been converted to λ = 1.1587(1) Å for the purpose of directly comparing the patterns that were collected at different wavelengths in this figure. The signal to noise ratio for the data collected using the hot air blower attachment is much lower than for the other attachments due to the reduced beam width required to ensure that the volume of sample diffracting the X-rays is at the desired temperature. The temperatures quoted for the data collected using the hot air blower have been calibrated using a procedure recommended by the beamline scientists to correct for the systematic error between the temperature recorded at the thermocouple and the actual sample temperature.

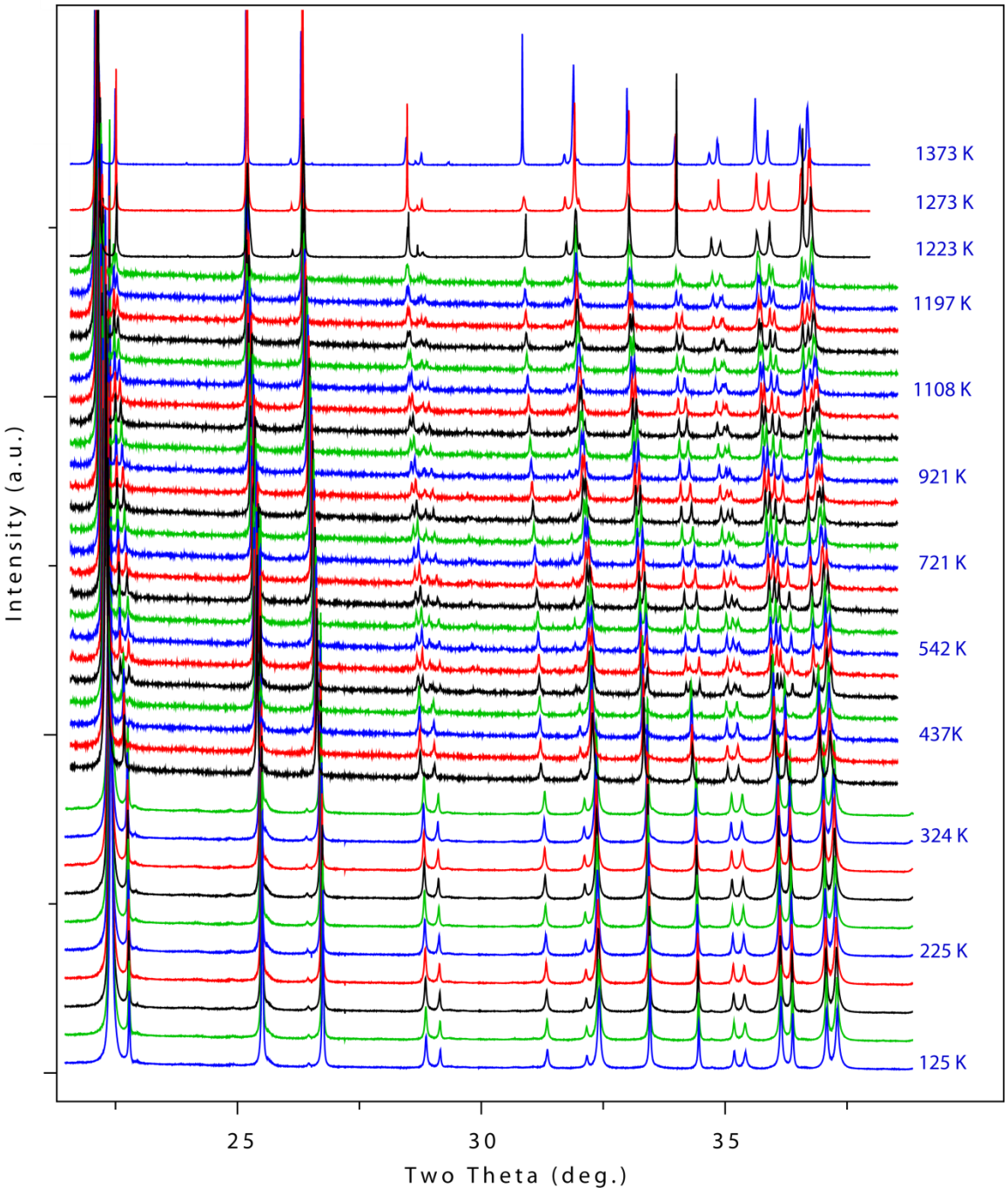

Figure 4.21: Synchrotron X-ray powder diffraction patterns collected from $Sr_2TiSi_2O_8$ between 125 K - 1373 K. Note that the temperatures quoted are the calibrated temperatures instead of the set point temperatures. Step sizes (based on set point temperatures) are quoted in Table 4.5.

A close up of the 22° ≤ 2θ ≤ 30° region between 125 K - 542 K is provided in Figure 4.22 where the red asterisk identifies the 240 reflection at 25.6° that corresponds to the orthorhombic phase. The presence of this weak reflection at and above 125 K means that the orthorhombic phase persists in a very small proportion below ambient temperature. The intensity of this and other

reflections corresponding to the orthorhombic phase increases at approximately 490 K. For example, the black asterisks identify the 400 and 040 reflections at approximately 22.7° two theta and the 422 and 242 reflections at approximately 28.8° two theta that begin to increase in intensity at approximately 490 K. These observations are the first to provide evidence that the orthorhombic phase is present at and below ambient temperature, in addition to showing that the proportion of this phase increases on heating. This is also consistent with the conclusions drawn from the electron diffraction experiment whereby the tetragonal phase was shown to coexist with the orthorhombic phase at ambient temperature before converting into the orthorhombic phase on heating.

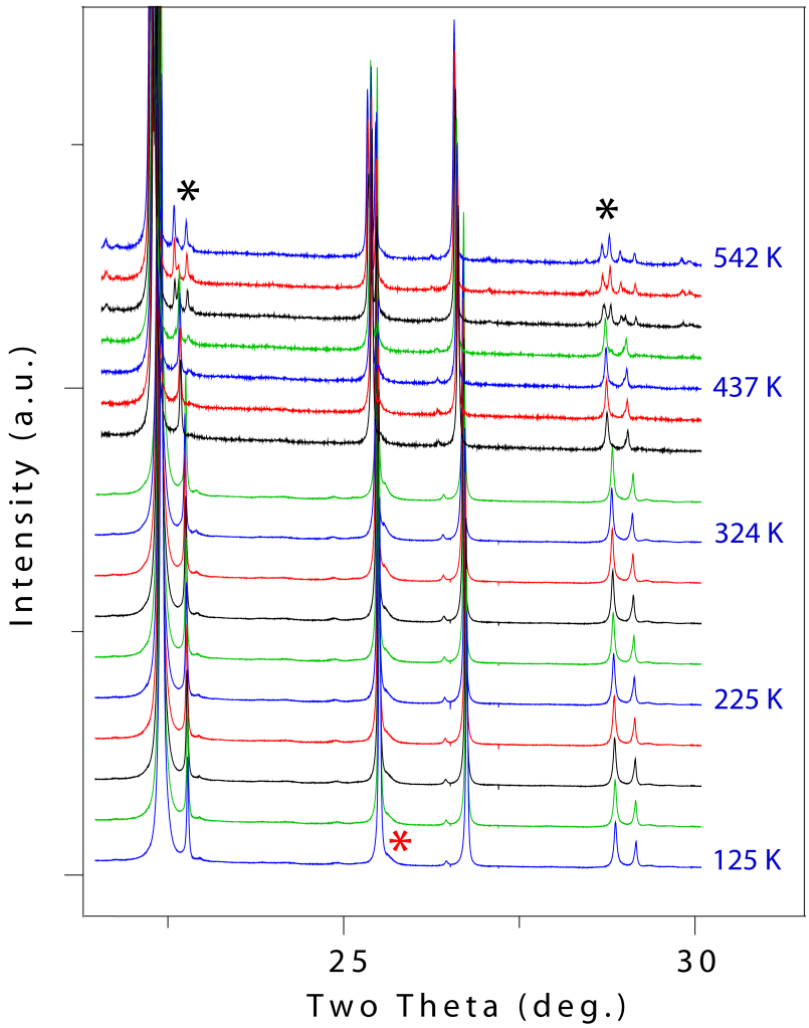

Figure 4.22: A close up view of the 22° ≤ 2θ ≤ 30° region between 125 K - 542 K where the red asterisk indicates the evidence for the orthorhombic phase at 125 K. The black asterisks indicate reflections that appear in the patterns as the proportion of the orthorhombic phase increases on heating.

The orthorhombic phase was not included in the Rietveld refinement models below ambient temperature due to an insufficient amount of intensity in the reflections corresponding to this phase. Hence, single phase *X*4*bm*(α, α, ½)*0gg* models were refined against the X-ray diffraction data between 125 K - 275 K, and two phase models containing both the tetragonal and orthorhombic phases were refined against all patterns that contained sufficient contributions from both phases (425 K - 500 K). By 567 K, no evidence of the *X*4*bm* phase was observed, suggesting that the transition from the tetragonal to orthorhombic phase had reached completion.

Only the atomic positions and atomic displacement parameters for the dominant phase were refined in each model. This is because the insufficient intensity in the reflections corresponding to the orthorhombic phase led to unreasonable bond distances and hence produced chemically implausible results. Although leaving these parameters unrefined for the minor phase is not ideal, the difficulties are understandable when considering how little of the orthorhombic phase is present below 437 K and the high degree of reflection overlap from the two phases between 437 K - 490 K.

The orthorhombic phase was modelled using a single phase model with the *Cmm*2 space group for temperatures between 567 K - 1273 K. The experimental data and important parameters for the refinement of the orthorhombic phase at 567 K are provided in Table 4.6. The refined atomic positions and atomic displacement parameters are provided in Figure 4.6, and the structure is illustrated in Figure 4.23. The structural parameters for all models refined against the synchrotron X-ray powder diffraction data collected from $Sr_2TiSi_2O_8$ between 125 K - 1373 K are provided in Appendix B of the attached Appendix DVD.

Table 4.6: Experimental data and important parameters for $Sr_2TiSi_2O_8$ at 567 K as determined by refinement against synchrotron X-ray powder diffraction data.

Parameter	$Sr_2TiSi_2O_8$
Wavelength (Å)	λ = 1.15864(1)
Molar mass (g mol^{-1})	407.28
Crystal system	Orthorhombic
Space group	*Cmm*2
Z	4
a (Å)	11.74251(6)
b (Å)	11.82907(6)
c (Å)	5.04202(3)
V ($Å^3$)	700.352(1)
D_{calc} (g cm^{-3})	3.86144(5)
Linear abs. coeff. (mm^-	14.9
R_B (%)	9.02
R_{wp} (%)	4.33

Table 4.7: Atomic positions and atomic displacement parameters (ADP's) determined from refinement against synchrotron X-ray powder diffraction data collected from $Sr_2TiSi_2O_8$ at 567 K.

	x	y	z	U_{iso}
Sr1	0	0.3279(1)	0	0.0375(5)
Sr2	0.1711(1)	0	0	0.0389(5)
Ti	0.25	0.25	0.4575(6)	0.0273(6)
Si1	0	0.1286(3)	0.463(1)	0.040(1)
Si2	0.3706(3)	0	0.475(1)	0.017(1)
O1	0.1082(6)	0.1907(6)	0.362(1)	0.057(2)
O2	0	0	0.374(2)	0.039(4)
O3	0.3116(7)	0.0987(7)	0.386(2)	0.104(3)
O4	0.5	0	0.408(3)	0.072(6)
O5	0	0.1275(7)	0.820(2)	0.015(2)
O6	0.3694(7)	0	0.832(2)	0.014(2)
O7	0.25	0.25	0.805(2)	0.064(3)

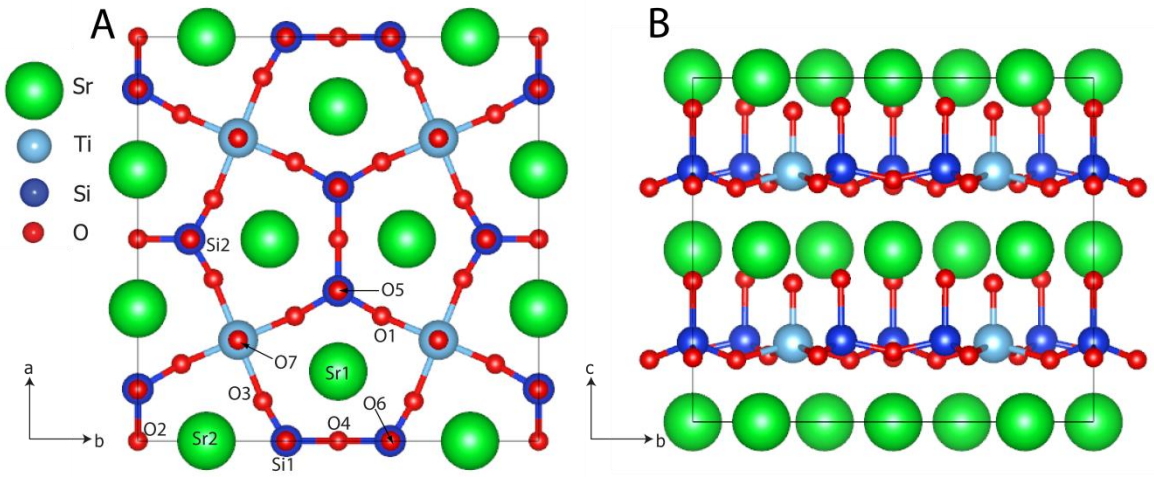

Figure 4.23: Orthorhombic $Sr_2TiSi_2O_8$ structure projected along the [001]- (A) and [100]-directions at 567 K as refined against synchrotron X-ray powder diffraction data.

The reflections that split during the tetragonal to orthorhombic phase transition (*e.g.* the 132 and 312 reflections at 22° two theta) recombine at approximately 1323 K. A single phase *X*4*bm* model successfully described the data collected between 1323 K - 1373 K, showing that a second phase transition occurs from the orthorhombic to the tetragonal phase on heating.

The *a*, *b*, and *c* unit cell parameters for both phases of $Sr_2TiSi_2O_8$ between 125 K - 1373 K are plotted in Figure 4.24, where the *a*, *b*, and *c* unit cell parameters for the orthorhombic phase have been converted into the tetragonal setting to allow direct comparison between the two phases. The line of best fit for cell parameter *a* of the tetragonal phase is plotted between 542 K - 1273 K as a_0 which will be used in the coming discussion of spontaneous orthorhombic strain across the phase transitions. Tables of the structural data including unit cell parameters, atomic positions, and atomic displacement parameters from the variable temperature study are included in Appendix B on the attached Appendix DVD.

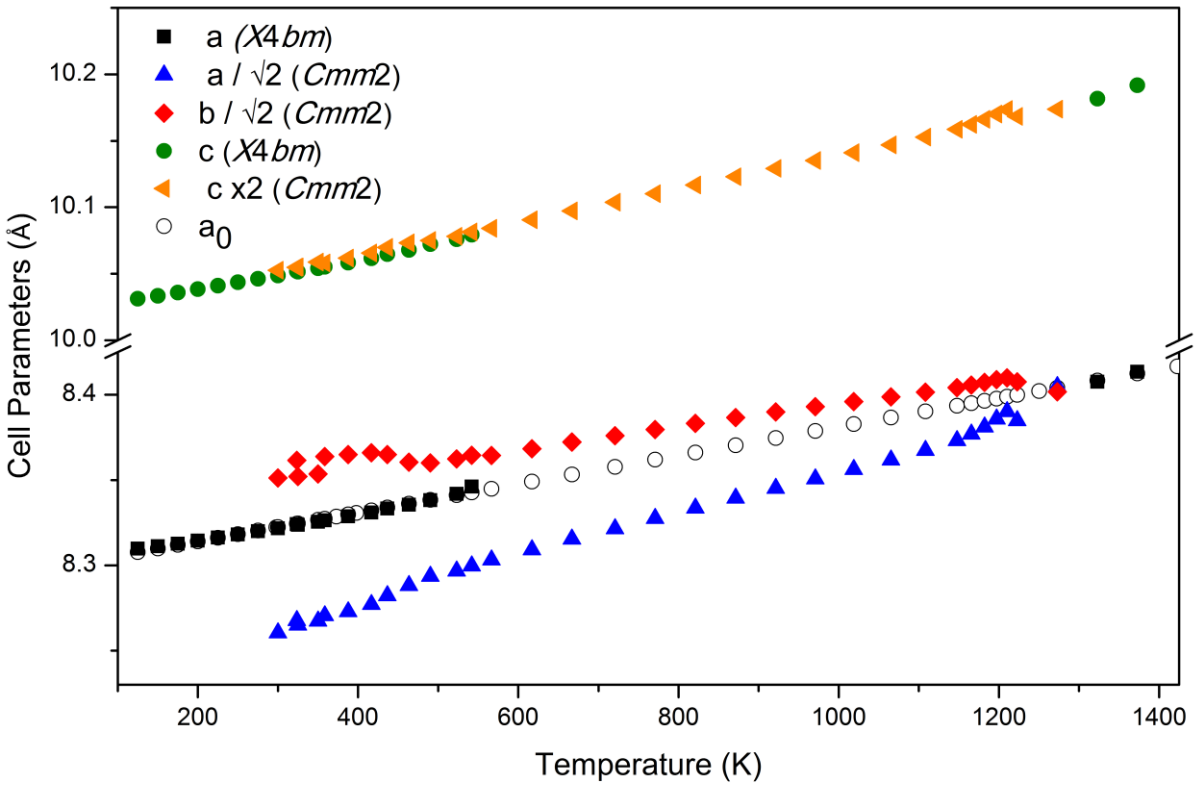

Figure 4.24: Unit cell parameters *a*, *b*, and *c* for the $Sr_2TiSi_2O_8$ *Cmm*2 phase, and unit cell parameters *a* and *c* for the *X*4*bm* phase between 125 K - 1373 K. Unit cell parameters *a* and *b* for the *Cmm*2 phase have been converted to the tetragonal setting to allow for direct comparison with the *X*4*bm* phase. Hollow circles represent the line of best fit for the tetragonal unit cell parameters (a_0).

The presence of the two phase transitions in Figure 4.24 means that the $Sr_2TiSi_2O_8$ phase diagram contains a mixture of the tetragonal and orthorhombic phases at low temperatures which convert into a single orthorhombic phase until further heating induces another phase transition to a single tetragonal phase. Although this behaviour is atypical of conventional phase transitions, there are several examples of compounds that display similar phase behaviour. A summary of these compounds has been provided in Table 4.8. Two examples of compounds that exhibit only the symmetry lowering phase transition without an additional transition to a higher symmetry phase have also been included.

Table 4.8: Compounds that have been reported to show symmetry reducing phase transitions on heating. Transition temperatures are provided for each phase transition. LT = Low Temperature, HT = High Temperature.

	$Ba_2NaNb_5O_{15}$[11]	$La_{2-x}Ba_xCuO_4$ $(0.05 \leq x \leq 0.15)$[1,2-14]	Rochelle salt $KNa(C_4H_4O_6) \cdot 4H_2O$[15]	NaOH[16]	$PbRuO_3$[17]	NaSn[18]
LT Space Group	P4nc	I4/mmm	$P2_12_12$	Cmcm	Imma	$I4_1/acd$
LT Transition Temperature	110 K	~50 K	~250 K	535 K	90 K	757 K
Intermediate Space Group	$Ccm2_1$	Bmab	$P2_1$	$P2_1/m$	-	-
HT Space Group	P4bm	$P4_2/ncm$	$P2_12_12$	Fm3m	Pnma	Fddd
HT Transition Temp	565 K	300 K	~300 K	578 K	-	-
Additional Notes	Two incommensurate phases coexist between 547 K - 582 K	Superconductor. Significant change in physical properties at phase transitions. Soft-mode phonon instability drives transition.	Piezoelectric. Order-disorder transition.	-	Ferromagnetic. Hybridisation of electron orbitals changes the symmetry of the ground state.	Order-disorder transition.

Two of the compounds in Table 4.8 are of particular interest. Firstly, it was mentioned in section 4.3.1 that transmission electron microscopy has been used to show that $Ba_2NaNb_5O_{15}$ samples contain two coexisting incommensurately modulated phases. Other work has shown that $Ba_2NaNb_5O_{15}$ also displays six phase transitions between 4 K - 850 K.[19-21] Similarly to $Sr_2TiSi_2O_8$, one of these transitions is a symmetry lowering transition on heating, involving the tetragonal *P4nc* phase transforming into an orthorhombic $Ccm2_1$ phase at approximately 110 K.[20,22] The structure also transforms into the higher symmetry *P4bm* space group on continued heating to approximately 565 K.[11] Single crystal X-ray diffraction has also been used to show that the coexistence region of the two phases occurs between approximately 530 K - 570 K.[22] $Ba_2NaNb_5O_{15}$ therefore displays similarities to $Sr_2TiSi_2O_8$ in the form of the coexistence of the two incommensurately modulated phases and the symmetry lowering transition on heating followed by an additional transition to the higher symmetry space group. However, $Sr_2TiSi_2O_8$ contains both phases over a significantly larger range of temperatures.

The second compound of interest in Table 4.8 is $PbRuO_3$, whereby the low temperature *Imma* phase transforms into a lower symmetry *Pnma* phase on heating. $PbRuO_3$ is relevant to the discussion of $Sr_2TiSi_2O_8$ because the low temperature *Imma* phase contains an unusual *A*-site distortion which produces a near-regular square pyramidal coordination with five short Pb-O bonds. Hence, both $Sr_2TiSi_2O_8$ and $PbRuO_3$ both contain square pyramidal geometries in their structure. The unusual lowering of symmetry on heating was discussed in terms of coupling of electron localisation to the lattice through Ru-orbital ordering, and it was proposed that the strong hybridisation of the Ru 4*d* with Pb 6*s* and 6*p* states are responsible for inducing the alternative (lower symmetry) ground state.[17] Although the high and low symmetry phases of $PbRuO_3$ do not coexist, the reasoning for the transition may be relevant to the discussion of $Sr_2TiSi_2O_8$ because the role of the square pyramidal coordination environment in $PbRuO_3$ and $Sr_2TiSi_2O_8$ may play an important role in the required orbital hybridisation to produce the high symmetry ground state structure that inverts the usual group-subgroup symmetry relationship between the two phases. However, understanding this complex behaviour for $Sr_2TiSi_2O_8$ would require a very thorough investigation that incorporates the changes in the incommensurately modulated phases and their effect on the free energy in the system as the compound is heated. Such a study is well beyond the scope of the current project. Once it was established that a symmetry lowering transition on heating was not necessarily a unique observation, the nature of the phase transitions were investigated further. The phase transitions for $Sr_2TiSi_2O_8$ will now be discussed.

On heating from 125 K - 464 K, the only change in the X-ray diffraction patterns corresponds to conventional thermal expansion. Heating above 464 K induces changes in the sample where the proportion of the orthorhombic phase increases until complete phase conversion has occurred by 567 K. Figure 4.25 shows the calculated proportion of each phase from Rietveld refinement against the data collected between 125 K - 850 K, demonstrating how the rate of conversion from the tetragonal to the orthorhombic phase rapidly increases between 542 K - 567 K. The

coexistence of both phases below the transition temperature also indicates that transition is of the discontinuous first order type.

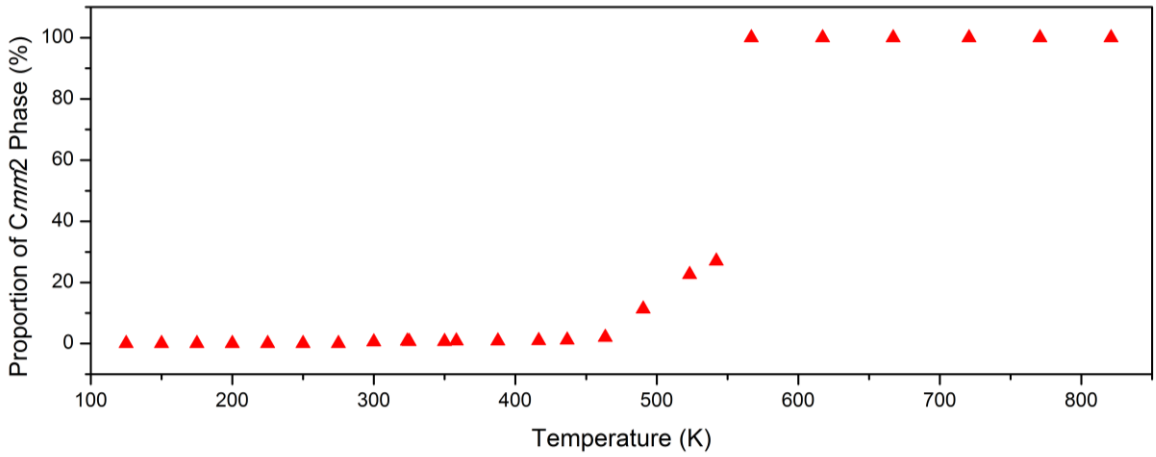

Figure 4.25: Percentage of the proportion of the *Cmm*2 phase relative to the *X*4*bm* phase present for $Sr_2TiSi_2O_8$ between 125 K- 850 K.

The increase in the intensity of the 240 reflection corresponding to the orthorhombic phase in Figure 4.22 at 25.6° on heating from 125 K suggests that the phase conversion slowly occurs as the sample is heated from 125 K, and that the rate of this conversion rapidly increases as the temperature approaches 567 K. The absence of the tetragonal phase in the diffraction patterns at 567 K leads to the conclusion that the first order transition from the mixture of the tetragonal and orthorhombic phases to the single orthorhombic phase has reached completion.

Further heating above 567 K continues the thermal expansion of the orthorhombic phase in a manner that linearly deceases the orthorhombic strain as the structure approaches the phase transition to the tetragonal phase at approximately 1323 K. The collection of additional diffraction patterns between 1273 K - 1373 K using the Pt-strip furnace attachment was necessary to investigate the structure above the maximum limit of the hot air blower attachment of 1273 K. The additional data collected using the Pt-strip attachment demonstrated that the strain drops to zero as the structure re-adopts the tetragonal setting. However, the change in heating attachments introduces the potential for a discrepancy in the measured temperatures.

The samples mounted on the Pt-strip furnace contained significant preferred orientation due to the possible growth of small $Sr_2TiSi_2O_8$ crystallites on the surface of the Pt-strip at high temperatures. The preferred orientation in these patterns produced large fluctuations in the relative intensity of the reflections, meaning that reliable models could not be refined against these data. However, these data served their purpose of confirming that the reflections that appeared to be converging up to 1250 K in the data collected from the hot air blower did so by 1323 K on the Pt-strip furnace.

The spontaneous strain was calculated for the orthorhombic phase using the unit cell parameters determined from synchrotron X-ray powder diffraction. Spontaneous strain is correlated to the order parameter, Q, allowing more information about the nature of the transition to be determined. The orthorhombic spontaneous strain (e_{ortho}) is calculated by determining the difference between e_1 and e_2 which represent the strain of the *a* and *b* unit cell parameters of the orthorhombic phase, respectively, relative to the equivalent tetragonal unit cell parameter *a* under the same conditions (a_0). The nomenclature used to represent these values for thermally induced phase transitions is $e_1(T)$, $e_2(T)$, and $e_{ortho}(T)$, which represent the orthorhombic strain of the unit cell parameters *a*, and *b*, and difference between e_1 and e_2 as a function of temperature, respectively. $e_1(T)$, $e_2(T)$, and $e_{ortho}(T)$ are defined mathematically in Equation 4.4 and Equation 4.5.[23,24]

$$\boldsymbol{e_1(T) = \frac{a_{ortho}(T) - a_0(T)}{a_0(T)} \quad , \quad e_2(T) = \frac{b_{ortho}(T) - a_0(T)}{a_0(T)}} \qquad \textbf{Equation 4.4}$$

$$\boldsymbol{e_{ortho}(T) = [e_2(T) - e_1(T)]} \qquad \textbf{Equation 4.5}$$

Because the orthorhombic phase of $Sr_2TiSi_2O_8$ has a unit cell that is a multiple of the parent tetragonal unit cell and its development relates to points in the Brillouin zone which are away from the gamma point, it is an improper ferroelastic phase that has $e_{ortho} \propto Q^2$.[24] It should be noted

that the letter Q is also used to represent the mechanical quality factor as calculated from RUS experiments. Clarification of the use of Q in this thesis is provided where relevant.

The e_{ortho} strain parameter for $Sr_2TiSi_2O_8$ was calculated from the refined unit cell parameters of the orthorhombic phase and plotted between 300 K - 1250 K in Figure 4.26. The decrease in e_{ortho} (proportional to Q^2) does not linearly approach zero as the structure approaches the high temperature phase transition, providing evidence that the transition is not displaying second order behaviour.

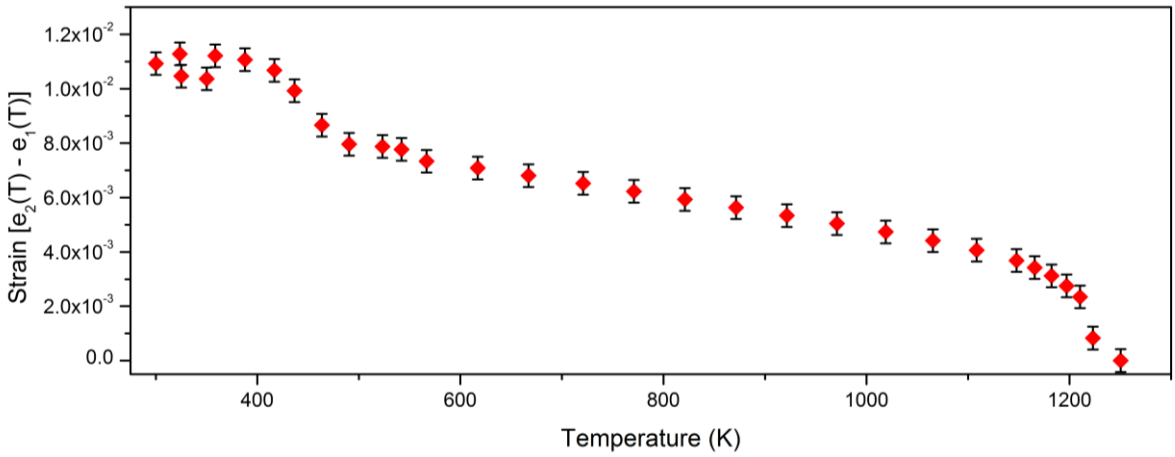

Figure 4.26: Orthorhombic strain in the $Sr_2TiSi_2O_8$ structure between 300 K - 1250 K, providing evidence that the high temperature phase transition does not display second order behaviour.

e_{ortho}^2 (proportional to Q^4) is plotted in Figure 4.27 where there are changes in the strain behaviour at approximately 500 K and 1150 K as the structure approaches both phase transitions. However, it should be noted that the experimental uncertainties associated with the very small numbers calculated for e_{ortho}^2 are significantly larger than the data points themselves. Although the reduction of e_{ortho}^2 may be within error of a linear trend, the high level of experimental uncertainty prevents any formal conclusions to be drawn about the type of transitions observed.

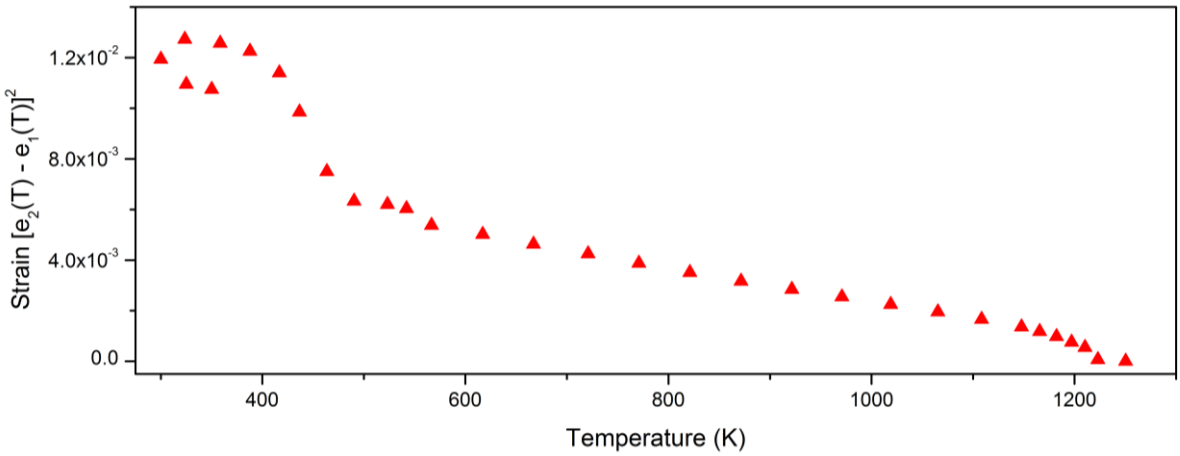

Figure 4.27: Square of the orthorhombic strain in the $Sr_2TiSi_2O_8$ structure between 300 K - 1250 K. Note that the experimental uncertainty in the determination the very small strain values is larger than the values themselves.

Although the potential for a modulation in the $Sr_2TiSi_2O_8$ structure above 1323 K cannot be reliably investigated, it is likely that the structure adopts the prototypic tetragonal structure at high temperature as has been shown for $Ba_2TiSi_2O_8$ at 433 K by Markgraf *et al.*[25] and suggested for $Ba_2TiGe_2O_8$ at 1073 K by Höche *et al.*[3] Further evidence supporting this conclusion will be presented in the discussion of the phase transitions identified in the $Ba_{2x}Sr_{2-2x}TiSi_2O_8$ system in section 6.2.1.2.

Variable temperature high intensity neutron diffraction data were collected from a $Sr_2TiSi_2O_8$ sample during heating and cooling at 2.5 K intervals between 275 K - 600 K as shown in Figure 4.28. A significant reduction in the intensity of the 748 reflection at approximately 95° two theta is observed at 480 K until two reflections are clearly visible when the transition reaches completion at 500 K. The onset temperature for the increased rate of phase conversion as determined from the neutron diffraction experiment is 62 K lower than the temperature determined from the synchrotron experiments (*c.f.* 480 K versus 542 K from neutron and synchrotron X-ray powder diffraction, respectively) and the completion temperatures from the

neutron experiment is 67 K lower than the value determined from the synchrotron experiment (*c.f.* ~500 K versus 567 K from neutron and synchrotron X-ray powder diffraction, respectively).

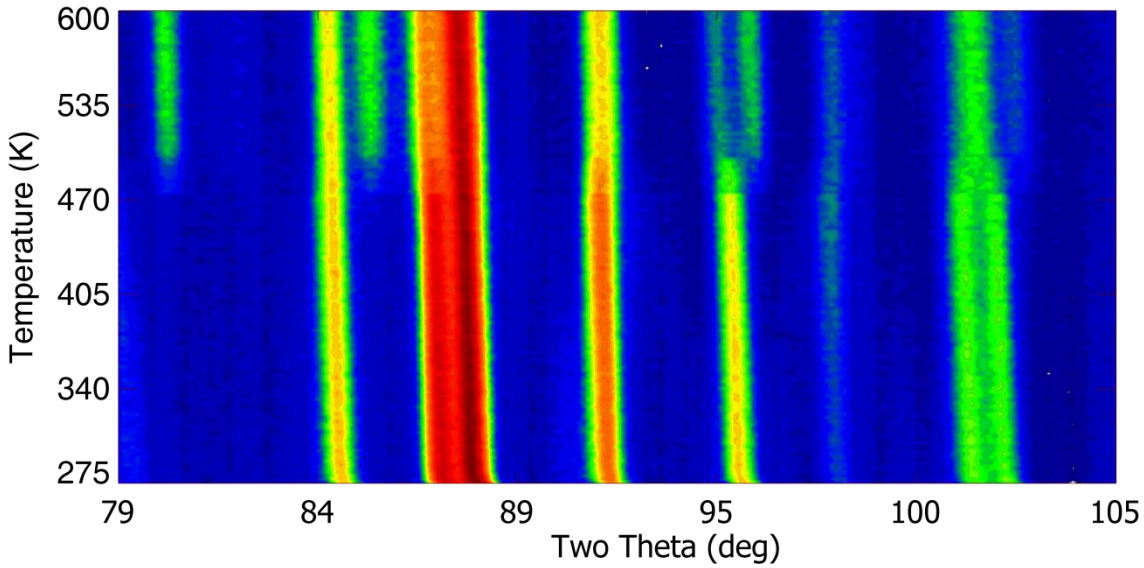

Figure 4.28: High intensity neutron powder diffraction ramping plot collected at 2.5 K intervals on heating between 275 K - 600 K.

The high intensity neutron diffraction data collected on cooling between 305 K - 600 K in Figure 4.29 demonstrate that the phase transition is completely reversible. The intensity of the 600 reflection at approximately 95° begins to decrease in intensity at 448 K and has completely disappeared by 422 K, indicating that the range of temperatures over which the transition occurs is similar on heating and cooling (~20 K from the point at which the conversion rate rapidly increases to completion). However, both the transition onset and completion temperatures determined from the cooling data are approximately 55 K lower than the heating data, indicating thermal hysteresis in the transition between the two phases. The next section will discuss the data collected using resonant ultrasound spectroscopy to support the conclusions drawn from the diffraction experiments.

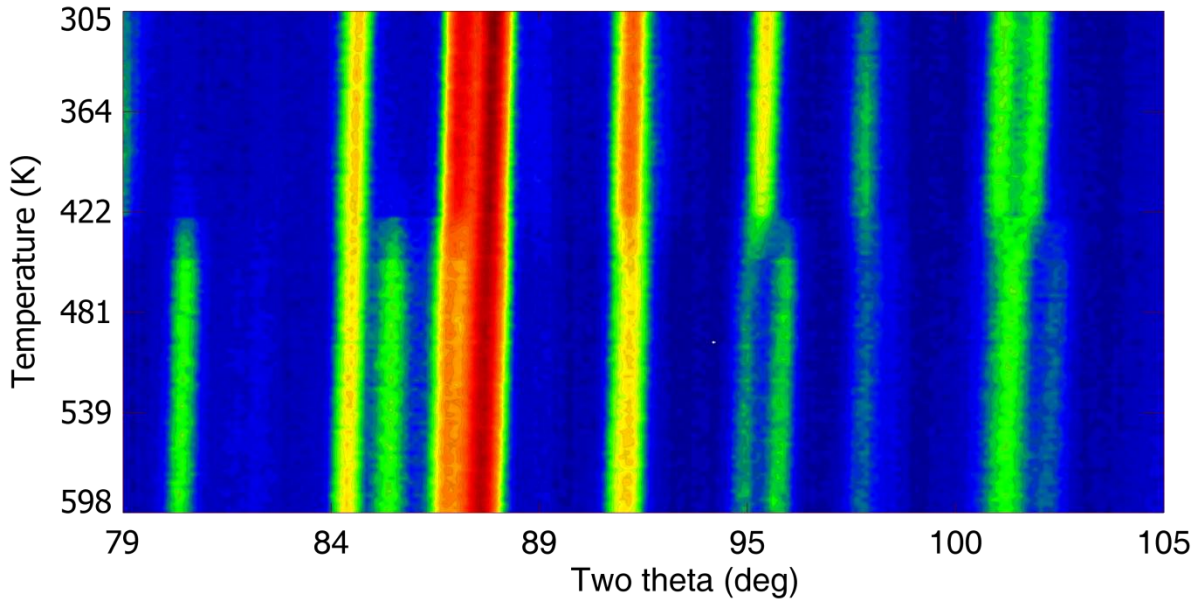

Figure 4.29: High intensity neutron powder diffraction ramping plot collecting at 2.5 K intervals on cooling between 305 K - 600 K.

4.3.4 Resonant Ultrasound Spectroscopy from $Sr_2TiSi_2O_8$

Resonant Ultrasound Spectroscopy data were collected from a polycrystalline $Sr_2TiSi_2O_8$ parallelepiped of dimensions 3.233 x 1.723 x 1.714 mm^3 (with 90° angles between each face) between 200 kHz - 1200 kHz as shown in Figure 4.30. Spectra were collected on cooling at 5 K intervals between 1090 K - 1360 K and 270 K - 650 K to monitor the transitions at 1273 K and 480 K respectively. Spectra were collected at 10 K intervals for temperatures outside these ranges. Large variations in the position of each resonance occur near the temperatures of interest that were identified from the diffraction experiments.

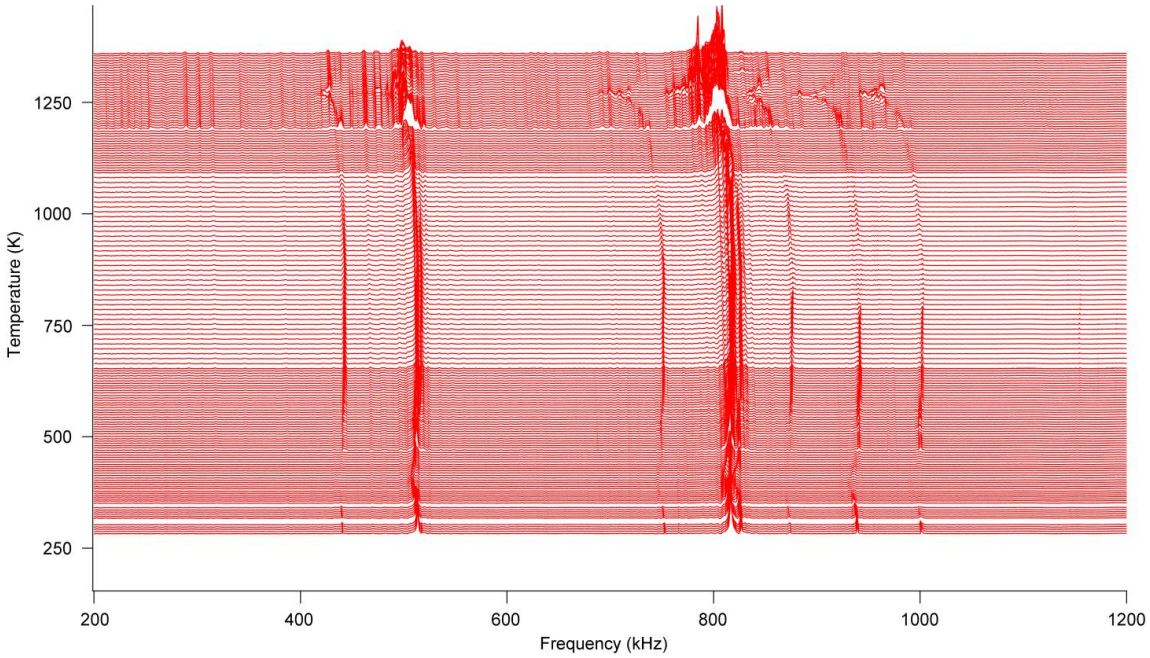

Figure 4.30: Resonant ultrasound spectra collected from a polycrystalline $Sr_2TiSi_2O_8$ sample between 200 kHz - 1200 kHz showing large variations in the positions of resonances between 273 K - 1360 K.

The position of the resonance at approximately 818 kHz was determined across both of the phase transitions that were identified in the diffraction experiments. This resonance was chosen because its behaviour is representative of the rest of the spectrum and it is well resolved from adjacent resonances, making the modelling of its position more reliable than other resonances in the spectrum. A close up of the resonances at 818 kHz (red) and the fitted Lorentzian functions (black) across the tetragonal to orthorhombic transition are plotted in Figure 4.31.

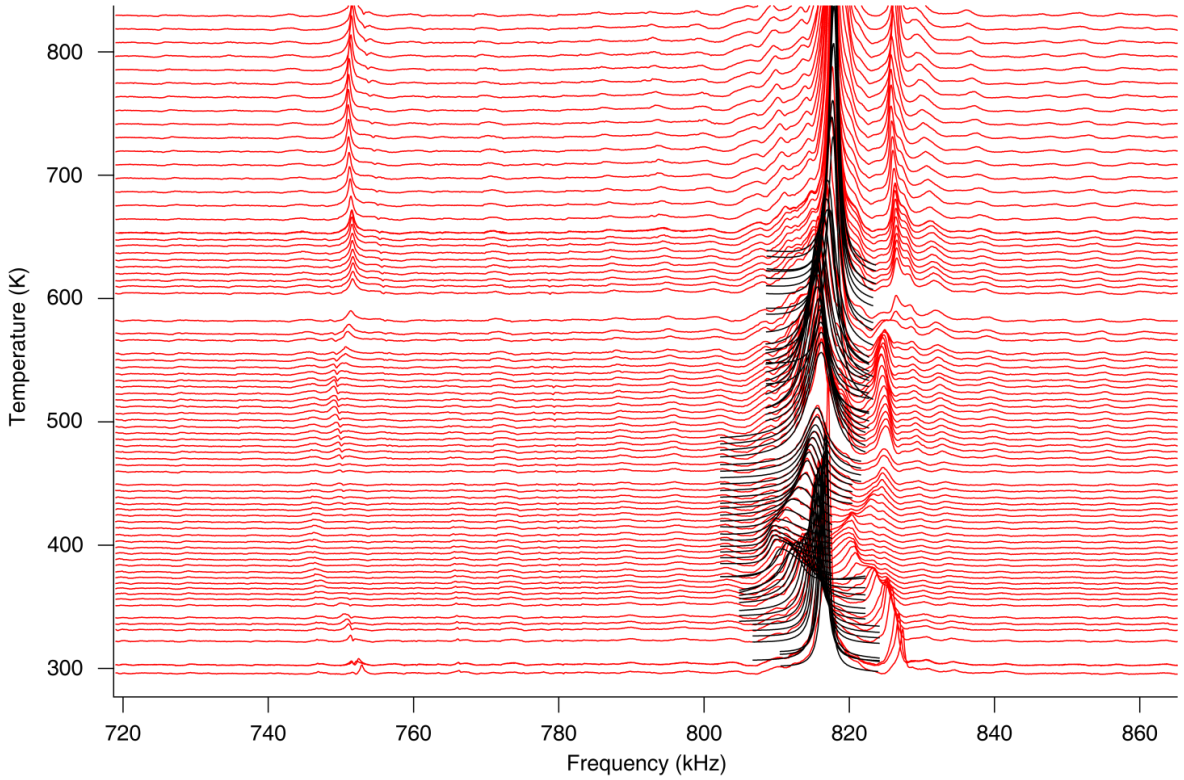

Figure 4.31: Close up of the peak at approximately 818 kHz from the resonant ultrasound spectra collected from a $Sr_2TiSi_2O_8$ polycrystalline sample (red lines). The black lines represent the asymmetric Lorentzian functions fitted to calculate the position of each peak.

The square of the frequency of the resonance (proportional to the elastic moduli) at approximately 818 kHz is plotted against temperature in green in Figure 4.32. The softening of the elastic moduli reaches a minimum at 391 K, which is approximately 150 K lower than the temperature at which the rate of phase conversion rapidly increases as determined from the diffraction experiments. The discontinuity in the elastic moduli at 470 K suggests that a significant structural change may have occurred. This coincides with an anomaly in the rate of heat flow measured using differential scanning calorimetry though a 16.9 mg polycrystalline $Sr_2TiSi_2O_8$ sample at 480 K as shown in blue in Figure 4.32.

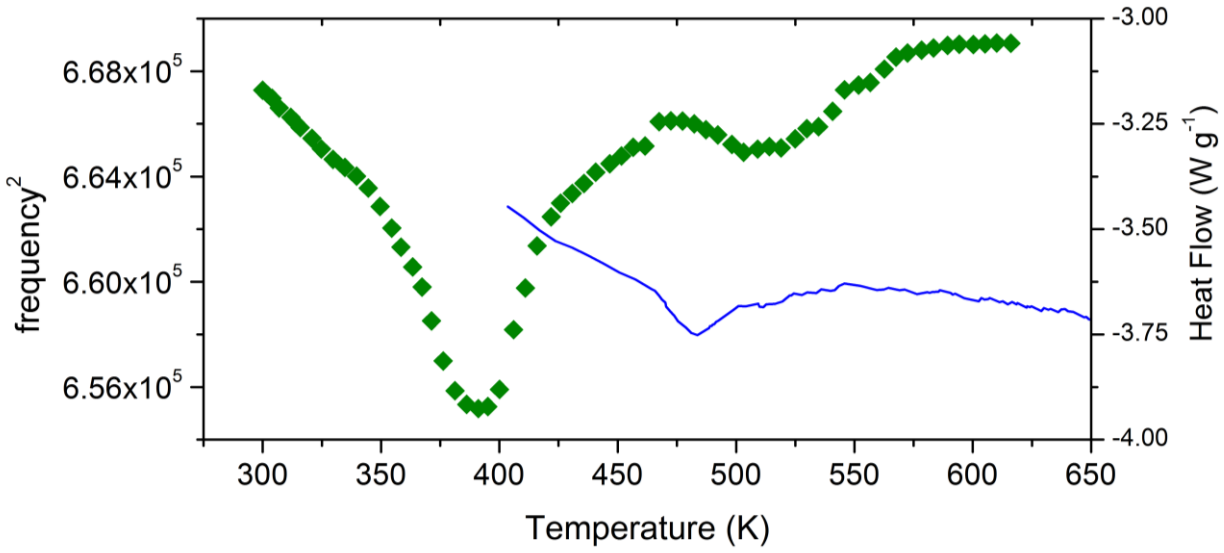

Figure 4.32: The square of the frequency for the 818 kHz resonance as a function of temperature from resonant ultrasound spectroscopy of a polycrystalline $Sr_2TiSi_2O_8$ sample between 300 K - 625 K (red) and the heat flow as determined from differential scanning calorimetry (blue) between 400 K - 650 K.

The inverse mechanical quality factor was plotted for $Sr_2TiSi_2O_8$ between 300 K - 625 K (Figure 4.33), showing a maximum in the relaxation of the structure that coincides with the minimum in the elastic constant that was calculated from the position of the resonances in the spectrum.

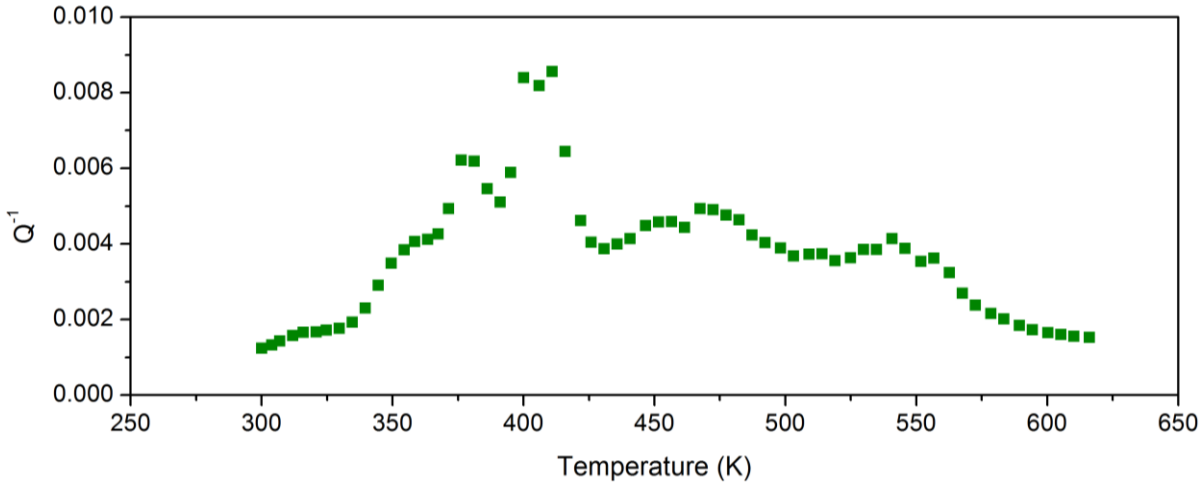

Figure 4.33: Inverse mechanical quality factor for the 818 kHz resonance as a function of temperature from resonant ultrasound spectroscopy of a polycrystalline $Sr_2TiSi_2O_8$ sample between 300 K - 625 K.

The square of the position of the 818 kHz resonance was also calculated as a function of temperature between 1180 K - 1340 K to further investigate the transition from the orthorhombic to the tetragonal phase (Figure 4.34). Softening of the elastic moduli occurs on heating until a sharp minimum at 1258 K. The behaviour of the elastic constants across the transition from the two incommensurate phases to the single incommensurate phase is similar to the significant elastic softening observed from $Ba_2NaNb_5O_{15}$ where the structure transforms from the orthorhombic $Ccm2_1$ phase to the tetragonal $P4bm$ phase at approximately 575 K.[19] The minimum in the $Sr_2TiSi_2O_8$ data is approximately 65 K lower than temperature determined from diffraction studies (*c.f.* 1323 K). However, this may be attributed to the ceramic material behaving slightly differently to the loose powder in the capillary for the diffraction experiments.

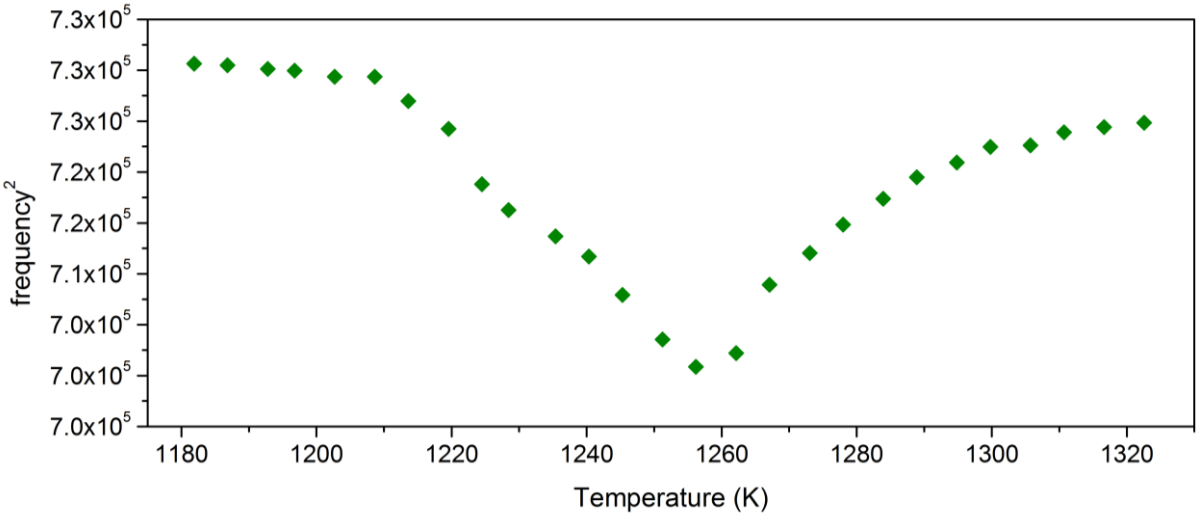

Figure 4.34: The square of the frequency for the 818 kHz resonance as a function of temperature from resonant ultrasound spectroscopy of a polycrystalline $Sr_2TiSi_2O_8$ sample between 1190 K - 1333 K.

The FWHM could not be determined for the majority of the data points between 1180 K - 1320 K because of the very high degree of convolution between the resonances of the sample and the rods holding the sample in the instrument. Evidence of the widening of the 818 kHz resonance that prevented the calculation of the FWHM visible in Figure 4.31.

The features identified in the resonant ultrasound spectra have been useful in supporting the conclusions drawn from the diffraction experiments. In particular, the minima in the elastic moduli at 391 K and 1265 K both occur within the regions at which interesting behaviour was observed in the diffraction experiments, demonstrating that the structural changes in $Sr_2TiSi_2O_8$ have a significant effect on the elastic properties of the bulk sample. The following section will discuss the physical property measurements conducted on $Sr_2TiSi_2O_8$, including the investigation of the dielectric and piezoelectric properties, and the search for ferroelectric behaviour.

4.3.5 Physical Property Measurements

Physical property measurements were conducted on polycrystalline $Sr_2TiSi_2O_8$ samples synthesised using the methods outlined in Chapter 2 to investigate the dielectric, piezoelectric, and ferroelectric properties.

The dielectric properties were measured using an Agilent 4284A LCR (Inductance, Capacitance, Resistance) meter. Ferroelectric measurements were performed on a Cypher scanning probe microscope from Asylum Research using an internal 15x high voltage amplifier and Olympus AC240TM electrilevers, spring constant $k \sim 2$ N/m, and tip radius ~ 25 nm. Single frequency measurements were performed at 10 kHz applied frequency, ~1 V applied and a contact force of approximately 100 nN. The dual frequency resonance-enhanced approach (DART, Asylum Research) was also used, with a contact force of approximately 100 nN and an applied voltage of about 45 mV. Piezoresponse curves were collected from ceramic samples using an AC signal ($f \sim 10$ kHz, $V_{AC} = \sim 0.75$ V, phase offset = 180 °) superimposed on a 0.2 Hz triangular square-stepping wave with bias up to ± 60 V and a read/write time of 25 ms.

The dielectric properties were measured from a pellet pressed from polycrystalline $Sr_2TiSi_2O_8$ of 13 mm diameter and 2 mm thickness. Silver paste was painted on the flat surfaces of the disc to

measure the capacitance across the pellet. The capacitance and loss tangent (briefly discussed in section 3.3.3) were measured between 10 Hz - 1 MHz to determine the change in properties over a wide range of frequencies. The measured capacitance was not converted into a dielectric constant because the surface area of the sample was not deemed sufficiently greater than the distance between the electrodes to ensure that a constant electric field was applied across the sample. However, the close relationship between the capacitance and dielectric constant of a material means that the capacitance can be used to indirectly investigate the behaviour of the dielectric constant of the sample.

The capacitance measured for the $Sr_2TiSi_2O_8$ sample was very low as shown in Figure 4.35. At low frequency, the capacitance is approximately $3x10^{-12}$ F, reducing to approximately $2.6x10^{-12}$ F at high frequency. This trend is identical to the $Ba_2TiSi_2O_8$ sample discussed in Chapter 3. However, the values are approximately an order of magnitude lower. It is not clear from the data collected why such a large difference is observed between the $Ba_2TiSi_2O_8$ and $Sr_2TiSi_2O_8$ samples, but it would be interesting to investigate this behaviour further.

The dielectric loss measured from the $Sr_2TiSi_2O_8$ sample was also approximately an order of magnitude lower than the $Ba_2TiSi_2O_8$ sample investigated. It is unclear whether this is an artefact due to the difference in the quality of the sample preparation. Further work is required to understand these measurements.

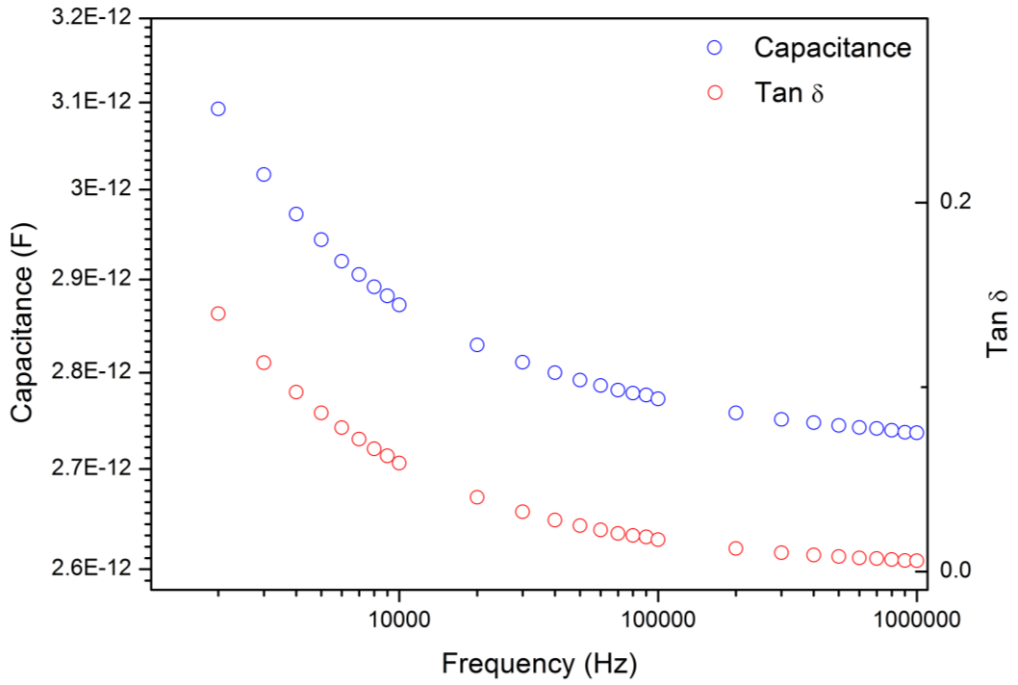

Figure 4.35: Capacitance (blue) and loss tangent (red) measured from a $Sr_2TiSi_2O_8$ pellet from 10 Hz - 1 MHz.

The $Sr_2TiSi_2O_8$ sample was shown to be piezoelectric through the measurement of the induced mechanical response from switching spectroscopy. Figure 4.36A shows the out of plane mechanical deviation and phase of the piezoresponse when the switching field is on. The linear relationship between the induced mechanical deviation and the applied voltage is indicative of a good piezoelectric material. The surface potential of the sample is approximately 4 V, as indicated by the reversal of phase. Figure 4.36B shows results obtained from the identical sample with the switching field turned off. The absence of any systematic mechanical deviation or reversal of phase after the field has been applied shows that no poling had occurred and hence provides no evidence of ferroelectricity.

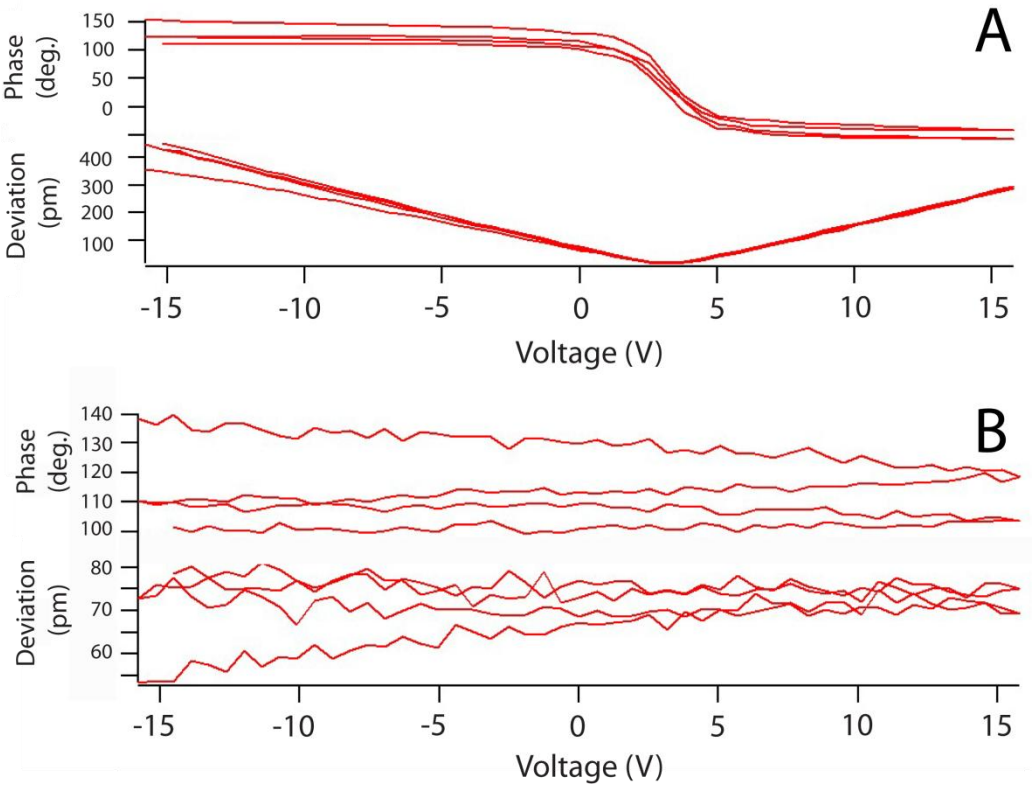

Figure 4.36: Out of plane mechanical deviation and phase recorded from switching spectroscopy conducted on $Sr_2TiSi_2O_8$ with applied field on (A) and off (B).

The piezoelectric coefficient was quantified to be 27 pm V^{-1} from the out of plane mechanical deviations that were detected in the PFM experiment using the method described in Section 1.3.1. This value is higher the value determined for $Ba_2TiSi_2O_8$ and has been compared against other common piezoelectric materials in Table 4.9. It is unclear from this study why the intrinsic piezoelectric coefficient calculated for $Sr_2TiSi_2O_8$ is higher than that calculated for $Ba_2TiSi_2O_8$, however higher sample quality, or the presence of the phase boundaries due to the presence of the two coexisting phases at ambient temperature could be contributing factors.

Table 4.9: Comparison of the intrinsic piezoelectric coefficient for $Sr_2TiSi_2O_8$, $Ba_2TiSi_2O_8$ and well-known piezoelectric materials.

Material	d_{33} (pm V^{-1})	Reference
$Ba_2TiSi_2O_8$	5	Current study
$Sr_2TiSi_2O_8$	27	Current study
Quartz	2.3	Smith[26]
$BaTiO_3$	190	Jaffe *et al.*[27]
$PbTiO_3$	50	Ueda *et al.*[28]
$PbZr_{0.48}Ti_{0.52}O_3$	110	Berlincourt *et al.*[29]

The phase of the induced polarisation was also mapped using piezoresponse force microscopy from a small region of a crystalline showing domain structure. Figure 4.37 shows that two different domains are present, with different components in the plane of the surface and out of the plane of the surface of the crystal. This behaviour is identical to that observed for $Ba_2TiSi_2O_8$, and demonstrates the piezoelectricity of the sample.

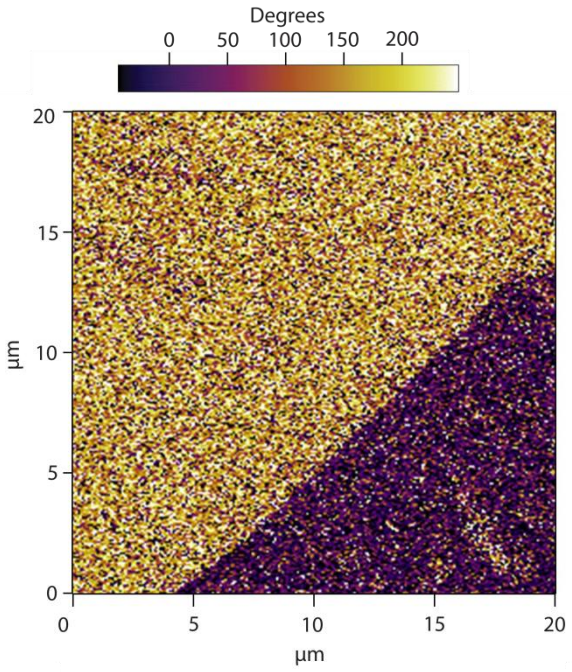

Figure 4.37: Image of the phase signals detected using piezoresponse force microscopy from polycrystalline $Sr_2TiSi_2O_8$.

The ferroelectric properties of $Sr_2TiSi_2O_8$ were also investigated using a ferroelectric analyser. The polarisation versus applied electric field loop collected from $Sr_2TiSi_2O_8$ in Figure 4.38 resembles the data collected from $Ba_2TiSi_2O_8$ where a very small polarisation in the order of pico-Coulombs was observed. The lack of change in concavity and the extremely small polarisation (~ 60 pico-Coloumbs) are typical properties of a polarisation versus electric field loop that from a non-ferroelectric material that is dominated by leakage currents.[30] Hence, it was concluded that no evidence of ferroelectricity was observed from the $Sr_2TiSi_2O_8$ sample investigated in this project. This is further supported by the smooth change in current as the voltage was increased and decreased across the sample (Figure 4.39).

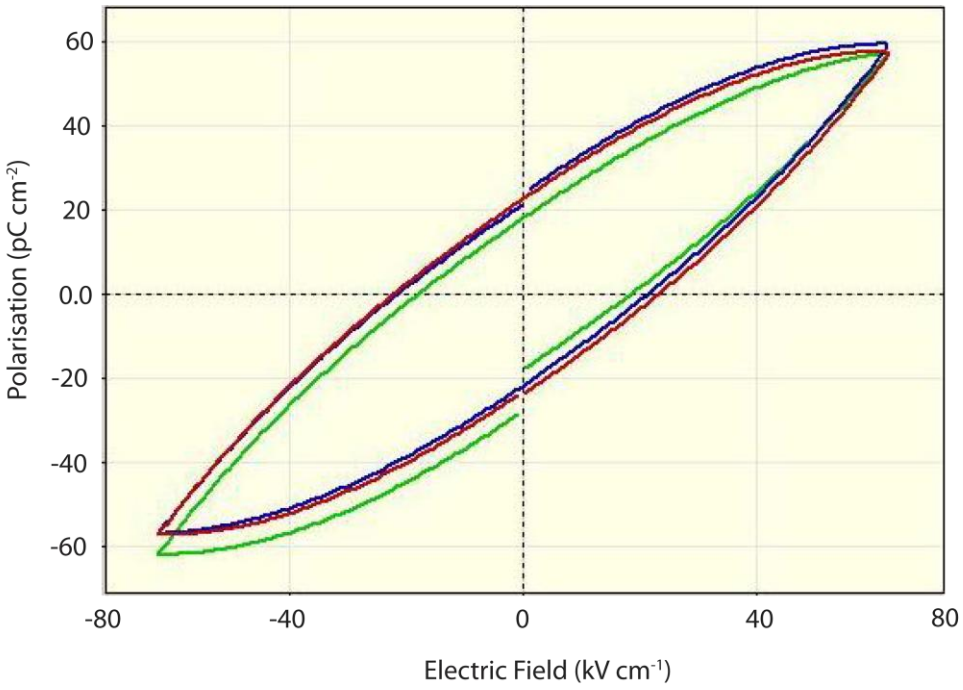

Figure 4.38: Polarisation versus electric field curve collected from polycrystalline $Sr_2TiSi_2O_8$. The lack of saturation at high field and the small induced polarisation indicate that no ferroelectric properties are present.

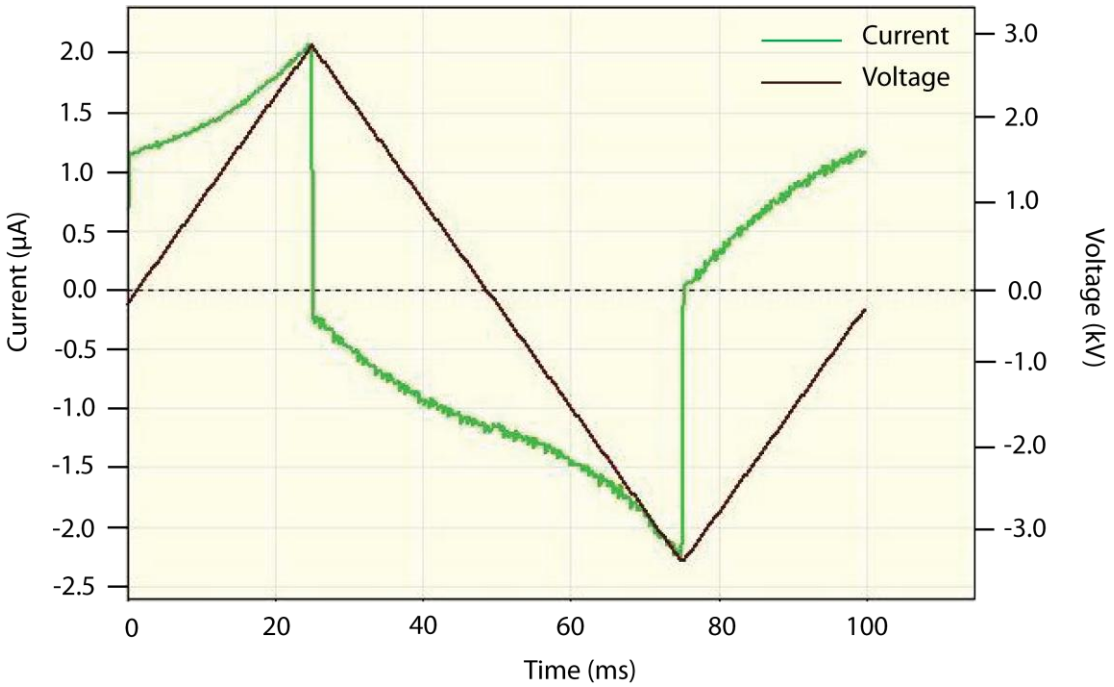

Figure 4.39: Current (left axis) and voltage (right axis) versus time curve collected from polycrystalline $Sr_2TiSi_2O_8$. The smooth change in current as the voltage is varied provides additional evidence that the sample does not exhibit ferroelectricity.

The combination of the lack of poling in the switching spectroscopy experiment, the lack of induced polarisation in the ferroelectric analyser, and the continuous change in current as the voltage is varied across the sample all lead to the conclusion that the polycrystalline $Sr_2TiSi_2O_8$ sample investigated in this project does not exhibit ferroelectricity.

4.4 Summary

The $Sr_2TiSi_2O_8$ structure has been characterised at ambient temperature using a combination of electron, X-ray, and neutron diffraction. Electron diffraction patterns collected at ambient temperature showed that crystallites of $Sr_2TiSi_2O_8$ contain two very similar incommensurately modulated phases. The overlapping of the main reflections of both phases suggested that the orthorhombic phase has unit cell dimensions that are very similar to those of the tetragonal phase, and that the symmetry of the satellite reflections must be taken into account to differentiate between the two phases. The two phases were indexed using the $X4bm(\alpha, \alpha, ½)0gg$

and *Cmm*2(0, β, 0)*s*00 space groups. This provides evidence of a new space group that is adopted by the fresnoite structure-type, given that it is different to the orthorhombic $Ba_2TiGe_2O_8$ space group that has been previously reported in the literature.[6]

Despite the difficulties associated with modelling a sample that contains two very similar phases, the average $Sr_2TiSi_2O_8$ structure was determined from synchrotron X-ray powder diffraction data for the first time. A full model of the modulated structure of $Sr_2TiSi_2O_8$ was also refined against high intensity neutron powder diffraction data for the first time. The largest displacements from the average $Sr_2TiSi_2O_8$ structure were experienced by the oxygen-3 ions in a similar fashion to $Ba_2TiSi_2O_8$ in Chapter 3. The introduction of the modulation improved the average bond valence sum for the strontium, titanium, silicon, and oxygen-4 ions, while small deviations from the ideal bond valence sums were experienced by the remaining ions. The greatest improvement in bond valence sum occurred for the strontium ion, providing further support that the bonding requirements of the ions on the *A*-site are a significant driving force for the modulation in the fresnoite structure type.

The collection of high resolution images from $Sr_2TiSi_2O_8$ crystallites in the electron microscope produced visual evidence of the ring-like structure in $Sr_2TiSi_2O_8$. Evidence of the different phases in adjacent regions of crystallites was also collected, confirming that the appearance of the different phases changes across modulation phase boundaries. Fast Fourier transform calculations from these high resolution images produced images that contained satellite reflections corresponding to either (or both) structure(s), confirming that although the difference between the two phases is very subtle, evidence of the modulation is identifiable in the high resolution images. It was also shown for the first time that the act of collecting of a high resolution image could drive a reversible structural phase transition between the tetragonal and orthorhombic phases. Variable temperature electron diffraction confirmed the presence of a reversible structural phase transition that reduces the symmetry of the structure on heating.

Single phase tetragonal models were refined against variable temperature synchrotron X-ray powder diffraction data to monitor the changes in the $Sr_2TiSi_2O_8$ structure between 125 K - 275 K. X-ray and neutron powder diffraction were used to establish that the rate of conversion from the tetragonal to the orthorhombic phase rapidly increases between approximately 542 K - 567 K.

Two phase Rietveld models consisting of both the *X*4*bm* and *Cmm*2 phases were developed between 300 K - 542 K. A combination of the analysis of the orthorhombic strain, heat flow curves, and the variation in the elastic moduli from resonant ultrasound spectroscopy were used to establish that the reversible first order phase transition between the tetragonal to the orthorhombic phase is complete by approximately 567 K. Single phase models of the orthorhombic structure were refined against data collected between 567 K - 1273 K until the structure undergoes a phase transition to what is believed to be the prototypic *X*4*bm* phase at approximately 1323 K as determined from the reduction of the orthorhombic strain to zero and the minima observed in the elastic moduli. The calculation of the spontaneous strain of the orthorhombic phase provided evidence that the high temperature transition does not display second order behaviour. It was shown that the e_{ortho}^2 parameter (proportional to Q^4) decreases linearly to zero as the structure approaches the transition, however no formal conclusions could be drawn due to the high degree of experimental uncertainty in the numbers calculated for e_{ortho}^2.

An investigation of some of the physical properties of polycrystalline $Sr_2TiSi_2O_8$ samples found that the capacitance and loss tangents followed the same trends as the $Ba_2TiSi_2O_8$ sample in Chapter 3, but were an order of magnitude lower. The presence of piezoelectricity was confirmed from switching spectroscopy experiments, and the intrinsic piezoelectric response coefficient was calculated to be approximately 27 pm V^{-1}. No evidence of ferroelectric domains or domain switching was found from the polarisation versus applied field curves or piezoresponse force

microscopy. This demonstrates that neither $Sr_2TiSi_2O_8$ nor $Ba_2TiSi_2O_8$ ceramic samples synthesised in this project are ferroelectrically active, despite the literature predicting and showing that the $Ba_2TiSi_2O_8$ member of the fresnoite family of compounds can exhibit ferroelectricity.

Chapter 5 Structural Investigation of $Ba_2TiGe_2O_8$

5.1 Introduction

The $Ba_2TiGe_2O_8$ structure and its phase transitions have been comprehensively investigated by several research groups in the past. $Ba_2TiGe_2O_8$ was first reported to have a structure similar to the parent compound, $Ba_2TiSi_2O_8$.[73,199] However, later studies established important structural differences between these two compounds. In 1973, Kimura *et al.*[77] used X-ray precession photographs to correctly identify that $Ba_2TiGe_2O_8$ displays orthorhombic symmetry. However, the space group was incorrectly determined to be *Iba*2. The same study also investigated some physical properties for $Ba_2TiGe_2O_8$, finding no evidence of ferroelectricity, but observing ferroelastic behaviour in a single crystal. Anomalies in differential thermal analysis curves and the domain widths in single crystals on heating and cooling established that a phase transition from an optically biaxial to a uniaxial state exists near 1083 K. Large anomalies in the elastic moduli for $Ba_2TiGe_2O_8$ were also observed across the phase transition temperature. Additionally, this work suggested that a 11x superstructure occurs in the *b*-direction and that this is closely related to the ferroelastic behaviour of the compound.

In 1981, Ijima *et al.*[57] established that $Ba_2TiGe_2O_8$ crystallises in the orthorhombic *mm*2 point group at ambient temperature. The average structure was determined from X-ray diffraction using Cu K_α radiation, showing that half of the bridging Ge-O-Ge bond angles on the [001]-projection deviate by about 10° from 180°. These deviations were proposed to be responsible for the long period superstructure at ambient temperature. Ijima *et al.*[57] also reported that $Ba_2TiGe_2O_8$ undergoes a ferroelastic phase transition at approximately 1143 K to a high temperature tetragonal 4mm point group.[57] Although the Ijima *et al.*[57] study was performed after the Kimura *et al.*[77] study, the phase transition temperature of 1083 K determined by Kimura

et al. was reported with more certainty and hence this should be taken as the most appropriate value from the literature.

In 1985, Halliyal *et al*.[200] found clear evidence of a low temperature structural phase transition in a single crystal of $Ba_2TiGe_2O_8$ through the measurement of the dielectric permittivity, pyroelectric coefficient, and the piezoelectric planar coupling coefficient. Markgraf *et al*.[55] used single crystal intensity data to establish that the average $Ba_2TiGe_2O_8$ structure crystallises in the *Cmm*2 space group. Precession X-ray photographs were used to show that the phase transition exhibits hysteresis (~223 K on cooling and ~273 K on heating) and involves the modulation along **a*** locking into a value of 1/3 on cooling. Hysteresis was also observed in the dielectric and the pyroelectric properties of $Ba_2TiGe_2O_8$ as the temperature was cycled through the low temperature phase transition.

In 1999, Höche *et al*.[50] compared the incommensurate modulations in $Ba_2TiSi_2O_8$, $Sr_2TiSi_2O_8$, and $Ba_2TiGe_2O_8$, establishing that fewer satellite reflections are observed in the electron diffraction patterns collected from $Ba_2TiGe_2O_8$ than $Ba_2TiSi_2O_8$. Superstructure reflections were found to occur at 0.36b*, 0.64b* and at combinations of these values, supporting the work of Markgraf *et al*.[55] on the same compound.[55] Höche *et al*. conducted a more comprehensive study of the incommensurately modulated structure of $Ba_2TiGe_2O_8$ in 2003, establishing that $Ba_2TiGe_2O_8$ crystallises in the *Cmm*2(0, β, ½)*s*00 space group with β ~ 0.635 at ambient temperature.[71] The structure was refined against time of flight neutron powder diffraction data collected from a ground up single crystal. The modulation parameters obtained from the refinement support the theory that rigid unit modes are involved in the modulation of the structure and that the improvement in the bond valence sum of both of the barium positions are likely driving forces for the need of a displacive modulation.

The investigation of the structure and thermally induced phase transitions of $Ba_2TiGe_2O_8$ in polycrystalline form is of high importance because it is likely that many potential applications of the fresnoite structure type will require the compound to be processed and utilised in bulk polycrystalline form rather than as single crystals. This chapter will discuss the use of synchrotron X-ray and neutron powder diffraction to investigate polycrystalline samples of $Ba_2TiGe_2O_8$ at a variety of temperatures, including both of the known phase transitions. Furthermore, resonant ultrasound spectroscopy data collected on heating and cooling across the two phase transitions will be presented and discussed.

5.2 Synthesis

Polycrystalline samples of $Ba_2TiGe_2O_8$ were prepared using a method adapted from Höche *et al*.[50] Stoichiometric quantities of $BaCO_3$, TiO_2 and GeO_2 were thoroughly mixed before melting in a platinum crucible at 1400 °C for two hours. The melt was cooled to ambient temperature, rehomogenised, pressed into pellets of 13 mm or 20 mm diameter using a uniaxial press (depending on sample size) and heated at 850 °C for one week. X-ray diffraction using Cu K_α radiation after this heating step showed a small number of very weak reflections that did not correspond to the $Ba_2TiGe_2O_8$ structure. A thorough search of the JCPDS database identified that some of the unindexed reflections may correspond to a very small proportion of $BaGeO_3$.[201] The remaining reflections could not be indexed by any one structure, suggesting that they correspond to a small proportion of at least two additional impurity phases. These additional phases were not considered in the models refined in this thesis because of their tiny contribution to the pattern. Further heating at higher temperatures for longer periods of time (*e.g.* 1000 °C for 168 hours) did not improve the purity of the sample, suggesting that the synthesis of 100 % phase pure polycrystalline samples may not be possible.

5.3 Results & Discussion

The results in this chapter will be discussed in two sections. Firstly, the characterisation of the $Ba_2TiGe_2O_8$ structure at ambient temperature as determined from synchrotron and neutron powder diffraction will be discussed. This will focus on the difficulties encountered in the use of a modulated structure approach to characterising $Ba_2TiGe_2O_8$ from polycrystalline samples and comparisons will be drawn to the comprehensive study of the incommensurate structure by Höche *et al.*[71]

Secondly, the changes to the $Ba_2TiGe_2O_8$ structure between 125 K - 1273 K will be discussed as determined from synchrotron and neutron powder diffraction. This discussion will be complemented by the presentation and analysis of resonant ultrasound spectroscopy data collected from a $Ba_2TiGe_2O_8$ single crystal.

5.3.1 $Ba_2TiGe_2O_8$ structure at ambient temperature

The observed, calculated, and difference plots from the refinement of the $Ba_2TiGe_2O_8$ structure at ambient temperature against synchrotron X-ray powder diffraction data are provided in Figure 5.1. The unexplained intensity at ~18 degrees two theta resembles a similar miscalculation of the equivalent reflection for $Sr_2TiSi_2O_8$ in Section 4.3.1, however, the inclusion of preferred orientation correction could not be included such that the fit could be improved.

The refinement of atomic positions produced unrealistic bonding environments around the germanium, titanium and oxygen ions. The inclusion of rigid unit restrictions for the GeO_4 polyhedra allowed the refinement to proceed while keeping sensible bond angles and lengths for the GeO_4 polyhedra without significantly reducing the quality of the fit. The rigid unit restrictions

were applied through the definition of four symmetrically equivalent units comprised of the germanium and surrounding oxygen ions using the 'molecule' restriction command in Jana2006.

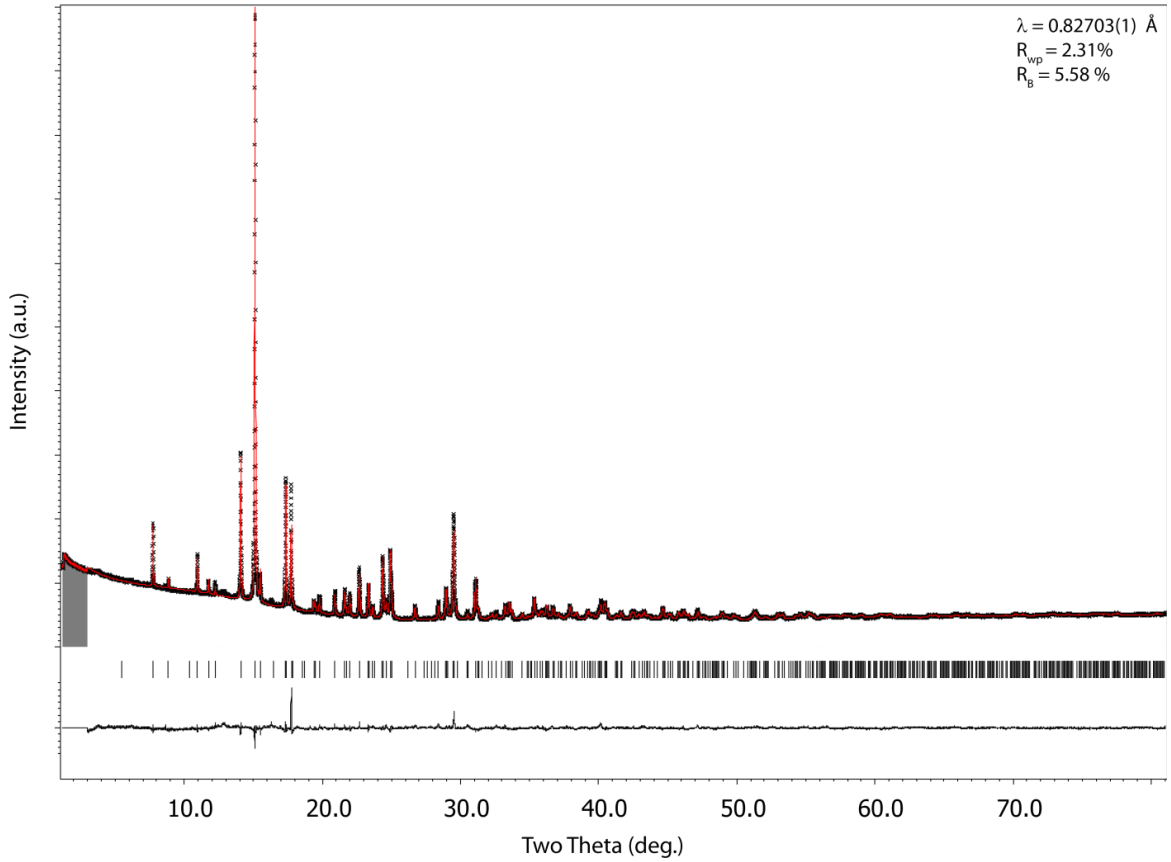

Figure 5.1: Observed, calculated, and difference plots from the refinement of the $Ba_2TiGe_2O_8$ structure at ambient temperature against synchrotron X-ray powder diffraction data. Black crosses and the red line represent the observed and calculated diffraction patterns, respectively. The vertical black lines represent the Bragg reflection positions and the continuous black line represents the difference between the observed and calculated patterns.

The absence of satellite reflections in the synchrotron X-ray powder diffraction pattern meant that only the average structure could be determined from these data. A doubled unit cell in the *c*-direction has been used as reported by Höche *et al.* to represent the average structure in an analogous way to the modulated structure.[71] The structural model converged with R_B = 2.31 % and R_{wp} = 5.58 % using the orthorhombic X*mm*2 space group (representing the *Cmm*2 space group that incorporates the modulation vector of magnitude ½ in the **c*** direction). The experimental data and important parameters for the refinement are provided in Table 5.1.

Atomic displacement parameters (ADP's) were refined isotropically because the inclusion of anisotropic ADP's produced non-positive definite values.

Table 5.1: Experimental data and important parameters for the refinement of the $Ba_2TiGe_2O_8$ average structure at ambient temperature.

Parameter	$Ba_2TiGe_2O_8$
Wavelength (Å)	λ = 0.82703(1)
Molar mass (g mol^{-1})	595.73
Crystal System	Orthorhombic
Space Group	*Xmm*2
Z	8
a (Å)	12.2762(3)
b (Å)	12.2635(3)
c (Å)	10.7259(1)
V (Å^3)	1614.77(4)
D_{calc} (g cm^{-3})	4.8994(1)
Linear abs. coeff. (mm^{-}	26.804
R_B	5.58 %
R_{wp}	2.31 %

The refined $Ba_2TiGe_2O_8$ average structure at ambient temperature is illustrated in Figure 5.2 where the barium and oxygen ions have been labelled. The *Xmm*2 setting is related to the parent *X*4*bm* space group of $Ba_2TiSi_2O_8$ and $Sr_2TiSi_2O_8$ by a 45 degree rotation about the [001]-axis of the structure with the doubled *c* unit cell parameter as reported by Höche *et al.*[71] creating the non-standard centering.

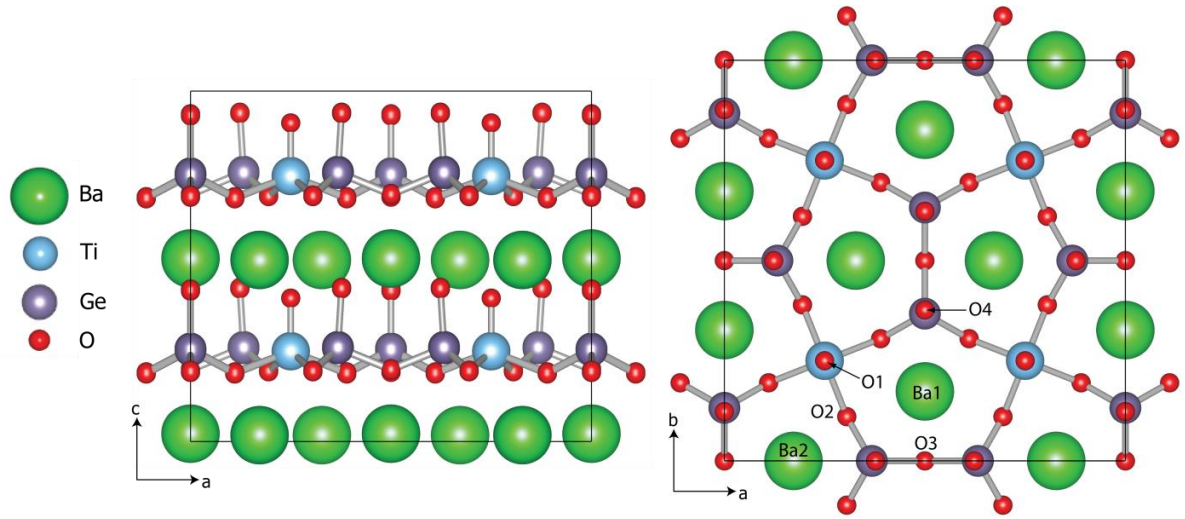

Figure 5.2: The $Ba_2TiGe_2O_8$ average structure at ambient temperature as refined against synchrotron X-ray powder diffraction data projected along the [010]- (left) and [001]- (right) directions.

The refined atomic positions and atomic displacement parameters for the $Ba_2TiGe_2O_8$ average structure at ambient temperature are provided in Table 5.2 where the Ge, O2, O3, and O4 ions constitute the rigid polyhedra defined in the model. The refinement of the oxygen and titanium ions produced an excessively short axial bond for the TiO_5 square pyramid (1.625(2) Å instead of ~1.70 Å for similar Ti environments[68-70]). Short axial bond lengths have been determined for other compounds containing TiO_5 square pyramids (*c.f.* Section 1.5). However, the axial Ti-O1 bond in this study is still considered too short, even in the context of these other compounds. The model of $Ba_2TiGe_2O_8$ structure determined by Höche *et al.*[71] from neutron powder diffraction data collected from a ground up single crystal contained an axial Ti-O bond length of 1.73 Å which is significantly longer than the equivalent bond calculated in the current study. A consequence of the short Ti-O bond is that the titanium ion is significantly overbonded with a bond valence sum of 4.46(7) (*c.f.* 4.140(5) from Höche *et al.*[71]). Although these values are not ideal, they are the most reasonable parameters that could be obtained from the data available from the polycrystalline $Ba_2TiGe_2O_8$ samples in the current study.

Table 5.2: Atomic positions and atomic displacement parameters (ADP's) for $Ba_2TiGe_2O_8$ at ambient temperature as determined from refinement against synchrotron X-ray powder diffraction data.

	Ba1	Ba2	Ti	Ge	O1	O2	O3	O4
x	0	0.1723(4)	0.25	0	0.25	0.1104(4)	0	0
y	0.32677(9)	0	0.25	0.13245(8)	0.25	0.19450(4)	0	0.1233(5)
z	0.5224(1)	0.51824(4)	0.2578(7)	0.2540(4)	0.409(1)	0.1872(4)	0.117(9)	0.4236(6)
U_{iso} ($Å^2$)	0.0095(3)	0.0109(3)	0.0140(8)	0.0090(3)	0.023(3)	0.045(2)	0.020(4)	0.008(2)

In contrast to the synchrotron data, significant intensity was observed for some satellite reflections in the high intensity neutron powder diffraction data collected from Wombat. The sample on which Höche *et al*. performed a thorough investigation into the full (3+1)-dimensional structure of $Ba_2TiGe_2O_8$ was a single crystal which had been ground up into polycrystalline form. Ideally, the characterisation would have been performed on the sample in single crystal form. However, the presence of pronounced internal stresses that were frozen in during the high temperature phase transition on cooling after synthesis meant that this was not possible. Given that Höche *et al*.[50] and Wong *et al*.[202] have both discussed the importance of the type of synthesis on the formation of the fresnoite structure type, this neutron diffraction study aims to investigate $Ba_2TiGe_2O_8$ as a bulk polycrystalline material that has been synthesised as a powder rather than a single crystal.

The high intensity neutron powder diffraction pattern collected from Wombat is compared to the pattern published from the time of flight high resolution powder diffractometer (HRPD) at ISIS by Höche *et al*.[71] in Figure 5.3.

The resolution of the reflections in the data collected from Wombat is significantly lower than that achieved on HRPD at ISIS, and although the signal to noise ratio is also not as high as for the ISIS pattern, it is sufficient to provide evidence of the modulated structure in comparable regions of the pattern. High resolution neutron powder diffraction data were also collected from Echidna, however, the slight increase in resolution was not beneficial for this study because the

significantly reduced signal to noise ratio reduced the intensity of the satellite reflections relative to the main reflections. For this reason, the following discussion is based on the high intensity neutron powder diffraction data collected from Wombat.

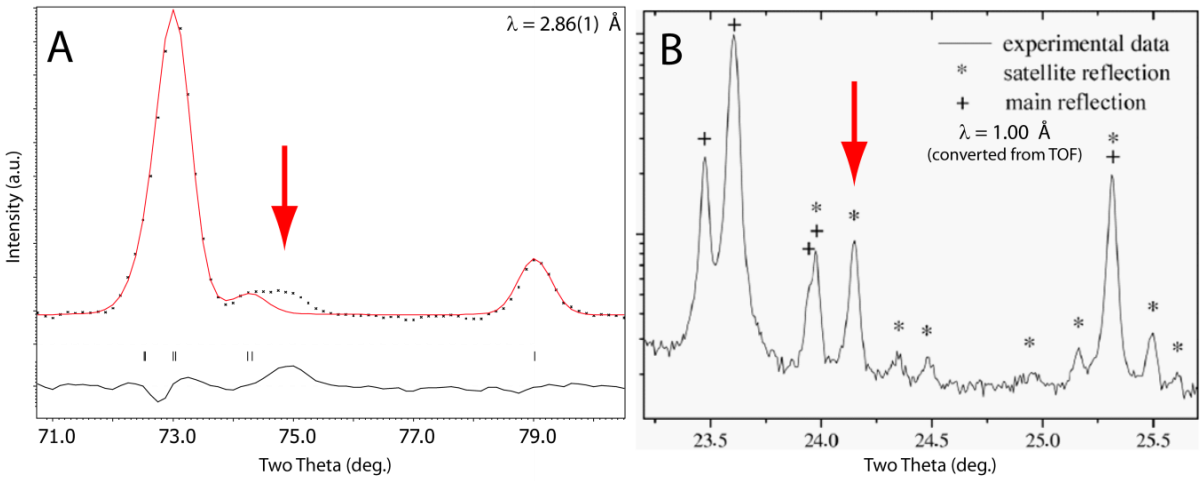

Figure 5.3: Comparison of a region of interest in the $Ba_2TiGe_2O_8$ neutron diffraction patterns collected from Wombat (A), and ISIS (B, from Höche *et al.*).[71] Peak markers in A represent calculated main reflections. Red arrows indicate satellite reflections that were observed in both patterns.

Numerous strategies were employed in the attempt to model the (3+1)-dimensional structure by refinement against high intensity neutron powder diffraction data. A starting model using the atomic positions and modulation amplitudes refined by Höche *et al.*[71] also trialled, where the systematic refinement of each parameter dramatically improved the fit of the model to the data, but the bond distances and bond valence sums showed that the refinement was converging on a physically unreasonable model. Similarly, the systematic refinement of modulation amplitudes from arbitrarily small values (*c.f.* 0.001) did not produce reasonable results. The observed, calculated, and difference plots form the refinement of the $Ba_2TiGe_2O_8$ average structure at ambient temperature is provided in Figure 5.4. The unindexed reflections at 35.5°, 39.7°, 48.1°, 70.0°, and 75.0°, 100.7° two theta correspond to the positions of the $112\bar{1}$, $131\bar{1}$, 3101, 3131, 3331, 6201 satellite reflections calculated by the Höche *et al*. model. However, it is possible that these reflections may correspond to an unidentified impurity phase. The inability to refine a plausible

(3+1)-dimensional model of the $Ba_2TiGe_2O_8$ structure meant that only the average structure could be determined in this study.

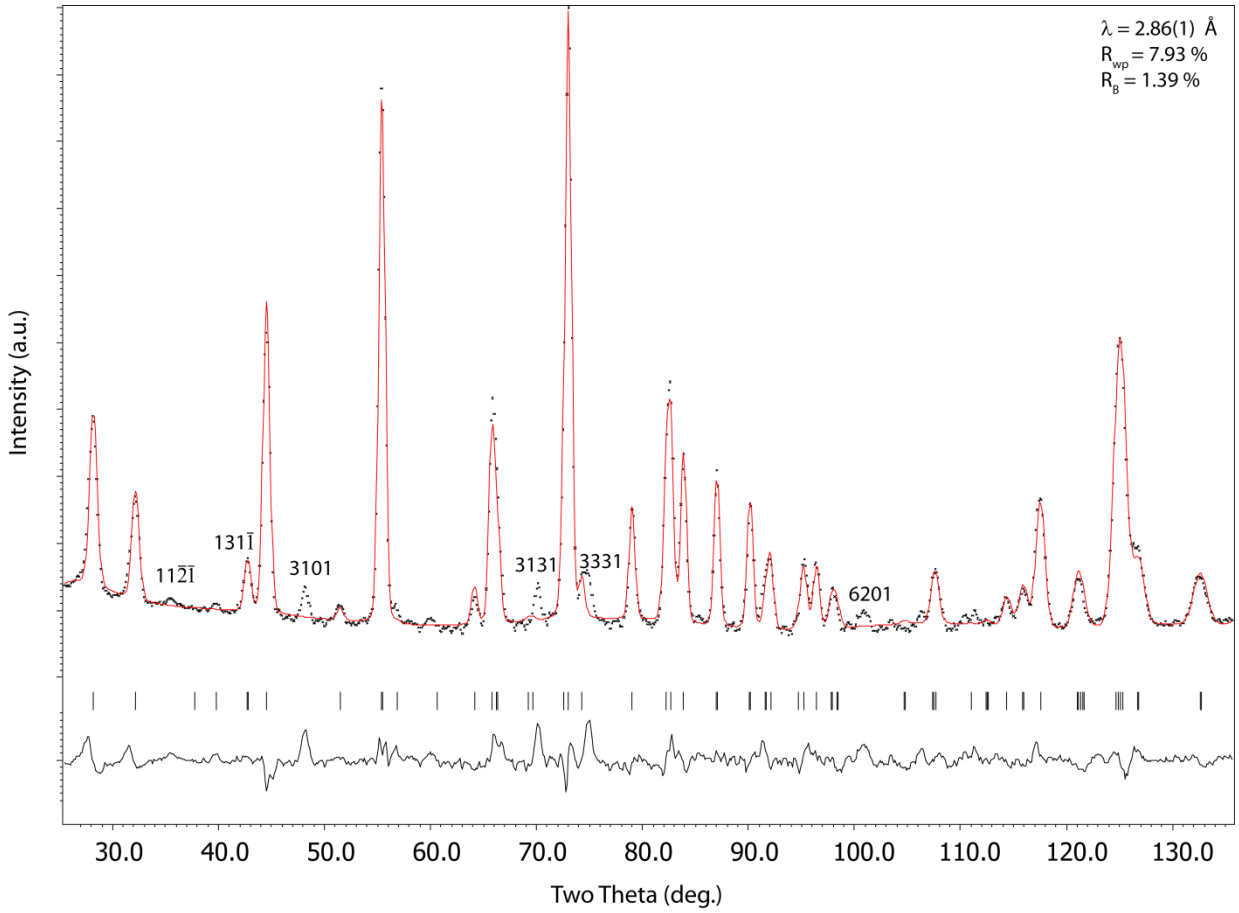

Figure 5.4: Observed, calculated, and difference plots from the refinement of the $Ba_2TiGe_2O_8$ average structure at ambient temperature against high intensity neutron diffraction data. The labelled reflections represent unindexed intensity that corresponds to the published Höche *et al*. model but may also correspond to an unidentified impurity phase.

The experimental data and important parameters for the refinement of the average $Ba_2TiGe_2O_8$ structure against the high intensity neutron powder diffraction data are provided in Table 5.3. The fit of the model to the Bragg reflections corresponding to the average structure is good (R_B = 1.39 %), however the weighted profile fit (R_{wp} = 7.93 %) is significantly higher because it takes the fit of the entire profile into account including the regions where satellite intensity has not been accounted for in the model.

Table 5.3: Experimental data and important parameters for the refinement of the average $Ba_2TiGe_2O_8$ structure against high intensity neutron powder diffraction data.

Parameter	$Ba_2TiGe_2O_8$
Wavelength (Å)	2.86(1) Å
Molar mass (g mol^{-1})	595.73
Crystal System	Orthorhombic
Space group	*Xmm*2
a (Å)	12.251(4)
b (Å)	12.238(4)
c (Å)	10.704(9)
V ($Å^3$)	1604.9(3)
D_{calc} (g cm^{-3})	4.9296(9)
Z	8
Linear abs. coeff. (mm^{-1})	0.01006
R_B	1.39 %
R_{wp}	7.93 %

The refined atomic positions for the $Ba_2TiGe_2O_8$ average structure are provided in Table 5.4. When compared to the atomic positions refined against the synchrotron data set, the greatest differences occur in the properties of the TiO_5 square pyramid. The bond lengths and bond valence sums for the titanium ion in the square pyramid as determined from refinement against synchrotron and neutron data sets are both compared to the values obtained by Höche *et al.*[71] in Table 5.5. The length of the axial bond determined from the neutron diffraction data is significantly greater than the value calculated from refinement against synchrotron data and longer than the distance calculated by Höche *et al.*[71] (*c.f.* 1.73 Å). Conversely, the bonds from the titanium ion to the basal oxygen ions are significantly shorter in the model determined from neutrons than the other two studies. This variability demonstrates that the size of the square pyramid is different in these models, suggesting that some variability in the atomic positions is present. This variability has caused the unreasonably high bond valence sum for the titanium ion of 4.4(1).

Table 5.4: Atomic positions and atomic displacement parameters (ADP's) for $Ba_2TiGe_2O_8$ at ambient temperature as determined from refinement against high intensity neutron powder diffraction data.

	Ba1	Ba2	Ti	Ge	O1	O2	O3	O4
x	0	0.163(5)	0.25	0	0.25	0.1123(3)	0	0
y	0.0327(5)	0	0.25	0.1271(7)	0.25	0.1957(7)	0	0.1244(8)
z	0.043(3)	0.003(2)	0.2499(2)	0.256(2)	0.419(2)	0.193(3)	0.173(3)	0.416(2)
U_{iso} ($Å^2$)	0.02(3)	0.02(3)	0.01(1)	0.009(3)	0.007(6)	0.052(4)	0.042(7)	0.014(4)

Table 5.5: Bond lengths and bond valence sums for the titanium ion in $Ba_2TiGe_2O_8$ at ambient temperature as determined from refinement against synchrotron and neutron powder diffraction data. Data from Höche *et al.*[71] are also provided for comparison.

	Synchrotron	Neutron	Höche *et al.*
Ti-O1 (axial)	1.63(2)	1.79(3)	1.73(2)
Ti-O2a	1.948(5)	1.88(1)	1.99(1)
Ti-O2b	1.945(5)	1.87(1)	1.99(1)
Ti-O2c	1.970(5)	1.90(2)	1.95(1)
Ti-O2d	1.931(5)	1.86(1)	1.95(1)
Ti Bond Valence Sum	4.46(7)	4.4(1)	4.140(5)

The difficulty in refining plausible models against these diffraction data suggests that other factors must be present to complicate an otherwise reasonably straight forward structural refinement. Although Höche *et al*. were able to successfully refine a plausible (3+1)-dimensional model against HRPD data, the sample was ground up from a single crystal grown via the Czochralski method. The superior signal to noise ratio and resolution of the data collected by Höche *et al*. are potentially significant contributing to their success in producing a stable, plausible refinement of the modulated structure. However, the fact that the specimen was grown as a single crystal means that it is more likely that the stoichiometry is constant across the entire sample. In contrast, the samples in the current project were synthesised in polycrystalline form via conventional solid state synthetic methods, increasing the likelihood of sample inhomogeneity. This supported by the work of Wong *et al*.[153] that has shown that sample inhomogeneity in the $Ba_{2x}Sr_{2-2x}TiSi_2O_8$ system is present and that this has a direct influence of the modulation characteristics of each sample.

The following section will discuss the investigation of the $Ba_2TiGe_2O_8$ structure at non-ambient temperatures with a focus on the structural phase transitions that have been reported by Markgraf *et al*.[55] and Ijima *et al*.[57]

5.3.2 $Ba_2TiGe_2O_8$ structure at non-ambient temperatures

Synchrotron X-ray powder diffraction data were collected from the powder diffraction beamline at the Australian synchrotron on heating between 125 K - 350 K, and 298 K - 1273 K using the low temperature cryostream and high temperature hot air blower attachments, respectively. The unit cell parameters that were calculated from Rietveld refinement against synchrotron X-ray powder diffraction data between 125 K - 1273 K are provided in Figure 5.5. Firstly, the 'lock-in' transition close to ambient temperature will be discussed, followed by the high temperature transition that has been reported to occur at 1083 K.

5.3.2.1 Low temperature transition in $Ba_2TiGe_2O_8$

The unit cell parameters and volume that were calculated from Rietveld refinement against synchrotron X-ray powder diffraction data are presented in Figure 5.5 and Figure 5.6, respectively. A change in gradient of the unit cell volume was identified on heating close to the temperature at which the lock-in transition is reported to occur. The temperature of this transition was identified to be 370 K from the intersection of the lines of best fit to the unit cell volume above (red) and below (green) the low temperature transition in Figure 5.6.

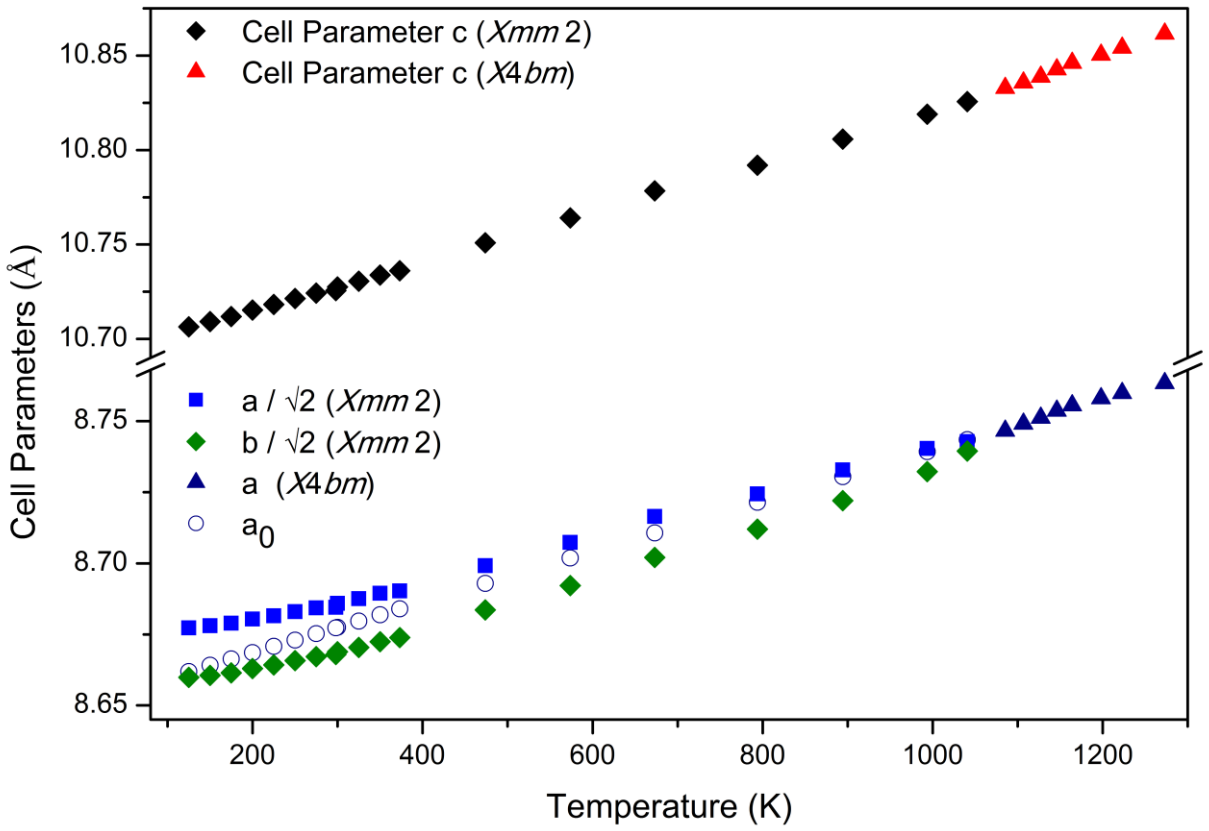

Figure 5.5: Unit cell parameters *a*, *b*, and *c* for the $Ba_2TiGe_2O_8$ orthorhombic phase, and cell parameter *a* and *c* for the tetragonal phase between 125 K - 1273 K. Unit cell parameters *a* and *b* for the orthorhombic phase have been converted into the tetragonal setting to allow for direct comparison with the tetragonal phase. a_0 represents the line of best fit for the tetragonal phase which has been extrapolated to 125 K.

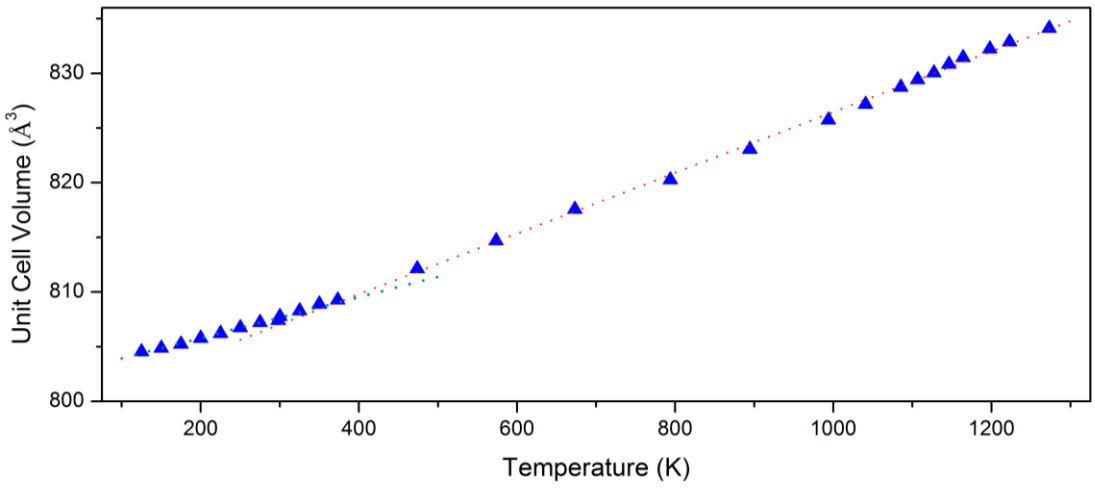

Figure 5.6: Unit cell volume of the $Ba_2TiGe_2O_8$ average structure between 125 K - 1273 K as calculated from Rietveld refinement against synchrotron X-ray powder diffraction data. Data points for the orthorhombic phase have been converted to the tetragonal setting to allow for the direct comparison between the two phases. Linear fits to the unit cell volume above and below the low temperature transition are plotted in red and green, respectively.

The orthorhombic strain (proportional to Q^2) was calculated between 125 K - 1273 K using the extrapolation of the cell parameters with zero strain from the tetragonal phase (a_0) and Equations 4.4 and 4.5 (Figure 5.7). The strain exhibits similar behaviour to $Sr_2TiSi_2O_8$ at high temperatures whereby the rate of reduction in the strain increases as the structure approaches the transition; providing evidence that the high temperature is not first order in nature.

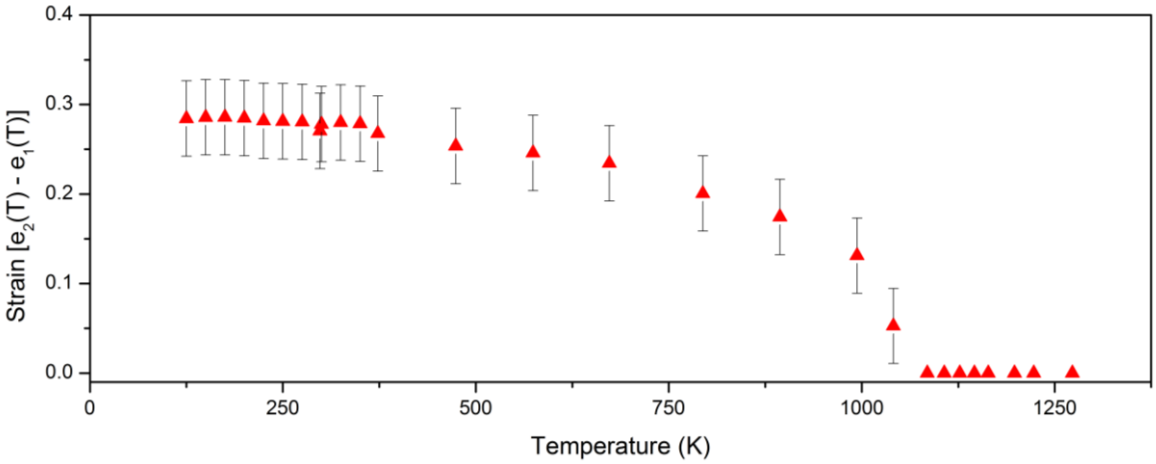

Figure 5.7: Orthorhombic strain in $Ba_2TiGe_2O_8$ on heating between 125 K - 1273 K as calculated from cell parameters determined from Rietveld refinement against synchrotron X-ray powder diffraction data.

The e_{ortho}^2 parameter was also calculated for the $Ba_2TiGe_2O_8$ structure between 125 K - 1273 K (Figure 5.8) to identify any trends in the order parameter that could provide further information about the nature of the high temperature phase transition. However, the uncertainty in the calculated values is significantly larger than the data points. For this reason, no definitive conclusions about the order of the transition can be drawn from the strain analysis.

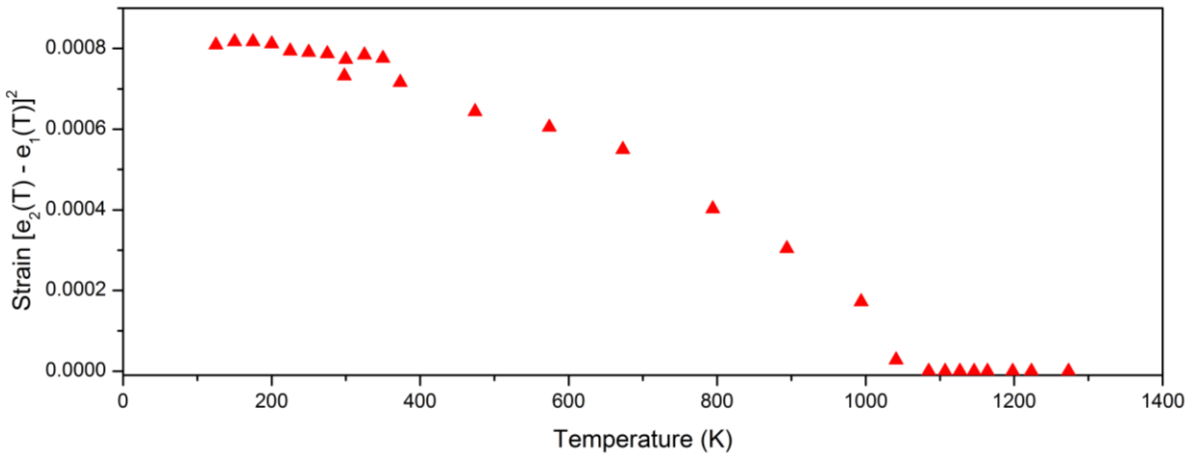

Figure 5.8: Square of the orthorhombic strain in $Ba_2TiGe_2O_8$ on heating between 125 K - 1273 K as calculated from cell parameters determined from Rietveld refinement against synchrotron X-ray powder diffraction data. Note that the uncertainty calculated for the data points are very large relative to the absolute values.

High intensity neutron powder diffraction patterns were collected at 2.5 K intervals on heating and cooling between 160 K - 320 K to determine whether any further evidence of changes in the satellite reflections could be identified across the phase transition. An abrupt change in the position of the 004 and $151\bar{1}$ reflections at 66° and 70° two theta, respectively at 220 K on cooling as shown in Figure 5.9 coincides with the transition temperature of 223 K as determined by Halliyal *et al.*[200] and Markgraf *et al.*[55] from the changes in the dielectric constant, pyroelectric coefficient, and X-ray precession photographs.

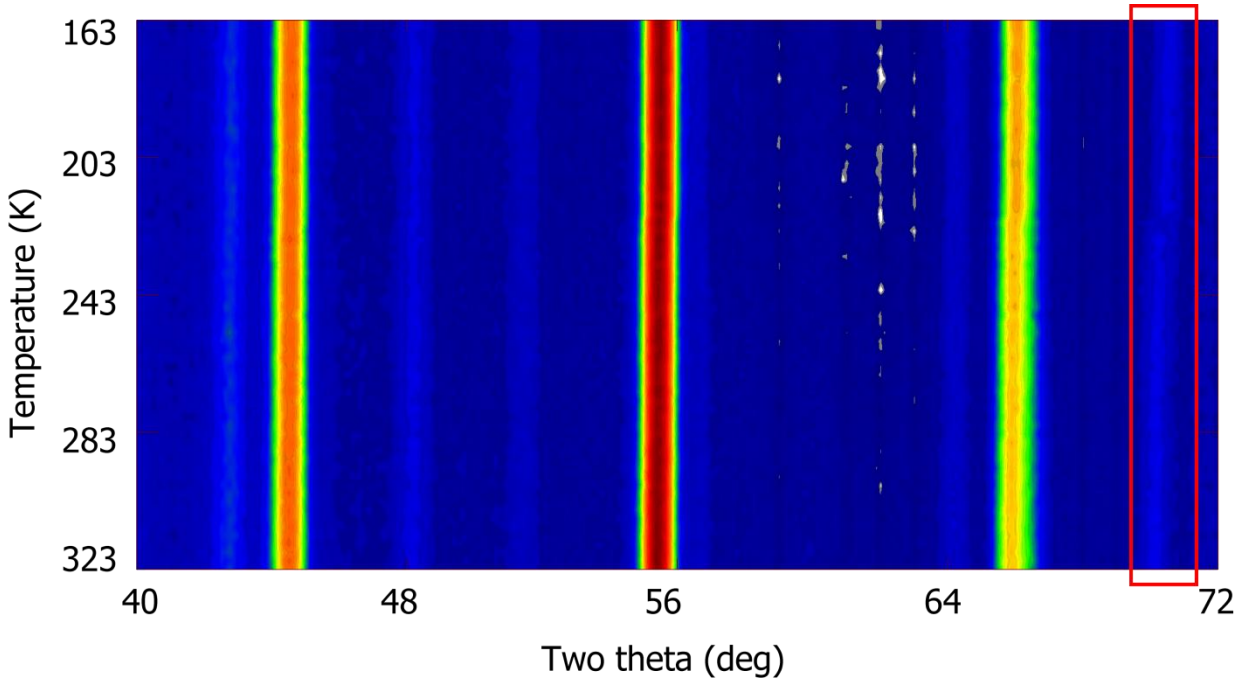

Figure 5.9: Ramping plot showing variable temperature high intensity neutron powder diffraction data collected from $Ba_2TiGe_2O_8$ on cooling from 320 K - 160 K at λ = 2.86(1) Å. The red box identifies the $151\bar{1}$ reflection that shows an abrupt change in position at 220 K.

The change in position of these reflections may be attributed to a shift in the position of the satellite reflections. The change in the position of the $151\bar{1}$ reflection at 220 K is shown in Figure 5.10 where the evidence suggests that something structurally significant may have occurred at this temperature. Such changes were not observed for any other satellite reflections. The only other reflection to show this change was the 004 reflection which is not expected to include contributions from any satellite reflections according to the modulation parameters published by

Höche *et al.*[71] that were trialled against the current data set. This suggests that the change is either an artefact of the experiment, or that the structural change has a significant effect on the magnitude of unit cell parameter *c*. However, the evidence suggests that the shift in the reflections may be an artefact of the experiment because no corresponding change was observed in the unit cell parameter *c* determined from synchrotron X-ray powder diffraction. Also, no evidence of the transition could be identified in the neutron diffraction data set collected while heating over the identical temperature range. It would be extremely difficult to ascertain more information about the 'lock-in' transition from these data sets because of the subtle nature of the change between the commensurate and incommensurate phase.

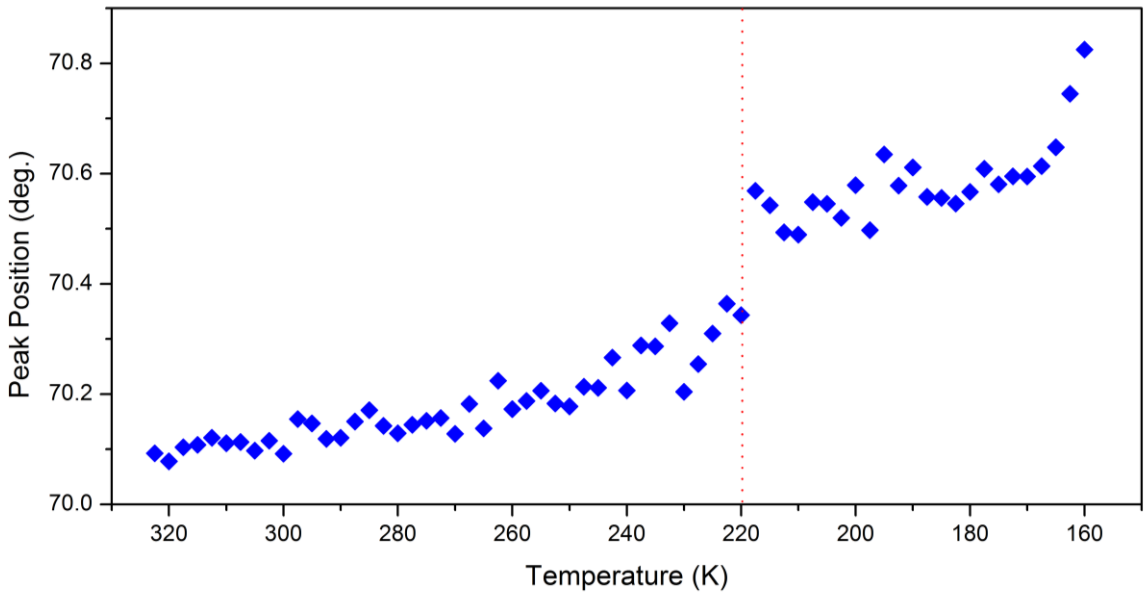

Figure 5.10: Position of the $151\bar{1}$ reflection for $Ba_2TiGe_2O_8$ on cooling between 323 K - 160 K as determined from high intensity neutron powder diffraction data.

Resonant ultrasound spectroscopy data were collected between 200 Hz - 1200 kHz between 192 K - 305 K on heating and 188 K - 232 K on cooling from a $Ba_2TiGe_2O_8$ single crystal of dimensions 4.184 x 2.684 x 2.364 mm^3 and mass = 0.140 g that was supplied by Prof. T. Höche (Leibniz-Institut für Oberflächenmodifizierung e.V., Leipzig, Germany). The change in the position of the resonances at approximately 493 kHz and 502 kHz in Figure 5.11 are representative of the

resonances in the spectrum and neatly demonstrate the coupling between the elastic moduli and the structural changes across the lock-in phase transition.

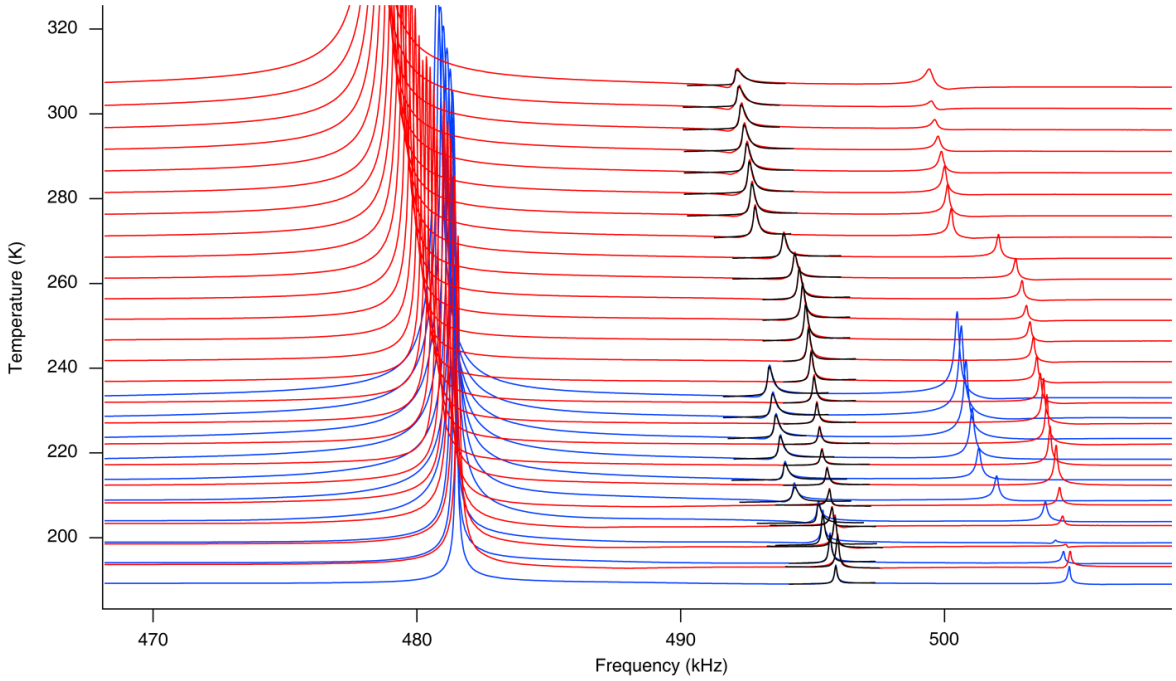

Figure 5.11: Resonant ultrasound spectroscopy data collected from a $Ba_2TiGe_2O_8$ single crystal between 200 kHz - 1200 kHz and 190 K - 305 K on heating (red) and cooling (blue). The black lines are the Lorentzian peaks that have been modelled to describe the resonance at 493 kHz at each temperature.

The positions of the resonances at approximately 493 kHz and 553 kHz were determined by fitting an asymmetric Lorentzian function using the method described in section 2.5.5. The square of the frequency (proportional to the elastic modulus) for both resonances is plotted against temperature in Figure 5.12 where hysteresis in the change in the elastic moduli is observed. The transition was determined to occur at 206 K on cooling and 268 K on heating, providing a reasonable agreement with the published values of ~223 K on cooling and ~273 K on heating.[55]

The reliability and consistency of the data obtained from the resonant ultrasound spectroscopy study demonstrate that the elastic moduli are appropriate parameters to use in the investigation of transitions such as the $Ba_2TiGe_2O_8$ 'lock-in' transition where clear evidence of the phase transition may not be easily gathered from other techniques such as X-ray or neutron diffraction.

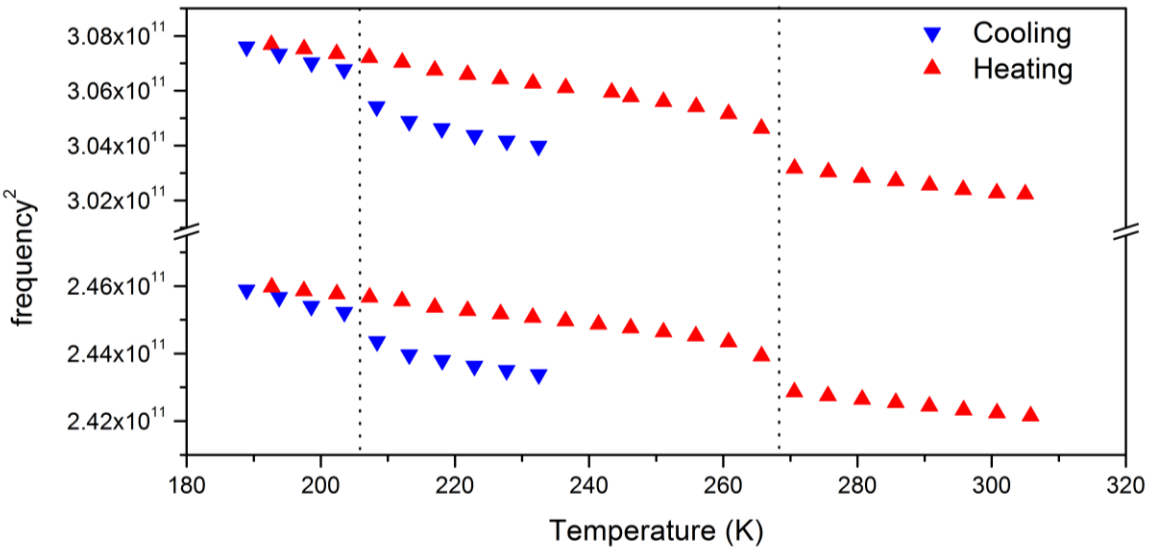

Figure 5.12: The square of the position of the resonances at approximately 493 kHz and 553 kHz from resonant ultrasound spectroscopy data between 185 K - 310 K indicating hysteresis in the low temperature phase transition.

The inverse mechanical quality factor was determined for the resonances between 185 K - 310 K and plotted in Figure 5.13. A small maxima is observed on cooling, and a discontinuity observed on heating in the temperature ranges corresponding to the discontinuity in the elastic moduli identified in Figure 5.12. The hysteresis in the changes in the relaxation behaviour of the structure as it passes through these temperatures provides further evidence of the hysteresis in the two low temperature phase transitions of $Ba_2TiGe_2O_8$.

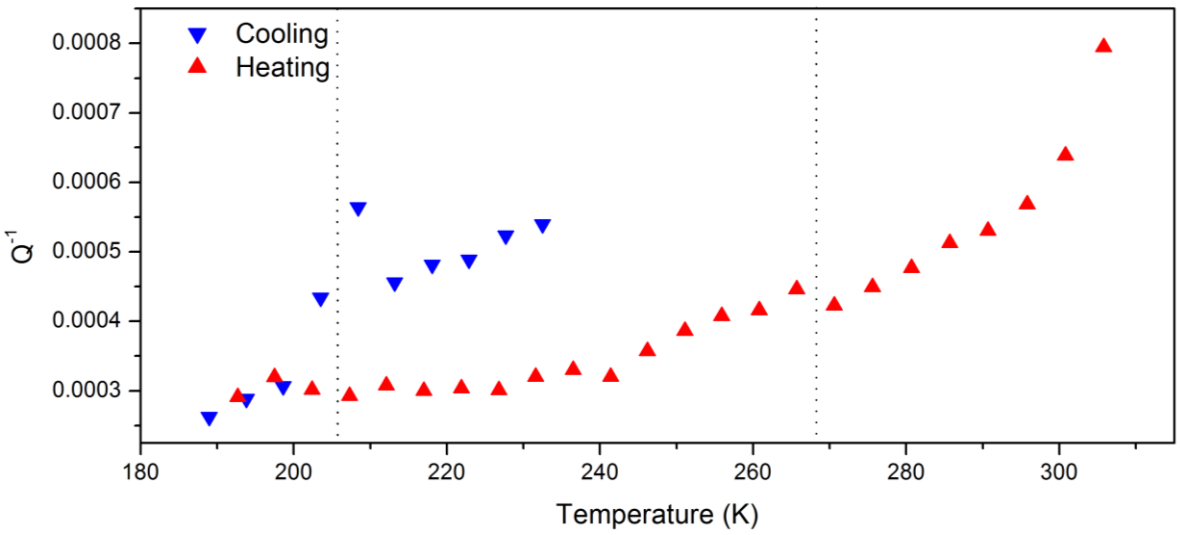

Figure 5.13: The inverse quality factor of the resonances at approximately 493 kHz and 553 kHz from resonant ultrasound spectroscopy data between 185 K - 310 K.

5.3.2.2 High temperature transition in $Ba_2TiGe_2O_8$

The high temperature phase transition from the orthorhombic phase to the higher symmetry 4*mm* phase as reported by Kimura *et al.*[77] could be identified from the convergence of the *a* and *b* unit cell parameters calculated from variable temperature synchrotron X-ray powder diffraction data (Figure 5.5). The high temperature phase was successfully refined using the parent *X*4*bm* space group, showing that heating up to the ferroelastic phase transition removes the need for the structure to deviate from the parent *X*4*bm* space group that is adopted by $Ba_2TiSi_2O_8$. The experimental data and important parameters for the refinement of the $Ba_2TiGe_2O_8$ structure at 1085 K are provided in Table 5.6.

Table 5.6: Experimental data and important parameters for the characterisation of $Ba_2TiGe_2O_8$ at 1085 K.

Parameter	$Ba_2TiGe_2O_8$
Wavelength (Å)	λ = 0.82703(1)
Molar mass (g mol^{-1})	595.73
Space group	*X*4*bm*
Z	4
a (Å)	8.74657(3)
c (Å)	10.83282(2)
V (Å^3)	828.740(4)
D_{calc} (g cm^{-3})	4.7731(3)
Linear abs. coeff. (mm^{-}	26.113
R_B	8.01 %
R_{wp}	3.22 %

The observed, calculated, and difference plots from the refinement of the $Ba_2TiGe_2O_8$ structure at 1085 K against synchrotron X-ray powder diffraction data are provided in Figure 5.14, indicating an excellent fit of the calculated pattern to the observed pattern. The atomic positions and atomic displacement parameters refined for this structure are provided in Table 5.7. Structural parameters for the refined structures at all other temperatures are available in Appendix B of the attached Appendix DVD.

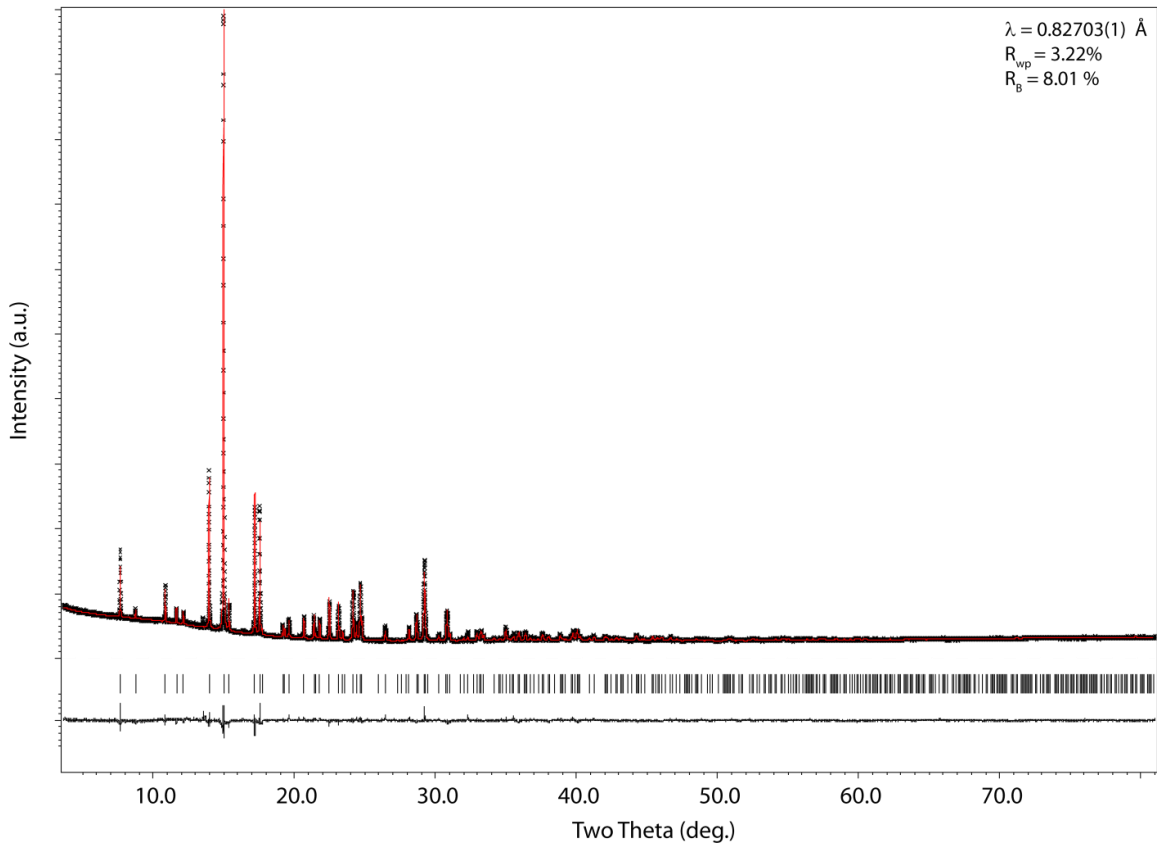

Figure 5.14: Observed, calculated, and difference plots from the refinement of the $Ba_2TiGe_2O_8$ structure at 1085 K.

Table 5.7: Atomic positions and atomic displacement parameters for $Ba_2TiGe_2O_8$ at 1085 K as determined from refinement against synchrotron X-ray powder diffraction data.

	Ba	Ti	Ge	O1	O2	O3	O4
x	0.32742(6)	0	0.1315(1)	0	0.1294(6)	0.2938(6)	0
y	0.82742	0	0.6315	0.5	0.6294	0.5821(7)	0
z	0.0060(1)	-0.2617(7)	-0.2499(3)	-0.309(1)	-0.0809(7)	-0.3042(6)	-0.109(2)
U_{iso} (Å²)	0.0399(2)	0.030(1)	0.0024(4)	0.0230(4)	0.033(3)	0.063(3)	0.099(6)

The constant volume expansion across the transition 1085 K in Figure 5.6 supports the work of Schmid *et al.*[60] and Iijima *et al.*[57] where the gradual decrease in the spontaneous birefringence to zero was used to show that the transition is second order.

Considering the change in the *a* and *b* cell parameters of the orthorhombic phase as the structure approaches the transition shows that cell parameter *a* does not deviate greatly from conventional, linear thermal expansion. Rather, as the structure approaches the transition, cell parameter *b* increases its rate of thermal expansion until it converges with cell parameter *a*. This behaviour

suggests that the reduction of strain in the structure is primarily driven by changes that occur in the [010]-direction rather than the [100]-direction. This is strongly supported by the birefringence measured from $Ba_2TiGe_2O_8$ single crystals by Iijima *et al.*[71] The relevant figure from Iijima *et al*. demonstrating this behaviour is provided in Figure 5.15A where the birefringence of crystals cut perpendicularly to the *b*-axes increases at a greater rate than crystals cut perpendicularly to the *a*-axis until the birefringence is equal at the phase transition temperature. A close up of the relevant region of the calculated unit cell parameters determined from the current study is provided in Figure 5.15B where similar behaviour to the birefringence is observed.

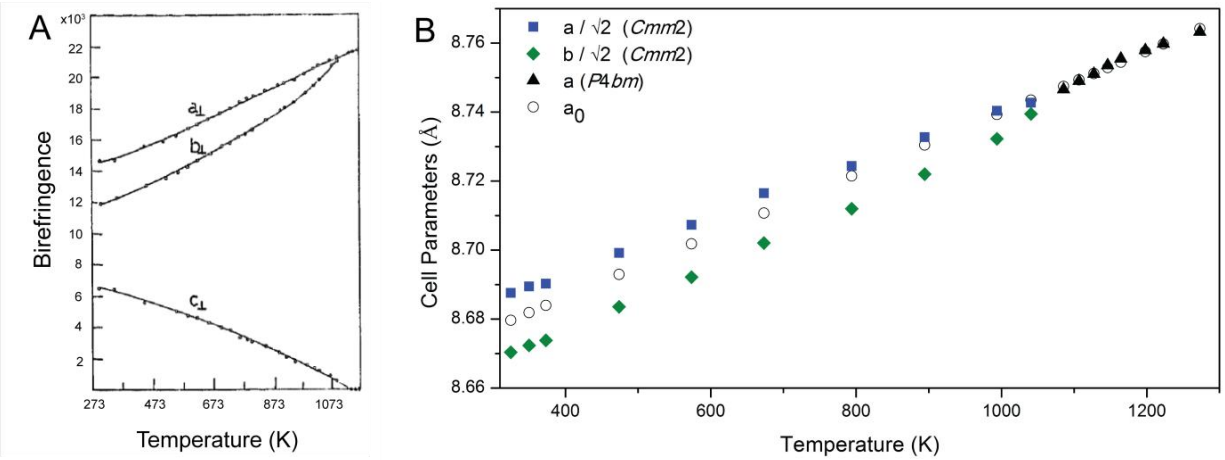

Figure 5.15A: Birefringence measured from $Ba_2TiGe_2O_8$ single crystals cut perpendicularly to the *a*-, *b*-, and *c*-axes between 273 K - 1173 K. This figure has been ammended from Iijima *et al.*[57] B) Close up of the unit cell parameters calculated in this study showing similar behaviour to the birefringence in part A.

Resonant ultrasound spectroscopy data were collected between 200 Hz - 1100 kHz on cooling from 1245 K - 293 K from the sample single crystal described on section 5.3.2.1. The resonance positioned at approximately 330 kHz was modelled at each temperature such that the change in elastic moduli could be monitored across the high temperature transition as shown in Figure 5.16.

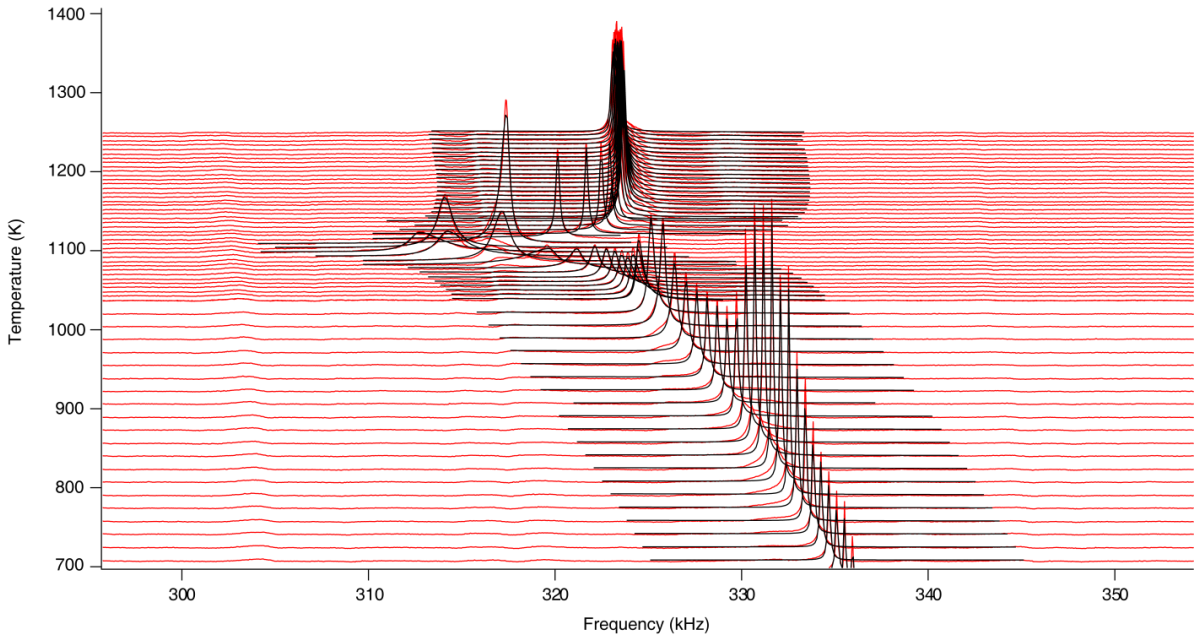

Figure 5.16: Resonant ultrasound spectroscopy data collected from a ceramic $Ba_2TiGe_2O_8$ sample between 200 kHz - 1100 kHz and 495 K - 1250 K (red). The position and FWHM of the resonance at approximately 330 kHz were determined from modelling the data at each temperature (black).

The square of the position of the resonance at approximately 330 kHz shows softening of the elastic moduli on heating up to the transition at approximately 1097 K as shown in Figure 5.17. Elastic softening is a typical property observed in structures as they approach phase transitions.[168,171] These results are consistent with those obtained from the high temperature synchrotron X-ray powder diffraction experiments where the transition temperature was found to be approximately 1085 K. Similarly, these values are consistent with the those reported by Kimura *et al*. (*c.f.* 1083 K), indicating that the high temperature phase transition temperature is consistent across polycrystalline and single crystal $Ba_2TiGe_2O_8$ samples.

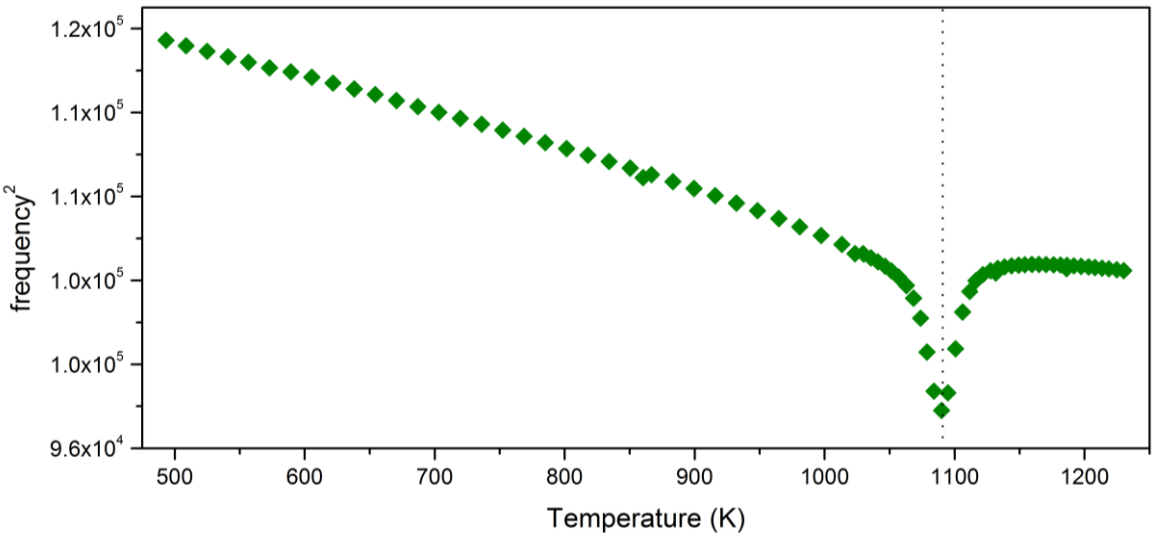

Figure 5.17: The square of the position of the resonance at approximately 335 kHz from resonant ultrasound spectroscopy data between 495 K - 1250 K indicating that the minima in the elastic moduli occurs at 1097 K.

The inverse mechanical quality factor was determined for the resonances between 493 K - 1250 K and plotted in Figure 5.18, demonstrating that a maxima in the acoustic dissipation of the compound coincides with the high temperature phase transition.

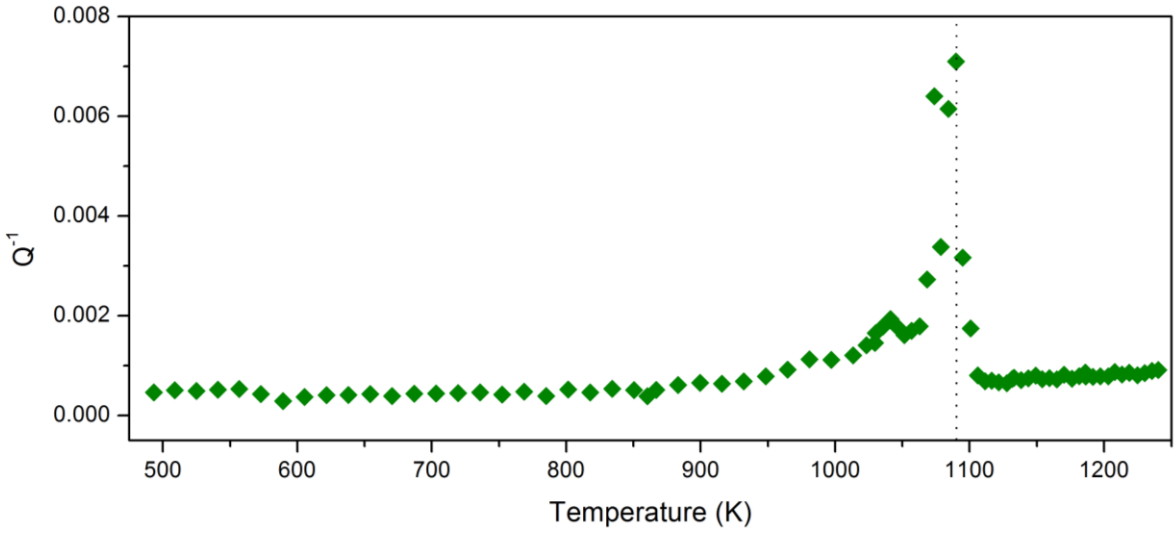

Figure 5.18: The inverse quality factor of the resonance at approximately 335 kHz from resonant ultrasound spectroscopy data between 495 K - 1250 K.

5.4 Summary

It has been shown that the refinement of the modulated structure of $Ba_2TiGe_2O_8$ against synchrotron and neutron powder diffraction data collected from samples synthesised via conventional solid state methods is not possible against the data collected in this project. Moreover, the refinement of the average structure was also shown to be a difficult process whereby the refinement of atomic positions produced unreasonable bond lengths and hence unreasonable bond valence sums for the titanium and oxygen ions. The position of the titanium ion was shown to be the most unstable parameter, producing an excessively short bond to the axial oxygen ion and longer bonds to the basal oxygen ions in the square pyramid when refined against synchrotron data, and conversely, a long axial bond and four short bonds to the basal oxygen ions when refined against neutron powder data. This has demonstrated the high level of difficulty in refining the $Ba_2TiGe_2O_8$ structure from polycrystalline samples that have been synthesised via conventional solid state routes. The origin of these difficulties may be attributed to the presence of inhomogeneous nanodomains as discussed by Wong *et al.*[124] for $Ba_2TiSi_2O_8$ and $Sr_2TiSi_2O_8$ that are more likely to occur in bulk polycrystalline materials over the single crystal samples that have been investigated previously.

Calculation of the orthorhombic strain across the low temperature 'lock-in' transition from the commensurate to incommensurate structures revealed a possible change in gradient in the vicinity of the transition, however the lack of satellite reflections made the characterisation of this transition impossible. High intensity neutron powder diffraction data collected in 2.5 K intervals on heating and cooling across the transition showed an abrupt change in the position of the 004 and $151\bar{1}$ reflections at 220 K on cooling, however this behaviour was not reproduced when the sample was heated through the transition, demonstrating that this may not be a real feature of the sample. The changes in the resonant ultrasound spectra at 206 K on cooling and 268 K on heating showed that there is strong coupling between the elastic moduli and the changes in structure

from the incommensurate to the commensurate phase. This conclusion demonstrates how resonant ultrasound spectroscopy is an excellent technique for the investigation of subtle phase transitions that involve very small changes in the structure which can be difficult to identify using diffraction techniques.

The phase above 1085 K was successfully refined against powder diffraction data using the *X*4*bm* space group for the first time, establishing that the structure adopts the symmetry of the parent fresnoite structure on heating. The $Ba_2TiGe_2O_8$ structure was shown to undergo constant volume expansion occurs on heating, however, no formal conclusions could be drawn from the strain analysis owing to the large uncertainty in the calculated values for e_{ortho}^2. It was also established that the structural changes that occur to reduce the spontaneous strain as the temperature approaches the phase transition temperature are primarily in the *b*-direction rather than the *a*- or *c*-directions. This is consistent with the optical birefringence measurements conducted by Iijima *et al*.[57] where similar behaviour was observed. The softening of the elastic moduli from resonant ultrasound spectroscopy as the structure approaches the ferroelastic transition occurred at 1097 K in reasonable agreement with the transition temperature determined from synchrotron X-ray diffraction and previously reported single crystal studies (*c.f.* 1085 K and 1083 K, respectively).

Chapter 6 Formation and Phase Diagrams for the $Ba_{2x}Sr_{2-2x}TiGe_{2y}Si_{2-2y}O_8$ System

6.1 Introduction

The work contained in this chapter investigates the structure of members of the $Ba_{2x}Sr_{2-2x}TiGe_{2y}Si_{2-2y}O_8$ ($0 \leq x \leq 1$; $0 \leq y \leq 1$) system that contain more than one type of ion on either the *A*- and/or *M*-site. The investigation of these compounds is of high interest because it will develop an understanding of how substitutions on the *A*- and/or *M*-sites change the structure and temperatures of the phase transitions of the end members.

At present, only a small number of studies have investigated the $Ba_{2x}Sr_{2-2x}TiGe_{2y}Si_{2-2y}O_8$ ($0 \leq x \leq 1$; $0 \leq y \leq 1$) system. These include the variable temperature analysis of single crystals using X-ray diffraction by Iijima *et al.*[88] and the measurement of dielectric constants, optical birefringence, and pyroelectric coefficients by Schmid *et al.*[60] which have been used to construct a composition versus temperature phase diagram describing the phase behaviour of the $Ba_2TiGe_{2y}Si_{2-2y}O_8$ system. A discontinuity in the change in the unit cell parameters of samples across the $Ba_2TiGe_{2y}Si_{2-2y}O_8$ system has been used to establish that the morphotropic phase boundary separating the tetragonal and orthorhombic phases at ambient temperature occurs at approximately $y = 0.5$.[88,153] Changes in the physical properties of members of the system were also used to infer the presence of the phase transition. The temperature of the transition was shown to decrease linearly from 1103 K for the $y = 1$ ($Ba_2TiGe_2O_8$) member to 400 K for the $y = 0.6$ ($Ba_2TiGe_{1.2}Si_{0.8}O_8$) member. The absence of any changes in the physical properties for the $y < 0.6$ members was used to suggest that the morphotropic phase boundary must occur between $0.5 \leq y \leq 0.6$.[60]

In 2011, a study on the $Ba_{2x}Sr_{2-2x}TiSi_2O_8$ ($0 \leq x \leq 1$) system using diffraction from Cu K_α radiation was reported by Wong *et al.*[124] Selected area electron diffraction patterns and high resolution

transmission electron microscopy images collected from members of the $Ba_{2x}Sr_{2-2x}TiSi_2O_8$ ($0 \leq x \leq 1$) system were used to identify nanometric domain intergrowths where regions close to the ideal stoichiometry exhibit commensurate modulations, and regions deviating from the ideal stoichiometry exhibit incommensurate modulations. The results of this study demonstrate how complex the formation properties of the $Ba_{2x}Sr_{2-2x}TiSi_2O_8$ ($0 \leq x \leq 1$) system are, and why the characterisation of polycrystalline samples within this system can be extremely difficult. Other work contained in the PhD thesis by Wong has been conducted on the $Ba_2TiGe_{2y}Si_{2-2y}O_8$ ($0 \leq y \leq 1$) system where an inflection in the trend of the unit cell parameters was presented to suggest that a phase boundary occurs at $Ba_2TiGeSiO_8$ ($y = 0.5$).[153]

In 1999, Höche *et al*.[50] proposed that the relative sizes of the ions occupying the *A*- and *M*- sites of the general $A_2M_3O_8$ fresnoite structure type are important in determining which space group will be adopted for fresnoite compounds of different stoichiometries (see section 1.5). A summary of the different stoichiometries that are possible within the $Ba_{2x}Sr_{2-2x}TiGe_{2y}Si_{2-2y}O_8$ ($0 \leq x \leq 1$; $0 \leq y \leq 1$) system and their predicted space groups at ambient temperature based on the relative sizes of the ionic radii was provided in Chapter 1 and is reproduced in Table 6.1 for reference in this chapter. The limits of the ratio of the ionic radii that were chosen by Höche *et al*.[50] to define which compositions may form with different symmetries were based on only the formation of the four end members and one compound of mixed composition. Hence, the synthesis and characterisation of selected members in the $Ba_{2x}Sr_{2-2x}TiGe_{2y}Si_{2-2y}O_8$ ($0 \leq x \leq 1$; $0 \leq y \leq 1$) system will improve the understanding of which compositions do and do not form, in addition to understanding where the compositional phase boundaries between compounds of different symmetries may occur. Furthermore, the variable temperature investigation of selected members within individual series will provide new information about any changes in the phase transition properties or temperatures that have been discussed for the three end members. These results will be summarised in new phase diagrams for the selected series of interest within the $Ba_{2x}Sr_{2-2x}TiGe_{2y}Si_{2-2y}O_8$ system.

Table 6.1: A summary of the various ratios of mean ionic radii for compositions in the $Ba_{2x}Sr_{2-2x}TiGe_{2y}Si_{2-2y}O_8$ ($0 \leq x \leq 1$, $0 \leq y \leq 1$) system as calculated using Equation 1.3. The ionic radii used in the determination of these values were Ba = 156 pm; Sr = 140 pm; Si = 40 pm; Ge = 53 pm from Shannon.[87]

		x in $Ba_{2x}Sr_{2-2x}TiGe_{2y}Si_{2-2y}O_8$										
		0	0.1	0.2	0.3	0.4	0.5	0.6	0.7	0.8	0.9	1
y in $Ba_{2x}Sr_{2-2x}TiGe_{2y}Si_{2-2y}O_8$	0	3.50 (STS)	3.54	3.58	3.62	3.66	3.70	3.74	3.78	3.82	3.86	3.90 (BTS)
	0.1	3.39	3.43	3.47	3.51	3.54	3.58	3.62	3.66	3.70	3.74	3.78
	0.2	3.29	3.32	3.36	3.40	3.44	3.47	3.51	3.55	3.59	3.62	3.66
	0.3	3.19	3.23	3.26	3.30	3.33	3.37	3.41	3.44	3.48	3.52	3.55
	0.4	3.10	3.13	3.17	3.20	3.24	3.27	3.31	3.35	3.38	3.42	3.45
	0.5	3.01	3.05	3.08	3.11	3.15	3.18	3.22	3.25	3.29	3.32	3.35
	0.6	2.93	2.96	3.00	3.03	3.06	3.10	3.13	3.16	3.20	3.23	3.26
	0.7	2.85	2.88	2.92	2.95	2.98	3.01	3.05	3.08	3.11	3.14	3.18
	0.8	2.78	2.81	2.84	2.87	2.90	2.94	2.97	3.00	3.03	3.06	3.10
	0.9	2.71	2.74	2.77	2.80	2.83	2.86	2.89	2.92	2.96	2.99	3.02
	1	2.64 (STG)	2.67	2.70	2.73	2.76	2.79	2.82	2.85	2.88	2.91	2.94 (BTG)

6.2 Results & Discussion

This section will be divided into five parts where each will discuss the synthesis and formation of systems of interest constituting individual rows or columns in Table 6.1.

6.2.1 $Ba_{2x}Sr_{2-2x}TiSi_2O_8$ System

6.2.1.1 The $Ba_{2x}Sr_{2-2x}TiSi_2O_8$ System at Ambient Temperature

The synthesis of the end members of this system ($Ba_2TiSi_2O_8$ and $Sr_2TiSi_2O_8$) required a maximum temperature of 1250 °C. However, the $Sr_2TiSi_2O_8$ end member required a greater number of grinding and re-heating steps (six) compared to the $Ba_2TiSi_2O_8$ end member (four). Members within this system were synthesised using the same method used for the end members, where more heating steps were used for the Sr-rich end than the Ba-rich end to produce samples of the highest purity possible. A small proportion of $SrTiO_3$ and $SrSiO_3$ was present in some of the $0 \leq x \leq 0.5$ members of the system. The proportion of these impurity phases could be reduced with continued heating at 1250 °C. However, they could not be completely removed. The use of higher reaction temperatures was not beneficial because higher proportions of $SrTiO_3$ were formed as was observed for the $Sr_2TiSi_2O_8$ end member.

No satellite reflections were observed in the synchrotron X-ray powder diffraction patterns collected from the $Ba_{2x}Sr_{2-2x}TiSi_2O_8$ system. Hence, only the average structures of each compound have been considered. The main phase in all members of the $Ba_{2x}Sr_{2-2x}TiSi_2O_8$ system was identified as displaying the same symmetry as has been previously reported.[124] However, weak reflections corresponding to an orthorhombic fresnoite phase were observed for the $x \leq 0.5$ members of the system at approximately 16.1° and 16.2° two theta. These reflections indicate that a two phase mixture of tetragonal and orthorhombic phases exists at ambient temperature instead of only one phase as has been previously reported for this system.[124] Although extremely

weak, the reflections corresponding to the orthorhombic phase contained sufficient intensity to justify their inclusion in the models for the $x < 0.2$ members of the system. It has been assumed that the orthorhombic phase forms in the same space group as the $Sr_2TiSi_2O_8$ end member due to the similarity in stoichiometry and the conditions of synthesis. The intensity of the reflections corresponding to the orthorhombic phase in the $x \geq 0.2$ members of the system were present as tiny bumps that were barely observable over the background. Hence, only single phase tetragonal models could be developed for these compounds.

The unit cell parameters (Figure 6.1) and volume (Figure 6.2) of the main tetragonal phases at ambient temperature across the $Ba_{2x}Sr_{2-2x}TiSi_2O_8$ system were calculated from Rietveld refinement against synchrotron X-ray powder diffraction data. The linear increase in these parameters shows that Vegard's law[203,204] is obeyed. This is a slightly different result to the work contained in the PhD thesis by Wong[153] who observed a small inflection in the cell parameters at $x = 0.5$.[153] The potential for order correlation and/or a change in the modulation were two suggestions presented for this behaviour. However, no evidence supporting the presence of an inflection was found in the current study. It is difficult to determine whether a true discrepancy exists between this study and the study performed by Wong because the unit cell parameters calculated by Wong were based on refinement against diffraction patterns collected using Cu K_α radiation rather than a synchrotron source. The high signal to noise ratio and excellent resolution obtained from the Australian synchrotron provides a strong argument that the behaviour observed in the current study is representative of the true behaviour of the samples synthesised and investigated in this project. The structural data for each member across the system are provided in Appendix B of the attached Appendix DVD.

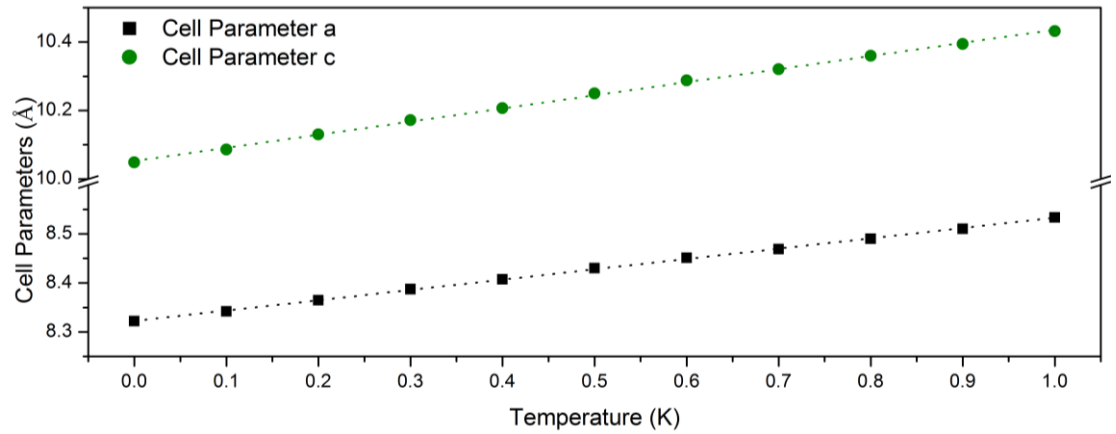

Figure 6.1: Unit cell parameters across the $Ba_{2x}Sr_{2-2x}TiSi_2O_8$ ($0 \leq x \leq 1$) system at ambient temperature as determined from Rietveld refinement against synchrotron X-ray powder diffraction data.

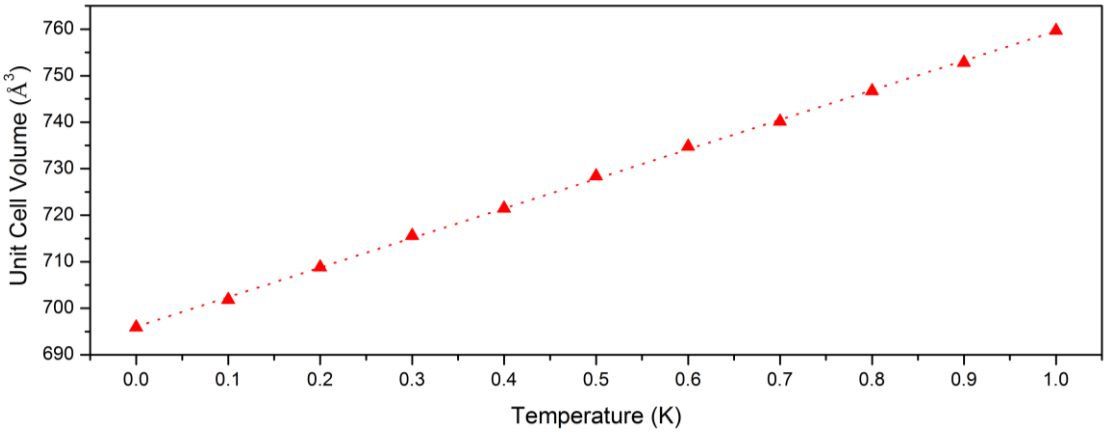

Figure 6.2: Unit cell volume across the $Ba_{2x}Sr_{2-2x}TiSi_2O_8$ ($0 \leq x \leq 1$) system at ambient temperature as determined from Rietveld refinement against synchrotron X-ray powder diffraction data.

Previous work has shown that the titanium ion in fresnoite compounds can exist in geometries other than square pyramidal. For example, Farges *et al.*[205] have shown that some "glassy" fresnoite samples can contain a small proportion of titanium in tetrahedral and octahedral geometries (~20 % each) in addition to the square pyramidal geometry (~60 %), and Coats *et al.*[52] have reported that the titanium ion can occupy some of the tetrahedral sites of the structure (rather than silicon) when additional titanium is available during the reaction. X-ray absorption near edge spectra (XANES) were collected across the titanium edge at approximately 4980 eV from members within the $Ba_{2x}Sr_{2-2x}TiSi_2O_8$ ($0 \leq x \leq 1$) system (Figure 6.3) to investigate

whether any evidence supporting multiple titanium coordination environments could be gathered. The absorbance of each data set was normalised in the pre-edge and post-edge regions such that direct comparisons could be made between different samples. The x = 0.3 member has been omitted from the figure because the signal to noise ratio of the spectra was very low. This has been attributed to insufficiently small particle sizes as a result of poor sample preparation.

The pre-edge feature of the titanium *K*-edge (at approximately 4971 eV in Figure 6.3) provides the most information about the X-ray absorption characteristics of titanium ions, where the line shape is indicative of the coordination environment and the intensity is dependent on the degree of mixing of the titanium *d*-orbitals and the orbitals of the neighbouring ions.[205,206]

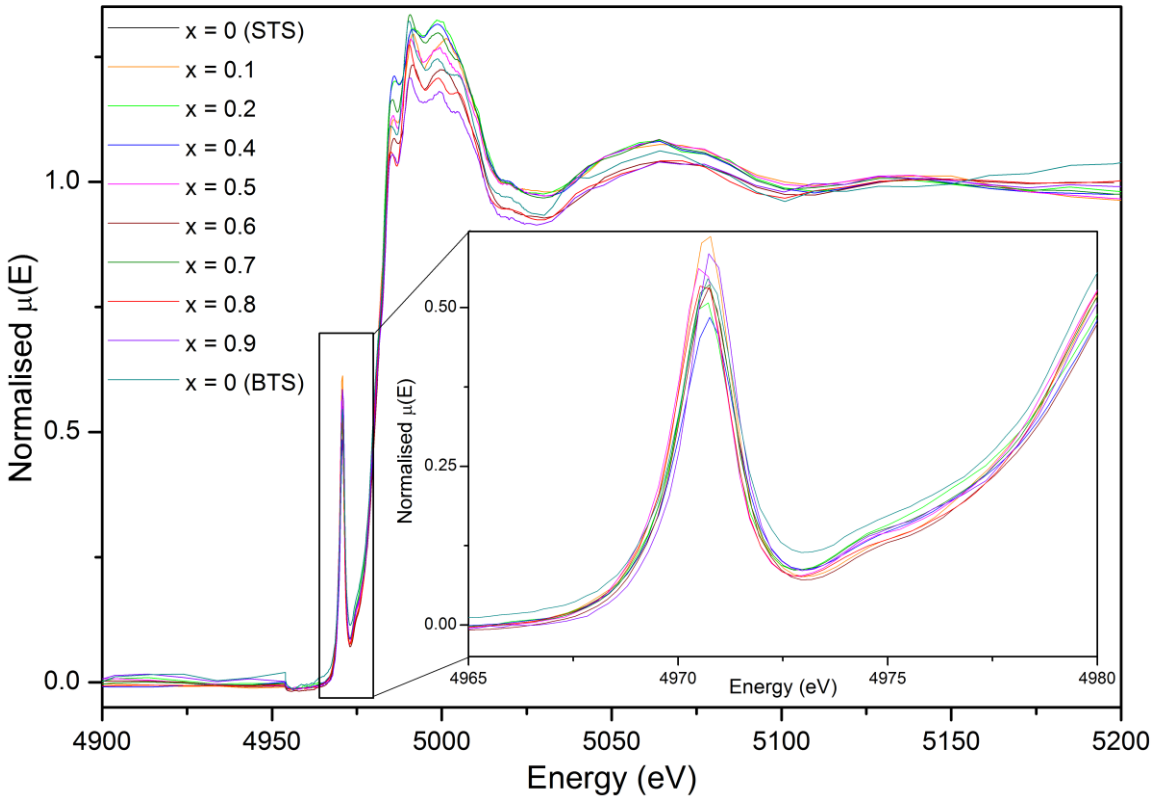

Figure 6.3: X-ray absorption spectra collected for each member of the $Ba_{2x}Sr_{2-2x}TiSi_2O_8$ ($0 \leq x \leq 1$) system. Note that the x = 0.3 spectra has been excluded due to a poor single to noise ratio. The insert shows a close up of the pre-edge feature of the titanium edge for each compound.

To better understand the XANES spectra collected from the fresnoite compounds, a range of titanium-containing materials with well defined titanium geometries were also investigated so the properties of the pre-edge and edge features of the fresnoite spectra could be compared to known standards. The spectra collected from the standards were also compared to spectra in the literature to check they were an accurate reflection of the behaviour of each different type of titanium geometry.[205-207] The spectra collected from the standards are provided in Figure 6.4 where the geometry of the titanium ion in each standard is labelled in brackets. The distinctive splitting of the pre-edge feature in the spectra collected from the standards containing titanium in an octahedral geometry ($SrTiO_3$ and TiO_2) was absent in the spectra collected from the fresnoite compounds. Similarly, relative intensity and splitting of the pre-edge feature in the standards containing titanium in a trigonal bipyramidal geometry ($K_2Ti_2O_5$ and $H_2Ti_2O_5$) did not match the pre-edge feature observed for the fresnoite compound. The absence of the jump in the edge feature observed for the standard with titanium in the tetrahedral geometry (Li_4TiO_4) also did not match the behaviour of the edge feature for the titanium in fresnoite. Hence, the absence of splitting of the pre-edge feature of the spectra collected from the fresnoite compounds combined with the absence of the jump in the edge feature meant that the fresnoite compounds could be best described by the standard containing titanium in the square pyramidal geometry (In_2TiO_5). It was therefore concluded that that the samples contain titanium ions in only the square pyramidal geometry rather than a glassy mixture of multiple coordination environments or the titanium ion residing inside the tetrahedra that normally contains the silicon ions. These observations are consistent with previous XANES studies on the $Ba_2TiSi_2O_8$ and $Sr_2TiSi_2O_8$ end members.[183,205,208,209]

The most noteworthy attribute of the absorption spectra collected from fresnoite materials is the very high relative intensity of the pre-edge feature even in comparison to other square pyramidal compounds as described by Farges *et al*.[205] The high relative intensity of this feature is indicative of strong mixing between the occupied *d*-orbitals of the titanium ion and the neighbouring

p-orbitals of the surrounding oxygen ions and is a direct consequence of the highly compressed square pyramidal geometry of the titanium ion.

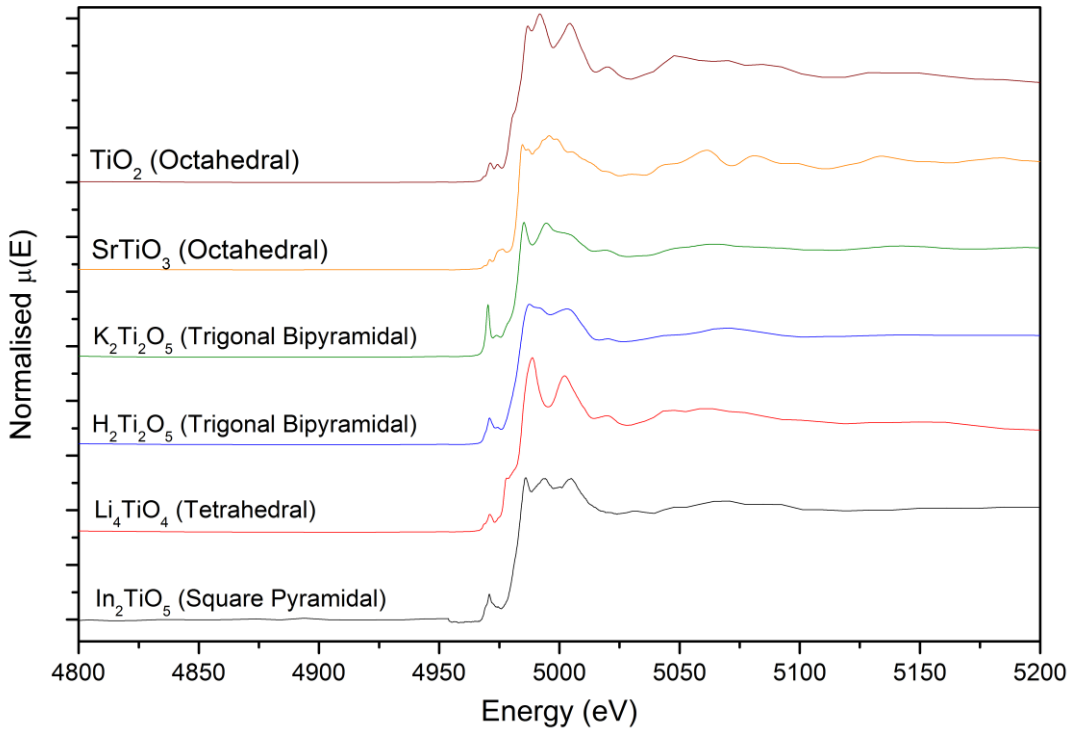

Figure 6.4: Titanium *K*-edge XANES spectra for selected reference compounds containing four-coordinated, five-coordinated, and six-coordinated titanium ions.

Although the line shape of the pre-edge feature is consistent across the entire system, the intensity varies from sample to sample (see inset in Figure 6.3). The change in intensity of the pre-edge feature of the titanium *K*-edge demonstrates that there is variability in the overlap of the titanium *d*- and oxygen *p*-orbitals, suggesting that the bond lengths between the titanium ions and the surrounding oxygen ions are not constant across the series. However, there is no systematic change in the intensity of the pre-edge feature across the series and hence there is no evidence of any trends in the degree of orbital overlap around the titanium ion. Similarly, no systematic trend in the titanium to oxygen bond lengths were identified in the structures refined against the synchrotron powder diffraction data. The apparent randomness in the intensity of the pre-edge feature of the X-ray absorption spectra suggests that the degree of orbital overlap in the

$Ba_{2x}Sr_{2-2x}TiSi_2O_8$ ($0 \leq x \leq 1$) system is either independent of stoichiometry, or that more complex phase properties such as the inhomogeneous distribution of nanodomains within the sample may be affecting the intensity of each spectrum.

6.2.1.2 The $Ba_{2x}Sr_{2-2x}TiSi_2O_8$ System at Non-Ambient Temperatures

Part of the interest in the $Ba_{2x}Sr_{2-2x}TiSi_2O_8$ ($0 \leq x \leq 1$) system is the potential to understand the effect that mixing the proportion of the strontium or barium ions will have on the phase transitions discussed for $Ba_2TiSi_2O_8$ and $Sr_2TiSi_2O_8$ in Chapters 3 and 4, respectively.

The $Ba_2TiSi_2O_8$ structure is known to undergo a structural phase transition from the incommensurately modulated $X4bm(\alpha, \alpha, 0)0gg$ phase to the prototypic $P4bm$ phase at 433 K.[50,53] Clear evidence of this transition in $Ba_2TiSi_2O_8$ samples synthesised in this project was gathered in Chapter 3 where the anomalies in the changes in the individual *a* and *c* unit cell parameters and the elastic moduli coincided with the previously reported transition temperature.

The unit cell parameters for members of the $Ba_{2x}Sr_{2-2x}TiSi_2O_8$ ($0.5 \leq x \leq 1.0$) system were determined from Rietveld refinement against diffraction patterns collected with Cu K_α radiation at temperatures ranging from 300 K to up to 1050 K (Figure 6.5). The change in the gradient of the unit cell parameter *a* has been used to identify the temperature of the transition from the $X4bm(\alpha, \alpha, 0)0gg$ phase to the prototypic $X4bm$ phase. This method was shown to be useful for identifying the transition temperature for the $Ba_2TiSi_2O_8$ end member in section 3.3.2 despite the absence of satellite reflections in the diffraction patterns. The black vertical black lines in Figure 6.5 represent the temperature of the phase transitions as determined from the intersection of the linear fits of the unit cell parameter *a* for the high and low temperature phases, respectively. The temperature of the phase transition increases as more strontium is substituted onto the *A*-site until no phase transition is observed for the $x \leq 0.4$ members. The phase transition temperatures

for each composition are provided, showing that the temperature of the phase transition from the incommensurately modulated $X4bm(\alpha, \alpha, 0)0gg$ phase to the prototypic $X4bm$ phase increases approximately linearly as strontium is substituted for barium on the *A*-site up to the $x = 0.5$.

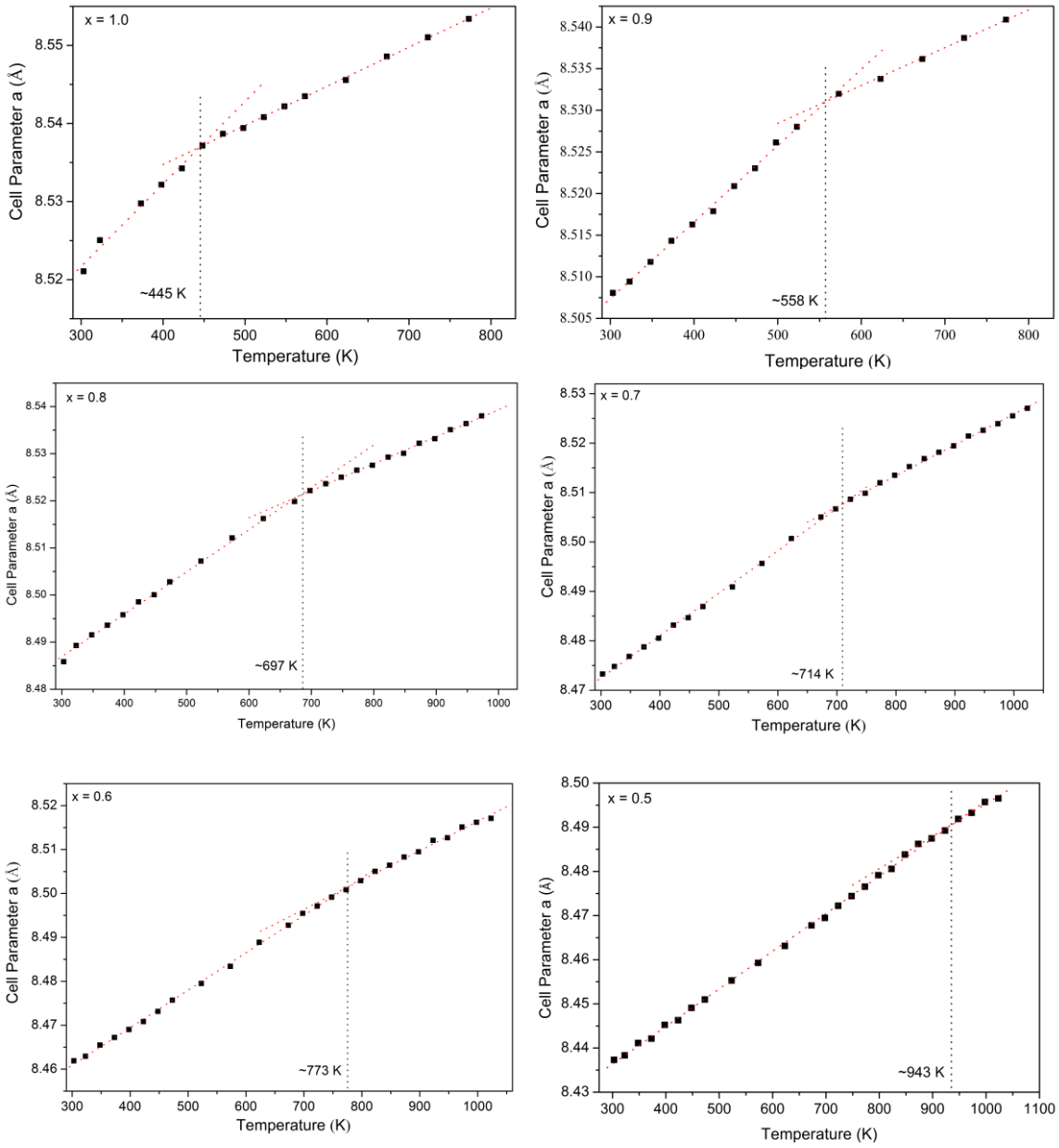

Figure 6.5: Unit cell parameter *a* for members of the $Ba_{2x}Sr_{2-2x}TiSi_2O_8$ ($0.5 \leq x \leq 1$) system calculated from Rietveld refinement against diffraction data collected with Cu K_α radiation between 300 K - 1050 K. The vertical lines represent the phase transition temperatures from the incommensurate phase to the prototypic phase as determined from the intersection of the lines of best fit for the high and low temperature phases, respectively.

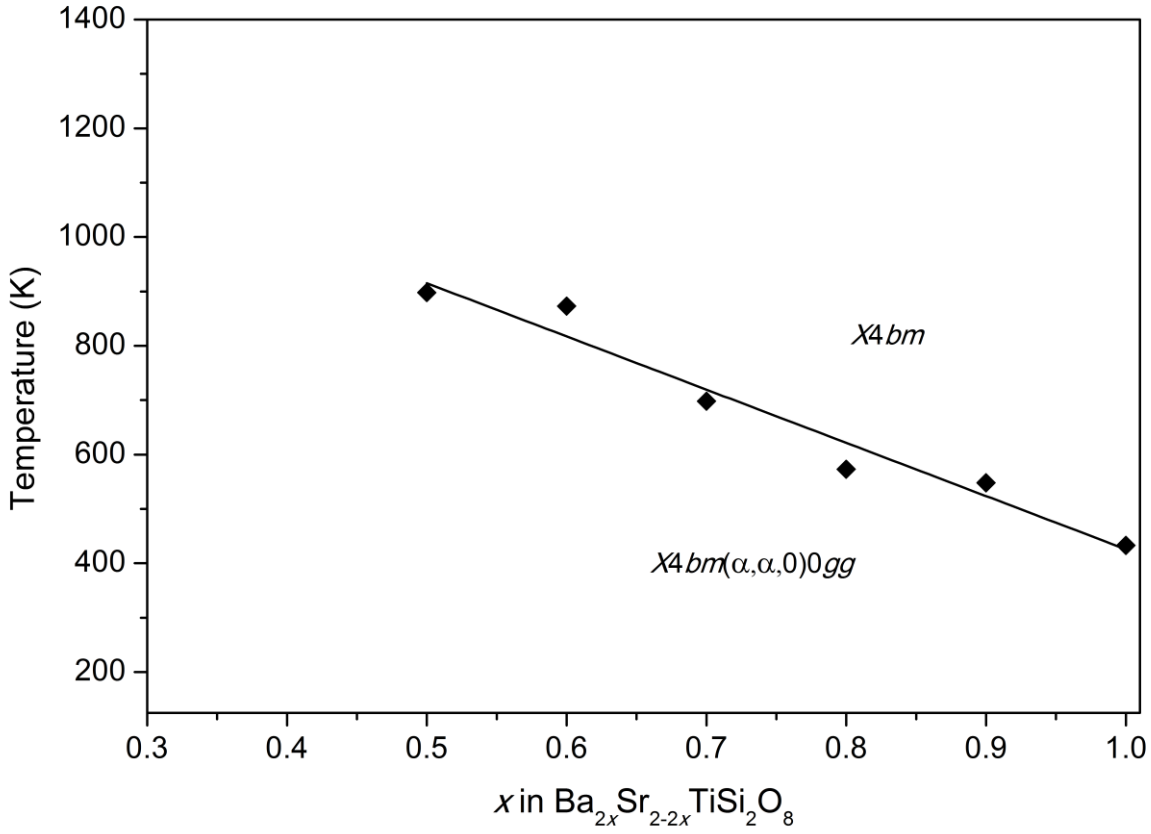

Figure 6.6: $X4bm(\alpha, \alpha, 0)0gg \rightarrow X4bm$ phase transition temperatures for the $Ba_{2x}Sr_{2-2x}TiSi_2O_8$ ($0.5 \leq x \leq 1$) system.

It is also desirable to investigate the phase behaviour of members at the strontium-rich end of the $Ba_{2x}Sr_{2-2x}TiSi_2O_8$ system. The $Sr_2TiSi_2O_8$ end member was shown to exhibit complex phase behaviour involving the coexistence of two incommensurately modulated phases at ambient temperature that undergo a phase transition at approximately 567 K to a single orthorhombic phase, followed by another higher temperature transition to a tetragonal phase at 1323 K.

The $x = 0.05$ and $x = 0.10$ members of the system were further investigated using variable temperature synchrotron X-ray powder diffraction to understand the effect that making small substitutions of barium for strontium has on phase behaviour of $Sr_2TiSi_2O_8$. The variable temperature investigation of these compounds will now be discussed individually.

6.2.1.3 $Ba_{0.1}Sr_{1.9}TiSi_2O_8$ (x = 0.05)

Synchrotron X-ray powder diffraction patterns were collected from $Ba_{0.1}Sr_{1.9}TiSi_2O_8$ between 150 K - 1221 K. Very weak reflections at 15.9° and 18.1° two theta were shown to correspond to an orthorhombic phase (marked with asterisks in Figure 6.7) at ambient temperature.

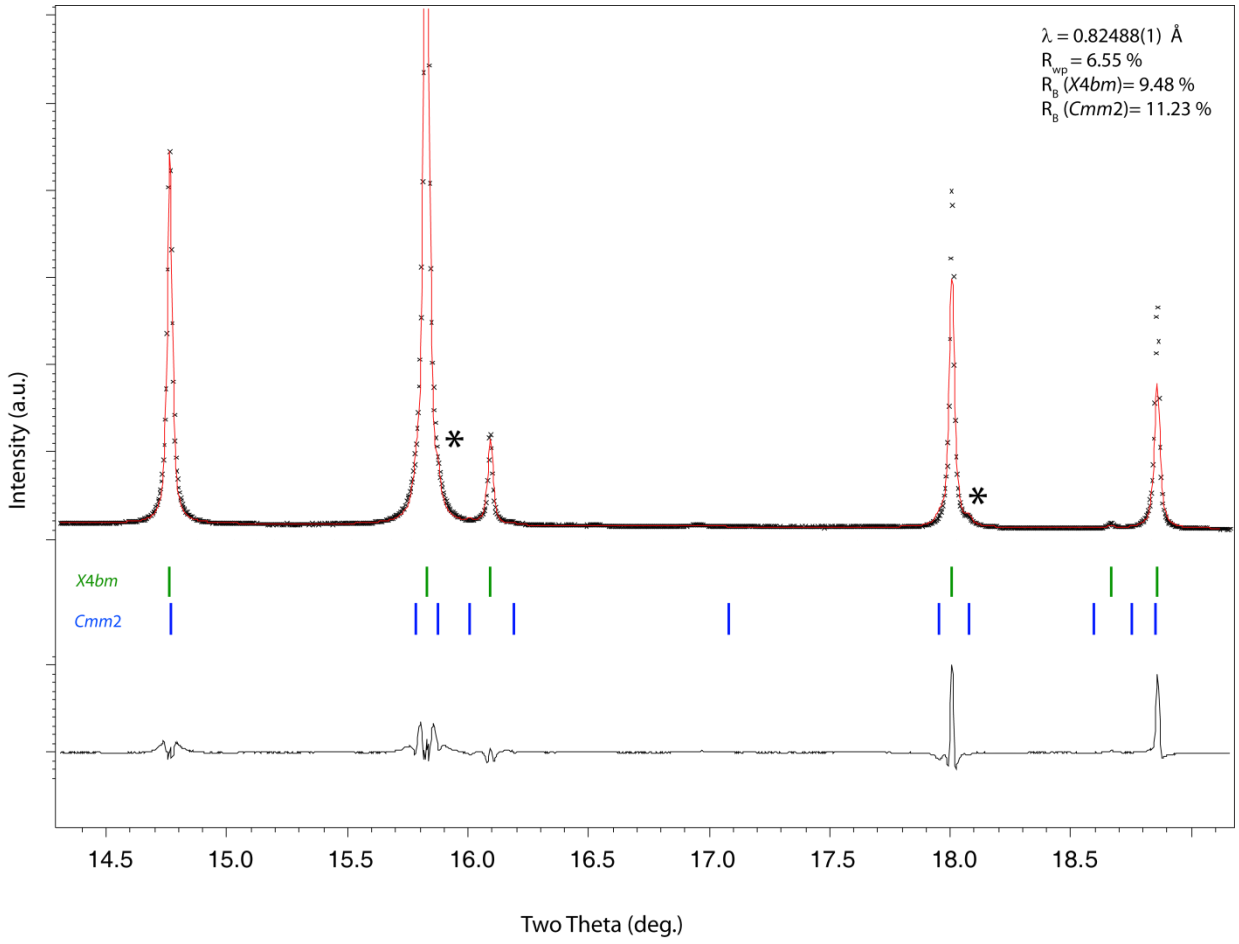

Figure 6.7: Close up of the observed, calculated, and difference plots from the Rietveld refinement of the $Ba_{0.1}Sr_{1.9}TiSi_2O_8$ structure at ambient temperature against synchrotron X-ray powder diffraction data collected at λ = 0.82488(1) Å. Green and blue reflection markers identify calculated reflections corresponding to the tetragonal and orthorhombic phases, respectively. Asterisks mark the positions of observed (but very weak) reflections corresponding to the orthorhombic phase.

The intensity of the weak reflections at 15.9° and 18.1° two theta reduced to almost zero on cooling to 125 K, indicating that the proportion of the orthorhombic phase is reduced on cooling below ambient temperature. The intensities of these reflections below ambient temperature were so small that insufficient information was available to reliably refine any parameters for the

orthorhombic phase. However, the presence of a tiny proportion of the orthorhombic phase indicates that the sample is a two phase mixture at low temperatures in a similar way to what was shown for $Sr_2TiSi_2O_8$ in chapter 4.

Figure 6.8 shows how the intensity of the reflections corresponding to the orthorhombic phase increase on heating, suggesting that $Ba_{0.1}Sr_{1.9}TiSi_2O_8$ undergoes a phase transformation from the *X*4*bm* to the *Cmm*2 phase on heating in a similar manner to $Sr_2TiSi_2O_8$. Further evidence of this transition was observed in the form of the splitting of the 220 and 310 reflections of the tetragonal phase at 16.1° and 18° two theta, respectively.

The convergence of the 312 and 132 reflections and the loss of all intensity corresponding to the 220 reflection from the orthorhombic phase in Figure 6.8 shows that $Ba_{0.1}Sr_{1.9}TiSi_2O_8$ adopts the tetragonal space group at approximately 1221 K (*c.f.* 1323 K for the $Sr_2TiSi_2O_8$ end member as determined in section 4.3.3.2). It is proposed that the $x = 0.05$ member adopts the prototypic *X*4*bm* symmetry above this transition based on the increasing trend in the *X*4*bm*(α, α, 0)*0gg* to *X*4*bm* transition temperatures in the barium-rich members of the $Ba_{2x}Sr_{2-2x}TiSi_2O_8$ system.

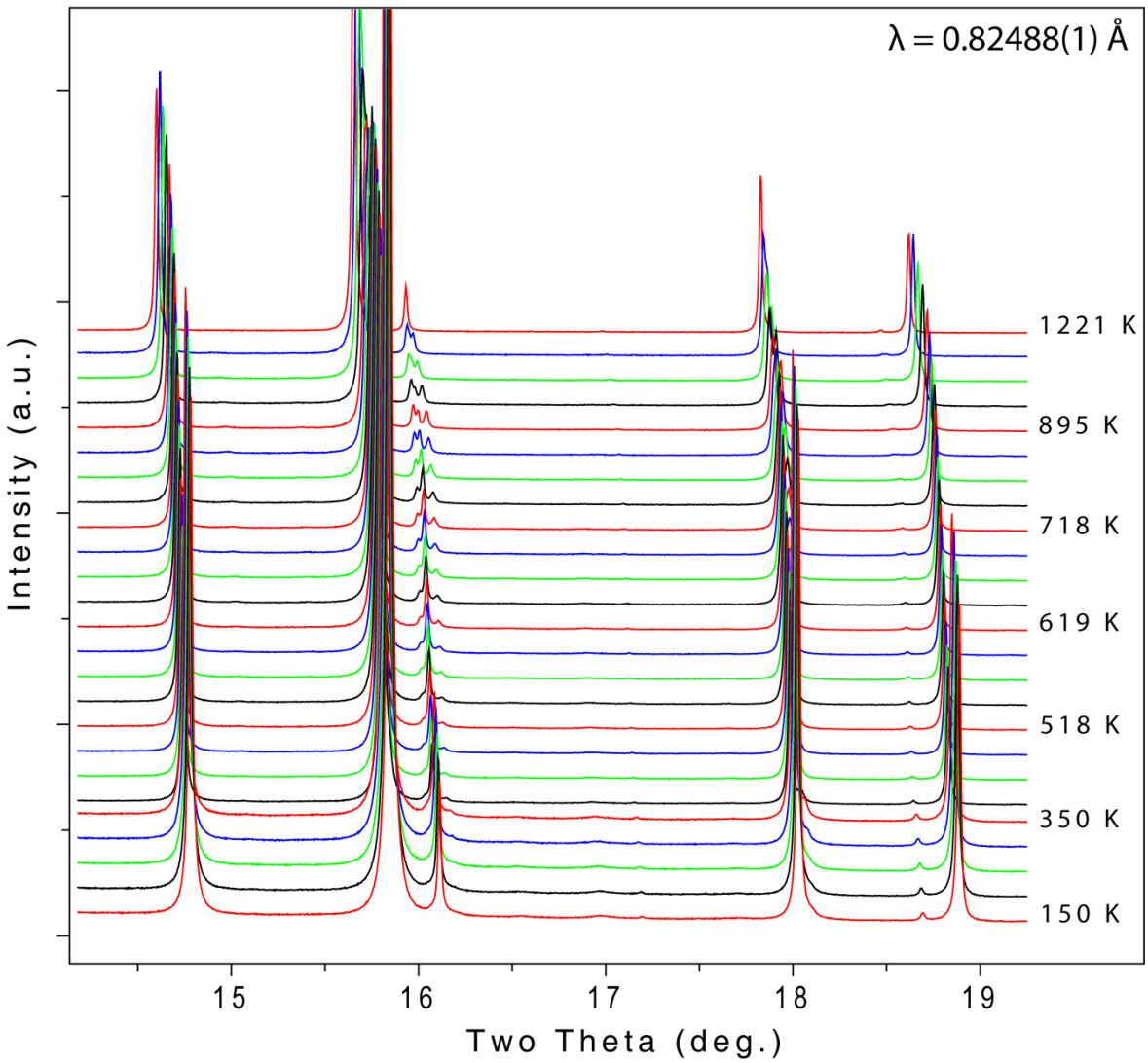

Figure 6.8: Synchrotron X-ray powder diffraction patterns collected from $Ba_{0.1}Sr_{1.9}TiSi_2O_8$ between 150 K - 1221 K showing peak splitting and recombination at 16.1° two theta.

The unit cell parameters were calculated from Rietveld refinement against synchrotron X-ray powder diffraction data collected between 150 K - 1273 K (Figure 6.9). Although similar peak splitting to the closely related $Sr_2TiSi_2O_8$ end member was observed, the specific behaviour of this compound is not identical. The coexistence of the tetragonal and orthorhombic phases occurs from ambient temperature up to 1164 K, indicating that an extremely large coexistence region of these phases exists as the tetragonal phase transforms into the orthorhombic phase on heating. This is in contrast to the complete conversion of the tetragonal phase into the orthorhombic phase at 567 K in $Sr_2TiSi_2O_8$.

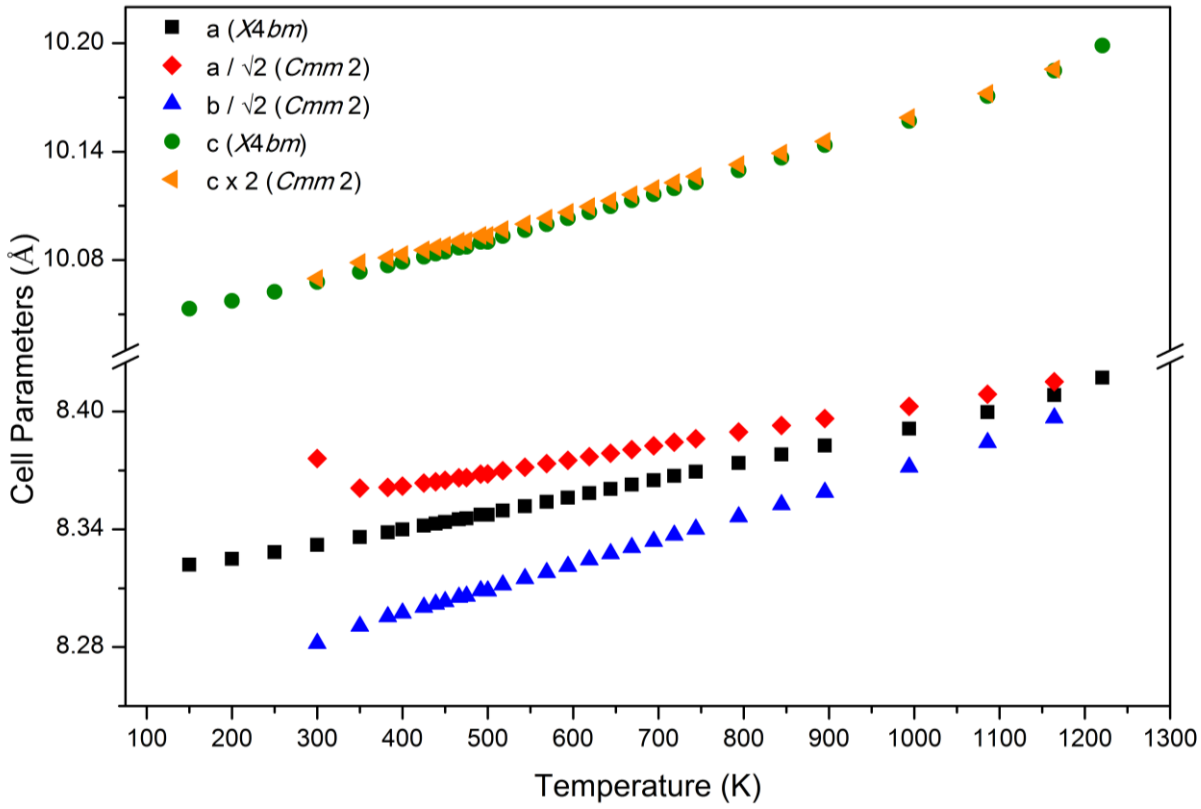

Figure 6.9: $Ba_{0.1}Sr_{1.9}TiSi_2O_8$ unit cell parameters between 150 K - 1373 K as calculated from Rietveld refinement against synchrotron X-ray powder diffraction. Unit cell parameters *a* and *b* for the orthorhombic phase have been converted into the tetragonal setting to allow for direct comparison with the tetragonal phase.

The proportion of the tetragonal phase above ambient temperature is shown to decrease as the phase conversion from the tetragonal to the orthorhombic phase occurs in Figure 6.10. The change in the proportion of the two phases shows that the rate of conversion from the tetragonal to the orthorhombic phase increases as the temperature is increased until approximately 80 % of the sample has adopted the orthorhombic space group at 1164 K. Continued heating above 1164 K does not significantly change the proportion of either phase until a phase transition occurs at 1221 K where the mixture of the tetragonal and orthorhombic phases transforms into a single tetragonal phase.

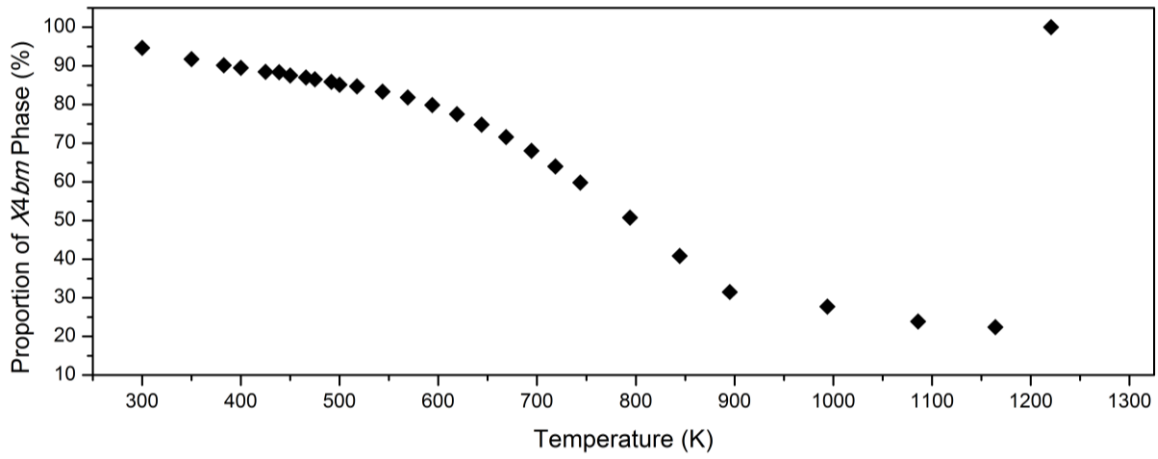

Figure 6.10: The proportion of the *X*4*bm* phase relative to the C*mm*2 phase for $Ba_{0.1}Sr_{1.9}TiSi_2O_8$ (x = 0.05) as calculated from Rietveld refinement against synchrotron X-ray powder diffraction data.

The spontaneous strain in the orthorhombic phase was calculated from the unit cell parameters between 300 K - 1164 K using the equations and method discussed for $Sr_2TiSi_2O_8$ in section 4.3.3.2 (Figure 6.11). The linear reduction in the spontaneous strain on heating shows that strain is driving the transition as would be expected for a continuous second order transition. Similarly to the $Sr_2TiSi_2O_8$ end member, the strain appears to drop to zero at the transition, however, the magnitude of this drop is considered small enough as to not contradict the second order nature of the transition.

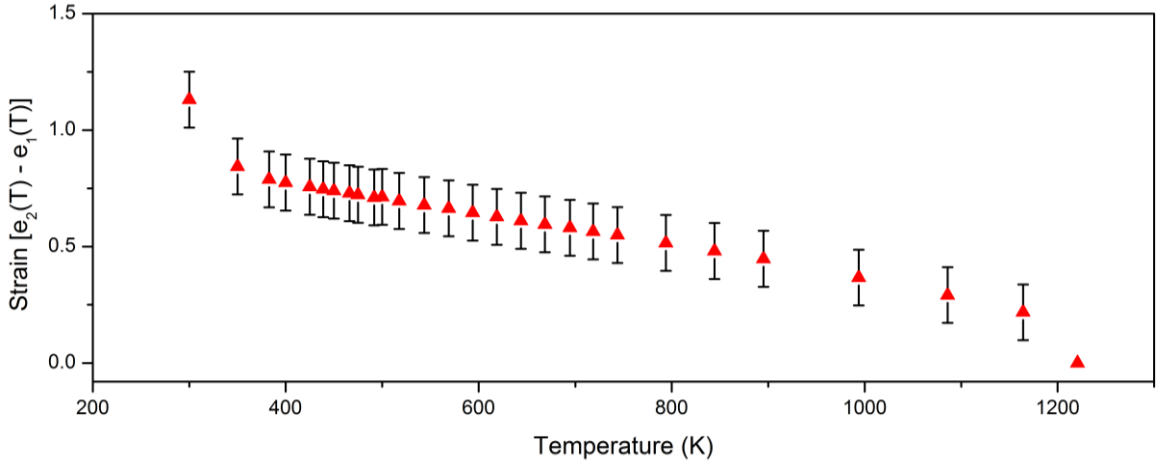

Figure 6.11: Spontaneous strain in the orthorhombic phase for $Ba_{0.1}Sr_{1.9}TiSi_2O_8$ (x = 0.05) as calculated from the difference between the *a* and *b* unit cell parameters relative to the unit cell parameter *a* for the tetragonal phase at the same temperature.

Resonant ultrasound spectroscopy data were collected between 300 kHz - 1200 kHz and 295 K -1295 K from a ceramic parallelepiped of dimensions 2.723 mm x 1.960 mm x 1.529 mm that was cut from a sintered $Ba_{0.1}Sr_{1.9}TiSi_2O_8$ pellet (Figure 6.12). Large variations in the position of many resonances and hence the elastic moduli are observed in the temperature range where the phase conversion from the tetragonal to orthorhombic phase was shown to occur from diffraction studies.

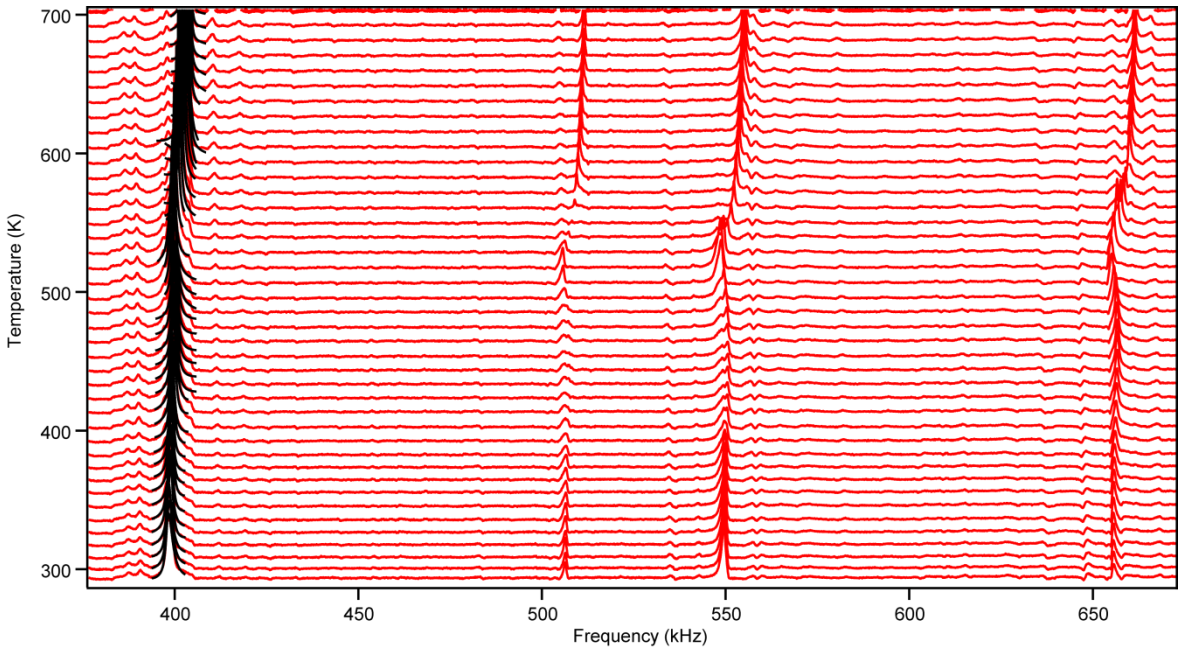

Figure 6.12: A close up of the resonant ultrasound spectra collected from a $Ba_{0.1}Sr_{1.9}TiSi_2O_8$ parallelepiped between 376 kHz - 673 kHz and 292 K - 702 K. The black lines overlapping the resonances at approximately 400 kHz represent the modelled peaks that were used to determine the position of this resonance.

The resonances at 548 kHz and 663 kHz in Figure 6.12 were sufficiently well resolved from other resonances and showed sufficiently large variations with temperature for further analysis. The position of these resonances were modelled between 300 K - 1073 K to investigate the behaviour of the sample as the tetragonal phase undergoes the gradual (and incomplete) phase transformation to the orthorhombic phase. The square of the position of each resonance at each temperature shows significant elastic softening to a minimum at 516 K as shown in Figure 6.13. The sharp minima suggest that a distinct change in the crystalline structure occurs at this

temperature. However, this does not coincide with a significant change in the unit cell parameters or orthorhombic strain as determined from diffraction studies (*c.f.* Figure 6.9 and Figure 6.11, respectively). Comparison of the position of the minima in the elastic moduli (Figure 6.13) and the change in proportion of the two phases on heating (Figure 6.10) reveals that the rapid increase in the elastic moduli after the minima coincides with the increasing rate of phase conversion from the tetragonal to orthorhombic phase. This suggests that the increasing elastic moduli may be a key factor in the conversion from the tetragonal to the orthorhombic phase and that the maxima in the elastic moduli at approximately 820 K may be related to the point at which the rate of phase conversion suddenly reduces at approximately 895 K in Figure 6.10.

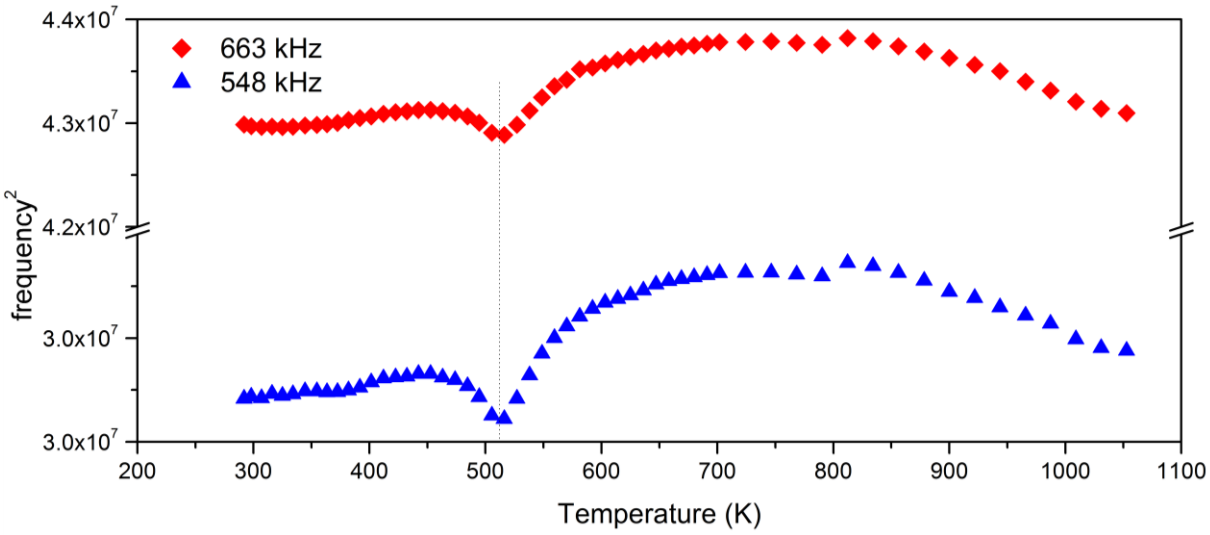

Figure 6.13: Variations in the square of the frequencies for two selected peaks from the resonant ultrasound spectra collected from a ceramic $Ba_{0.1}Sr_{1.9}TiSi_2O_8$ sample between 292 K - 1052 K. The minima in the position of the frequency of both peaks represents a minimum in the elastic softening at 516 K. The small jump at approximately 805 K is caused by an uncertainty in the position of the resonances due to the convolution of the overlapping resonance frequencies of the sample and the rods that hold the sample in the instrument.

The inverse mechanical quality factor was determined for the two selected resonances at 548 kHz and 663 kHz between 292 K - 1052 K and plotted in Figure 6.14. The difference between the changes in the mechanical quality factor calculated from the two resonances is distinct, but not surprising, given that the different resonances are likely to be subject to different relaxation mechanisms as the structure passes through the transition. This is particularly prevalent at temperatures above and below the low temperature phase transition at approximately 516 K where the 548 kHz resonance varies dramatically while the resonance at approximately 663 kHz does not display any significant changes.

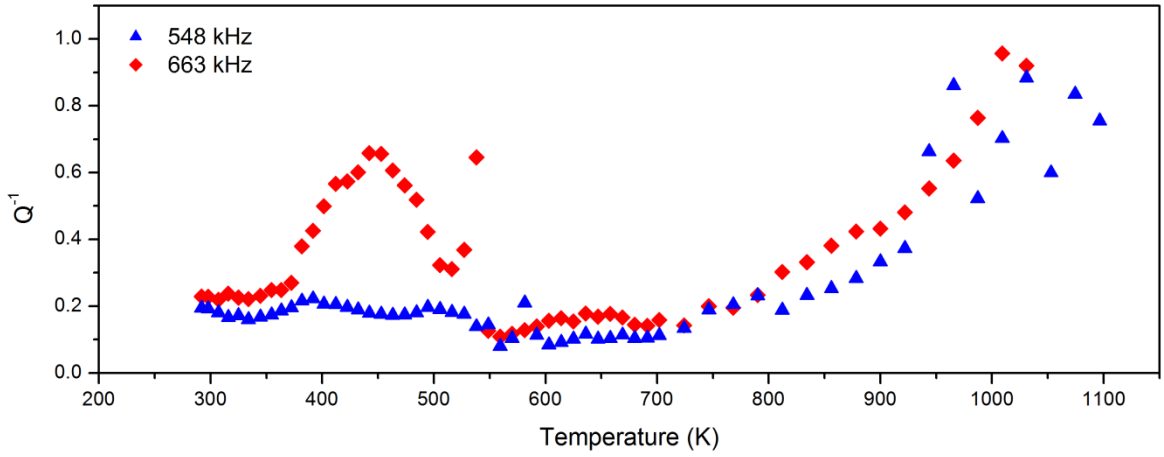

Figure 6.14: The inverse mechanical quality factor of the two selected resonances at 548 kHz and 663 kHz from resonant ultrasound spectroscopy data between 292 K - 1052 K.

6.2.1.4 $Ba_{0.2}Sr_{1.8}TiSi_2O_8$ (x = 0.10)

Synchrotron X-ray powder diffraction patterns were collected from $Ba_{0.2}Sr_{1.8}TiSi_2O_8$ between 125 K - 1221 K at λ = 0.82488(1) Å. Very weak reflections at 16.2° and 18.1° two theta correspond to an orthorhombic phase (marked by asterisks in Figure 6.15) at ambient temperature.

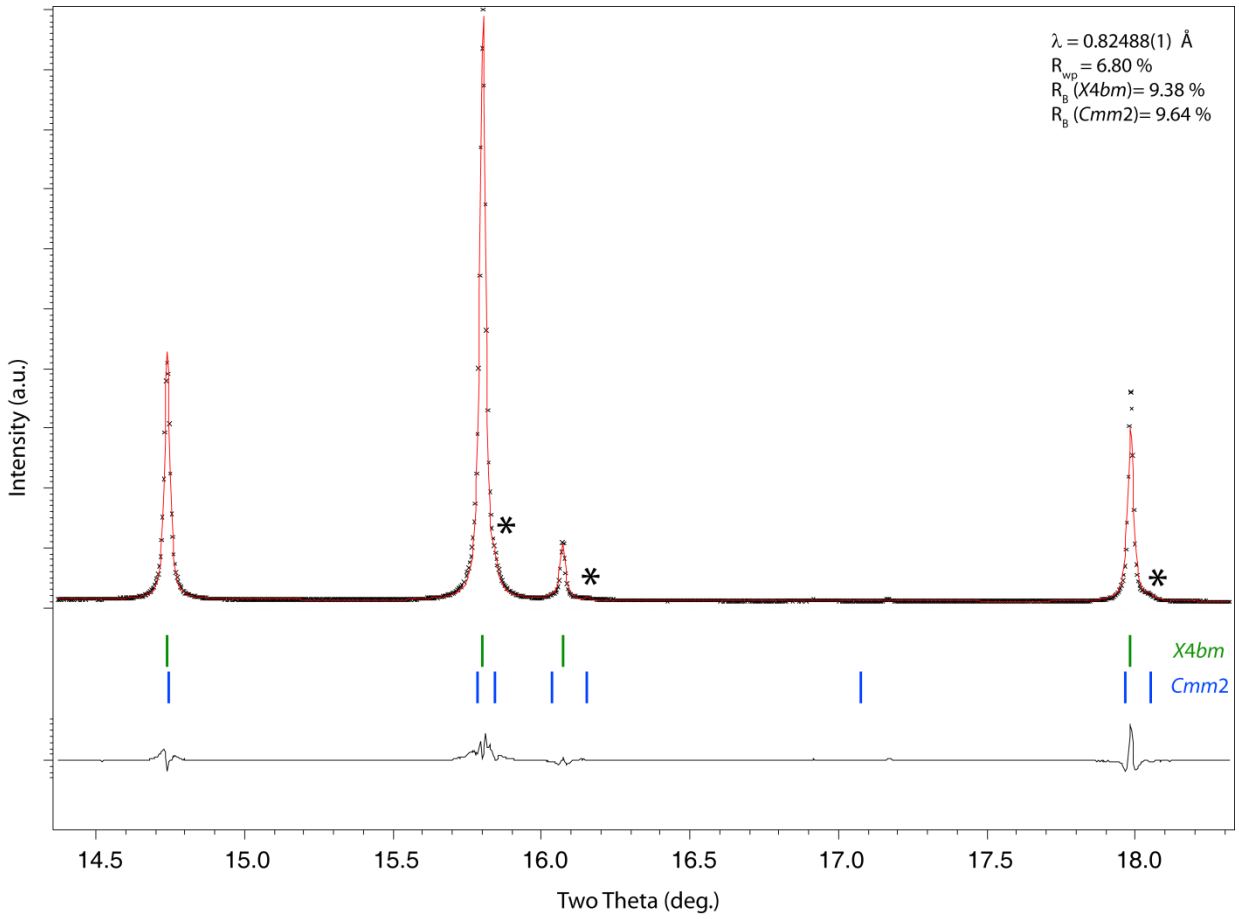

Figure 6.15: Observed, calculated, and difference plots from the refinement of the $Ba_{0.2}Sr_{1.8}TiSi_2O_8$ structure at ambient temperature against synchrotron X-ray powder diffraction data collected at λ = 0.82488(1) Å. Green and blue reflection markers identify positions of calculated reflections corresponding to the tetragonal and orthorhombic phases, respectively. Asterisks identify the very weak reflections corresponding to the orthorhombic phase.

The weak reflections corresponding to the orthorhombic phase were observed in all diffraction patterns collected at and below ambient temperature. Hence, unlike the $x \leq 0.05$ members of the system, both phases could be modelled between 125 K - 298 K.

A close up of a region of interest from the synchrotron X-ray powder diffraction patterns collected from $Ba_{0.2}Sr_{1.8}TiSi_2O_8$ between 125 K - 1221 K is shown in Figure 6.16. Although no obvious peak splitting is observed, the broadening of the 220 reflection at 16.1° two theta (indicated by the asterisk) provides evidence that phase conversion from the tetragonal to the orthorhombic phase is occurring. This is supported by the increase in the FWHM of the 220 reflection up to a maximum of 0.039° at approximately 1125 K in Figure 6.17.

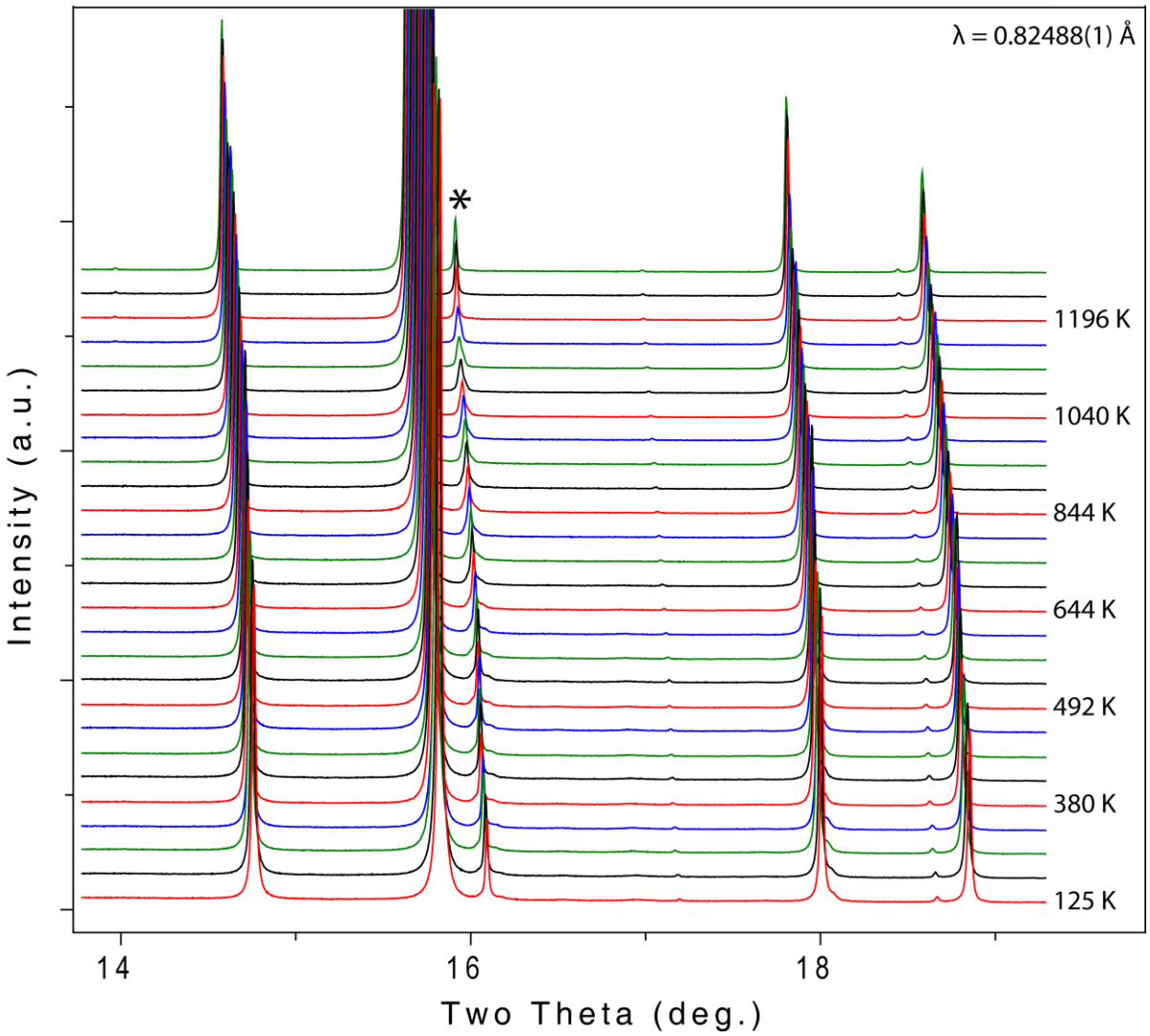

Figure 6.16: Synchrotron X-ray powder diffraction patterns collected from $Ba_{0.2}Sr_{1.8}TiSi_2O_8$ between 125 K - 1221 K at λ = 0.82488(1) Å where the asterisk indicates the 220 reflection that shows broadening on heating.

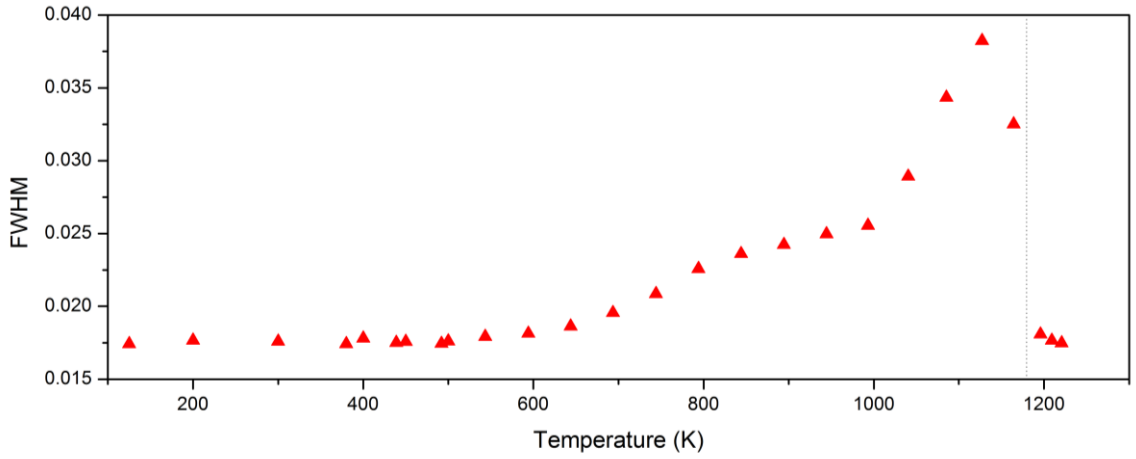

Figure 6.17: The FWHM calculated for the 220 reflection in the diffraction patterns collected from $Ba_{0.2}Sr_{1.8}TiSi_2O_8$ ($x = 0.10$) between 150 K - 1221 K. The vertical line indicates the temperature at which the 310 and 310 reflections have converged, representing the temperature at which the structure has adopted the high temperature tetragonal phase.

The Rietveld refinement of two phase models against these data was used to show that the broadening is a product of the 400 and 040 reflections from the orthorhombic phase increasing in intensity on either side of the 220 reflection from the tetragonal phase. This is shown in the observed, calculated, and difference plots for the structure at 1127 K in Figure 6.18 where the red asterisks identify the 400 and 040 reflections corresponding to the orthorhombic phase and the black asterisk identifies the 220 reflection corresponding to the tetragonal phase. No broadening was observed in the reflection at 15.67° two theta because the separation of the 312 and 132 reflections from the orthorhombic phase is not large enough to make an observable difference with respect to the 212 reflection from the tetragonal phase. The sudden reduction of the FWHM down to approximately 0.0175° two theta at 1196 K corresponds to the convergence of the 400 and 040 reflections as the structure adopts the high temperature tetragonal phase in a similar manner to the $x \leq 0.05$ members of the system.

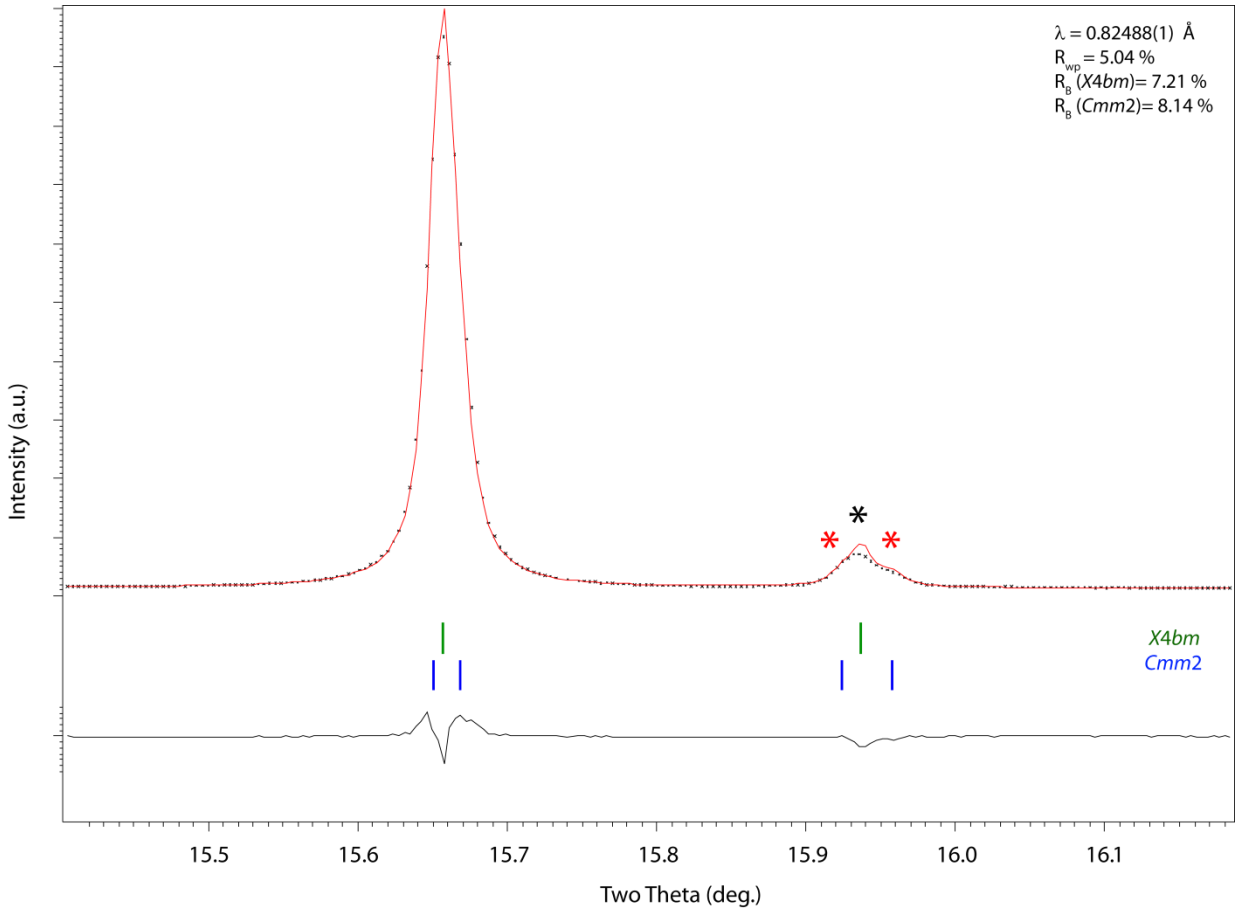

Figure 6.18: Observed, calculated, and difference plots from the refinement for the $Ba_{0.2}Sr_{1.8}TiSi_2O_8$ structure at 1127 K against synchrotron X-ray powder diffraction data. Red asterisks identify the 400 and 040 reflections corresponding to the orthorhombic phase, and the black asterisk identifies the 220 reflection corresponding to the tetragonal phase.

The unit cell parameters calculated for $Ba_{0.2}Sr_{1.8}TiSi_2O_8$ from Rietveld refinement against synchrotron X-ray powder diffraction data collected between 125 K - 1221 K are plotted in Figure 6.19. The coexistence of both phases occurs until 1164 K where the sample undergoes the phase transition back to the tetragonal phase as has been shown for the $x \leq 0.05$ members of the system. It can also be seen in Figure 6.19 that the difference in the *c* unit cell parameters for the two phases also gradually reduces to zero at the phase transition temperature.

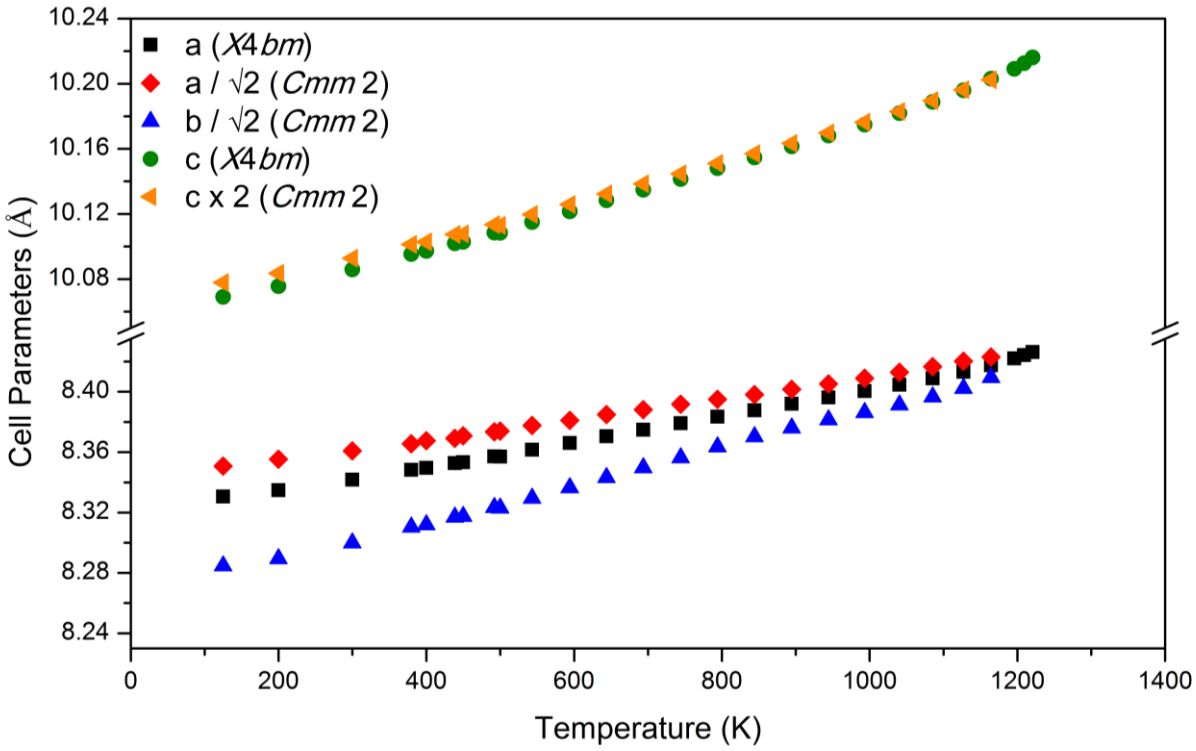

Figure 6.19: $Ba_{0.2}Sr_{1.8}TiSi_2O_8$ unit cell parameters between 125 K - 1221 K as calculated from Rietveld refinement against synchrotron X-ray powder diffraction. Unit cell parameters *a* and *b* for the orthorhombic phase have been converted into the tetragonal setting to allow for direct comparison with the tetragonal phase.

The spontaneous orthorhombic strain was calculated from the unit cell parameters between 125 K - 1164 K. As observed for $Sr_2TiSi_2O_8$ and $Ba_{0.1}Sr_{1.9}TiSi_2O_8$, the spontaneous strain linearly decreases until a small drop to zero occurs where the orthorhombic phase transforms into the tetragonal phase.

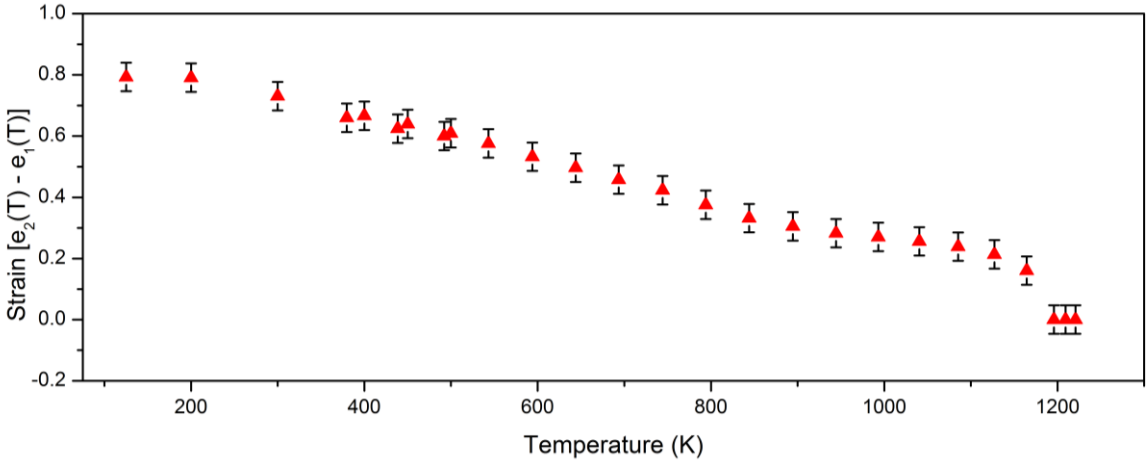

Figure 6.20: Spontaneous strain in the orthorhombic phase for $Ba_{0.2}Sr_{1.8}TiSi_2O_8$ (x = 0.10) as calculated from the difference between the a and b unit cell parameters relative to the unit cell parameter a for the tetragonal phase at the same temperature.

The change in the relative proportions of each phase between 125 K - 1164 K in Figure 6.21 is different to that observed for the $x \leq 0.05$ members of the system. The $Sr_2TiSi_2O_8$ and $Ba_{0.1}Sr_{1.9}TiSi_2O_8$ members of the system both displayed a significant decrease in the proportion of the tetragonal phase on heating, until the phase transitions at 1323 K and 1221 K converted all the orthorhombic phase into the high temperature tetragonal phase. However, $Ba_{0.2}Sr_{1.8}TiSi_2O_8$ displays significantly less phase conversion from the tetragonal phase to the orthorhombic phases on heating. The minimum proportion of the tetragonal phase for $Ba_{0.2}Sr_{1.8}TiSi_2O_8$ reaches approximately 70 % at 1270 K as opposed to approximately 20 % at 1164 K for $Ba_{0.1}Sr_{1.9}TiSi_2O_8$ or 0 % (full phase conversion) at 567 K for $Sr_2TiSi_2O_8$ as summarised in Table 6.2.

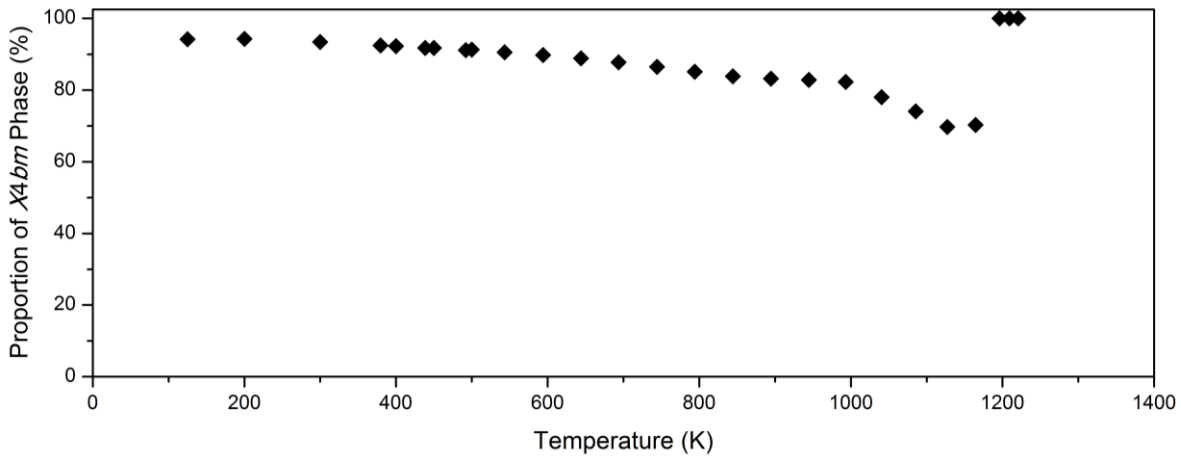

Figure 6.21: The proportion of the *X4bm* phase relative to the *Cmm*2 phase for $Ba_{0.2}Sr_{1.8}TiSi_2O_8$ ($x = 0.10$) as calculated from Rietveld refinement against synchrotron X-ray powder diffraction data.

Table 6.2: Summary of phase proportion information for $x \leq 0.10$ members of the $Ba_{2x}Sr_{2-2x}TiSi_2O_8$ system.

Composition	Minimum Proportion of *X4bm* Phase	Temperature of Minimum Proportion
$Sr_2TiSi_2O_8$ ($x = 0$)	0 %	567 K
$Ba_{0.1}Sr_{1.9}TiSi_2O_8$ ($x = 0.05$)	20 %	1164 K
$Ba_{0.2}Sr_{1.8}TiSi_2O_8$ ($x = 0.10$)	70 %	1270 K

The difference in the properties of the coexisting phases in members of the $Ba_{2x}Sr_{2-2x}TiSi_2O_8$ system is not simple to understand. However, from the summary of the minimum proportions of tetragonal phases and their corresponding temperatures in Table 6.2, it can be seen that increased proportions of barium in $Ba_{2x}Sr_{2-2x}TiSi_2O_8$ reduces the minimum amount of tetragonal phase that will be retained rather than transforming into the orthorhombic phase on heating. Moreover, the temperature at which the minimum proportion of the tetragonal phase occurs is increased by the presence of more barium. Hence, it can be concluded that the inclusion of more barium in the $Ba_{2x}Sr_{2-2x}TiSi_2O_8$ structure suppresses the existence of the orthorhombic phase.

The $x = 0.2$ member of the $Ba_{2x}Sr_{2-2x}TiSi_2O_8$ system was also investigated using synchrotron X-ray powder diffraction between 298 K - 873 K as shown in Figure 6.22. Although very weak reflections corresponding to the orthorhombic phase were observed above the background

(marked with red asterisks in Figure 6.22), their intensity was not sufficient to be included in any refinement. The presence of a reflection corresponding to the $SrSiO_3$ impurity phase very close to the reflections corresponding to the orthorhombic fresnoite phase also made the identification of changes in either of the fresnoite phases difficult to quantify ($SrSiO_3$ reflection marked by the black asterisk in Figure 6.22).

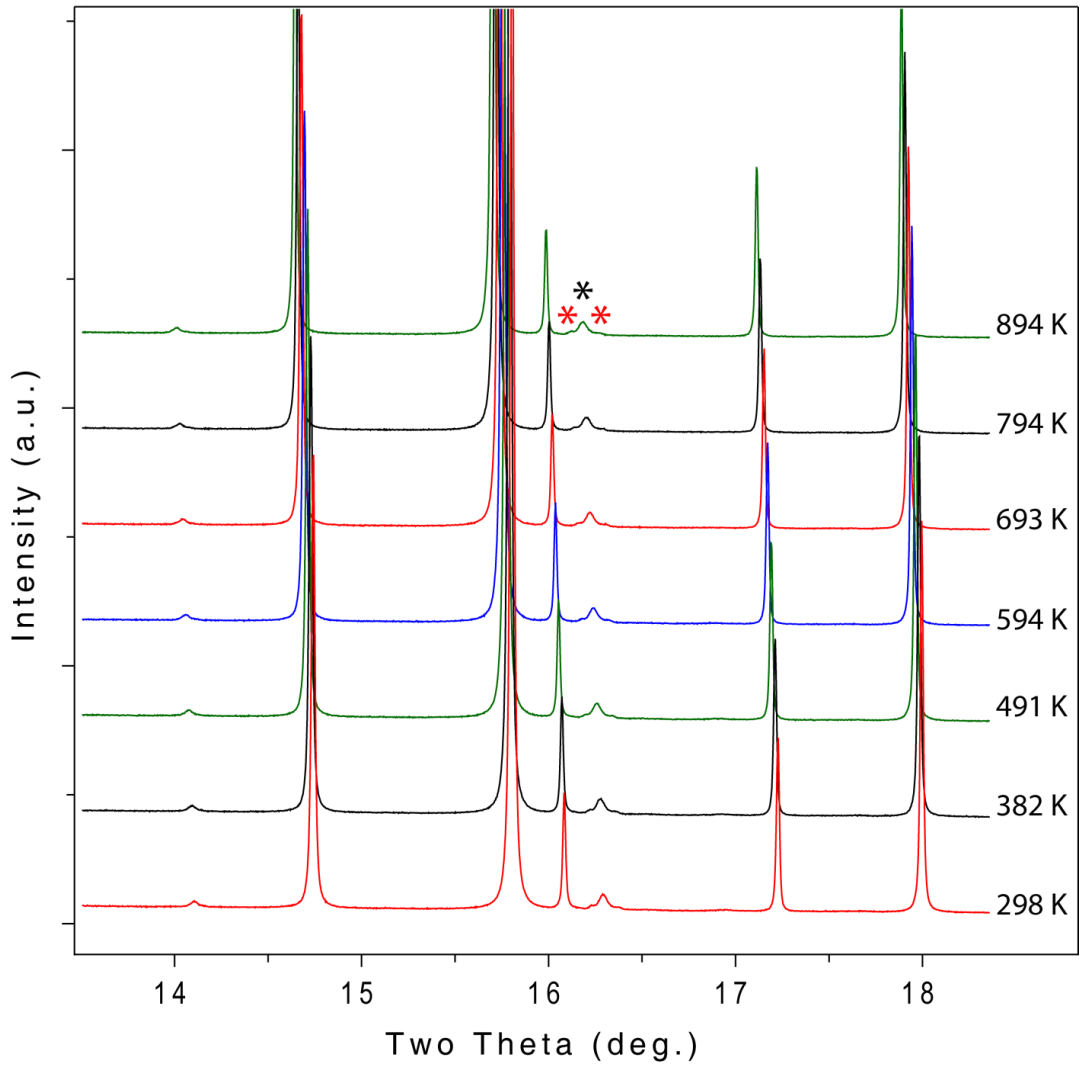

Figure 6.22: Synchrotron X-ray powder diffraction patterns collected from $Ba_{0.4}Sr_{1.6}TiSi_2O_8$ between 298 K - 894 K at λ = 0.82488(1) Å. The red and black asterisks identify reflections corresponding to the orthorhombic fresnoite and impurity $SrSiO_3$ phases, respectively.

No changes other than thermal expansion were observed over the temperature range investigated. However, this is expected seeing as the temperature at which the proportion of the orthorhombic phase increases as more barium is substituted for strontium. Collecting data at

higher temperatures would be beneficial to determine whether the relative proportion of the orthorhombic phase increases above 873 K. This was not performed in the current study because of restrictions on beam time at the synchrotron during the experiment.

The different phases present in the members across the $Ba_{2x}Sr_{2-2x}TiSi_2O_8$ system have been discussed in this section. Firstly, the variable temperature diffraction studies of the barium-rich members of the system showed that the phase transition from the incommensurately modulated *X*4*bm*(α, α, 0)*0gg* phase to the prototypic *X*4*bm* phase increases approximately linearly up to the $x = 0.5$ member. No evidence of this phase transition was observed for the $x < 0.5$ members of the system.

The identification of a two phase mixture at ambient temperature consisting of a main *X*4*bm* phase and a very small proportion of *Cmm2* phase for the $x \leq 0.5$ members of the system also provided important information about the complex phase behaviour of the $Ba_{2x}Sr_{2-2x}TiSi_2O_8$ system. The decreasing proportion of the orthorhombic phase relative to the tetragonal phase at ambient temperature as more barium was substituted into the $Sr_2TiSi_2O_8$ structure is consistent with the results from the barium-rich end of the system where no orthorhombic phase was identified. Some aspects of the complex phase behaviour discussed for $Sr_2TiSi_2O_8$ in chapter 4 were also observed for the $x = 0.05$ and $x = 0.10$ members of the system. The proportion of the tetragonal phase relative to the orthorhombic phase in these compounds was shown to decrease on heating as the spontaneous strain of the orthorhombic phase approached zero. However, the minimum proportion of the tetragonal phase remaining was found to increase with higher barium content, suggesting that more barium in the fresnoite structure suppresses the existence of the orthorhombic phase. This is also supported by the observation that the $x \geq 0.5$ members of the system show the *X*4*bm*(α, α, 0)*0gg* to prototypic *X4bm* phase transition without the need for the intermediate orthorhombic phase to form.

The $x = 0.05$ and $x = 0.10$ compounds were also both shown to undergo structural phase transitions to a high temperature tetragonal phase at 1221 K and 1196 K, respectively. The presence of a modulation in the high temperature phase could not be determined because of the difficulties associated with observing satellite reflections in the powder diffraction patterns and the inability to conduct electron diffraction at such high temperatures. However, extrapolating the trend in the $X4bm(\alpha, \alpha, 0)0gg$ to $X4bm$ phase transition temperatures from the barium-rich end of the series suggests that the adoption of the prototypic $X4bm$ phase for the strontium-rich members of the system is a plausible conclusion based on the information available. The phase behaviour of the $Ba_{2x}Sr_{2-2x}TiSi_2O_8$ ($0 \leq x \leq 1$) system that has been determined in this section is summarised in the phase diagram in Figure 6.23.

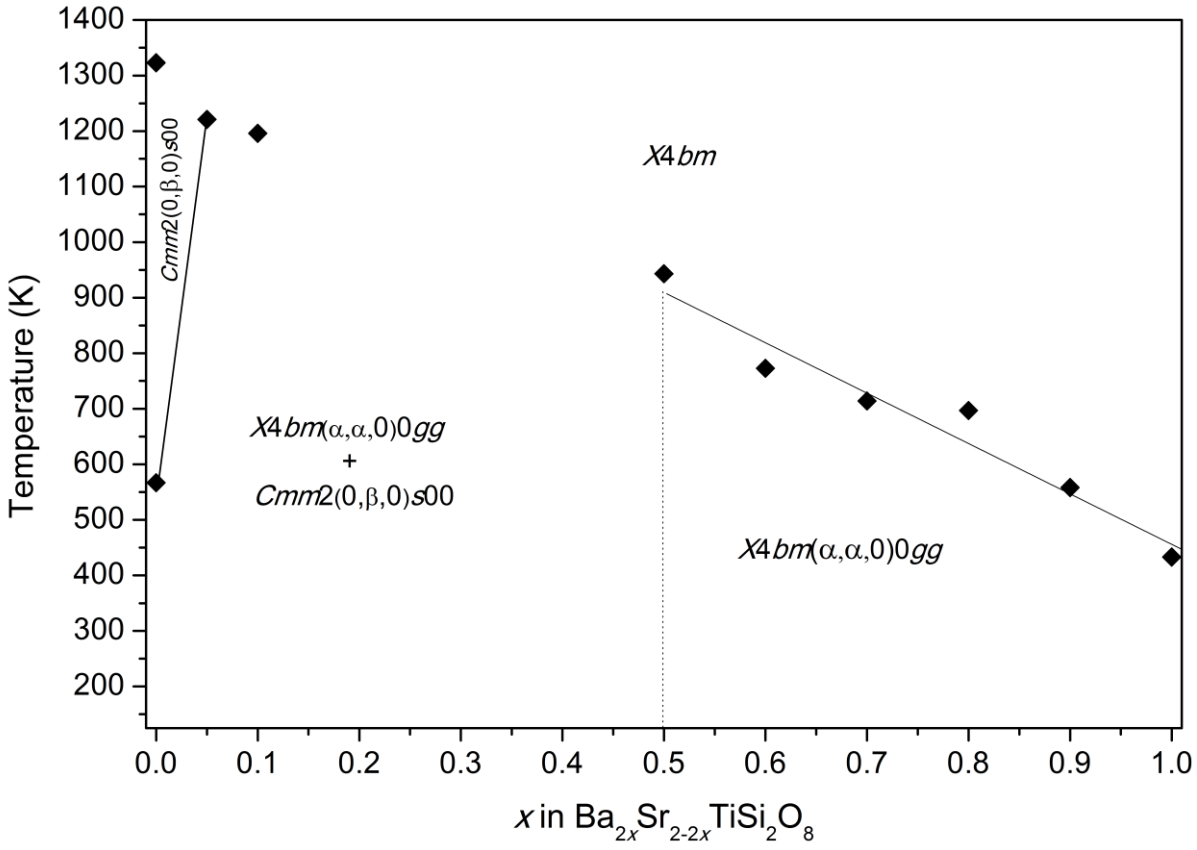

Figure 6.23: Phase diagram for the $Ba_{2x}Sr_{2-2x}TiSi_2O_8$ ($0 \leq x \leq 1$) system. Solid lines represent experimentally determined phase boundaries. The dotted line represents the hypothetical phase boundary separating the two phase (tetragonal and orthorhombic) region from the single phase (tetragonal) region.

6.2.2 $Sr_2TiGe_{2y}Si_{2-2y}O_8$ System

The $Sr_2TiGe_{2y}Si_{2-2y}O_8$ system is an appropriate choice for investigation because the $Sr_2TiSi_2O_8$ end member has been shown to exhibit complex and unusual phase behaviour over a wide range of temperatures, while $Sr_2TiGe_2O_8$ does not form a fresnoite phase at all. Members of the $Sr_2TiGe_{2y}Si_{2-2y}O_8$ system were synthesised and characterised to determine the range of compositions that form fresnoite phases, and how the substitution of germanium for silicon changes the phase behaviour that was observed for $Sr_2TiSi_2O_8$.

Members of the $Sr_2TiGe_{2y}Si_{2-2y}O_8$ system were synthesised using a method based on the synthesis of the $Sr_2TiSi_2O_8$ end member. The synthesis of pure fresnoite compounds containing germanium was more challenging than for the $Sr_2TiSi_2O_8$ end member because the inclusion of germanium in the reaction reduced the melting point of the mixture. Samples that melted during synthesis were found to form a $SrTiO_3$ main phase rather than the desired fresnoite phase. Longer reaction times (~3 - 5 days) and lower reaction temperatures (between 1100 °C and 1200 °C) were used to reduce the proportion of the $SrTiO_3$ phase in each sample. However, a small proportion of $SrTiO_3$ was still evident in the diffraction pattern collected from the $y = 0.2$ member after multiple heating steps at 1100 °C. The $y > 0.2$ members formed significant proportions of $SrTiO_3$ when the reaction temperature was above 1100 °C, and a mixture of reactants and other non-fresnoite phases were formed when the reaction temperature was below 1100 °C. Figure 6.24 shows that the proportion of $SrTiO_3$ increases with increasing germanium content for the $Sr_2TiGe_{2y}Si_{2-2y}O_8$ ($0 \leq y \leq 0.4$) system.

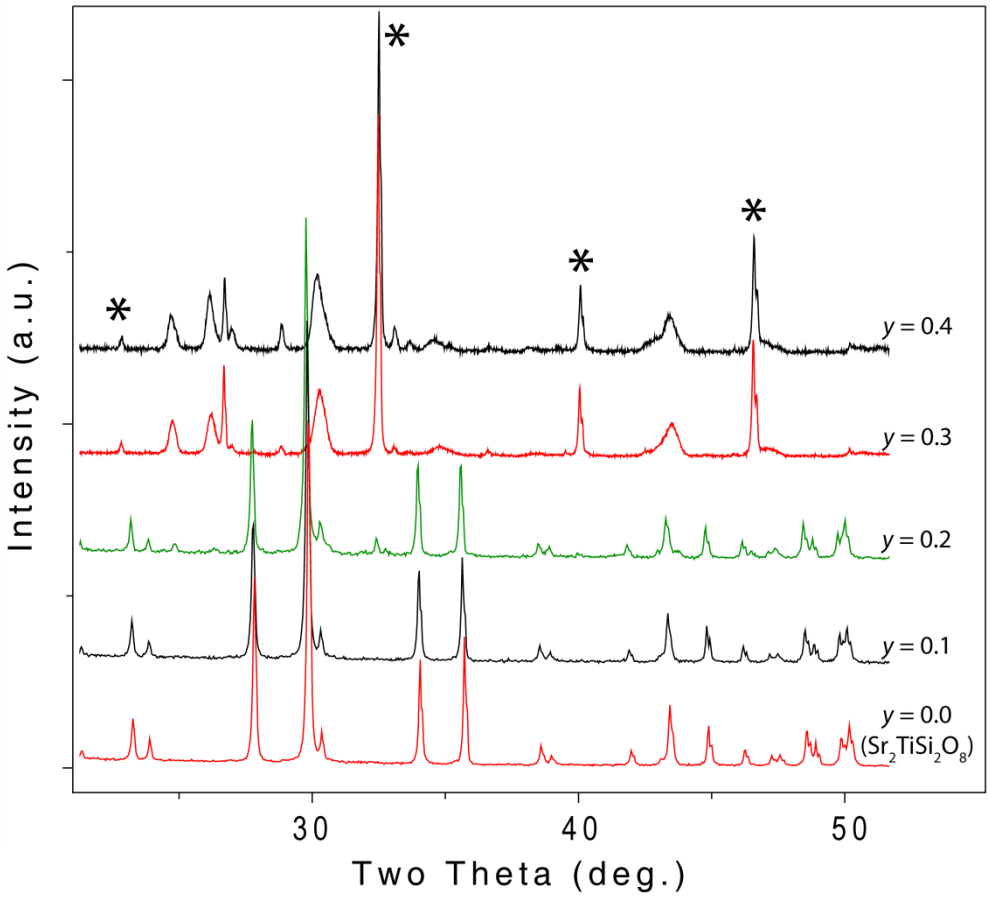

Figure 6.24: X-ray powder diffraction patterns collected from members of the $Sr_2TiGe_{2y}Si_{2-2y}O_8$ ($0 \leq y \leq 0.4$) system at ambient temperature using Cu K_α radiation. These are the best samples synthesised for each composition. Asterisks identify reflections corresponding to the $SrTiO_3$ impurity phase.

It can hence be concluded that fresnoite structures form for the $y \leq 0.2$ members of the system, while mixtures of other non-fresnoite phases form for the $y \geq 0.3$ members. A summary of the most appropriate reaction temperatures used for the successful synthesis of members of the $Sr_2TiGe_{2y}Si_{2-2y}O_8$ system is provided in Table 6.3.

Table 6.3: Summary of the maximum heating temperatures, heating durations, and melting points for members of the $Sr_2TiGe_{2y}Si_{2-2y}O_8$ system.

Composition in $Sr_2TiGe_{2y}Si_{2-2y}O_8$	Maximum Heating Temperature Used	Heating Time	Melting Point
$y = 0.0$ (STS)	1250 °C	6 x 20 hours	1300 °C
$y = 0.1$	1200 °C	5 x 20 hours	1250 °C
$y = 0.2$	1100 °C	5 x 20 hours	1200 °C

6.2.2.1 $Sr_2TiGe_{0.2}Si_{1.8}O_8$ (y = 0.1)

The synchrotron X-ray powder diffraction patterns collected from the $y = 0.1$ member of the $Sr_2TiGe_{2y}Si_{2-2y}O_8$ system between 298 K - 1323 K at $\lambda = 1.15864(1)$ Å are provided in Figure 6.25. No evidence of an orthorhombic phase coexisting with the main tetragonal phase was found at ambient temperature.

Similarly to the $Sr_2TiSi_2O_8$ end member, peak splitting that indicates the increasing proportion of the orthorhombic phase is evident on heating. The separation between the split reflections reduces as the structure approaches the maximum temperature investigated using the hot air blower at 1209 K. Given that the Pt-strip furnace was useful in showing that the $Sr_2TiSi_2O_8$ end member undergoes the orthorhombic to tetragonal phase transition at 1323 K, this attachment was used to collect diffraction patterns from $Sr_2TiGe_{0.2}Si_{1.8}O_8$ at higher temperatures. The difference in the background for the patterns collected using the Pt-strip furnace and the hot air blower can be attributed to the different signal to noise ratios due to differences in the beam widths and geometry of the sample required for the two apparatus.

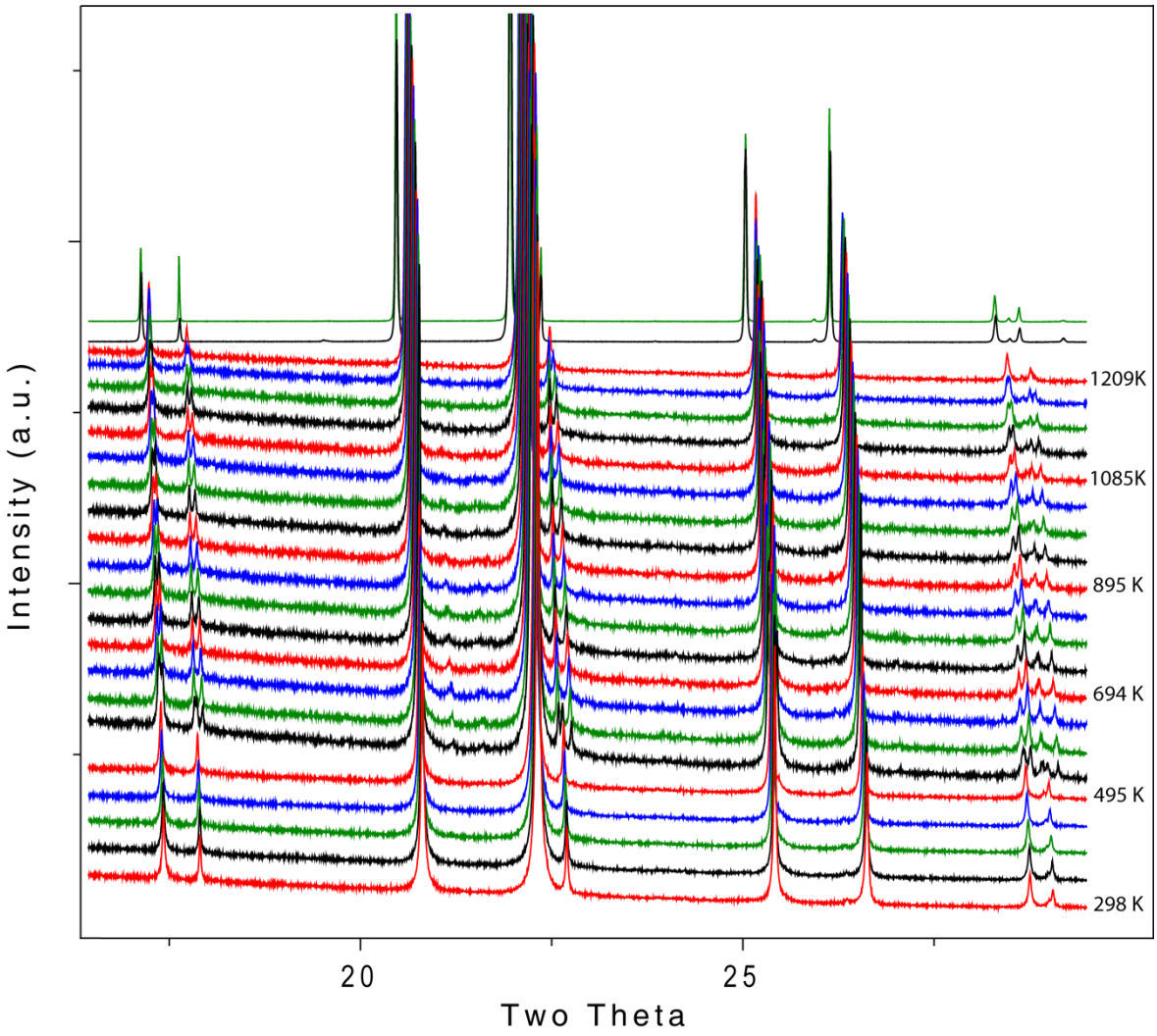

Figure 6.25: Synchrotron X-ray powder diffraction patterns collected from $Sr_2TiGe_{0.2}Si_{1.8}O_8$ between 298 K - 1209 K (hot air blower) and 1273 K - 1323 K (Pt-strip furnace) at λ = 1.15864(1) Å.

The unit cell parameters calculated for the $y = 0.1$ member from Rietveld refinement against the synchrotron X-ray powder diffraction data are plotted in Figure 6.26. The refinement of models against the data collected above 1209 K (from the Pt-strip furnace attachment) was not possible because a significant amount of preferred orientation of crystallites was evident in all diffraction patterns collected from samples mounted on the Pt-strip. This has been attributed to the growth of small crystals on the Pt-strip at high temperatures which can dominate the diffraction statistics when insufficient sample rotation or rocking is used during the collection. This produced large variations in the relative intensities of each reflection in different collections from the same

sample. The samples were rocked back and forth between 7° - 8.5° to the horizontal at a rate of approximately 1.5 Hz. However, the evidence suggests that although these were the largest steps that could be taken to minimise the preferred orientation, they were insufficient to produce data suitable for Rietveld refinement. The cell parameters determined from the sample while on the Pt-strip furnace were determined to be significantly larger (approximately 0.3 %) than those determined when the sample was in capillaries (including patterns collected at ambient temperature). Hence, the cell parameters calculated from these data cannot be directly compared to those determined using the hot air blower and have not been shown in Figure 6.26. However, the convergence of the 312 and 132, and the 400 and 040 reflections in the diffraction patterns collected at 1273 K and 1323 K demonstrates that the structure has adopted the high temperature tetragonal structure in an analogous way to the $Sr_2TiSi_2O_8$ member.

Single phase tetragonal models were refined against the synchrotron X-ray powder diffraction data between ambient temperature and 495 K. Although no evidence of the orthorhombic phase was identified within this temperature range, it should be noted that the orthorhombic phase may still be present in small proportions that cannot be identified using powder diffraction techniques. The satellite reflections in electron diffraction patterns collected from $Sr_2TiGe_{0.2}Si_{1.8}O_8$ would need to be investigated to establish whether any of the orthorhombic phase coexists with the tetragonal phase in polycrystalline form at ambient temperature in an analogous way to $Sr_2TiSi_2O_8$.

Continued heating of $Sr_2TiGe_{0.2}Si_{1.8}O_8$ induces a phase transformation from the tetragonal phase to the orthorhombic phase in a similar manner to the $Sr_2TiSi_2O_8$ end member. The two phases coexist at 539 K and the phase transformation is complete by approximately 597 K. Continued heating up to 1273 K confirmed that the 132 and 312 reflections converge above 1209 K, indicating that the structure has adopted the tetragonal structure as was shown for the $Sr_2TiSi_2O_8$ end member.

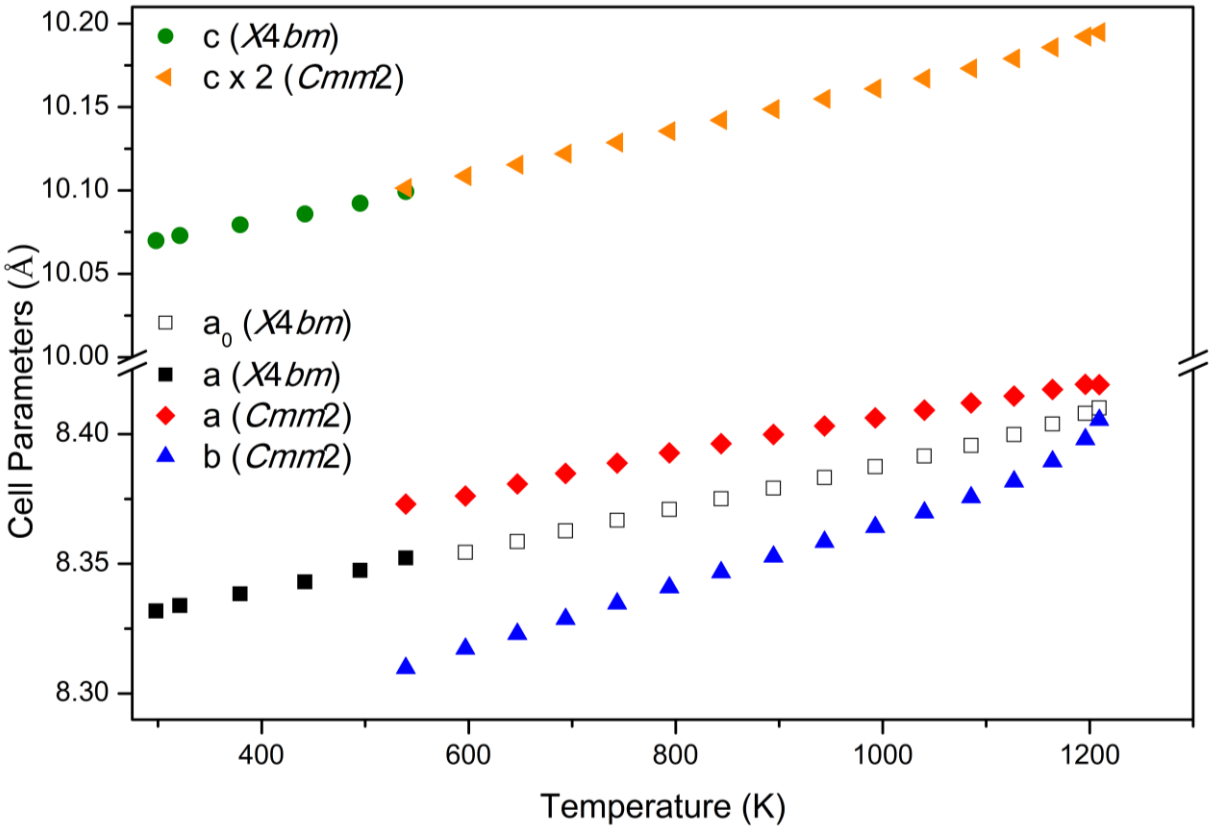

Figure 6.26: Unit cell parameters for $Sr_2TiGe_{0.2}Si_{1.8}O_8$ between 298 K - 1323 K as calculated from Rietveld refinement against synchrotron X-ray powder diffraction data. Unit cell parameters *a, b*, and *c* for the orthorhombic phase have been converted into the tetragonal setting to allow for direct comparison with the tetragonal phase.

The calculation of the $Sr_2TiGe_{0.2}Si_{1.8}O_8$ orthorhombic strain from the *a* and *b* unit cell parameters determined from synchrotron X-ray powder diffraction shows an identical trend to the $Sr_2TiSi_2O_8$ end member whereby the strain decreases to zero occurs at the phase transition temperature of 1273 K (Figure 6.27). The refined parameters for this compound at each temperature are provided in Appendix B of the attached Appendix DVD.

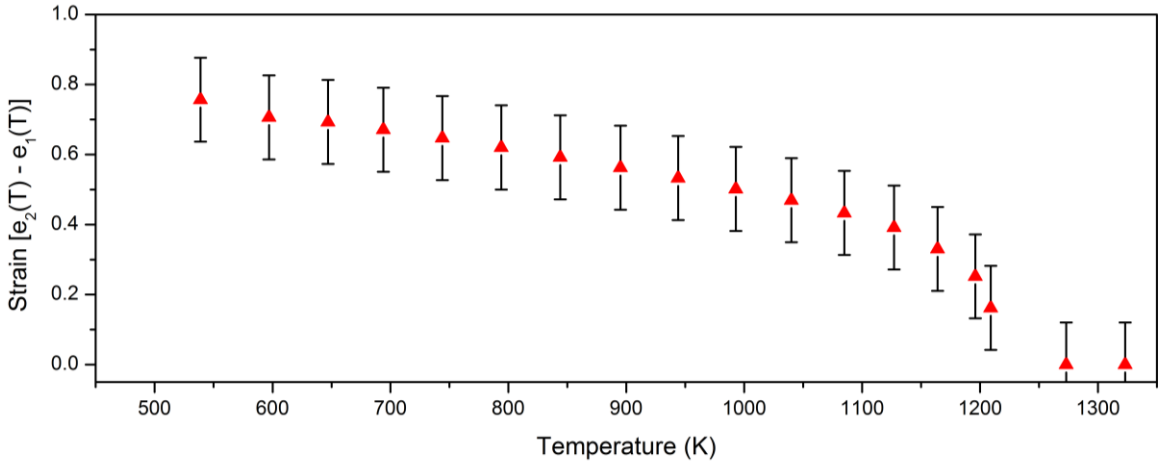

Figure 6.27: Orthorhombic strain in $Sr_2TiGe_{0.2}Si_{1.8}O_8$ between 539 K - 1323 K as calculated from the *a* and *b* unit cell parameters determined from Rietveld refinement against synchrotron X-ray powder diffraction data.

6.2.2.2 $Sr_2TiGe_{0.4}Si_{1.6}O_8$ (y = 0.2)

Synchrotron X-ray powder diffraction patterns were collected from the $y = 0.2$ member of the $Sr_2TiGe_{2y}Si_{2-2y}O_8$ system between 298 K - 1210 K at $\lambda = 1.15864(1)$ Å (Figure 6.28). The $y = 0.2$ sample was shown to contain a small proportion of $SrTiO_3$ as a secondary phase that could not be removed during synthesis. No evidence of reflections corresponding to the orthorhombic phase was found between ambient temperature and 523 K. Similar behaviour to the $y = 0.1$ member is observed in $Sr_2TiGe_{0.4}Si_{1.6}O_8$ where heating above 298 K induces a phase transformation from the tetragonal to orthorhombic phase which is visible by 567 K.

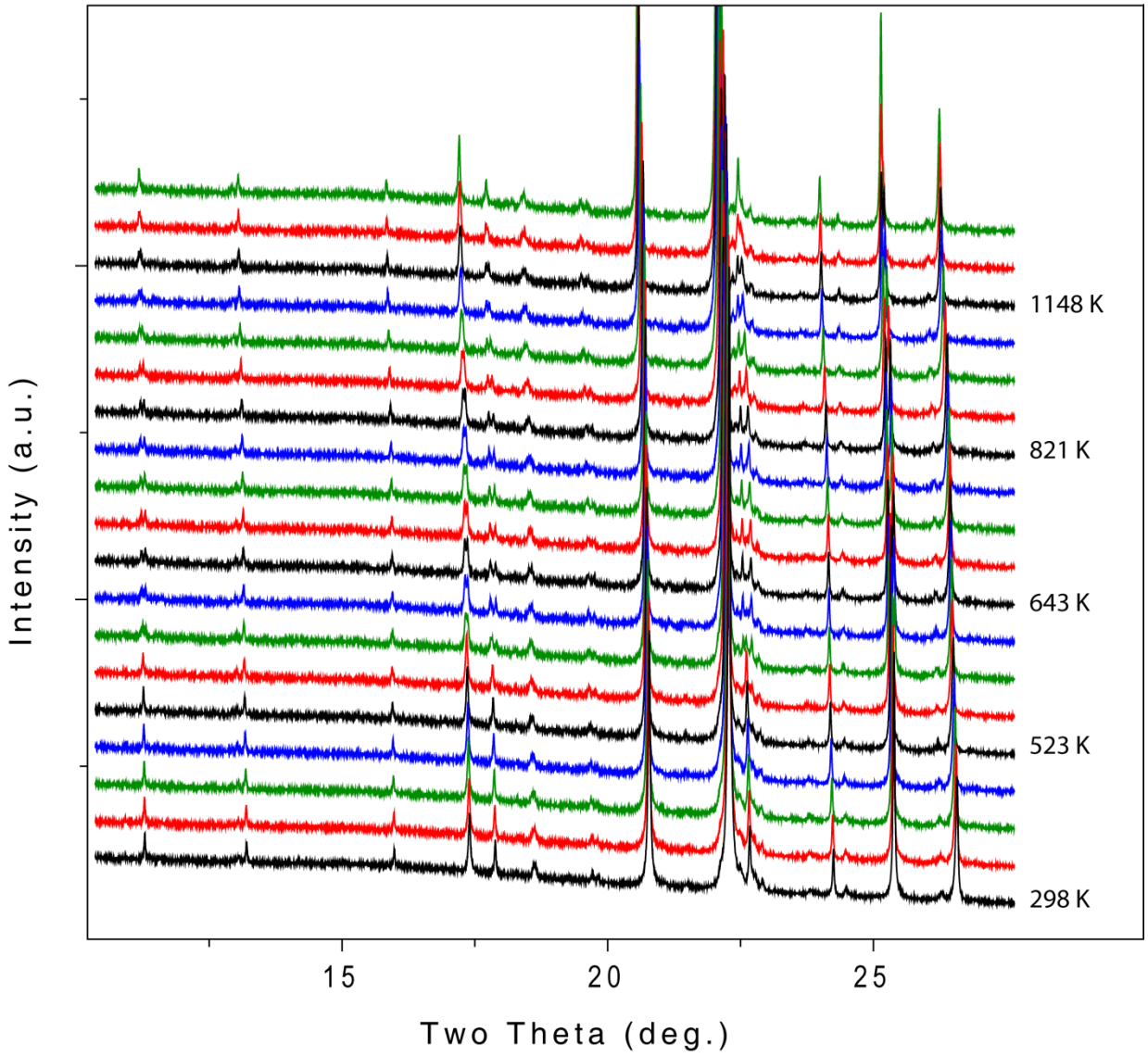

Figure 6.28: Synchrotron X-ray powder diffraction patterns collected from $Sr_2TiGe_{0.4}Si_{1.6}O_8$ between 298 K - 1210 K at λ = 1.15864(1) Å.

The unit cell parameters calculated for $Sr_2TiGe_{0.4}Si_{1.6}O_8$ from Rietveld refinement against the synchrotron X-ray powder diffraction data collected between 298 K - 1210 K are plotted in Figure 6.29. The diffraction patterns collected between 617 K - 1182 K were modelled using single phase orthorhombic models in a similar manner to the $Sr_2TiSi_2O_8$ end member and $y = 0.1$ member. Further heating to 1210 K causes the structure to undergo another phase transition from the orthorhombic phase to the tetragonal phase as observed for the $y \leq 0.1$ members of the $Sr_2TiGe_{2y}Si_{2-2y}O_8$ system.

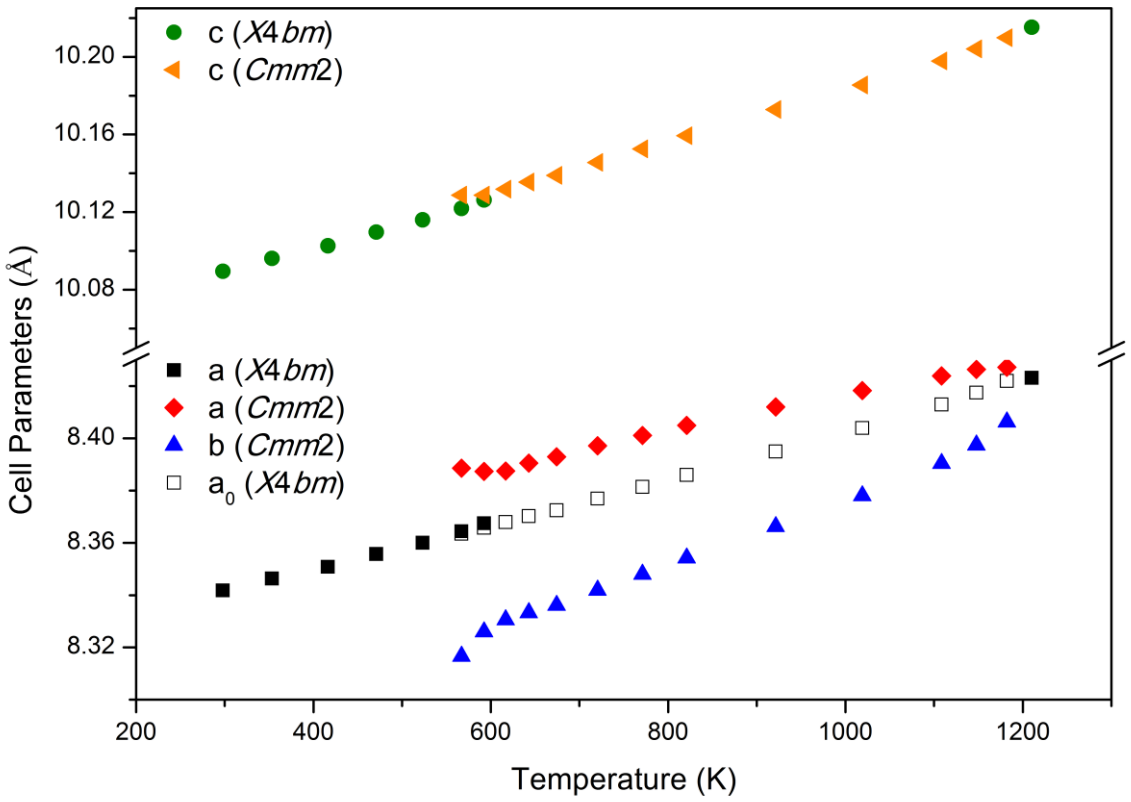

Figure 6.29: $Sr_2TiGe_{0.4}Si_{1.6}O_8$ unit cell parameters between 298 K - 1210 K as calculated from Rietveld refinement against synchrotron X-ray powder diffraction data. Unit cell parameters *a, b*, and *c* for the *Cmm*2 phase have been converted into the tetragonal setting to allow for direct comparison with the *X*4*bm* phase.

The orthorhombic strain was calculated between 567 K - 1182 K from the unit cell parameters in Figure 6.30. The strain in the orthorhombic phase significantly drops as phase conversion from the tetragonal phase occurs, however, once the sample contains only the single orthorhombic phase, the strain decreases to zero at 1210 K as the orthorhombic to tetragonal phase transition occurs. The refined parameters for this compound at each temperature are provided in Appendix B of the attached Appendix DVD.

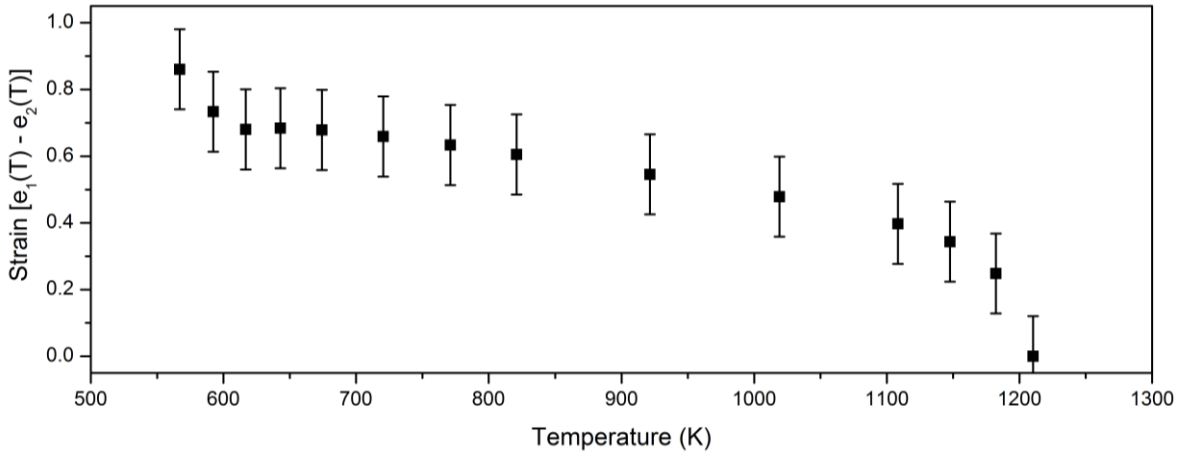

Figure 6.30: The orthorhombic strain in $Sr_2TiGe_{0.4}Si_{1.6}O_8$ between 550 K - 1210 K as calculated from the *a* and *b* unit cell parameters determined from Rietveld refinement against synchrotron X-ray powder diffraction data.

The investigation of the $Sr_2TiGe_{2y}Si_{2-2y}O_8$ system has produced new information about the phase behaviour of the fresnoite structure type. Firstly, it has been shown that compositions with $y \leq 0.2$ form phases of the fresnoite structure type, while compositions with $y > 0.2$ form a main perovskite phase in addition to other, unidentified non-fresnoite phases.

The variable temperature studies of the $Sr_2TiGe_{2y}Si_{2-2y}O_8$ system have shown that the complex phase behaviour observed for the $Sr_2TiSi_2O_8$ end member is observed up to the $y = 0.2$ member. It has been shown that increasing the germanium content in the $Sr_2TiGe_{2y}Si_{2-2y}O_8$ system increases the temperature at which the orthorhombic phase forms. The temperature at which the fresnoite structure undergoes the orthorhombic to tetragonal phase transition was shown to reduce from 1323 K from the $Sr_2TiSi_2O_8$ end member to 1210 K for the $y = 0.2$ member. This is similar behaviour to that observed for the analogous phase transition in the $Ba_{2x}Sr_{2-2x}TiSi_2O_8$ system as discussed in section 6.2.1. The phase formation properties and phase transitions determined in this section have been summarised in the new phase diagram for the $Sr_2TiGe_{2y}Si_{2-2y}O_8$ system in Figure 6.31 where the four- and five-dimensional space groups have been stated based on the evidence from the behaviour of the $Sr_2TiSi_2O_8$ end member.

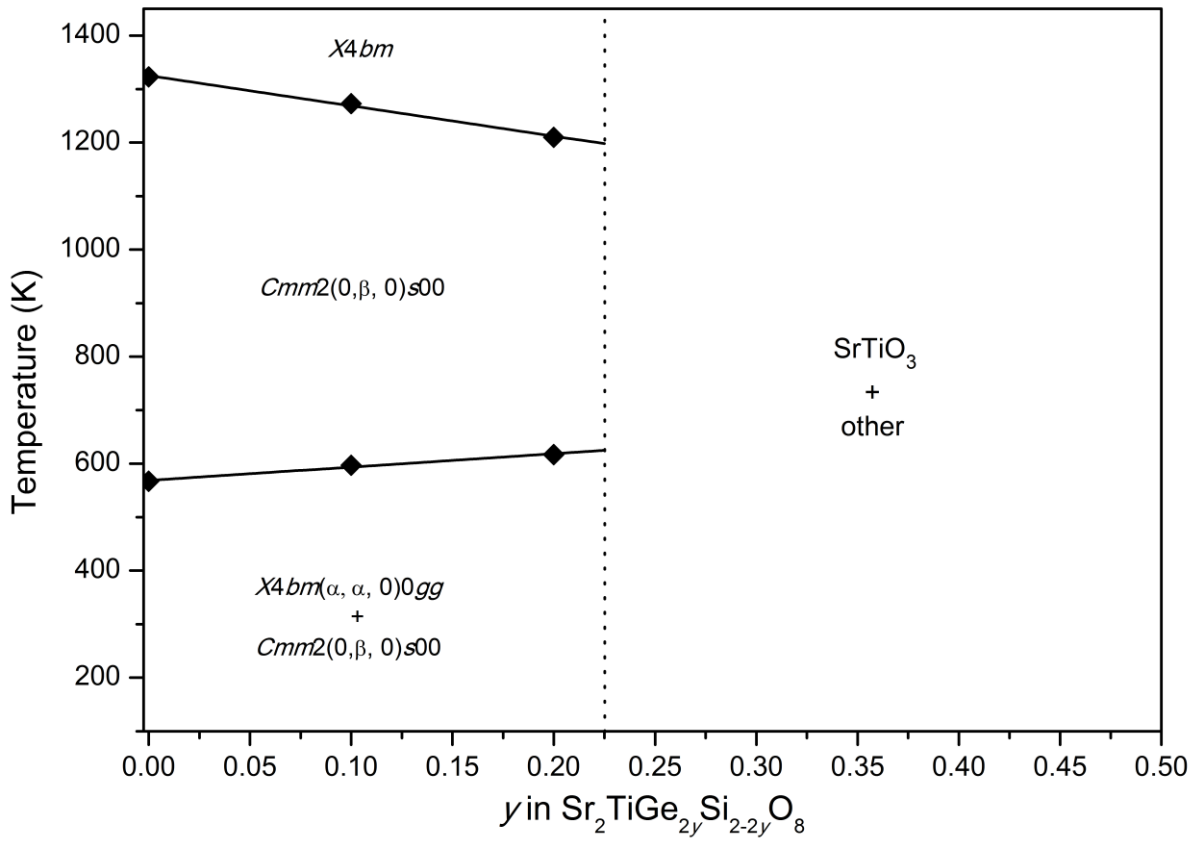

Figure 6.31: Phase diagram for the $Sr_2TiGe_{2y}Si_{2-2y}O_8$ ($0 \leq y \leq 0.5$) system. Solid lines represent experimentally determined phase boundaries. The dotted line represents the phase boundary separating the regions of compositions that form fresnoite phases and non-fresnoite phases that has been determined to exist between $0.2 \leq y \leq 0.3$.

6.2.3 $Ba_2TiGe_{2y}Si_{2-2y}O_8$ System

The $Ba_2TiGe_{2y}Si_{2-2y}O_8$ ($0 \leq y \leq 1$) system is relatively well understood due the interest in the difference in symmetry of the structures of the $Ba_2TiSi_2O_8$ and $Ba_2TiGe_2O_8$ end members. The results from previous investigations of this system were summarised in section 6.1. This section discusses the synthesis and characterisation of samples across the $Ba_2TiGe_{2y}Si_{2-2y}O_8$ ($0 \leq y \leq 1$) system at ambient temperature to provide further insight into the behaviour of the unit cell as substitutions are made onto the *M*-site across the series.

Samples in the $Ba_2TiGe_{2y}Si_{2-2y}O_8$ system were synthesised using methods similar to the respective end members. The $y \leq 0.7$ members of the system were synthesised using a procedure based on the method used for $Ba_2TiSi_2O_8$ where stoichiometric ratios of the relevant oxides and carbonates were heated for 20 hours at 1000 °C, 1100 °C, 1200 °C, followed by heating for 20 hours at 1250 °C up to four times with intermittent grinding. The $y > 0.8$ members were synthesised via the melt method that was used for the $Ba_2TiGe_2O_8$ end member where stoichiometric ratios of precursors were melted in a platinum crucible at 1400 °C for one hour, pulverised, and heated at 850 °C for 20 hours up to three times with intermittent grinding.

Synchrotron X-ray powder diffraction patterns were collected from members across the $Ba_2TiGe_{2y}Si_{2-2y}O_8$ ($0 \leq y \leq 1$) system at ambient temperature are provided in Figure 6.32. The splitting of the 322 reflection into the 602 and 062 reflections (~25.4° two theta) and the 312 reflection into the 150 and 510 reflections (~19.8° two theta) suggests that the phase boundary between the tetragonal and orthorhombic space groups occurs at approximately $y = 0.6$

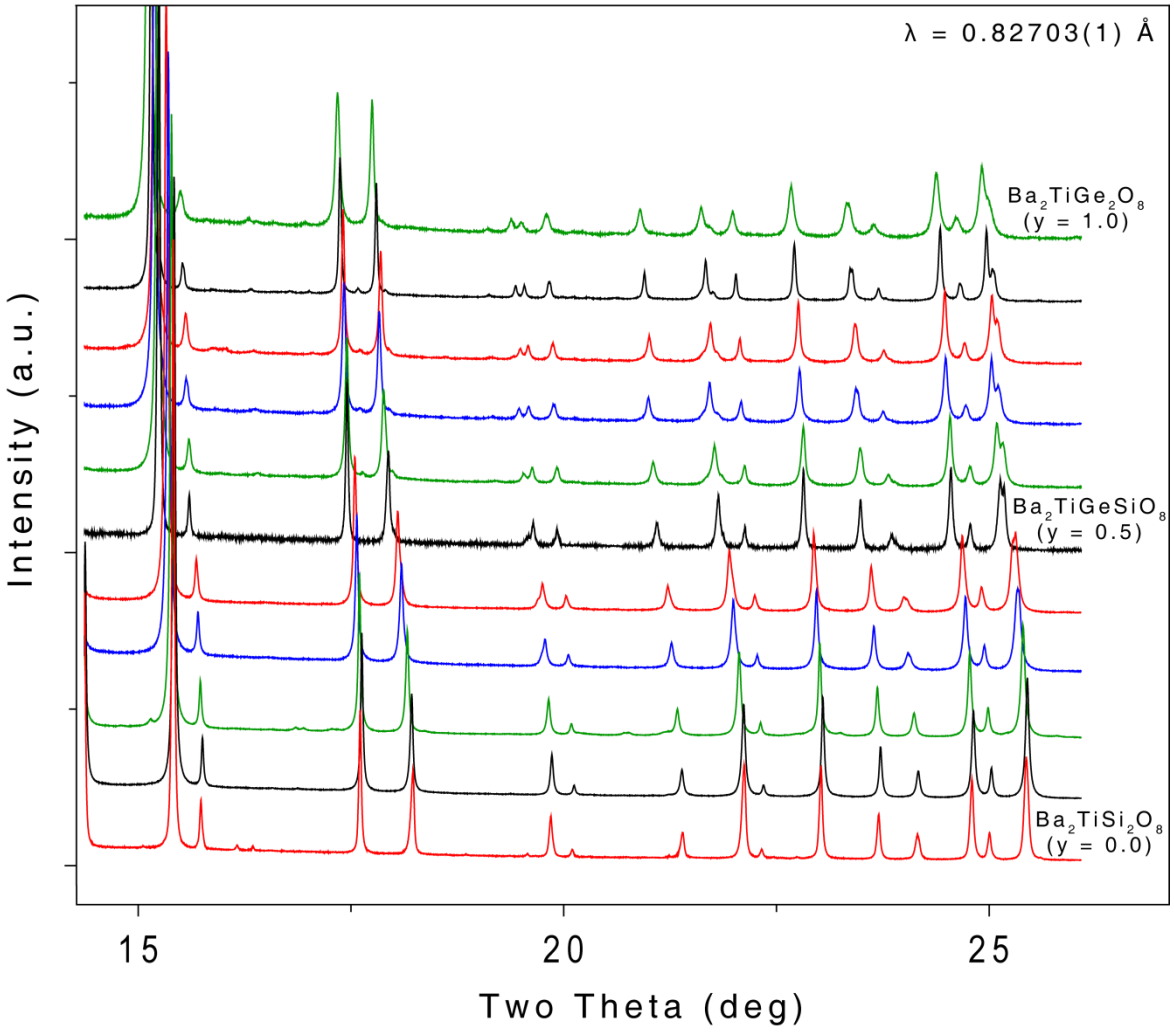

Figure 6.32: Synchrotron diffraction patterns collected from members of the $Ba_2TiGe_{2y}Si_{2-2y}O_8$ ($0 \leq y \leq 1$, $y = 0.1$ steps) system at ambient temperature.

The unit cell parameters calculated for members across the $Ba_2TiGe_{2y}Si_{2-2y}O_8$ ($0 \leq y \leq 1$) system at ambient temperature from Rietveld refinement against the synchrotron X-ray powder diffraction patterns are plotted in Figure 6.33. The discontinuity observed by Iijima *et al.*[88] at approximately $y = 0.55$ is present in the trend in cell parameters determined from the current study. However, despite the high quality of the data obtained in this experiment, the refinement of the *a* and *b* unit cell parameters for the orthorhombic phase was not simple because the separation between the split reflections differentiating these parameters was extremely low. This has been reflected in the small variability in the cell parameters (Figure 6.33) and volume (

Figure 6.34) across the series. However, a change in the trend of the parameters is evident between $y = 0.4$ and $y = 0.5$ in agreement with the work conducted by Iijima *et al.*[88] and Wong.[153] The change in the trend in the unit cell parameters between y = 0.7 and y = 0.8 suggests other behaviour such as a possible additional phase transition may be present. However, this was unable to be determined from the data collected in this study.

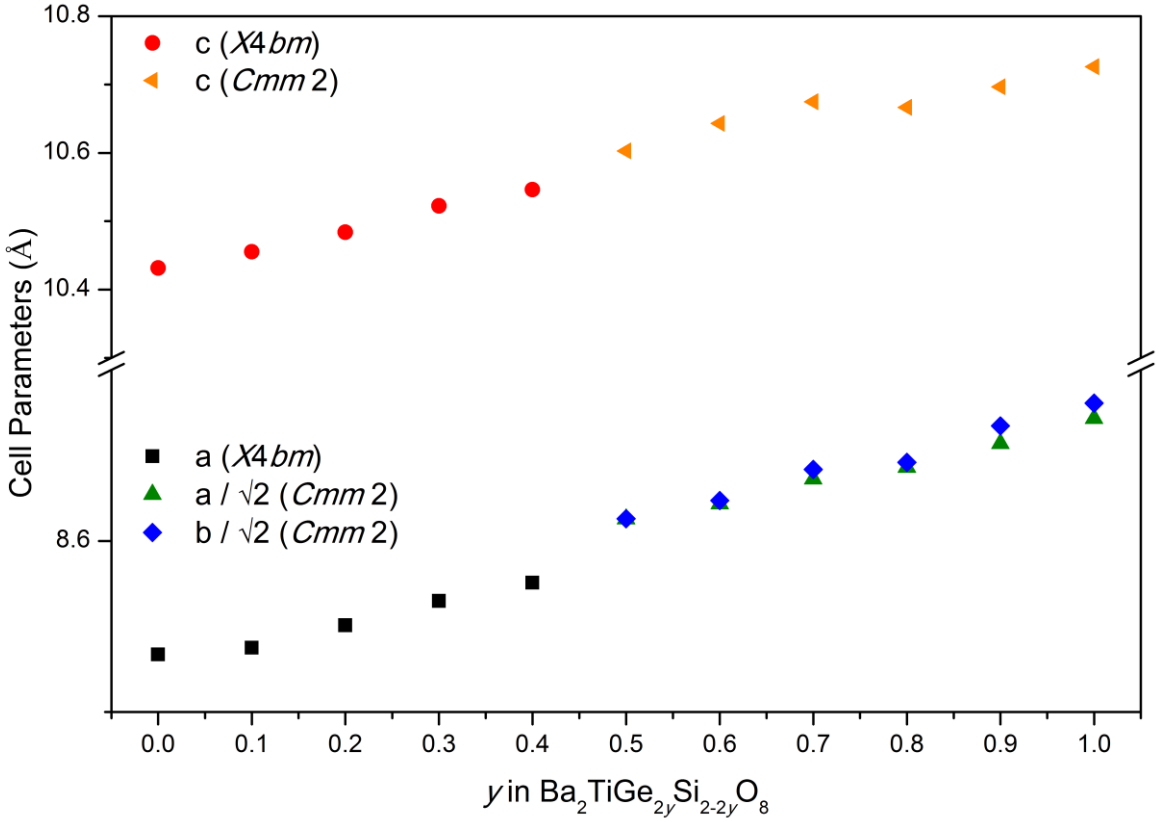

Figure 6.33: Unit cell parameters for members across the $Ba_2TiGe_{2y}Si_{2-2y}O_8$ ($0 \leq y \leq 1$) system at ambient temperature as calculated from Rietveld refinement against synchrotron X-ray powder diffraction patterns collected at $\lambda = 0.82703(1)$ Å. Unit cell parameters *a* and *b* from the orthorhombic phase have been converted into the tetragonal setting to allow for direct comparison with the tetragonal phase.

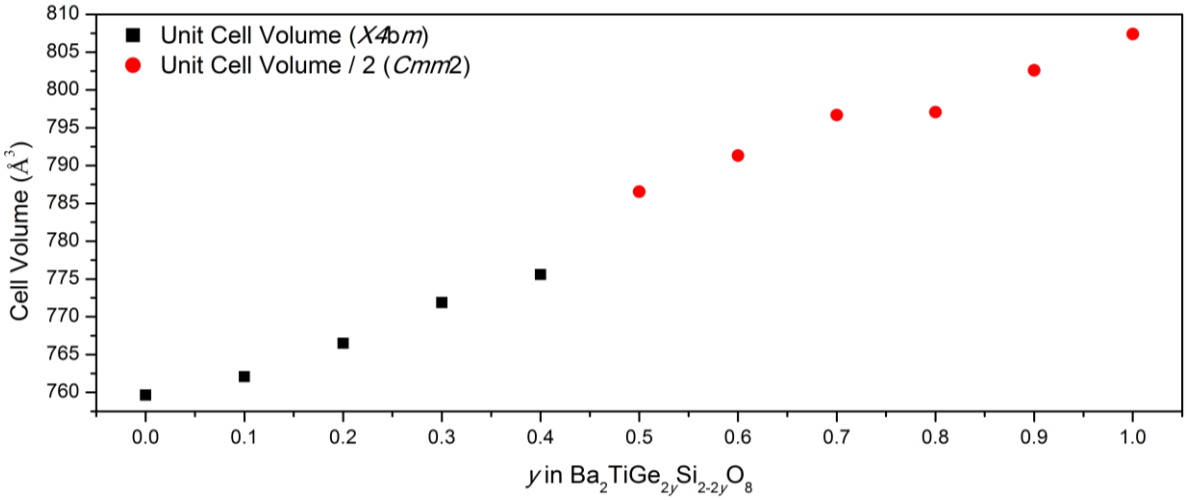

Figure 6.34: Unit cell volume for members across the $Ba_2TiGe_{2y}Si_{2-2y}O_8$ ($0 \leq y \leq 1$) system at ambient temperature as calculated from Rietveld refinement against synchrotron X-ray powder diffraction patterns collected at λ = 0.82703(1) Å. Data points for the *Cmm*2 phase have been converted into the tetragonal setting to allow for direct comparison with the *X*4*bm* phase.

6.2.4 $Ba_{2x}Sr_{2-2x}TiGe_2O_8$ System

Until now, it has not been known whether any $x < 1$ members of the system will form structures of the fresnoite structure type or which space group they may adopt. This section will discuss the formation of fresnoite phases within this system.

The synthesis of compounds in the $Ba_{2x}Sr_{2-2x}TiGe_2O_8$ system was attempted using the two solid state synthetic routes that have been utilised for $Ba_2TiGe_2O_8$ and $Ba_2TiSi_2O_8$ respectively. The success in using the melt method to produce pure $Ba_2TiGe_2O_8$ samples suggests that this should be the most likely method to produce fresnoite compounds for germanium-rich compositions. This involved mixing stoichiometric proportions of the relevant oxides and carbonates, melting at 1400 °C for one hour, thoroughly grinding, pressing into pellets and heating for 48 hours at 850 °C. However, the diffraction patterns collected from all samples in the $Ba_{2x}Sr_{2-2x}TiGe_2O_8$ ($x < 1$) system contained a significant number of reflections that could not be indexed with a unit cell based on a fresnoite structure type. The high number and different shape of the reflections

suggests the compounds contain a significant proportion of at least one unidentified non-fresnoite phase.

The second method of synthesis that was attempted was based on the slower route used for the $Ba_2TiSi_2O_8$ and $Sr_2TiSi_2O_8$ members of the fresnoite family of compounds. Although the crystallinity of the compounds produced was slightly higher than those synthesised via the melt method, the diffraction patterns could not be indexed using a unit cell based on the fresnoite structure type. Seeing as the $x = 1$ ($Ba_2TiGe_2O_8$) member is well known to form a stable fresnoite phase[50,57], it can be concluded that a formation boundary exists between $0.9 \leq x \leq 1.0$ in the $Ba_{2x}Sr_{2-2x}TiGe_2O_8$ system. The location of this phase formation boundary is in agreement with the predictions that can be made based on the ratio of ionic radii in the fresnoite structure type as presented by Höche *et al*.[50]

6.2.5 $BaSrTiGe_{2y}Si_{2-2y}O_8$ System

Similarly to the $Ba_{2x}Sr_{2-2x}TiGe_2O_8$ system, work on the $BaSrTiGe_{2y}Si_{2-2y}O_8$ system has never been reported in the literature. This system is of interest for multiple reasons. Firstly, it is not known if or where there may be a compositional phase boundary between the tetragonal phase (known for $BaSrTiSi_2O_8$) and a possible orthorhombic phase for members containing germanium at ambient temperature (which would be predicted by the change in the ratio of the ionic radii). It is also not known how much germanium can be incorporated into the $BaSrTiGe_{2y}Si_{2-2y}O_8$ system before non-fresnoite phases form preferentially over fresnoite phases.

Because the aim of studying this system was to identify potential phase boundaries dividing fresnoite structures of different symmetries or compositions where fresnoite structures no longer form, the $y \geq 0.3$ members were initially investigated. Seeing as the $y = 0.0$ and $y = 0.3$ members were shown to adopt the same symmetry, the $y < 0.3$ members were not investigated. The $y \geq 0.3$

members were synthesised using procedures based on the synthetic methods used for the $Ba_{2x}Sr_{2-2x}TiSi_2O_8$ system whereby stoichiometric ratios of the relevant oxides and carbonates were mixed and heated for 20 hours at 1000 °C initially, followed by heating at higher temperatures with intermittent grinding. The presence of germanium reduced the melting point of the mixture. Hence, to prevent the onset of melting and the formation of the perovskite phase, samples in the $BaSrTiGe_{2y}Si_{2-2y}O_8$ system were not heated above 1150 °C. After the initial 1000 °C heating step, three further 48 hour heating steps at 1150 °C with intermittent regrinding produced samples of the highest purity possible for the members that form fresnoite phases.

The $y \leq 0.6$ members of the system formed pure fresnoite phases. The $y \geq 0.7$ members contained a mixture of many phases, including very small proportions of a fresnoite phase. However, these proportions were so small relative to the other non-fresnoite phases that they did not warrant any further investigation. Hence, it has been established that pure fresnoite phases can only be formed for the $y \leq 0.6$ members of the $BaSrTiGe_{2y}Si_{2-2y}O_8$ system.

Synchrotron diffraction patterns were collected from selected members of interest in the $BaSrTiGe_{2y}Si_{2-2y}O_8$ system to determine which space group could most correctly describe each member (Figure 6.35). No evidence of an orthorhombic phase was found in any of the $y \leq 0.6$ members at ambient temperature. Hence, all compounds were modelled using the *X*4*bm* space group.

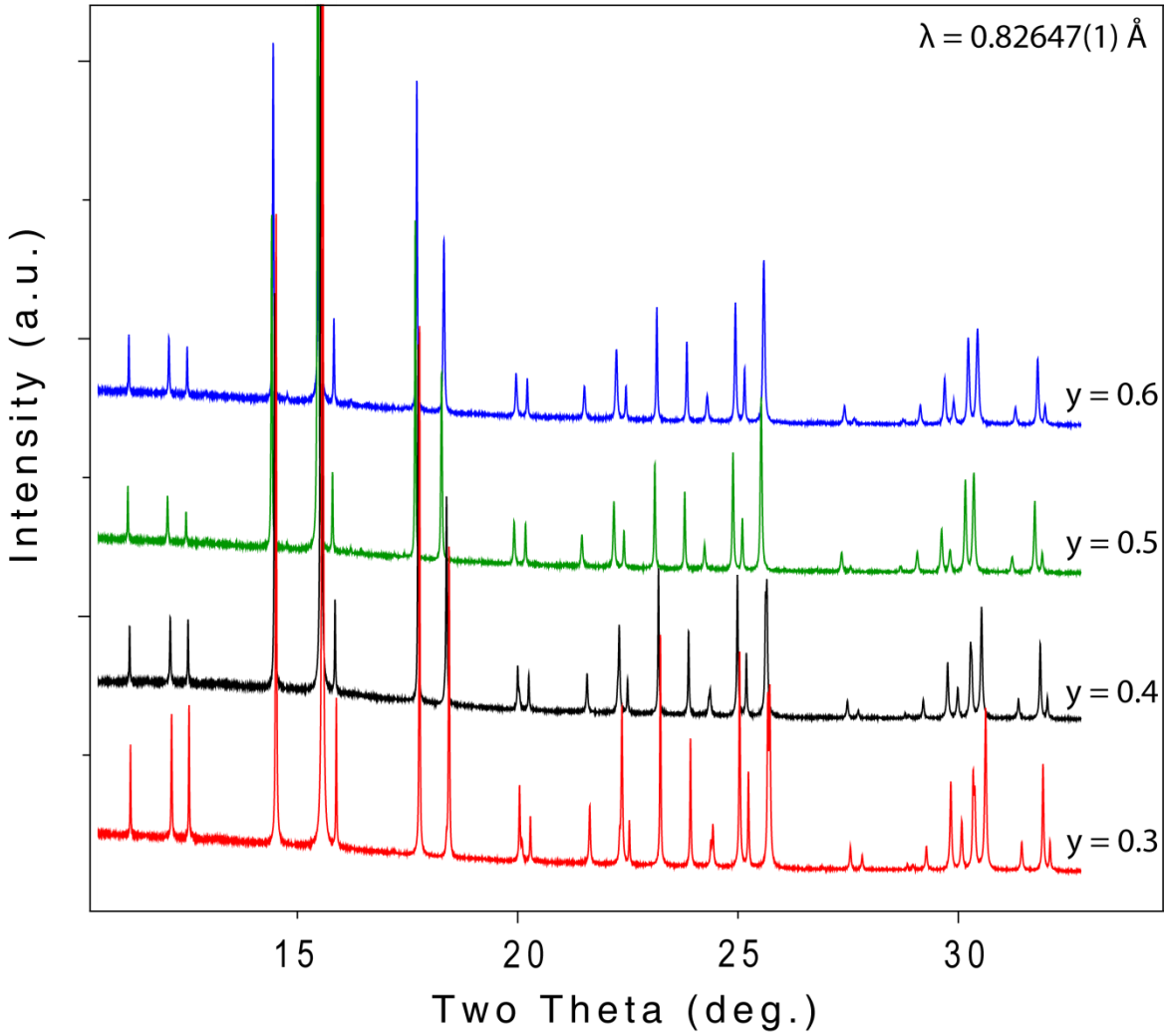

Figure 6.35: Synchrotron X-ray diffraction patterns collected from the $BaSrTiGe_{2y}Si_{2-2y}O_8$ ($0.3 \leq y \leq 0.6$) system at ambient temperature.

The cell parameters for the $0 \leq y \leq 0.6$ members of the $BaSrTiGe_{2y}Si_{2-2y}O_8$ system at ambient temperature were calculated from Rietveld refinement against synchrotron X-ray powder diffraction patterns collected at λ = 0.82647(1) Å. The expansion of the unit cell as germanium is substituted for silicon does not follow the expected linear increase as predicted by Vegard's law.[203] Instead, a maximum in the unit cell parameters and volume occur at the $y = 0.5$ member, followed by reduced values for the $y = 0.6$ member. The magnitude of the reduction of both the *a* and *c* unit cell parameters from the $y = 0.5$ to the $y = 0.6$ member is too large to be considered within experimental error (error bars as calculated from the refinement are smaller than the data points). Additionally, the $0.3 \leq y \leq 0.6$ members of the system were synthesised at the same time,

under the same conditions, and data were collected from these samples sequentially at the synchrotron. Hence, although it is uncharacteristic of metal oxide compounds, it is deemed likely that the cell contraction observed from the $y = 0.5$ to the $y = 0.6$ member is a real feature of the $BaSrTiGe_{2y}Si_{2-2y}O_8$ system. It is possible that other factors could be contributing to this result, such as a phase transition to another phase (such as a different tetragonal phase, or an orthorhombic phase) between $0.5 \leq y \leq 0.6$. However, no evidence such as the appearance of new reflections, or reflection splitting could be gathered from the synchrotron powder diffraction data to conclude that this is the case.

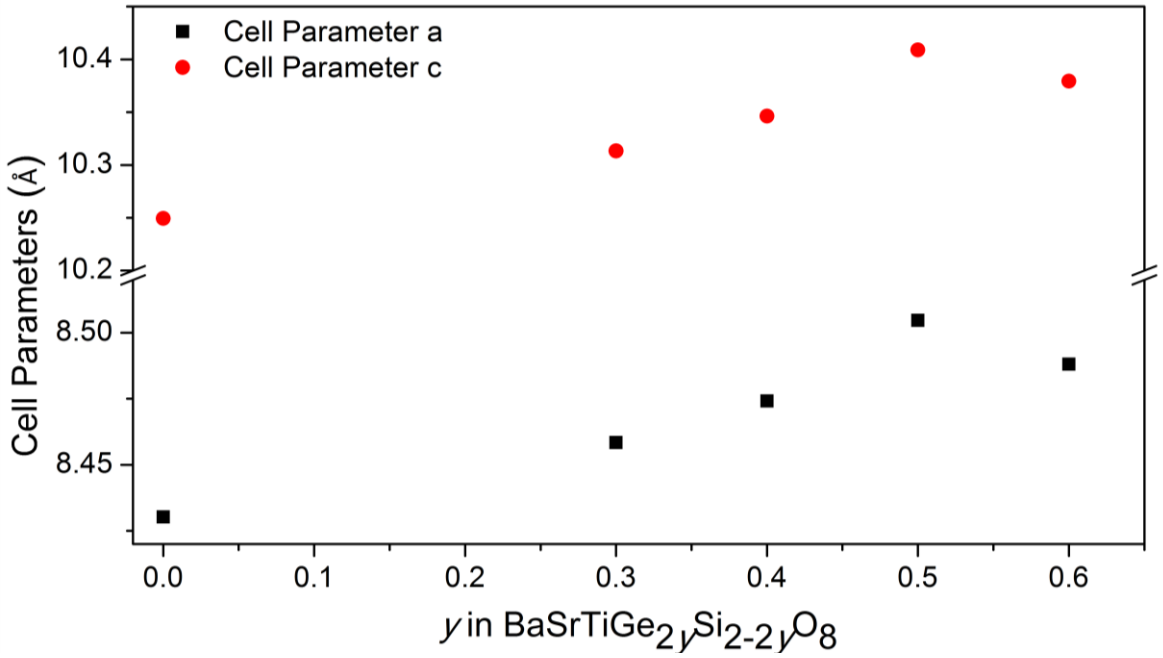

Figure 6.36: Unit cell parameters *a* and *b* for the $BaSrTiGe_{2y}Si_{2-2y}O_8$ ($0 \leq y \leq 0.6$) system at ambient temperature as calculated from Rietveld refinement against synchrotron X-ray powder diffraction patterns collected at λ = 0.82647(1) Å.

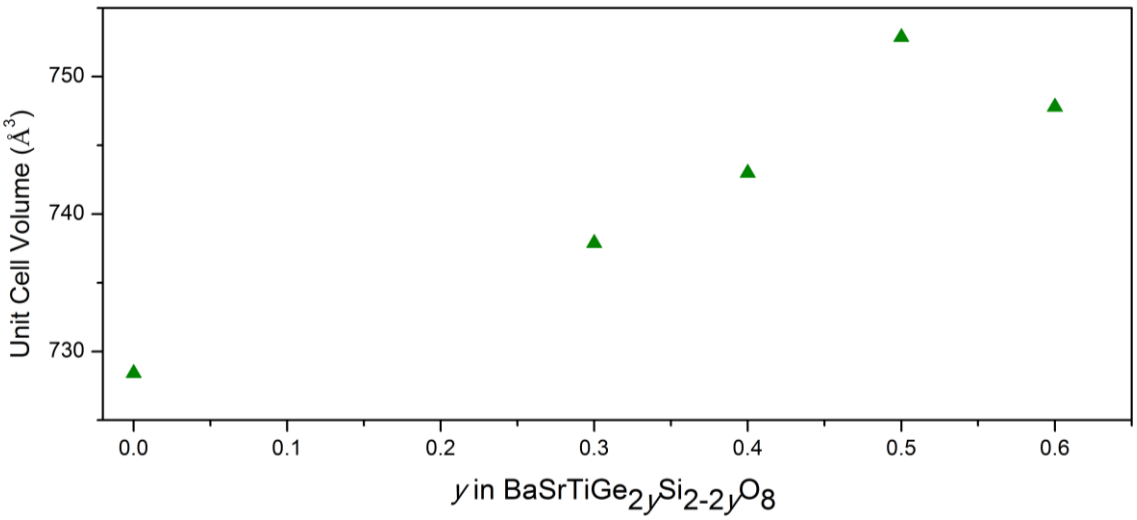

Figure 6.37: Unit cell volume for members across the $BaSrTiGe_{2y}Si_{2-2y}O_8$ ($0 \leq y \leq 0.6$) system at ambient temperature as calculated from Rietveld refinement against synchrotron X-ray powder diffraction patterns collected at λ = 0.82647(1) Å.

The variable temperature synchrotron X-ray powder diffraction patterns in Figure 6.38 were collected from the $BaSrTiGe_{0.6}Si_{1.4}O_8$ member of the system between 298 K - 1210 K to determine whether any of the phase transitions that have been identified in the $Sr_2TiSi_2O_8$ or $Ba_2TiSi_2O_8$ members may occur on heating.

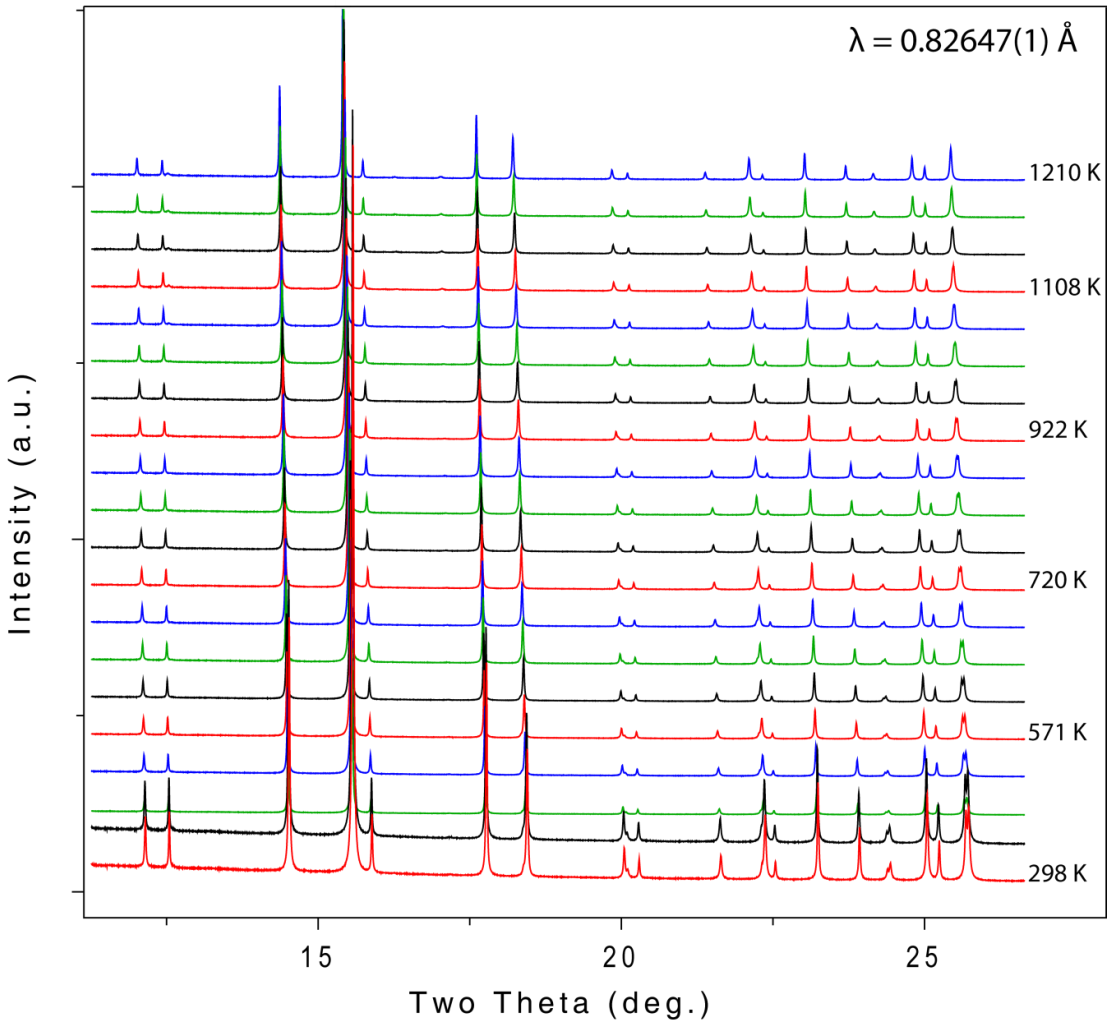

Figure 6.38: Synchrotron X-ray powder diffraction patterns collected from $BaSrTiGe_{0.6}Si_{1.4}O_8$ between 298 K - 1210 K at λ = 0.82647(1) Å.

The convergence of the 332 and 314 reflections on heating at approximately 26° two theta in Figure 6.38 suggests that a phase transition may be occurring. However, Rietveld refinement against these data established that a single *X*4*bm* phase was sufficient to index and model the data across the entire temperature range investigated. The unit cell parameters and volume calculated from Rietveld refinement against the synchrotron X-ray diffraction data collected between 298 K - 1210 K indicate that linear thermal expansion occurs on heating as shown in Figure 6.39, confirming that the $BaSrTiGe_{0.6}Si_{1.4}O_8$ structure is stable in the *X*4*bm* phase up to 1210 K. Variable temperature studies were not performed on other members of this system due to only a limited amount of synchrotron beam time being allocated to this project.

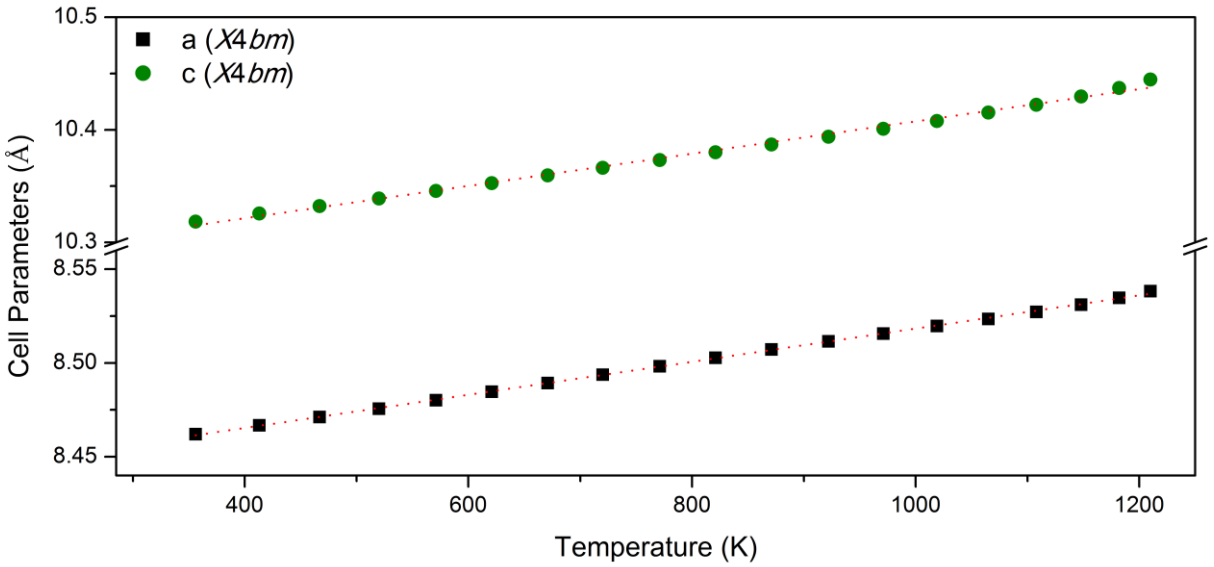

Figure 6.39: $BaSrTiGe_{0.6}Si_{1.4}O_8$ unit cell parameters between 298 K - 1210 K as calculated from Rietveld refinement against synchrotron X-ray powder diffraction data.

6.3 Summary

This chapter has provided new insight towards the formation and phase transitions in many of the individual systems within the $Ba_{2x}Sr_{2-2x}TiGe_{2y}Si_{2-2y}O_8$ system. Firstly, the phases that form at ambient temperature were investigated across the $Ba_{2x}Sr_{2-2x}TiSi_2O_8$ system, where it was established that the $x \leq 0.5$ members contained a main tetragonal phase in addition to a very small proportion of an orthorhombic phase. It was shown that the temperature of the transition from the two phase mixture to the single orthorhombic phase in the $Sr_2TiSi_2O_8$ end member can be increased by the substitution of up to 5 % barium on the *A*-site, and that the introduction of more barium prevents the structure from forming a single orthorhombic phase until the prototypic structure is formed at higher temperatures (*c.f.* 1323 K for $Sr_2TiSi_2O_8$, 1221 K for $x = 0.05$, and 1196 K for $x = 0.1$). The variable temperature studies at the barium-rich end of the $Ba_{2x}Sr_{2-2x}TiSi_2O_8$ system showed that the temperature of the *X*4*bm*(α, α, 0)*0gg* to prototypic *X*4*bm* transition linearly increases with strontium content on the *A*-site. These phase transitions were summarised in a new phase diagram for the $Ba_{2x}Sr_{2-2x}TiSi_2O_8$ system in Figure 6.23.

The $0 \leq y \leq 0.2$ members of the $Sr_2TiGe_{2y}Si_{2-2y}O_8$ system were shown to form phases of the fresnoite structure type, while the $y > 0.2$ members formed perovskite phases in addition to other non-fresnoite phases. Variable temperature studies showed that the complex phase behaviour of the $Sr_2TiSi_2O_8$ end member occurs in members up to $y = 0.2$. The inclusion of germanium into $Sr_2TiSi_2O_8$ was shown to increase the phase transition temperatures from the tetragonal to the orthorhombic phase as was shown for the inclusion of barium ions into $Sr_2TiSi_2O_8$ in the $Ba_{2x}Sr_{2-2x}TiSi_2O_8$ system. The temperature at which the structures transform from the orthorhombic phase to the high temperature tetragonal phase decreases from 1323 K for $Sr_2TiSi_2O_8$ to 1210 K for the $x = 0.1$ member. The results from this section have shown that the phase behaviour is more complex than would be predicted by considering only the ratio of the

ionic radii in the structure. The phase transitions were summarised in a new phase diagram for the $Sr_2TiGe_{2y}Si_{2-2y}O_8$ system in Figure 6.31.

The investigation of the $Ba_2TiGe_{2y}Si_{2-2y}O_8$ ($0 \leq y \leq 1.0$) system showed that the morphotropic phase boundary between the tetragonal $Ba_2TiSi_2O_8$ end member and the orthorhombic $Ba_2TiGe_2O_8$ end member occurs between $0.4 \leq y \leq 0.5$ in agreement with Iijima *et al.*[88], Schmid *et al.*[60], and Wong.[153] A discontinuity in the unit cell parameters between $0.7 \leq y \leq 0.8$ was also presented. However, no further information about this observation could be deduced using a powder diffraction approach.

It was shown that the $x \leq 0.9$ members of the $Ba_{2x}Sr_{2-2x}TiGe_2O_8$ system do not form structures with the fresnoite structure type. The presence of the formation boundary between $0.9 \leq x \leq 1.0$ is consistent with the predictions that would be made based on solely the ratio of the ionic radii in the structure.

The $BaSrTiGe_{2y}Si_{2-2y}O_8$ system was investigated for the first time, establishing that $y \leq 0.6$ compositions form fresnoite phases while $y > 0.7$ members do not. The substitution of germanium for silicon in the $BaSrTiGe_{2y}Si_{2-2y}O_8$ system produces unusual behaviour whereby the *a* and *c* unit cell parameters expand up to the $y = 0.5$ member followed by a contraction for the $y = 0.6$ member. Variable temperature studies of the $BaSrTiGe_{0.6}Si_{1.4}O_8$ member of the system showed that the structure retains the tetragonal symmetry between 298 K - 1210 K, showing that the behaviour of the $BaSrTiGe_{0.6}Si_{1.4}O_8$ member is different from the $Sr_2TiSi_2O_8$ and $Ba_2TiSi_2O_8$ family members which both show interesting phase transitions on heating.

Chapter 7 Conclusions

The $Ba_{2x}Sr_{2-2x}TiGe_{2y}Si_{2-2y}O_8$ ($0 \leq x \leq 1$; $0 \leq y \leq 1$) system defines a range of compositions between four end members ($Ba_2TiSi_2O_8$, $Sr_2TiSi_2O_8$, $Ba_2TiGe_2O_8$, and the hypothetical $Sr_2TiGe_2O_8$). Before this study, $Ba_2TiSi_2O_8$, $Sr_2TiSi_2O_8$, and $Ba_2TiGe_2O_8$ had been relatively well characterised at ambient temperature and shown to display promising physical properties such as piezoelectricity. Höche *et al*.[50] had proposed a stability field for compositions between these end members based on the ratio of ionic radii of the ions on the *A*- and *M*-sites. This thesis has further investigated the end members and members across five separate series within the $Ba_{2x}Sr_{2-2x}TiGe_{2y}Si_{2-2y}O_8$ ($0 \leq x \leq 1$; $0 \leq y \leq 1$) system to improve the understanding of this stability field. Members of this system were also characterised over a wide range of temperatures to further understand the known phase transitions and identify any new phase transitions. The conclusions drawn from these investigations are presented below.

7.1 Synthesis and phase behaviour of the $Ba_{2x}Sr_{2-2x}TiGe_{2y}Si_{2-2y}O_8$ ($0 \leq x \leq 1$) system at ambient temperature

7.1.1 $Ba_{2x}Sr_{2-2x}TiSi_2O_8$ series:

Synthesis of polycrystalline members of the $Ba_{2x}Sr_{2-2x}TiSi_2O_8$ ($0 \leq x \leq 1$) series requires considerably longer heating times than have been previously reported. Compounds in this series require between four and six 20 hour heating steps at 1250 °C to achieve the highest possible purity. The use of synthesis temperatures close to the melting point can lead to the irreversible formation of perovskite phases instead of fresnoite phases.

The absence of satellite reflections in all synchrotron X-ray powder diffraction patterns made the characterisation of the modulated structures a challenging exercise. However, the presence of

weak satellite reflections in neutron powder diffraction patterns collected from $Ba_2TiSi_2O_8$ and $Sr_2TiSi_2O_8$ meant that their modulated structures could be characterised using this technique for the first time.

Complex phase behaviour with two phases coexisting (the main *X4bm*(α, α, 0)*0gg* phase and a small proportion of a *Cmm*2(0, β, 0)*s*00 phase) is observed for compositions from $Sr_2TiSi_2O_8$ ($x = 0$) to $BaSrTiSi_2O_8$ ($x = 0.5$). The proportion of the orthorhombic phase reduces with increased barium content.

The polycrystalline $Ba_2TiSi_2O_8$ and $Sr_2TiSi_2O_8$ end members were shown to display piezoelectricity, but no ferroelectricity. This is in contrast to the previous work of Foster *et al*.,[51] who predicted and demonstrated ferroelectricity in polycrystalline and single crystal $Ba_2TiSi_2O_8$ samples that were synthesised using different methods to those used in this thesis.

7.1.2 $Sr_2TiGe_{2y}Si_{2-2y}O_8$ series

Complex phase behaviour with the two phases (the main *X4bm*(α, α, 0)*0gg* phase and a small proportion of the *Cmm*2(0, β, 0)*s*00 phase) coexisting is observed for compositions from $Sr_2TiSi_2O_8$ ($y = 0$) to $Sr_2TiGe_{0.4}Si_{1.6}O_8$ ($y = 0.2$). In a similar manner to the inclusion of barium in the $Ba_{2x}Sr_{2-2x}TiSi_2O_8$ series, the proportion of the orthorhombic phase reduces for members containing higher germanium content. No samples in this series crystallise with a main orthorhombic phase, and the boundary separating phases that do and do not form fresnoite phases occurs between $0.2 \leq y \leq 0.3$.

7.1.3 $Ba_2TiGe_{2y}Si_{2-2y}O_8$ series

The characterisation of the modulated structure for the polycrystalline $Ba_2TiGe_2O_8$ end member was not possible despite strong reflections in the neutron diffraction pattern that could be indexed as satellite reflections. This may be attributed due to the presence of an impurity phase or chemical inhomogeneity complicating the structural determination. The boundary separating the tetragonal and orthorhombic phases was determined to exist between $0.4 \leq y \leq 0.5$. This is consistent with the location of the phase boundary determined from previous studies.

7.1.4 $Ba_{2x}Sr_{2-2x}TiGe_2O_8$ and $BaSrTiGe_{2y}Si_{2-2y}O_8$ series

Members within these two series have been investigated for the first time in this thesis. The phase boundaries separating compositions that do and do not form fresnoite phases in the $Ba_{2x}Sr_{2-2x}TiGe_2O_8$ and $BaSrTiGe_{2y}Si_{2-2y}O_8$ series were determined to exist between $0.9 \leq x \leq 1.0$ and $0.6 \leq y \leq 0.7$, respectively.

7.2 Phase behaviour of the $Ba_{2x}Sr_{2-2x}TiGe_{2y}Si_{2-2y}O_8$ ($0 \leq x \leq 1$) system at non-ambient temperatures

Resonant ultrasound spectroscopy, X-ray powder diffraction, and transmission electron microscopy investigations of the $Ba_{2x}Sr_{2-2x}TiGe_{2y}Si_{2-2y}O_8$ ($0 \leq x \leq 1$) system over a wide range of temperatures have provided new information about known phase transitions in addition to discovering new phase transitions.

Resonant ultrasound spectroscopy has shown for the first time that strong coupling occurs between the elastic moduli of fresnoite samples and the subtle structural changes involved in their phase transitions. This was particularly useful for the identification of the incommensurate

to prototypic phase transition in $Ba_2TiSi_2O_8$ and the lock-in transition from the incommensurate to the commensurate structures in $Ba_2TiGe_2O_8$. The data collected in this project have demonstrated the appropriateness of this technique for the investigation of phase transitions with subtle structural changes that can be difficult to determine from powder diffraction experiments alone.

The change in the gradient of the unit cell parameters on heating $Ba_2TiSi_2O_8$ coincides with the previously reported incommensurate to prototypic transition at 433 K. This was shown to be a useful method for the identification of this transition in barium rich members of the $Ba_{2x}Sr_{2-2x}TiSi_2O_8$ ($0.5 \leq x \leq 1$) system using Cu K_α radiation whereby the transition temperature linearly reduces from 943 K for the $x = 0.5$ ($Ba_2TiSiGeO_8$) member to 433 K to the $x = 1.0$ ($Ba_2TiSi_2O_8$) end member. The phase transition was not observed for the $x < 0.5$ members of the series.

The $Ba_2TiGe_2O_8$ structure has been characterised across the 1085 K ferroelastic transition using synchrotron X-ray powder diffraction for the first time. The temperature dependent phase transitions discovered for the $Sr_2TiSi_2O_8$ structure demonstrated that this compound exhibits unusual and complex phase behaviour that is significant to any future investigation. Electron diffraction patterns collected at elevated temperatures have shown for the first time that the incommensurately modulated tetragonal phase converts into the incommensurately modulated orthorhombic phase on heating and that both phases can be present in the same region of the crystal after cooling back down to ambient temperature. Considering the information extracted from the electron diffraction and X-ray diffraction experiments, the cooling of $Sr_2TiSi_2O_8$ from its synthesis temperature at 1250 °C involves two phase transitions before reaching ambient temperature. Firstly, the structure must transform from the parent $X4bm$ phase to a single incommensurately modulated $Cmm2(0, \beta, 0)s00$ phase. This is followed by the more complex (and importantly, incomplete) conversion of the $Cmm2(0, \beta, 0)s00$ phase into the higher

symmetry incommensurately modulated $X4bm(\alpha, \alpha, 0)0gg$ phase. The fact that this transformation from the two phase mixture does not reach completion explains why two phases are observed at ambient temperature and means that it may be impossible to synthesise "single phase" $Sr_2TiSi_2O_8$ at ambient temperature. It may, however, be possible to conduct a single crystal investigation of the intermediate orthorhombic phase of $Sr_2TiSi_2O_8$ above approximately 567 K where the transition to the single orthorhombic phase is complete.

As was shown for the stable phases at ambient temperature, the inclusion of barium and germanium have similar effects on the phase transitions in compounds with similar compositions to $Sr_2TiSi_2O_8$. Specifically, higher proportions of barium or germanium in $Sr_2TiSi_2O_8$ increase the temperature of the phase transition from the two phase mixture to the single orthorhombic phase and reduces the phase transition temperature to the high temperature tetragonal phase. The maximum proportion of the orthorhombic phase that is converted from the tetragonal phase on heating is also reduced by higher barium or germanium content.

In summary, it can be seen that the structural behaviour of the $Ba_{2x}Sr_{2-2x}TiGe_{2y}Si_{2-2y}O_8$ ($0 \leq x \leq 1$; $0 \leq x \leq 1$) system is more complex than is apparent from the previously reported work on these compounds. The phase behaviour of this system cannot be accurately predicted by only considering the ratio of the ionic radii on the *A* and/or *M*-sites of the structure. While this method is sufficient to predict the tendency of fresnoite compounds to adopt tetragonal space groups when the ratio of ionic radii is reduced by substituting barium for strontium in the $Ba_{2x}Sr_{2-2x}TiSi_2O_8$ series, it does not reflect that both phases may be present for many compositions. Similarly, consideration of only the ratio of ionic radii does not explain the persistence of the tetragonal phase as this ratio is lowered by the increased proportion of germanium in the $Sr_2TiGe_{2y}Si_{2-2y}O_8$ and $BaSrTiGe_{2y}Si_{2-2y}O_8$ series. The predicted boundaries separating compositions that do and do not form fresnoite phases may also need readjusting. For example, while this boundary is correctly predicted for the $Ba_{2x}Sr_{2-2x}TiGe_2O_8$ ($0.9 \leq y \leq 1.0$) series, a large discrepancy

occurs between the predicted ($0.5 \leq y \leq 0.6$) and experimentally determined ($0.2 \leq y \leq 0.3$) boundaries for the $Sr_2TiGe_{2y}Si_{2-2y}O_8$ series.

The coexistence of two phases at ambient temperature is an inherent property of compounds with compositions close to that of the $Sr_2TiSi_2O_8$ member owing to the phase transitions on cooling from the synthesis temperature. However, these properties may be advantageous given that previous studies[55,56,59] have shown that physical properties such as the piezoelectric and pyroelectric coefficients of some fresnoite compounds are improved at structural phase transitions. With the improved understanding of the relationship between composition and phase transitions in fresnoite compounds it is possible that specific compositions could be investigated with the aim of tuning the transition temperatures so that optimised physical properties may be observed at temperatures appropriate for specific applications.

Chapter 8 References

[1] Newnham, R. E., *Acta Crystallographica A*, **1998**, *54*, 729.
[2] Hirose, M.; Matsushige, S.; Buma, S.; Kamiya, K., *IEEE Transactions on Industrial Electronics*, **1988**, *35*, 193.
[3] *"Lead and You. A guide to working safely with Lead", Issued by The United Kingdom Health and Safety Executive*, **2003**.
[4] *"Directive 2002/95/EC of the European Parliment and the Council of 27 January 2003 on the restriction of the use of certain hazardous substances in electrical and electronic equipment", Official Journal of the European Union*, **2003**.
[5] Li, Y.; Moon, K. S.; Wong, C. P., *Science*, **2005**, *308*, 1419.
[6] Frantti, J., *Journal of Physical Chemistry B*, **2008**, *112*, 6521.
[7] Halasyamani, P. S.; Poeppelmeier, K. R., *Chemistry of Materials*, **1998**, *10*, 2753.
[8] Stokes, H. T.; Campbell, B. J.; van Smaalen, S., *Acta Crystallographica Section A*, **2011**, *67*, 45.
[9] Takenaka, T.; Nagata, H., *Journal of the European Ceramic Society*, **2005**, *25*, 2693.
[10] Zhang, S.; Xia, R.; Lebrun, L.; Anderson, D.; Shrout, T. R., *Materials Letters*, **2005**, *59*, 3471.
[11] Scott, J. F.; Dearaujo, C. A. P., *Science*, **1989**, *246*, 1400.
[12] Alrich, R.; Schaper, L.; Nelms, D.; Leftwich, M., *The International Journal of Microcircuits and Electronic Packaging*, **2000**, *23*, 172.
[13] Newnham, R. E.; Cross, L. E., *Materials Research Society Bulletin*, **2005**, *30*, 845.
[14] Cross, L. E.; Newnham, R. E., *History of Ferroelectrics, Chapter in High Technology Ceramics*; American Ceramics Society, Westerville, OH, 1986; Vol. III.
[15] Schulz, M. J.; Sundaresan, M. J.; McMichael, J.; Clayton, D.; Sadler, R.; Nagel, B., *Journal of Intelligent Material Systems and Structures*, **2003**, *14*, 693.
[16] Jaffe, H., *Journal of the American Ceramic Society*, **1958**, *41*, 494.
[17] Lee, M. H.; Guo, R.; Bhalla, A. S., *Journal of Electroceramics*, **1998**, *2*, 229.
[18] Megaw, H. D., *Acta Crystallographica*, **1958**, *11*, 754.
[19] von Hippel, A., *Zeitschrift für Physik A Hadrons and Nuclei*, **1952**, *133*, 158.
[20] APC International Ltd., *Piezoelectric ceramics: principles and applications*; APC International, 2002.
[21] West, A. R., *Basic Solid State Chemistry*; 2nd ed.; John Wiley & Sons, 1996.
[22] Hadni, A., *Journal of Physics E*, **1981**, *14*, 1233.
[23] Newnham, R. E., *Properties of Materials*; Oxford University Press, 2005.
[24] Bell, A. J., *Applied Physics Letters*, **2000**, *76*, 109.
[25] Marrison, W. A., *The Bell System Technical Journal*, **1948**, *27*, 510.
[26] Wul, B., *Nature*, **1945**, *156*, 480.
[27] Coursey, P. R.; Brand, K. G., *Nature*, **1946**, *157*, 297.
[28] Takenaka, T.; Nagata, H.; Hiruma, Y.; Yoshii, Y.; Matumoto, K., *Journal of Electroceramics*, **2007**, *19*, 259.
[29] Ahart, M.; Somayazulu, M.; Cohen, R. E.; Ganesh, P.; Dera, P.; Mao, H. K.; Hemley, R. J.; Ren, Y.; Liermann, P.; Wu, Z. G., *Nature*, **2008**, *451*, 545.
[30] Noheda, B.; Gonzalo, J. A.; Guo, R.; Park, S. E.; Cross, L. E.; Cox, D. E.; Shirane, G. In *Fundamental Physics of Ferroelectrics 2000*; Cohen, R. E., Ed. **2000**; Vol. 535, p 304.
[31] Singh, A. K.; Pandey, D.; Yoon, S.; Baik, S.; Shin, N., *Applied Physics Letters*, **2007**, *91*.
[32] Pandey, D.; Singh, A. K.; Baik, S., *Acta Crystallographica A*, **2008**, *64*, 192.
[33] Welberry, T. R.; Goossens, D. J.; Withers, R. L.; Baba-Kishi, K. Z., *Metallurgical and Materials Transactions A*, **2010**, *41A*, 1110.
[34] Ragini; Ranjan, R.; Mishra, S. K.; Pandey, D., *Journal of Applied Physics*, **2002**, *92*, 3266.
[35] Noheda, B.; Gonzalo, J. A.; Cross, L. E.; Guo, R.; Park, S. E.; Cox, D. E.; Shirane, G., *Physical Review B*, **2000**, *61*, 8687.

[36] Fu, H. X.; Cohen, R. E., *Nature*, **2000**, *403*, 281.
[37] Bellaiche, L.; Garcia, A.; Vanderbilt, D., *Physical Review Letters*, **2000**, *84*, 5427.
[38] Guo, R.; Cross, L. E.; Park, S. E.; Noheda, B.; Cox, D. E.; Shirane, G., *Physical Review Letters*, **2000**, *84*, 5423.
[39] Ringgaard, E.; Wurlitzer, T., *Journal of the European Ceramic Society*, **2005**, *25*, 2701.
[40] Saito, Y.; Takao, H.; Tani, T.; Nonoyama, T.; Takatori, K.; Homma, T.; Nagaya, T.; Nakamura, M., *Nature*, **2004**, *432*, 84.
[41] von Hippel, A.; Breckenridge, R. G.; Chesley, F. G.; Tisza, L., *Industrial & Engineering Chemistry*, **1946**, *38*, 1097.
[42] Kwei, G. H.; Lawson, A. C.; Billinge, J. L., *Journal of Physical Chemistry*, **1993**, *97*, 2368.
[43] Hiruma, Y.; Nagata, H.; Takenaka, T., *Japanese Journal of Applied Physics Part 1*, **2006**, *45*, 7409.
[44] Takenaka, T.; Maruyama, K.; Sakata, K., *Japanese Journal of Applied Physics Part 1*, **1991**, *30*, 2236.
[45] Sasaki, A.; Chiba, T.; Mamiya, Y.; Otsuki, E., *Japanese Journal of Applied Physics Part 1*, **1999**, *38*, 5564.
[46] Ishii, H.; Nagata, T.; Takenaka, T., *Japanese Journal of Applied Physics Part 1*, **2001**, *40*, 5660.
[47] Ishibashi, Y., *Ferroelectrics*, **2002**, *267*, 191.
[48] Chakoumakos, B. C.; Custelcean, R.; Kamlyama, T.; Oikawa, K.; Sales, B. C.; Lumsden, M. D., *Journal of Solid State Chemistry*, **2007**, *180*, 812.
[49] Asahi, T.; Osaka, T.; Kobayashi, J.; Abrahams, S. C.; Nanamatsu, S.; Kimura, M., *Physical Review B*, **2001**, *6309*.
[50] Höche, T.; Rüssel, C.; Neumann, W., *Solid State Communications*, **1999**, *110*, 651.
[51] Foster, M. C.; Arbogast, D. J.; Nielson, R. M.; Photinos, P.; Abrahams, S. C., *Journal of Applied Physics*, **1999**, *85*, 2299.
[52] Coats, A. M.; Hirose, N.; Marr, J.; West, A. R., *Journal of Solid State Chemistry*, **1996**, *126*, 105.
[53] Markgraf, S. A.; Randall, C. A.; Bhalla, A. S.; Reeder, R. J., *Solid State Communications*, **1990**, *75*, 821.
[54] Markgraf, S. A.; Randall, C. A.; Bhalla, A. S., *Ferroelectrics Letters*, **1990**, *11*, 99.
[55] Markgraf, S. A.; Bhalla, A. S., *Phase Transitions*, **1989**, *18*, 55.
[56] Markgraf, S. A.; Halliyal, A.; Bhalla, A. S.; Newnham, R. E.; Prewitt, C. T., *Ferroelectrics*, **1985**, *62*, 17.
[57] Iijima, K.; Marumo, F.; Kimura, M.; Kawamura, T., *Nippon Kagaku Kaishi*, **1981**, *10*, 1557.
[58] Halliyal, A.; Bhalla, A. S.; Newnham, R. E.; Cross, L. E.; Gururaja, T. R., *Journal of Materials Science*, **1982**, *17*, 295.
[59] Halliyal, A.; Bhalla, A. S.; Markgraf, S. A.; Cross, L. E.; Newnham, R. E., *Ferroelectrics*, **1985**, *62*, 27.
[60] Schmid, H.; Genequand, P.; Tippmann, H.; Pouilly, G.; Guédu, H., *Journal of Materials Science*, **1978**, *13*, 2257.
[61] Alfors, J. T.; Stinson, M. C.; Matthews, R. A.; Pabst, A., *American Mineralogist*, **1965**, *50*, 314.
[62] Masse, R.; Grenier, J. C.; Durif, A., *Bulletin Societe de la Francaise Mineralogie et de Cristallographie*, **1967**, *90*, 20.
[63] Moore, P. B.; Louisnathan, J., *Science*, **1967**, *156*, 1361.
[64] Smith, J. V., *American Mineralogist*, **1953**, *38*, 643.
[65] Kusaka, K.; Hagiya, K.; Ohmasa, M.; Okano, Y.; Mukai, M.; Iishi, K.; Haga, N., *Physics and Chemistry of Minerals*, **2001**, *28*, 150.
[66] Brown, I. D.; Altermatt, D., *Acta Crystallographica B*, **1985**, *41*, 244.
[67] Gaewdang, T.; Chaminade, J. P.; Gravereau, P.; Garcia, A.; Fouassier, C.; Hagenmüller, P.; Mahiou, R., *Materials Research Bulletin*, **1993**, *28*, 1051.
[68] Nyman, H.; O'Keeffe, M.; Bovin, J. O., *Acta Crystallographica B*, **1978**, *34*, 905.
[69] Woodrow, P. J., *Nature*, **1964**, *204*, 375.
[70] Yakubovich, O.; Kireev, V.; Mel'nikov, O., *Crystallography Reports*, **2000**, *45*, 578.

[71] Höche, T.; Esmaeilzadeh, S.; Uecker, R.; Lidin, S.; Neumann, W., *Acta Crystallographica B*, **2003**, *59*, 209.
[72] Höche, T.; Neumann, W.; Esmaeilzadeh, S.; Uecker, R.; Lentzen, M.; Rüssel, C., *Journal of Solid State Chemistry*, **2002**, *166*, 15.
[73] Blasse, G., *Journal of Inorganic & Nuclear Chemistry*, **1968**, *30*, 2283.
[74] Kimura, M.; Doi, K.; Nanamatsu, S.; Kawamura, T., *Applied Physics Letters*, **1973**, *23*, 531.
[75] Kimura, M.; Fujino, Y.; Kawamura, T., *Applied Physics Letters*, **1976**, *29*, 227.
[76] Haussühl, S.; Eckstein, J.; Wallrafen, F.; Recker, K., *Journal of Crystal Growth*, **1977**, *40*, 200.
[77] Kimura, M.; Utsumi, K.; Nanamatsu, S., *Journal of Applied Physics*, **1976**, *47*, 2249.
[78] Lang, S. B., *Physical Review B*, **1971**, *4*, 3603.
[79] Gladkii, V. V.; Zheludev, I. S., *Kristallografiya*, **1965**, *10*, 50.
[80] Feltz, A.; Schmalfuss, S.; Langbein, H.; Tietz, M., *Zeitschrift Für anorganische*, **1975**, *417*, 125.
[81] Höche, T.; Esmaeilzadeh, S.; Withers, R. L.; Schirmer, H., *Zeitschrift Fur Kristallographie*, **2003**, *218*, 788.
[82] Galy, J.; Carpy, A., *Acta Crystallographica B*, **1975**, *31*, 1794.
[83] Withers, R. L.; Höche, T.; Liu, Y.; Esmaeilzadeh, S.; Keding, R.; Sales, B., *Journal of Solid State Chemistry*, **2004**, *177*, 3316.
[84] Liu, G.; Greedan, J. E., *Journal of Solid State Chemistry*, **1995**, *114*, 499.
[85] Andrukaitis, E.; Jacobs, P. W. M.; Lorimer, J. W., *Canadian Journal of Chemistry - Revue Canadienne de chimie*, **1990**, *68*, 1283.
[86] Barbar, S. K.; Roy, M., *Journal of the American Ceramic Society*, **2011**, *94*, 843.
[87] Shannon, R. D., *Acta Crystallographica A*, **1976**, *32*, 751.
[88] Iijima, K.; Marumo, F.; Kimura, M.; Kawamura, T., *Mineralogical Journal*, **1982**, *11*, 107.
[89] Abrahams, S. C., *Acta Crystallographica B*, **1988**, *44*, 585.
[90] Van Heurck, C.; Van Tendeloo, G.; Amelinckx, S., *Physics and Chemistry of Minerals*, **1992**, *18*, 441.
[91] Hemingway, B. S.; Evans, H. T.; Nord, G. L.; Haselton, H. T.; Robie, R. A.; McGee, J. J., *Canadian Mineralogist*, **1986**, *24*, 425.
[92] Van Smaalen, S., *Incommensurate crystallography*; Oxford University Press, USA, 2007.
[93] Van Smaalen, S., *Zeitschrift Fur Kristallographie*, **2004**, *219*, 681.
[94] Janner, A.; Janssen, T., *Physica A: Statistical and Theoretical Physics*, **1979**, *99*, 47.
[95] Janner, A.; Janssen, T., *Physical Review B*, **1977**, *15*, 643.
[96] De Wolff, P., *Acta Crystallographica A*, **1974**, *30*, 777.
[97] De Wolff, P. M., *Acta Crystallographica A*, **1977**, *33*, 493.
[98] Withers, R. L.; Schmid, S.; Thompson, J. G., *Progress in Solid State Chemistry*, **1998**, *26*, 1.
[99] Tsakalakos, T.; Jankowski, A. F., *Annual Review of Materials Science*, **1986**, *16*, 293.
[100] Terada, N.; Mitsuda, S.; Tanaka, Y.; Tabata, Y.; Katsumata, K.; Kikkawa, A., *Journal of the Physical Society of Japan*, **2008**, *77*, 054701.
[101] Song, Y. J.; Yang, H. X.; Tian, H. F.; Ma, C.; Qin, Y. B.; Zeng, L. J.; Shi, H. L.; Lu, J. B.; Li, J. Q., *Physical Review B*, **2010**, *81*.
[102] Axe, J. D., *Philosophical Transactions of the Royal Society of London Series B - Biological Sciences*, **1980**, *290*, 593.
[103] Rae, A. D.; Thompson, J. G.; Withers, R. L., *Acta Crystallographica B*, **1992**, *48*, 418.
[104] Janssen, T.; Tjon, J. A., *Physical Review B*, **1981**, *24*, 2245.
[105] Chapuis, G., *Crystal Engineering*, **2003**, *6*, 187.
[106] De Wolff, P. M.; Janssen, T.; Janner, A., *Acta Crystallographica A*, **1981**, *37*, 625.
[107] Withers, R. L.; Ling, C. D.; Schmid, S., *Zeitschrift Fur Kristallographie*, **1999**, *214*, 296.
[108] Ling, C. D.; Withers, R. L.; Schmid, S.; Thompson, J. G., *Journal of Solid State Chemistry*, **1998**, *137*, 42.
[109] Esmaeilzadeh, S., *Ferroelectrics*, **2001**, *250*, 63.
[110] Valldor, M.; Esmaeilzadeh, S.; Pay-Gomez, C.; Grins, J., *Journal of Solid State Chemistry*, **2000**, *152*, 573.

[111] Yamamoto, A., *Acta Crystallographica Section B-Structural Science*, **1982**, *38*, 1451.
[112] Perez-Mato, J. M.; Madariaga, G.; Zuniga, F. J.; Garcia Arribas, A., *Acta Crystallographica Section A*, **1987**, *43*, 216.
[113] Van Smaalen, S., *Crystallography Reviews*, **1995**, *4*, 79.
[114] Chang, Z. P.; Bhalla, A. S., *Materials Letters*, **1989**, *8*, 418.
[115] Dove, M. T.; Gambhir, M.; Hammonds, K. D.; Heine, V.; Pryde, A. K. A., *Phase Transitions*, **1996**, *58*, 121.
[116] Giddy, A. P.; Dove, M. T.; Pawley, G. S.; Heine, V., *Acta Crystallographica A*, **1993**, *49*, 697.
[117] Dove, M. T.; Hammonds, K. D.; Heine, V.; Withers, R. L.; Xiao, Y.; Kirkpatrick, R. J., *Physics and Chemistry of Minerals*, **1996**, *23*, 56.
[118] Hua, G. L.; Welberry, T. R.; Withers, R. L.; Thompson, J. G., *Journal of Applied Crystallography*, **1988**, *21*, 458.
[119] Dove, M. T.; Heine, V.; Hammonds, K. D., *Mineralogical Magazine*, **1995**, *59*, 629.
[120] Withers, R. L.; Tabira, Y.; Liu, Y.; Höche, T., *Physics and Chemistry of Minerals*, **2002**, *29*, 624.
[121] Hammonds, K. D.; Dove, M. T.; Giddy, A. P.; Heine, V.; Winkler, B., *American Mineralogist*, **1996**, *81*, 1057.
[122] Mann, M.; Abbott, E. E.; Kolis, J. W., *Journal of Crystal Growth*, **2010**, *312*, 3395.
[123] Abbott, E. E.; Mann, M.; Kolis, J. W., *Journal of Solid State Chemistry*, **2011**, *184*, 1257.
[124] Wong, C. L.; Ferraris, C.; White, T. J., *Journal of Solid State Chemistry*, **2011**, *184*, 1768.
[125] Bindi, L.; Dušek, M.; Petříček, V.; Bonazzi, P., *Acta Crystallographica B*, **2006**, *62*, 1031.
[126] Wallwork, K.; Kennedy, B. J.; Wang, D., *AIP Conference Proceedings*, **2007**, *879*.
[127] Schmitt, B.; Brönnimann, C.; Eikenberry, E. F.; Gozzo, F.; Hormann, C.; Horisberger, R.; Patterson, B., *Nuclear Instruments & Methods in Physics Research A*, **2003**, *501*, 267.
[128] Suard, E.; Hewat, A., *Neutron News*, **2001**, *12*, 30
[129] Studer, A. J.; Hagen, M. E.; Noakes, T. J., *Physica B - Condensed Matter*, **2006**, *385-86*, 1013.
[130] Schoenborn, B. P.; Langan, P., *Journal of Synchrotron Radiation*, **2004**, *11*, 80.
[131] Fried, J.; Harder, J. A.; Mahler, G. J.; Makowiecki, D. S.; Mead, J. A.; Radeka, V.; Schaknowski, N. A.; Smith, G. C.; Yu, B., *Nuclear Instruments & Methods in Physics Research A*, **2002**, *478*, 415.
[132] Young, R. A., *The Rietveld Method*; Oxford University Press, Chester, 1993.
[133] Howard, C. J.; Kennedy, S. J., *Materials Forum*, **1994**, *18*, 155.
[134] *Echidna Specifications Page*; Bragg Institute, ANSTO, Accessed 18/3/2011, http://www.ansto.gov.au/research/bragg_institute/facilities/instruments/echidna/specifications
[135] *Wombat Specifications Page*; Bragg Institute, ANSTO, Accessed 18/3/2011, http://www.ansto.gov.au/research/bragg_institute/facilities/instruments/wombat/specifications
[136] Bish, D. L.; Post, J. E., *Modern Powder Diffraction*; Mineralogical Society of America, Washington D.C., 1989.
[137] Ibberson, R. M.; David, W. I. F.; Knight, K. S., *The High Resolution Neutron Powder Diffractometer (HRPD) at ISIS - A User Guide*; Rutherford Appleton Laboratory Report, 1992.
[138] Lide, D. R., *CRC Handbook of Chemistry and Physics*; CRC Press, Internet Version, 2011.
[139] Pérez-Mato, J. M.; Madariaga, G.; Tello, M. J., *Physical Review B*, **1984**, *30*, 1534.
[140] Rietveld, H. M., *Journal of Applied Crystallography*, **1969**, *2*, 65.
[141] Young, R. A.; Wiles, D. B., *Journal of Applied Crystallography*, **1982**, *15*, 430.
[142] Hunter, B.; Howard, C. J., *A Computer Program for Rietveld Analysis of X-Ray and Neutron Powder Diffraction Patterns*; Lucas Heights Laboratories, 1998.
[143] Howard, C. J., *Journal of Applied Crystallography*, **1982**, *15*, 615.
[144] Jansen, E.; Schafer, W.; Will, G., *Journal of Applied Crystallography*, **1994**, *27*, 492.
[145] Hill, R. J.; Fischer, R. X., *Journal of Applied Crystallography*, **1990**, *23*, 462.
[146] Petříček, V.; Dušek, M.; Palatinus, L., *Jana2006. The Crystallographic Computing System*; Institute of Physics, Praha, Czech Republic, 2006.

[147] Migliori, A.; Sarrao, J. L., *Resonant Ultrasound Spectroscopy: Applications to Physics, Material Measurements and Nondestructive Evaluation*; 1 ed.; John Wiley and Sons Inc., New York, 1997.
[148] Maynard, J., *Physics Today*, **1996**, *49*, 26.
[149] Migliori, A.; Maynard, J. D., *Review of Scientific Instruments*, **2005**, *76*.
[150] McKnight, R. E. A. PhD Thesis, University of Cambridge, 2009.
[151] Young, K. F.; Frederikse, H. P. R., *Journal of Physical and Chemical Reference Data*, **1973**, *2*, 12.
[152] Kannan, C. V.; Shimamura, K.; Zeng, H. R.; Kimura, H.; Villora, E. G.; Kitamura, K., *Journal of Applied Physics*, **2008**, *104*, 114113.
[153] Wong, C. L. PhD Thesis, Nanyang Technological University, 2011.
[154] Mittemeijer, E. J.; Welzel, U., *Zeitschrift Fur Kristallographie*, **2008**, *223*, 552.
[155] Balzar, D., *Journal of Research of the National Institute of Standards and Technology*, **1993**, *98*.
[156] Balzar, D.; Ledbetter, H., *Journal of Applied Crystallography*, **1993**, *26*, 97.
[157] Bertaut, E. F., *Crystallography Reviews*, **1990**, *2*, 107
[158] Overhauser, A. W., *Physical Review B*, **1971**, *3*, 3173.
[159] Axe, J. D., *Physical Review B*, **1980**, *21*, 4181.
[160] Amarasekara, C. D.; Keesom, P. H., *Physical Review B*, **1982**, *26*, 2720.
[161] Sawada, A.; Satoh, T., *Journal of Low Temperature Physics*, **1978**, *30*, 455.
[162] Ashraf, M.; Swihart, J. C., *Physical Review Letters*, **1983**, *50*, 921.
[163] Bernard, L.; Currat, R.; Delamoye, P.; Zeyen, C. M. E.; Hubert, S.; Dekouchkovsky, R., *Journal of Physics C*, **1983**, *16*, 433.
[164] Chapman, L. D.; Colella, R., *Physical Review Letters*, **1984**, *52*, 652.
[165] Bindi, L.; Bonazzi, P., *Physics and Chemistry of Minerals*, **2005**, *32*, 89.
[166] Aizu, K., *Journal of the Physical Society of Japan*, **1987**, *56*, 603.
[167] Ishibashi, Y., *Ferroelectrics*, **1980**, *24*, 119.
[168] Carpenter, M. A.; Salje, E. K. H.; Graeme-Barber, A., *European Journal of Mineralogy*, **1998**, *10*, 621.
[169] Pokrovsky, V. L.; Talapov, A. L., *Physical Review Letters*, **1979**, *42*, 65.
[170] Melero, J. J.; Bartolomé, J.; Burriel, R.; Aleksandrova, I. P.; Primak, S., *Solid State Communications*, **1995**, *95*, 201.
[171] Carpenter, M. A.; Buckley, A.; Taylor, P. A.; Darling, T. W., *Journal of Physics-Condensed Matter*, **2010**, *22*.
[172] Hatta, I., *Journal of the Physical Society of Japan*, **1983**, *53*, 635.
[173] Carpenter, M. A., *Reviews in Mineralogy and Geochemistry*, **2000**, *39*, 35.
[174] Carpenter, M. A.; Li, B. S.; Liebermann, R. C., *American Mineralogist*, **2007**, *92*, 344.
[175] Sebastian, M. T.; Jantunen, H., *International Materials Reviews*, **2008**, *53*, 57.
[176] Wilk, G. D.; Wallace, R. M.; Anthony, J. M., *Journal of Applied Physics*, **2001**, *89*, 5243.
[177] Pan, K.; Liu, Y. Y.; Liu, Y. M.; Li, J. Y., *Journal of Applied Physics*, **2012**, *112*.
[178] Smith, W. A., *Procedings of the SPIE - The International Society for Optical Engineering*, **1992**, 1733.
[179] Jaffe, B.; Cook, W. R.; Jaffe, H., *Piezoelectric Ceramic*; Academic, New York, 1971.
[180] Ueda, I.; Kobayashi, S.; Ikegami, S., *National Technical Report*, **1972**, *18*, 413.
[181] Berlincourt, D. A.; Cmolik, C.; Jaffe, H., *Proceedings of the IEEE*, **1960**, *48*, 220.
[182] Scott, J. F., *Journal of Physics-Condensed Matter*, **2008**, *20*.
[183] Schneider, M.; Richter, W.; Keding, R.; Rüssel, C., *Journal of Non-Crystalline Solids*, **1998**, *226*, 273.
[184] Manolikas, C., *Physica Status Solidi A- Applied Research*, **1981**, *68*, 653.
[185] Mori, S.; Yamamoto, N.; Koyama, Y.; Uesu, Y., *Physical Review B*, **1997**, *55*, 11212.
[186] Barre, S.; Mutka, H.; Roucau, C., *Physical Review B*, **1988**, *38*, 9113.
[187] Schneck, J.; Primot, J.; Vondermuhll, R.; Ravez, J., *Solid State Communications*, **1977**, *21*, 57.
[188] Axe, J. D.; Moudden, A. H.; Hohlwein, D.; Cox, D. E.; Mohanty, K. M.; Moodenbaugh, A. R.; Xu, Y., *Physical Review Letters*, **1989**, *62*, 2751.

[189] Birgeneau, R. J.; Chen, C. Y.; Gabbe, D. R.; Jenssen, H. P.; Kastner, M. A.; Peters, C. J.; Picone, P. J.; Thio, T.; Thurston, T. R.; Tuller, H. L.; Axe, J. D.; Böni, P.; Shirane, G., *Physical Review Letters*, **1987**, *59*, 1329.
[190] Böni, P.; Axe, J. D.; Shirane, G.; Birgeneau, R. J.; Gabbe, D. R.; Jenssen, H. P.; Kastner, M. A.; Peters, C. J.; Picone, P. J.; Thurston, T. R., *Physical Review B*, **1988**, *38*, 185.
[191] Solans, X.; Gonzalez-Silgo, C.; Ruiz-Perez, C., *Journal of Solid State Chemistry*, **1997**, *131*, 350.
[192] Bleif, H.-J.; Dachs, H., *Acta Crystallographica Section A*, **1982**, *38*, 470.
[193] Kimber, S. A. J.; Rodgers, J. A.; Wu, H.; Murray, C. A.; Argyriou, D. N.; Fitch, A. N.; Khomskii, D. I.; Attfield, J. P., *Physical Review Letters*, **2009**, *102*.
[194] Richardson, J. W.; Long Price, D.; Sabougni, M.-L., *Physical Review Letters*, **1996**, *76*, 1852.
[195] Herrero-Albillos, J.; Marchment, P.; Salje, E. K. H.; Carpenter, M. A.; Scott, J. F., *Physical Review B*, **2009**, *80*.
[196] Ikeda, T., *Japanese Journal of Applied Physics*, **1974**, *13*.
[197] Scott, J. F.; Hayward, S. A.; Miyake, M., *Journal of Physics-Condensed Matter*, **2005**, *17*, 5911.
[198] Kiat, J. M.; Calvarin, G.; Schneck, J., *Physical Review B*, **1994**, *49*, 776.
[199] Masse, R.; Durif, A., *Bulletin De La Societe Francaise Mineralogie Et De Cristallographie*, **1967**, *90*, 407.
[200] Halliyal, A.; Bhalla, A. S.; Cross, L. E., *Ferroelectrics*, **1985**, *62*, 3.
[201] Tobbens, D. M.; Kahlenberg, V.; Gspan, C.; Kothleitner, G., *Acta Crystallographica B*, **2006**, *62*, 1002.
[202] Wong, C. L.; Madhavi, S.; Phonthammachai, N.; White, T. J., *Journal of Solid State Chemistry*, **2012**, *187*, 165.
[203] Vegard, L., *Zeitschrift Fur Physik*, **1921**, *5*, 17.
[204] Denton, A. R.; Ashcroft, N. W., *Physical Review A*, **1991**, *43*, 3161.
[205] Farges, F., *Journal of Non-Crystalline Solids*, **1996**, *204*, 53.
[206] Farges, F.; Brown, G. E.; Rehr, J. J., *Physical Review B*, **1997**, *56*, 1809.
[207] Yamamoto, T., *X-Ray Spectrometry*, **2008**, *37*, 572.
[208] Zhu, M. K.; Wang, B.; Liu, P.; Yan, H.; Ding, Z. Y., *Optical Materials*, **2003**, *23*, 323.
[209] Höche, T.; van Aken, P. A.; Grodzicki, M.; Heyroth, F.; Keding, R.; Uecker, R., *Philosophical Magazine*, **2004**, *84*, 3117.